

EFFECTIVE STRESS BASED CONSTITUTIVE MODELLING AND
ASSESSMENT OF SEISMIC PILE-SOIL INTERACTION
IN LIQUEFIABLE SOILS

A THESIS SUBMITTED TO
THE GRADUATE SCHOOL OF NATURAL AND APPLIED SCIENCES
OF
MIDDLE EAST TECHNICAL UNIVERSITY

BY

SEVİNÇ ÜNSAL ORAL

IN PARTIAL FULFILLMENT OF THE REQUIREMENTS
FOR
THE DEGREE OF DOCTOR OF PHILOSOPHY
IN
CIVIL ENGINEERING

MAY 2014

Approval of the thesis:

**EFFECTIVE STRESS BASED CONSTITUTIVE MODELLING AND
ASSESSMENT OF SEISMIC PILE-SOIL INTERACTION
IN LIQUEFIABLE SOILS**

submitted by **SEVİNÇ ÜNSAL ORAL** in partial fulfillment of the requirements
for the degree of **Doctor of Philosophy in Civil Engineering Department,**
Middle East Technical University by,

Prof. Dr. Canan Özgen
Dean, Graduate School of **Natural and Applied Sciences**

Prof. Dr. Ahmet Cevdet Yalçın
Head of Department, **Civil Engineering**

Prof. Dr. Kemal Önder Çetin
Supervisor, **Civil Engineering Dept., METU**

Examining Committee Members:

Prof. Dr. Orhan Erol
Civil Engineering Dept., METU

Prof. Dr. Kemal Önder Çetin
Civil Engineering Dept., METU

Prof. Dr. Yener Özkan
Civil Engineering Dept., METU

Doç. Dr. Levent Tutluoğlu
Mining Engineering Dept., METU

Prof. Dr. Bilge Siyahi
Dept. of Earthquake and Structural Eng., GYTE

Date:

29 .05.2014

I hereby declare that all information in this document has been obtained and presented in accordance with academic rules and ethical conduct. I also declare that, as required by these rules and conduct, I have fully cited and referenced all material and results that are not original to this work.

Name, Last Name: SEVİNÇ ÜNSAL ORAL

Signature :

ABSTRACT

EFFECTIVE STRESS BASED CONSTITUTIVE MODELLING AND ASSESSMENT OF SEISMIC PILE-SOIL INTERACTION IN LIQUEFIABLE SOILS

Ünsal Oral, Sevinç

Ph.D., Department of Civil Engineering

Supervisor: Prof Dr. Kemal. Önder Çetin

May 2014, 284 pages

The assessment of liquefaction-induced deformations of foundation soils located in seismically active regions has been a major concern for geotechnical earthquake engineers. In spite of the existing efforts, the prediction of these deformations has remained a "soft" area of practice. Inspired by this gap, a new fully coupled, two-dimensional, effective stress-based, nonlinear and simplified constitutive model, referred to as METUSAND, is developed. As a part of the model development efforts, a "C++" subroutine was implemented in commercially available software FLAC based on semi-empirical cyclic straining and excess pore water pressure assessment models of Cetin et al., Cetin and Bilge and Shamoto et al. For verification purposes, well known liquefaction-induced ground deformation case history sites of Wildlife Site, Imperial Valley, California, shaken by 1987 Superstition Hills earthquake and Port Island Array, Kobe, shaken by 1995 Hyogo-ken Nanbu earthquake are re-assessed by using

METUSAND. The analysis results confirmed that the proposed semi-empirical constitutive model METUSAND, can reliably predict liquefaction triggering and post liquefaction straining responses. Then, for the purpose of assessing lateral seismic deformation behavior of a single pile buried in liquefiable soils, series of numerical simulations were performed. On the basis of these numerical simulation results, and inspired by NAVFAC and Duncan Characteristic Load Method, semi-empirical models to assess seismic deformation performance of piles buried in liquefiable soils were developed. Again, these recommended models were validated with actual well documented centrifuge test results. The validation studies confirmed that the proposed framework can predict pile deformations accurately within a precision of a factor of maximum two.

Keywords: Seismic soil-pile interaction, liquefaction, lateral pile capacity, constitutive modelling, effective stress analyses.

ÖZ

EFEKTİF GERİLME TEMELLİ ZEMİN BÜNYE MODELLEMESİ VE SIVILAŞABİLİR ZEMİNLER İÇİNDEKİ KAZIKLARDA SİSMİK KAZIK-ZEMİN ETKİLEŞİMİNİN DEĞERLENDİRİLMESİ

Ünsal Oral, Sevinç

Doktora, İnşaat Mühendisliği Bölümü

Tez Yöneticisi: Prof. Dr. Kemal Önder Çetin

Mayıs 2014, 284 sayfa

Sismik olarak aktif bölgelerdeki zeminlerde, sıvılaşmaya bağlı deformasyonların belirlenmesi geoteknik deprem mühendisleri için büyük bir eksiklik olmaya devam etmektedir. Mevcut çalışmalara rağmen, bu deformasyon değerlerini tahmin etmek uygulamanın yumuşak karnıdır. Bu eksiklikten yararlanılarak, tamamıyla bütünleşik, iki boyutlu, efektif gerilme tabanlı ve doğrusal olmayan bir bünye modeli geliştirilmiş olup, METUSAND olarak anılacaktır. Geliştirilen model, C++ formatında DLL “altprogramı” olarak FLAC ticari yazılımına eklenmiştir. METUSAND, Cetin et al., Cetin ve Bilge, ve Shamoto et al. modellerinin yarı ampirik döngüsel gerilme ve aşırı boşluk suyu basıncı tahminine dayanmaktadır. Önerilen bünye modelinin geçerliliğini teyhid etmek amacı ile, tipik vaka örnekleri olan ve 1987 yılında meydana gelen “Superstition Hills” depreminde Kaliforniya eyaletinin “Imperial Vadisi” Wildlife sahasındaki ve 1995 yılında meydana gelen “Hyogo-ken Nanbu” depreminde Kobe’de “Port Island” sahasındaki zemin sıvılaşması modellenmiştir. Analiz sonuçlarına göre,

bahsedilen vaka örneklerinde meydana gelen zemin sıvılaşması tetiklenmesi ve sıvılaşma sonrası deformasyon değerleri METUSAND modeli ile elde edilen değerlerle uyumludur. Ardından, sıvılaşabilen bir zemine yerleştirilen tekil kazığın yatay sismik deformasyonunu incelemek amacıyla sayısal simülasyonlar yapılmıştır. NAVFAC ve Duncan Karakteristik Yük Yöntemi 'nden yararlanılarak ve sayısal simülasyon sonucu esas alınarak sıvılaşabilen zeminler içinde yer alan kazıkların sismik deformasyon davranışını belirlemek üzere yarı ampirik bağıntılar geliştirilmiştir. Geliştirilen bu bağıntılar iyi dökümanlanmış santrifüj deneyleri ile doğrulanmıştır. Doğrulama çalışmaları, sunulan yöntemin kazıkların yatay deformasyonlarını en fazla çarpı iki bölü iki mertebelerindeki bir hassasiyetle bulabileceğini kanıtlamıştır.

Anahtar Kelimeler: Sismik kazık-zemin etkileşimi, sıvılaşma, yatay kazık kapasitesi, bünye modeli, efektif gerilme analizi

To My Beloved Father İLYAS ÜNSAL who never gave up...

ACKNOWLEDGEMENTS

Words are not enough to express my grateful appreciation to my advisor, Prof. Dr. Kemal Önder Çetin, for his continuous encouragement and guidance throughout this study. Without his ambition, insightful remarks, unlimited assistance, patience and tolerance, this thesis would not have been possible. His wisdom and ever-strong confidence have changed and will continue to influence my life philosophy.

Thanks are also due to the members of my dissertation committee: Dr. M. Yener Özkan and Dr. Levent Tutluoğlu, for their constructive suggestions throughout this research period.

I would further like to thank to Dr. H. Tolga Bilge for his valuable guidance and support and also friendship throughout the study.

I would like to extend my gratitude to Prof. John Curran for giving me the opportunity to work with ROCSCIENCE. I owe further thanks to Dr. Alireza Azami for his positive approach and considerable support during my graduate studies in Toronto.

Never to be forgotten are my dearest friends; Damla Diker, Gülşah Fidan, Kamil Sulubulut, Yelda-Mesut Delice and Umut-Çiğdem Türer, whose friendship and moral support are invaluable for me.

I also would like to convey my deepest thanks to my parents İlyas-Nazmiye ÜNSAL, my sister Seçil Ünsal and mother-in-law and father-in-law Nesrin-Lütfi Oral for their support and encouragement.

Last but not least, the most special thanks and sincere appreciations of mine go to my husband Yaşar Zahit ORAL who dedicated his life, his love and all his understanding to me. Finally, thanks are for my little son Erdem Demir Oral, for being with me.

TABLE OF CONTENTS

ABSTRACT	V
ÖZ.....	VII
ACKNOWLEDGEMENTS	X
TABLE OF CONTENTS	XII
LIST OF FIGURES	XVII
LIST OF TABLES	XXII
LIST OF ABBREVIATIONS	XXIII
CHAPTERS.....	1
1. INTRODUCTION.....	1
1.1. Research Statement.....	1
1.2. Problem Significance and Limitations of Previous Studies.....	2
1.3. Scope of This Study.....	5
2. LITERATURE REVIEW ON CYCLIC RESPONSE OF SATURATED COHESIONLESS SOLIS.....	7
2.1. Introduction.....	7
2.2. Theoretical Framework for Liquefaction Susceptibility.....	8
2.2.1. Liquefaction Mechanisms and Influence of Dilatancy	10
2.2.2. Liquefaction Triggering Assessments	15
2.3. Cyclic Straining-induced Stiffness Degradation Response	17
2.3.1. Modulus Degradation and Damping Response of Granular Soils .	18
2.4. Cyclic Straining and Induced Pore Pressure Models.....	21
2.4.1. Stress Based Pore Pressure Models.....	21
2.4.2. Strain Based Pore Pressure Models.....	22
2.4.3. Other Pore Pressure Generation Models	24

2.4.4. Probabilistic Models for Cyclic Straining and Induced Pore Pressure	25
2.5. Comprehensive Liquefaction Constitutive Models	29
2.5.1. Total Stress-Based Models	30
2.5.2. Loosely Coupled Effective Stress-Based Models.....	31
2.5.3. Fully Coupled Effective Stress-Based Models	32
2.5.3.1. WANG (1990) Model	33
2.5.3.2. NTUA-SAND Model	33
2.5.3.3. UBCSAND Model (2009, 2012).....	34
2.5.3.4. PM4Sand Model (2012)	40
2.6. Conclusion.....	44
3. THEORETICAL BASIS OF THE PROPOSED CONSTUTUTIVE MODEL AND ITS NUMERICAL IMPLEMENTATION	45
3.1. Introduction	45
3.2. Description of Proposed METUSAND Model	46
3.2.1. Elastic Response	47
3.2.2. Effective-stress Based Nonlinear (Incrementally Linear) Soil Response	49
3.2.2.1. Yield Criterion.....	49
3.2.2.2. Modulus Degradation and Damping Response	51
3.2.2.3. Loading and Unloading Definitions and Plastic Shear Straining.....	58
3.2.2.4. Excess Pore Pressure Generation	60
3.2.3. Post-Liquefaction Soil Response	60
3.3. Numerical Implementation.....	68
3.4. Single Element Behavior of METUSAND	69
3.4.1. Comparison with Cyclic DSS Tests	73
3.4.2. Comparisons with Semi-Empirical Liquefaction Triggering Relationships.....	75
3.5. METUSAND Model Limitations and Challenges	79
4. VERIFICATION OF METUSAND MODEL.....	81
4.1. Introduction	81

4.2. Verification of the METUSAND Model Response with Wildlife Site Case History.....	82
4.2.1. Site Description, Instrumentation and Seismic Records	82
4.2.2. Idealized Soil Profile used in Finite Element Analyses	90
4.2.3. Numerical Static Analyses	92
4.2.4. Effective Stress-based Dynamic Response Analyses.....	95
4.2.5. Computed Dynamic Response and Comparison with Field Data ..	96
4.3. Prediction of Seismic Response of Port Island/Kobe Site	102
4.3.1. Site Description, Instrumentation and Seismic Records	102
4.3.2. Idealized Soil Profile Used in Finite Element Analyses	106
4.3.3. Initial Conditions and Static Analyses	107
4.3.4. Effective Stress Based Dynamic Analyses.....	109
4.3.5. Computed Dynamic Response and Comparison with Field Data	111
4.4. Conclusion	117
5. REVIEW ON METHODS FOR ASSESSMENT OF LATERALLY LOADED PILES RESPONSE.....	119
5.1. Introduction.....	119
5.2. Laterally Loaded Piles	121
5.3. The Ultimate Lateral Resistance of Laterally Loaded Piles	125
5.3.1. Brinch Hansen’s Method (1961)	127
5.3.2. Brom’s Method (1964).....	128
5.4. Methods of Calculating Mobilized Deflections	136
5.4.1. Elastic Continuum Method.....	136
5.4.2. Subgrade Reaction Method	137
5.4.3. P-y Curve Method	140
5.5. The Application of Subgrade Reaction Approach in Cohesionless Soil ..	143
5.5.1. Reese et al. (1974) Methodology	143
5.5.2. Method of Obtaining Soil Properties	144
5.5.3. Method of Calculating Non-dimensional Terms	149
5.5.4. Characteristic Load Method (CLM) (Duncan et al., 1994).....	154

6. DEVELOPMENT OF SEMI EMPRICAL MODELS TO ASSESS CYCLIC RESPONSE OF PILED FOUNDATIONS	159
6.1. Introduction	159
6.2. Numerical Modeling of Pile Elements in FLAC 7.0 Software	161
6.3. Numerical Analysis of Laterally Loaded Piles in Static Conditions..	164
6.4. Effective Stress Based Numerical Dynamic Analysis of Laterally Loaded Piles	171
6.5. Development of Semi-Empirical Models to Assess Cyclic Response of Laterally Loaded Piles in Saturated Cohesionless Soils.....	173
6.5.1. Model I for Dynamic Lateral Loading of Piles in Saturated Cohesionless Soils (Modified NAVFAC, 1986).....	173
6.5.1. Maximum Likelihood Framework for the Development of a Semi-Empirical Model: MODEL I.....	181
6.5.1. Model II for Dynamic Lateral Loading of Piles in Saturated Cohesionless Soils (Modified Duncan et al. 1994).....	189
6.5.1. Maximum Likelihood Framework for the Development of a Semi-Empirical Model: MODEL II	192
6.6. Validation of the Semi-Empirical Models through Experimental Investigations.....	198
6.6.1. CASE 1: Validation of the Model with Abdoun et al. (2003) Study .	198
6.6.2. CASE 2: Validation of the Model with Liu et al. (1995) Study.....	204
6.6.3. CASE 3: Validation of the model with He (2005) Study	210
6.6.4. CASE 4: Validation of the Model with Jakrapiyanun (2002) Study..	216
6.6.5. A summary of the Validation Efforts	221
6.7. Conclusion.....	223
7. SUMMARY AND CONCLUSIONS.....	227
7.1. Summary	227
7.2. Conclusion.....	230
7.3. Recommendations for Future Research	240
REFERENCES.....	241
APPENDICES	259

A.METUSAND DLL Module	259
B.Generic Simple Shear Test Input for METUSAND	277
C.Dynamic Analyses Combinations of Laterally Loaded Piles	280
CURRICULUM VITAE	283

LIST OF FIGURES

FIGURES

Figure 2.1. Ranges of Grain Size Distribution for Liquefaction Susceptible Soils (Tsuchida, 1970).....	9
Figure 2.2. Undrained stress-strain curve for a) loose sand and b) dense sand under seismic loading condition (Seed et al., 1989).....	10
Figure 2.3. Flow liquefaction and cyclic mobility susceptibility zones.....	11
Figure 2.4. Steady State line (after Castro and Poulos, 1977)	12
Figure 2.5. Phase transformation line at p'-q domain (after Ishihara, 1985).....	13
Figure 2.6. Stress-strain curves and effective stress paths for Banding Sand in CIU Tests (after Mohamad and Dobry, 1986)	14
Figure 2.7. Schematic diagram of cyclic liquefaction.....	14
Figure 2.8. SPT-based liquefaction triggering correlation for $M_w=7.5$ and $\sigma'_v = 1.0$ atm with adjustments for fines content (Cetin et al. 2004).....	17
Figure 2.9. Shear Moduli of Sands at Different Relative Densities.....	19
Figure 2.10. Hysteresis loop at smaller strains	20
Figure 2.11. Hysteresis loop at larger strain	20
Figure 2.12. Hysteretic stress-strain loop.....	21
Figure 2.13. Constant, cyclic shear-strain amplitude proposed by Byrne (1991). 24	24
Figure 2.14. Recommended maximum double amplitude shear strain boundary curves (Cetin et al., 2009).....	27
Figure 2.15. Recommended post cyclic volumetric strain boundary curves	27
Figure 2.16. Proposed r_u versus $\gamma_{max,N}$ model along with test results used in Cetin and Bilge (2012)	28
Figure 2.17. Yield surfaces for UBCSAND (Beaty and Byrne, 2011)	36
Figure 2.18. Relationship between stress ratio and plastic shear strains for UBCSAND (Beaty and Byrne, 2011)	37
Figure 2.19. Direction of plastic shear strains for UBCSAND.....	37
Figure 2.20. Critical state line and relative state parameter used in PM4Sand (Boulanger et al, 2012).....	40
Figure 2.21. Schematic of yield, critical, dilatancy, and bounding lines in q-p space (After Dafalias & Manzari, 2004)	41
Figure 2.22. Schematic of the bounding, dilation, and yield surfaces	42
Figure 3.1. Schematic illustration of METUSAND.....	46
Figure 3.2. Stress-Strain Relationship (Cetin and Bilge, 2014).....	53
Figure 3.3. Comparison of effective stress-based modulus degradation relationships (Cetin and Bilge, 2014) with existing models.....	54
Figure 3.4. Comparison of effective stress-based damping model (Cetin and Bilge, 2014) with existing models.....	55
Figure 3.5. Applied CSR (τ/σ'_{v0}) increased step by step in each loading cycle..	56
Figure 3.6. Shear stress-shear strain loop for increasing τ/σ'_{v0}	57

Figure 3.7. A comparison of the intrinsically developed damping values of METUSAND with existing strain dependent damping relations	57
Figure 3.8. Single Loading-Unloading cycle of the proposed model.....	59
Figure 3.9. Two post-liquefaction shear strain components observed in a typical cyclic undrained torsional shear test (Shamoto et al., 1998)	61
Figure 3.10. Post liquefaction physical states during undrained shear.....	62
Figure 3.11. Probable arrangement of sand particles during pre- and post-liquefaction undrained shearing (Shamoto et al., 1998)	63
Figure 3.12. Simple Shear Test (DSS) Simulation Model in FLAC	69
Figure 3.13. Simulation of METUSAND pre-liquefaction behavior ((N1)60 =7, $\sigma_{v0}' = 100$ kPa, $K_0 = 1.0$)	72
Figure 3.14. Simulation of METUSAND post-liquefaction behavior ((N1)60 =7, $\sigma_{v0}' = 100$ kPa, $K_0 = 1.0$)	73
Figure 3.15. Laboratory DSS and METUSAND response.....	74
Figure 3.16. Laboratory DSS and METUSAND response on undrained.....	75
Figure 3.17. Values of CRR predicted by METUSAND and compared to probabilistic semi-empirical relationships	78
Figure 3.18. Initial shear modulus, G_{max} obtained from different methods	78
Figure 3.19 Values of CRR predicted by METUSAND by using G_{max} obtained from different methods.....	79
Figure 4.1. Location Map of Wildlife Array (Holzer & Youd, 2007).....	83
Figure 4.2. Schematic cross section through Wildlife Liquefaction Array	84
Figure 4.3. Map of liquefaction effects caused by Superstition Hills earthquake, instrumentation, and CPT soundings (modified from Holzer et al., 1989a)..	85
Figure 4.4. Measured accelerations from Superstition Hills earthquake: North-South data (Holzer and Youd, 2007)	86
Figure 4.5. Measured accelerations from Superstition Hills earthquake: East-West data (Holzer and Youd, 2007).....	87
Figure 4.6. Pore water pressure time histories recorded during the 1987 Superstition Hills Earthquake (Holzer and Youd, 2007)	88
Figure 4.7. Excess pore pressure ratio, r_u at each piezometer (Holzer and Youd, 2007)	89
Figure 4.8. North-South shear stress-strain history at the Wildlife Site during liquefaction (Zeghal and Elgamal 1994)	90
Figure 4.9. Finite element/difference mesh and idealized soil profile	92
Figure 4.10. Finite element mesh and initial boundary condition	93
Figure 4.11. Initial vertical effective stress distribution of Wildlife site (kPa)	93
Figure 4.12. Initial horizontal effective stress distribution of Wildlife site(kPa)..	94
Figure 4.13. Initial pore water pressure distribution of Wildlife site (kPa).....	94
Figure 4.14. Material models and dynamic boundary condition.....	96
Figure 4.15. Computed and recorded acceleration time histories for ground surface and at 8 m depth	97
Figure 4.16. Computed and recorded response spectra for %5 damping at ground level.....	97
Figure 4.17. Excess pore pressure distribution, r_u , at $t=7.5$ sec.....	98
Figure 4.18. Excess pore pressure distribution, r_u , at $t=20$ sec.....	98

Figure 4.19. Excess pore pressure distribution, r_u , at $t=40$ sec.....	99
Figure 4.20. Excess pore pressure ratio vs dynamic time at location of field piezometers P1, P2, P3 and P5 at $t=40$ sec.....	99
Figure 4.21. Shear strain distribution, γ (%) at $t=40$ sn	100
Figure 4.22. Computed and recorded excess pore pressure ratio, r_u response ...	100
Figure 4.23. Computed and recorded excess pore pressure ratio, r_u response for piezometer P5	101
Figure 4.24. Areas of Damage in Hyogoken-Nanbu EQ of January, 1995	103
Figure 4.25. Port Island map after Nakakita and Watanabe (1981).....	104
Figure 4.26. Soil profile of the seismic array site at Port Island.....	104
Figure 4.27. Recorded horizontal accelerations with the down-hole array at Port Island (Cubrinovski et. al 1996)	106
Figure 4.28. Finite element/difference mesh and idealized soil profile.....	107
Figure 4.29. Initial Vertical Effective Stress Distribution of Port Island Site	108
Figure 4.30. Initial Horizontal Effective Stress Distribution of Port Island Site	108
Figure 4.31. Initial Pore Water Pressure Distribution of Port Island Site	109
Figure 4.32. Input motion used in numerical analyses	110
Figure 4.33. Material models and dynamic boundary condition	111
Figure 4.34. Computed and recorded acceleration time histories for ground surface and at 32 m depth.....	112
Figure 4.35. Computed and recorded response spectra for %5 damping at ground level.....	113
Figure 4.36. Excess pore pressure distribution, r_u , at $t=8.0$ sn.....	113
Figure 4.37. Excess pore pressure distribution, r_u , at $t=20$ sn.....	114
Figure 4.38. Excess pore pressure distribution, r_u , at $t=40$ sn.....	114
Figure 4.39. Excess pore pressure ratio vs dynamic time at depth 0.0m, 2.0 m, 4.0m and 7.0 m at $t=40$ sec.....	115
Figure 4.40. Shear strain vs dynamic time at depth 0.0m, 2.0 m, 4.0m and 7.0 m at $t=40$ sec.....	116
Figure 4.41. Shear strain distribution, γ (%) at $t=40$ sn	116
Figure 5.1. Collapse of some pile-supported structure during earthquakes.....	121
Figure 5.2. Short (rigid) pile failure mechanism and the nature of variation of pile deflection, moment and shear force	123
Figure 5.3. Long (elastic) pile failure mechanism and nature of variation of pile deflection, moment and shear force.....	124
Figure 5.4. Mobilization of lateral soil resistance on pile caused by lateral load for a free-head rigid pile (Prakash and Sharma, 1990).....	125
Figure 5.5. Brinch Hansen Method Coefficients K_q and K_c (Hansen,1961)	128
Figure 5.6. Soil reaction and bending moments on piles in cohesionless soils ...	130
Figure 5.7. Soil reaction and bending moments on piles in cohesive soils.....	131
Figure 5.8. Elastic Continuum Model approach (Poulos, 1971).....	137
Figure 5.9. Winkler idealization approach.....	138
Figure 5.10. Reese and Matlock (1956) approach	138
Figure 5.11. Graphical definition of P and Y (Reese and Welch, 1975)	141
Figure 5.12. Characteristic shape of p-y curves.....	141
Figure 5.13. Variation of p-y curves with depth	142

Figure 5.14. p-y curve characteristic shapes in sands.....	142
Figure 5.15. Relation between SPT –N values and the friction angle (Touma, 1972)	146
Figure 5.16. Variation of subgrade reaction constant with depth (Reese et al. 1974)	147
Figure 5.17. Coefficient of variation of subgrade reaction (NAVFAC, 1986) ...	150
Figure 5.18. Case I: Influence values for laterally loaded pile (NAVFAC, 1986)	152
Figure 5.19. Case II: Influence values for laterally loaded pile (NAVFAC,1986)	153
Figure 6.1. Representation of coupling springs on a pile element	162
Figure 6.2. Material behaviors of coupling springs for pile elements	163
Figure 6.3. FLAC St-1 and St-2 models of laterally loaded pile.....	166
Figure 6.4. Horizontal displacement contours of FLAC St-1 and St-2 models of laterally loaded piles	166
Figure 6.5. Ground deformations estimated by non-dimensional methods and numerical analyses	167
Figure 6.6. Schematic illustration of numerical analysis variables	168
Figure 6.7. Comparison of numerical analyses result with NAVFAC (1986) Method in static loading conditions	169
Figure 6.8. Comparison of numerical analyses result with Duncan et al. (1994), CLM Model in static loading conditions	170
Figure 6.9. Schematic illustration of numerical analysis variables	172
Figure 6.10. Variation of deflection coefficient F_{δ} in terms of L/T in dynamic analyses for free head piles	174
Figure 6.11. Variation of deflection coefficient F_{δ} in terms of L/T in dynamic analyses for fixed head piles	175
Figure 6.12. Dynamic coefficient of variation of subgrade reaction, f_{dyn}	177
Figure 6.13. Variation of deflection coefficient $F_{\delta,dyn}$ in terms of L/T_{dyn} in dynamic analyses for free head piles	179
Figure 6.14. Variation of deflection coefficient $F_{\delta,dyn}$ in terms of L/T_{dyn} in dynamic analyses for fixed head piles	180
Figure 6.15. Summary of the compiled database in F_{δ} vs. L/T_{dyn} domain along with the proposed model for free head piles	185
Figure 6.16. Summary of the compiled database in F_{δ} vs. L/T_{dyn} domain along with the proposed model for fixed head piles	186
Figure 6.17. Comparison between the measured and predicted F_{δ} values for fixed and free head piles by the proposed methodology	187
Figure 6.18. Difference between the measured and predicted F_{δ} for fixed and free head piles values by the proposed methodology.....	188
Figure 6.19. Dynamic analyses results given in CLM normalized domain	190
Figure 6.20. Dynamic analyses results given in modified CLM normalized field	191
Figure 6.21. Summary of the compiled database in y_t/D vs. $P/P_{c,ru}$ domain along with the proposed model.....	195

Figure 6.22. Comparison between the measured and predicted $P/P_{c,ru}$ values for by the proposed methodology	196
Figure 6.23. Difference between the measured and predicted P/P_c values by the proposed methodology	197
Figure 6.24. Setup of centrifuge Model-3 (Abdoun 1997)	199
Figure 6.25. Typical Results of Centrifuge Model-3 (Abdoun 1997)	200
Figure 6.26. Idealized model for semi-empirical approach	201
Figure 6.27. Comparison between the measured and predicted pile head displacement by Abdoun et al. (1997).....	203
Figure 6.28. Setup of centrifuge model (Liu et al 1995).....	204
Figure 6.29. Typical Results of Centrifuge Test PS07 Model-3 (Liu et al. 1995)	206
Figure 6.30. Idealized model of Liu et.al (1995) centrifuge model for semi-empirical approach	206
Figure 6.31. Comparison between the measured and predicted pile head displacement by Liu et al (1995).....	209
Figure 6.32. Setup of centrifuge model (He, 2005)	210
Figure 6.33. Typical Results of Large Size Laminar Box Test Model-4 (He, 2005)	212
Figure 6.34: Idealized model of He (2005) large size laminar box model for semi-empirical approach	213
Figure 6.35. Comparison between the measured and predicted pile head displacement by He, (2005).....	215
Figure 6.36. Setup of centrifuge model 7 (Jakrapiyanun, 2002).....	216
Figure 6.37. Idealized model of Jakrapiyanun (2005) large size laminar box model for semi-empirical approach.....	217
Figure 6.38. Comparison between the measured and predicted pile head displacement by He, (2005).....	220
Figure 6.39. Comparison between the measured and predicted pile head displacements	222
Figure 7.1. Schematic illustration of METUSAND.....	232
Figure 7.2. Values of CRR predicted by METUSAND and compared to probabilistic semi-empirical relationships.....	233
Figure 7.3. Flow Chart for Model I.....	237
Figure 7.4. Flow Chart for Model II	238
Figure 7.5. Comparison between the measured and predicted pile head displacements	239

LIST OF TABLES

TABLES

Table 3.1 Model Coefficients of Modulus Degradation Model (Cetin and Bilge, 2014)	52
Table 3.2 Model Coefficients of Damping Model (Cetin and Bilge, 2014).....	54
Table 3.3. Shamoto et al. (1998) post liquefaction constitutive relation parameters	67
Table 3.4. Input parameters for the illustrative elemental responses	71
Table 4.1. Geotechnical properties of Wildlife array instrumented site.....	91
Table 4.2. Geotechnical properties of idealized soil properties of Wildlife site ...	92
Table 4.3. Soil Properties (after Nakakita and Watanabe 1981)	105
Table 4.4. Geotechnical properties of idealized soil properties of Port Island Array	107
Table 5.1. Ultimate lateral load capacity of short and long piles in cohesionless soils (Broms, 1964a).....	133
Table 5.2. Ultimate lateral load capacity of short and long piles in cohesive soils (Broms, 1964b).....	134
Table 5.3. Lateral deflection at ground surface for piles (Broms, 1964 a,b).....	135
Table 5.4 Recommended values of subgrade reaction constant k, for sands	146
Table 5.5. Non-dimensional terms of Matlock and Reese, (1962) approach	149
Table 5.6. Characteristic Load Method Input Parameters (Duncan et alç 1994)	156
Table 5.7. Comparison of Analyses Methods of Characteristic Load and p-y Curves (Duncan et al. 1994)	157
Table 5.8. Minimum Pile Lengths for CLM Method (Duncan et al., 1994)	157
Table 6.1. MODEL I Parameters.....	183
Table 6.2. MODEL II Parameters	194
Table 6.3. Summary of the Assessment of the Proposed models parameters for Case 1 (Abdoun et. al, 1997)	202
Table 6.4. Summary of the Assessment of the Proposed models parameters for Case II (Liu et. al 1995)	208
Table 6.5. Summary of the Assessment of the Proposed models parameters for Case 1 (He, 2005)	214
Table 6.6. Summary of the Assessment of the Proposed models parameters for Case 4 (Jakrapiyanun, 2005).....	219

LIST OF ABBREVIATIONS

B	: Width of pile
CRR	: Cyclic resistance ratio
CSR _N	: Cyclic stress ratio at n th loading cycle
D	: Diameter of pile
D _R	: Relative density of soil
G _{max}	: Initial shear modulus
G ^e , G	: Elastic shear modulus
G ^P	: Plastic shear modulus
f	: Coefficient of variation of subgrade reaction
f _{dyn}	: Dynamic coefficient of variation of subgrade reaction
F _δ	: Deflection coefficient
F _{δ, dyn}	: Deflection coefficient in dynamic condition
K ₀	: Coefficient of earth pressure at rest
k _h , k, f	: Coefficient of variation of subgrade reaction
K _σ	: Correction factor for vertical effective confining stress
K _p	: Rankine passive earth pressure constant
K _{p, dyn}	: Passive earth pressure constant in dynamic conditions
N _{liq}	: Number of cycles to liquefaction
N	: Number of equivalent uniform loading cycles
N _{1,60,CS}	: Standard penetration test blow counts for clean sands
M	: Moment applied at the pile head
L	: Length of pile
r _u	: Excess pore-water pressure ratio
r _{u, N}	: Excess pore water pressure ratio at n th loading cycle
SA	: Spectral acceleration
T	: Relative stiffness factor
T _{dyn}	: Relative stiffness factor in dynamic condition

V_s	: Shear wave velocity
p	: Soil resistance per unit length
P_a	: Atmospheric pressure in the chosen units
P_t, Q, P	: Lateral load applied to the pile head
Q_u, P_{ult}	: Ultimate lateral capacity of pile
P_c	: Characteristic load
$P_{c,ru}$: Characteristic load in dynamic condition
σ'_{m0}	: Initial mean effective stress
σ'_m	: Mean effective stress
σ'_{v0}	: Initial vertical effective stress
σ'_v	: Vertical effective stress
Δu	: Increase in excess pore-water pressure
$\Delta \varepsilon_{vd}$: Volumetric shear strain increment
$\varepsilon_{vd}, \varepsilon_v$: Accumulated volumetric strain
γ	: Shear strain
$\gamma_{max,N}$: Maximum double amplitude cyclic shear strain at the end of n^{th} loading cycle
γ^P	: Plastic shear strain
γ_N	: Maximum single amplitude cyclic shear strain at n^{th} loading cycle
$\Delta \gamma_i$: Shear strain increment
γ_0	: Shear strain at zero effective confining stress state at post liquefaction phase
γ_d	: Shear strain at non-zero effective confining stress state at post liquefaction phase
γ_{sat}	: Saturated unit weight of soil
γ_{ru}	: Reduced saturated unit weight of soil in dynamic condition
$\Delta \varepsilon_v^P$: Plastic volumetric shear strain increment
ϕ_f	: Peak friction angle;
ϕ_{cv}	: Constant volume friction angle
ϕ'	: Internal friction angle

ϕ'_{ru}	: Reduced friction angle in dynamic condition
ϕ_{ss}	: Steady state friction angle of cohesionless soils
τ_f	: Shear strength at failure
τ	: Shear stress
δ	: Lateral deflection on pile
δ_{max, y_t}	: Lateral deflection of pile head

CHAPTER 1

INTRODUCTION

1.1. Research Statement

The aim of the research study here includes the development of a new constitutive framework for the effective stress-based assessment of soil liquefaction response of cohesionless soils. This research is not limited to the assessment of liquefaction triggering, cyclic pore pressure generation, corollary decrease in stiffness and shear strength and induced cyclic and post cyclic shear strains are also estimated. Within this scope, a new, fully coupled, two-dimensional, effective stress-based, nonlinear, semi-empirical constitutive model, referred to as METUSAND, is developed on the basis of semi-empirical cyclic straining and excess pore water pressure assessment models of Shamoto et al. (1998), Cetin et al. (2009), Cetin and Bilge (2012, 2014). A “C++” subroutine is written and compiled as a dynamic link library (DLL) file for use in commercially available FLAC software. METUSAND is then verified by well-documented liquefaction-induced ground failure case histories of Wildlife Site, Imperial Valley, California, which was shaken by 1987 Superstition Hills earthquake and Port Island Array, Kobe, shaken by 1995 Hyogo-ken Nanbu earthquake. The validation studies confirmed that the developed constitutive framework can not only model liquefaction triggering (i.e.: excess pore pressure generation) response but also capture effective stress and strain dependent degradation of modulus degradation and damping responses. Additionally, due to fact that the post liquefaction large straining response is assessed by Shamoto et al. (1998) framework, analyses could be extended to larger strain range.

By using METUSAND model, series of static and dynamic soil-pile interaction analyses were performed. Static analyses were performed to compare the findings with the ones of currently available and widely used methods of NAVFAC (1986) and Duncan (1994). As part of static and dynamic analyses, primarily the relative density state of potentially liquefiable soil, length and diameter of the pile, static lateral load and amplitude of the dynamic excitation were varied within realistic ranges. Founded on the results of these analyses, a probabilistically-based simplified framework is defined. Then, the validity of the simplified framework is confirmed with actual well documented centrifuge experiments.

1.2. Problem Significance and Limitations of Previous Studies

During earthquakes, the shaking of ground may cause a loss of strength or stiffness that causes the settlement of buildings, landslides, the failure of earth dams, or other hazards (Seed et al., 1990; Bardet et al., 1995; Sitar, 1995; Japanese Geotechnical Society, 1996). A significant number of cases of damage to pile-supported structures have also been observed in most major earthquakes (e.g.: Niigata, 1964; Alaska, 1964; Nihonkai-Chubu, 1983; Loma Prieta, 1989; Hyogoken-Nambu, 1995; and Ji-Ji, 1999 earthquakes).

Prediction of liquefaction-induced deformations of foundation soils located in seismically active regions has been a major concern of geotechnical earthquake engineers for years. In spite of the existing efforts, prediction of these deformations has still remained as a "soft" area of practice.

Currently available approaches for predicting the magnitude of liquefaction induced soil straining are categorized as i) laboratory test results and/or correlations of in situ "index" tests with observed field performance data (e.g.: Tokimatsu and Seed, 1984; Ishihara and Yoshimine, 1992; Shamoto et al., 1998; Zhang et al., 2002; Tsukamoto et al., 2004; Wu and Seed, 2004; Cetin et al., 2009) ii) finite element and/or finite difference based numerical analyses techniques

(e.g.: Martin et al., 1975; Seed et al., 1976; Finn et al., 1977; Wang, 1990; Byrne, 1991; Dawson et al., 2001, Liyanathirana and Poulos, 2002; Byrne et al., 2004 and Boulanger et al., 2010). Among them, semi empirical solutions are listed among the most commonly used alternatives due to large straining nature of the problem, which may produce numerical instability for continuum-based solutions. However, with the advances in numerical modeling techniques and constitutive models, numerical simulations have started to be increasingly popular. Constitutive models used for the static and cyclic response of saturated sands range from relatively simple, uncoupled models to more complex plasticity models or programs (i.e.: UBCSAND, Byrne et al., 2004; TARA-3, Finn et al., 1986; CYCLIC, Para, 1996, Elgamal et al., 2002; DYNAFLOW, Prevost, 2002; SANISAND, Taiebat et al., 2008 and PM4Sand, Boulanger et. al., 2012).

However, each complex model comes with a price, which can be listed as the determination of the input parameters under the constraint of limited available data. Especially, for typical conventional projects, relative density state of the cohesionless soils (or standard penetration blow count, $N_{1,60}$) could be the only input parameter available. Hence, a simpler model, which can capture the essentials of the cyclic response, should be the preferred goal.

The major response of saturated soils subjected to cyclic loading can be categorized under the following headings:

- i) Strain-dependent pore pressure generation response,
- ii) Strain and effective stress dependent modulus degradation and damping response,
- iii) Post-failure dilation and contraction responses,
- iv) Post failure accumulation of cyclic plastic strains.

In the literature there exist models that capture most of these responses with the price of increased number of model input parameters.

Motivated with the availability of METUSAND model, the numerical assessment of the soil-pile interaction in liquefiable soils was defined as the second aim of the thesis. Despite the large margin of safety employed in, the design of laterally loaded piles, collapse of pile foundations in liquefiable soils is still observed after major earthquakes. The failure of end bearing piles in liquefiable areas during earthquakes is, in most of the cases, attributed to the effects of liquefaction-induced lateral spreading, as discussed in Hamada (1992a), Tokimatsu et al. (1996), Ishihara (1998) and Finn and Thavaraj (2001). Ishihara (1998) assessed the magnitude of seismically induced loading on a pile by introducing the concepts of internal forces and bending moments occurred on pile head. Tokimatsu et al. (1998) described the soil-pile structure interaction in liquefiable soil by kinematic forces, which dominate and have a significant effect on pile performance particularly when permanent displacements occur. Tokimatsu and Nomura (1991) performed shaking table tests to study dynamic soil-pile interaction during liquefaction. Moreover, well-known codes of practice such as Japanese Highway Code of Practice (JRA 1996), NEHRP (USA code), and Eurocode 8 review the design methods of pile foundations in areas of seismic liquefaction, which are mostly based on simplified methods. However, still more needs to be done to close the ‘gap’ regarding the assessment of cyclic response of laterally loaded piles installed in liquefiable soils. For the purpose, NAVFAC (1986) and characteristic load concepts of Duncan et al. (1994) were studied and adopted to summarize our findings in a dimensionless, easy to use simplified assessment procedure.

Although the thesis topic covers a very broad range of problems, it will focus on mostly two major issues: a) effective stress based constitutive modeling of fully saturated cohesionless soils and b) assessment of laterally loaded piles deflection subjected to cyclic loading.

1.3. Scope of This Study

Following this introduction, in Chapter 2, an overview of the literature focusing on cyclic response of saturated cohesionless soils, liquefaction susceptibility, cyclically-induced straining and induced pore pressure models are presented. A review of current constitutive relations used in effective stress based dynamic numerical analyses is also summarized.

Chapter 3 presents a new, effective stress-based, nonlinear constitutive model, capable of modeling the non-linear hysteretic stress - strain response, excess pore water pressure generation and prediction of associated post-cyclic volumetric (reconsolidation) straining potential of saturated clean sands. Formulation and numerical implementation circumstances for the fully coupled two dimensional model and element test simulations are also described in this chapter.

In order to validate METUSAND model which was implemented in FLAC software and illustrate the capabilities and limitations of it, Chapter 4 presents seismic response assessment of Wildlife, California and Port Island, Kobe sites by using METUSAND model.

As the consequential part of the study, Chapter 5 presents a brief literature review relating to laterally loaded piles. Chapter 6 discusses an effective stress based assessment framework for seismic pile-soil interaction in liquefiable soils. For the purpose, effective stress based numerical simulations were performed for a number of soil, pile and earthquake combinations. On the basis of numerical simulations, a semi-empirical model was developed to assess cyclic response of laterally loaded piles in saturated cohesionless soils.

Finally, Chapter 7 concludes the study by summarizing the main findings and proposed tools, with comments and suggestions for future work.

CHAPTER 2

LITERATURE REVIEW ON CYCLIC RESPONSE OF SATURATED COHESIONLESS SOLIS

2.1. Introduction

Under an earthquake shaking, the pore water pressure in a saturated “loose” cohesionless soil will increase due to the tendency of the volume contraction if water drainage is prevented. This causes a reduced effective stress state and the reduction in stiffness, and even the liquefaction of the sand. Ishihara (1993) defines liquefaction as; “A state of particle suspension resulting from release of contacts between particles of sand constituting a deposit. Therefore, the type of soil most susceptible to liquefaction is one in which the resistance to deformation is mobilized by friction between particles under the influence of confining pressure.”

During earthquakes, the shaking of ground may cause a loss of strength or stiffness that result in the settlement of buildings, landslides, the failure of earth dams, or other hazards. (e.g.: Seed et al., 1990; Bardet et al., 1995; Sitar, 1995; Japanese Geotechnical Society, 1996). Landslides or flow failures due to liquefaction are observed firstly during the Zeeland coast of Holland slides, in 1937, at involving 7 million cubic meters of alluvial sands, and the Mississippi River slide, in 1944 near Baton Rouge containing about 4 million cubic meters of fine sands. Dam failures such as the Calaveras Dam in California, 1918, the Fort Peck Dam in Montana in 1938, and the Lower San Fernando Dam during the 1971 San Fernando Earthquake in California, are the few examples which were

triggered by the liquefaction of sands. Liquefaction of sands, induced by static loading (flow failure), firstly introduced by Arthur Casagrande in between 1935 and 1938. However, a great deal of attention about the subject of soil liquefaction by seismic loading was received in 1964, after two major earthquakes, Alaska-U.S.A. (1964), and Niigata-Japan (1964), resulting in significant damage and loss. During the 7.5-magnitude earthquake of June 16, 1964, in Niigata, Japan, the extensive liquefaction of sand deposits resulted in major damage to buildings, bridges, highways and utilities due to the tilting and sinking. It was estimated that more than 60,000 buildings and houses were destroyed. The Alaska earthquake in the same year, with a magnitude of 9.2, destroyed or damaged more than 200 bridges and caused massive landslides.

In this chapter, an overview of available literature regarding seismic soil liquefaction engineering and cyclic response of saturated cohesionless soils is presented. Within the confines of this chapter, a brief review on i) theoretical framework for liquefaction susceptibility, ii) cyclic stiffness reduction of cohesionless soils and iii) cyclic and post cyclic strains and induced pore pressure models are discussed.

2.2. Theoretical Framework for Liquefaction Susceptibility

There are a number of different ways to evaluate the liquefaction susceptibility of a soil deposit: i) historical criteria, ii) geological criteria, iii) compositional criteria and iv) state criteria. According to Kramer (1996); “Historical criterion is based on observations from earlier earthquakes and provides a great deal of information about the liquefaction susceptibility of certain types of soils and sites. The type of geologic process and saturation that created a soil deposit has a strong influence on its liquefaction susceptibility. A uniformly graded soil is more susceptible to soil liquefaction than a well-graded soil because the reduced tendency for volumetric strain of a well-graded soil decreases the amount of excess pore pressure that can develop under undrained conditions. Moreover, the

initial "state" of a soil is defined by its density and effective stress at the time it is subjected to rapid loading. At a given effective stress level, "looser" soils are more susceptible to liquefaction than dense soils. For a given density, soils at high effective stresses are generally more susceptible to liquefaction than soils at low effective stresses."

Ranges of grain size distribution for liquefaction susceptible soils, as defined by Tsuchida (1970), is given in Figure 2.1.

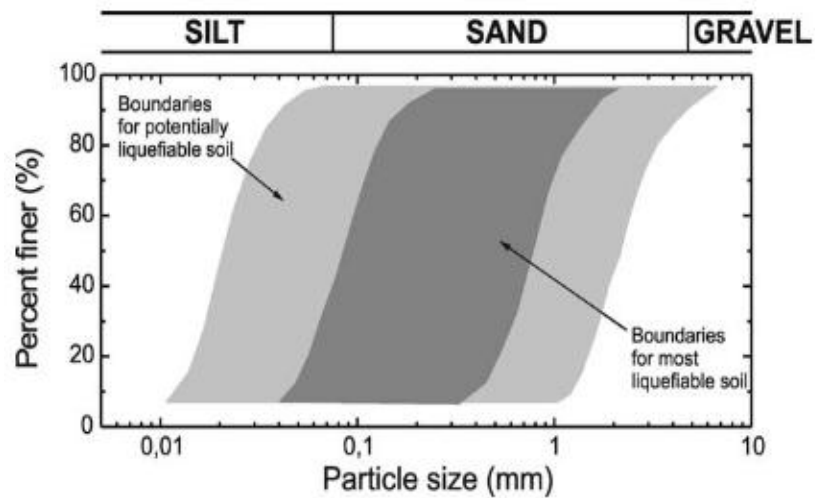


Figure 2.1. Ranges of Grain Size Distribution for Liquefaction Susceptible Soils (Tsuchida, 1970)

If the sand beneath an embankment or slope is very loose and has the strain softening stress-strain behavior as shown in Figure 2.2a, a seismic loading of sufficient intensity and duration can strain the soil over the peak of the stress-strain curve and trigger initial liquefaction. Once this condition is reached, shear resistance of the soil continuously declines until the steady state or residual strength is reached.

Dense sands have a tendency to dilate and generate negative pore water pressure. As a result, soil shearing resistance increases until a maximum value is reached, as

shown in Figure 2.2b. At the end of the shaking, the initial static shear stress is still less than the peak shear resistance.

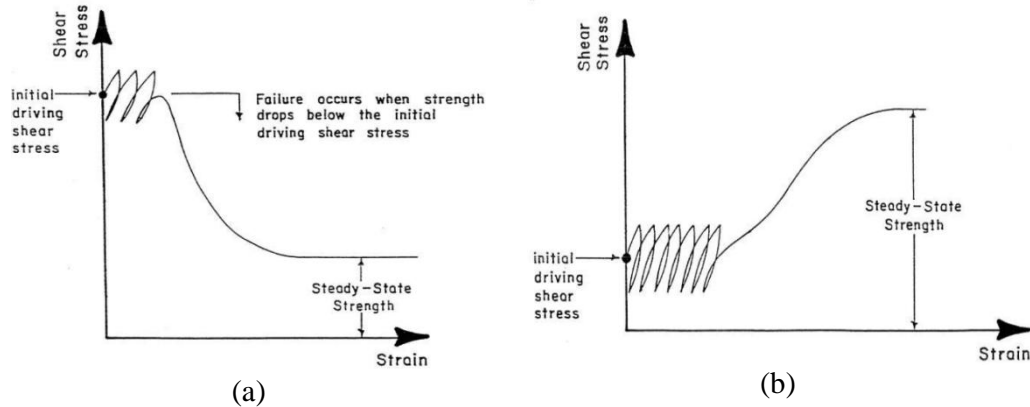


Figure 2.2. Undrained stress-strain curve for *a) loose sand* and *b) dense sand* under seismic loading condition (Seed et al., 1989)

2.2.1. Liquefaction Mechanisms and Influence of Dilatancy

Robertson (1994) state that “The engineering term of "liquefaction" has been used to define two related, yet different soil responses during earthquakes as flow liquefaction and cyclic softening. Although these mechanisms are quite different, it is difficult to distinguish them since they can lead to similar consequences.”

The Robertson and Fear (1996) has explained these concepts as follows;

- i) *Flow Liquefaction*: The undrained flow of saturated, contractive soil when subjected to cyclic or monotonic shear loading as the static shear stress exceeds the residual strength of the soil
- ii) *Cyclic softening*: Large deformations occurring during cyclic shear due to increase in pore water pressure that would tend to dilate in undrained, monotonic shear. Cyclic softening, in which deformations discontinue after cyclic loading stops, can be further classified as;
 - *Cyclic mobility*: Cyclic loads do not result in a reversal of shear stress and condition of zero effective stress does not

occur. Deformations accumulate in each cycle of shear stress.

- *Cyclic liquefaction*: It occurs when the initial, static shear stress is exceeded by the cyclic shear stresses to produce a stress reversal. This may help in attaining a condition of zero effective stress during which large deformations may develop.

Flow liquefaction and cyclic mobility susceptibility zones are shown in Figure 2.3. Soils in an initial state that below the Steady State Line are not susceptible to flow liquefaction whereas soils above the Steady State Line are susceptible to flow liquefaction, if the static shear stress exceeds the residual strength of the soil. Flow Liquefaction Surface (FLS) is the surface where *flow liquefaction* was initiated. Moreover, cyclic mobility can occur in dense as well as loose soils.

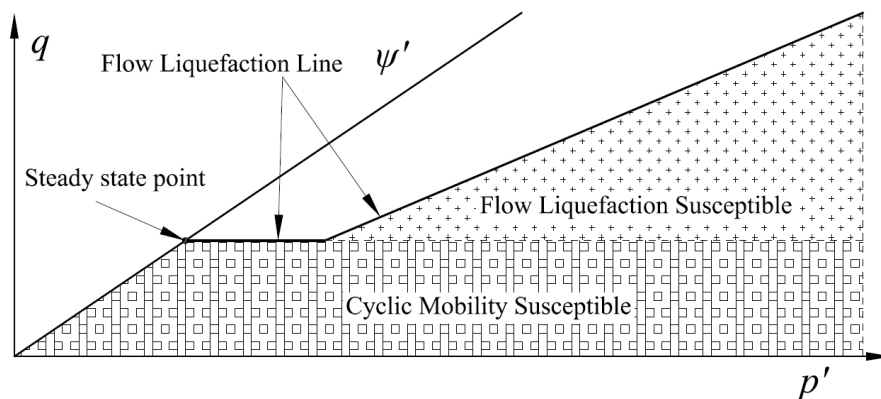


Figure 2.3. Flow liquefaction and cyclic mobility susceptibility zones
(after Robertson and Fear, 1996)

The difference between liquefaction and cyclic mobility through the use of state diagram is shown in Figure 2.4. The axes are void ratio (e) and effective minor principal stress and the steady state line is similar to Critical State line (Schofield and Wroth, 1968) where soil can shear at constant void ratio and at constant shear

stress. Castro and Poulos (1977) stated that liquefaction only occurs in specimens that are highly contractive .

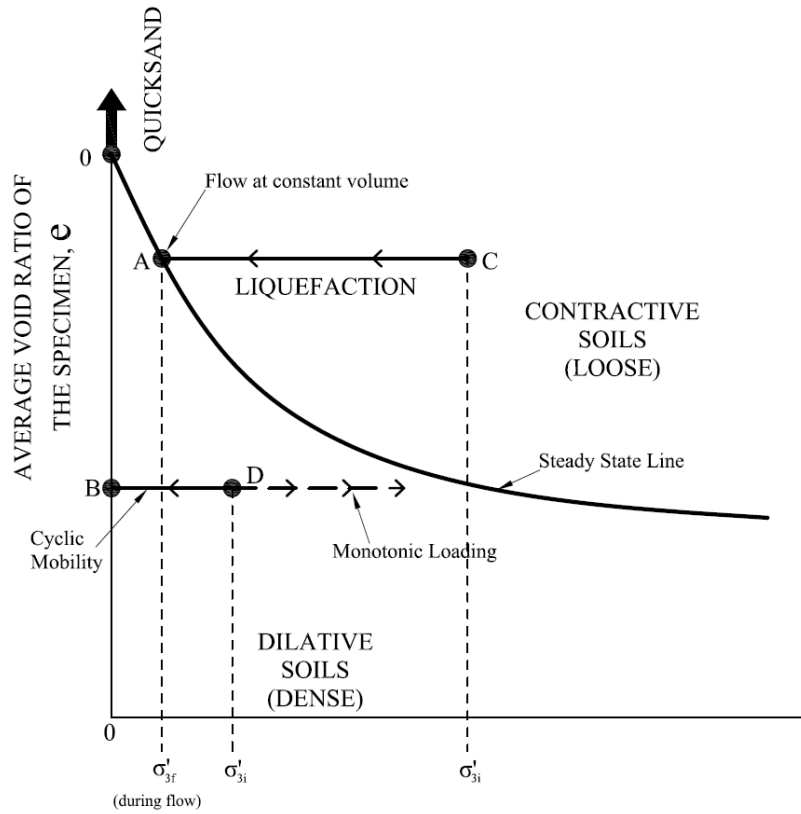


Figure 2.4. Steady State line (after Castro and Poulos, 1977)

Ishihara (1985) state that; “Cyclic mobility can occur even when static shear stress is lower than the steady state (or residual) shears strength. Medium dense to dense sands subjected to monotonic loading will initially exhibit contractive behavior, but then exhibit dilative behavior as they strain toward the steady state, as shown in Figure 2.5. Stress path at which the transformation from contractive to dilative behavior takes place is called a phase transformation line (PTL).”

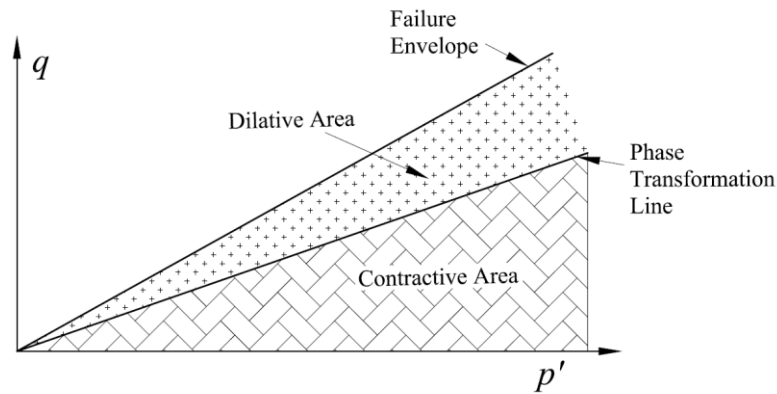


Figure 2.5. Phase transformation line at p' - q domain (after Ishihara, 1985)

Moreover, Mohamad and Dobry (1986) identified three kinds of sand behavior as follows:

- i) *Contractive*: denotes a behavior where the applied shear stress $q' = (\sigma_1' - \sigma_3')/2$ where σ_1' and σ_3' represent the major and minor effective stress respectively, first increases and then drops rapidly to a constant steady state or residual strength value. The corresponding stress path is shown in Figure 2.6 as test 4.
- ii) *Partially contractive*: denotes a behavior where the applied shear stress q after reaching a peak, drops to a steady state condition but for a limited range of axial strains, after which a dilative tendency takes over. The effective stress path given by Figure 2.6 test 2 shows an “elbow” at the point where the behavior changes from contractive to dilative.
- iii) *Dilative*: denotes a behavior where the applied shear stress q , never reach a steady state condition. Thus, dilatancy always controls the behavior (Figure 2.6 as test 6). However, the effective stress path could contain an "elbow" as that shown in Figure 2.6 test 5.

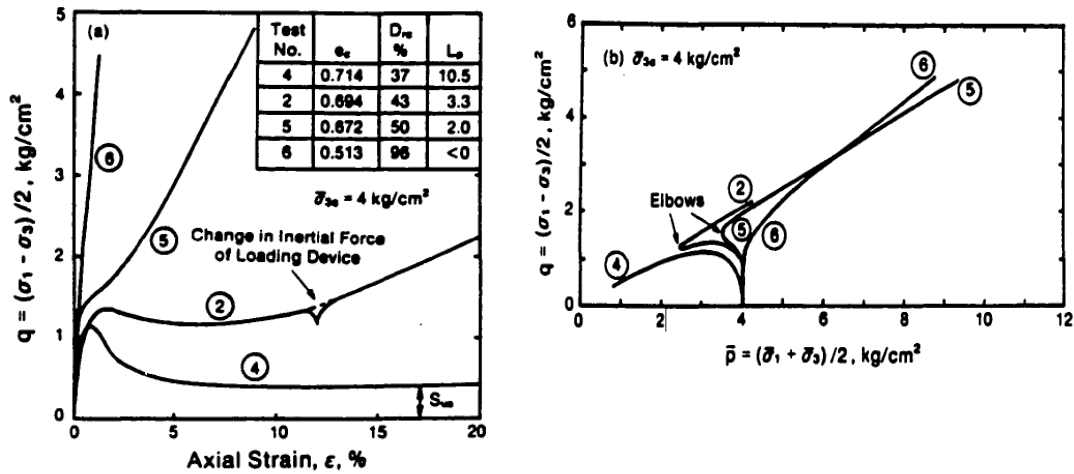


Figure 2.6. Stress-strain curves and effective stress paths for Banding Sand in CIU Tests (after Mohamad and Dobry, 1986)

Cyclic liquefaction mechanism is illustrated as shown in Figure 2.7. As the figures imply, it requires undrained cyclic loading during which shear stress reversals (phase 1) or zero effective stress state (phase 4) develops; and thus results in almost zero shear strength for non-cohesive soils. When shear stress is applied, pore water pressure drops as the material tends to dilate (phase 5), and stress strain response can produce large deformations.

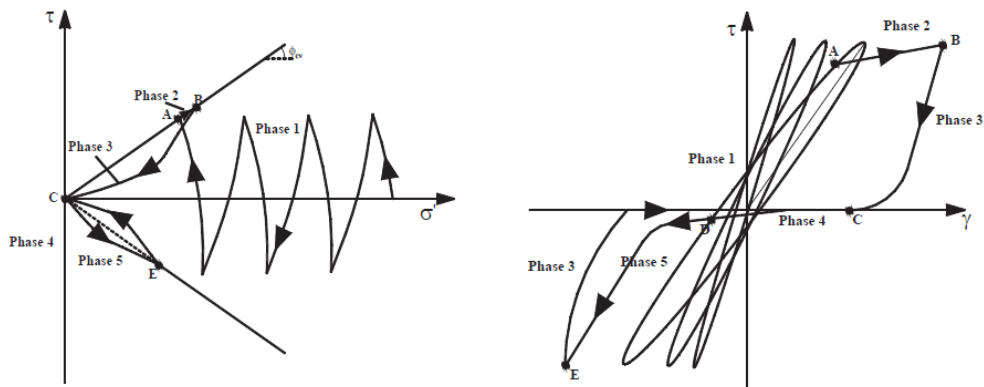


Figure 2.7. Schematic diagram of cyclic liquefaction

2.2.2. Liquefaction Triggering Assessments

If the soil is judged to be potentially liquefiable, the next step involves the assessment of liquefaction triggering potential under seismic or cyclic loading. Basically, semi-empirical field-based procedures are widely used for evaluating liquefaction potential during earthquakes, which have two essential components: (1) compiling case histories to develop an analytical framework, and (2) the development of a suitable in-situ index to represent soil liquefaction characteristics. There has been a number of SPT-based semi-empirical methods such as Seed et al. (1984); Ishihara (1985), Liao et al. (1988); Japanese Code of Bridge Design (1990), Youd and Noble (1997); Idriss and Boulanger (2004) and Cetin et al. (2004). The original simplified procedure of Seed and Idriss (1971) for calculating earthquake-induced cyclic shear stresses is still the essential component of liquefaction triggering framework.

In the following chapters, SPT based assessment of seismic soil liquefaction by Cetin et al. (2004) method will be used for the calibration of the new effective-stress based constitutive model discussed at this study, so a brief discussion about this method is given in this section.

Cetin et al. (2004) introduced new correlations based on a significantly extended database and improved knowledge on standard penetration test, site specific earthquake ground motions and in-situ cyclic stress ratios. The resistance of soils to liquefaction expressed by cyclic resistance ratio, (CRR) and probability of liquefaction (P_L) created by using higher-order probabilistic tools can be obtained by equations 2.1 and 2.2 respectively. Cetin et al. (2004) deterministic triggering boundary curves can be developed for probability of liquefaction 50 %, corresponding to a factor of safety, $FS=1$, as the authors recommended.

$$CRR(N_{1,60}, M_w, \sigma'_v, FC, P_L) = \exp \left[\frac{N_{1,60}(1+0.004FC) - 29.53 \ln(M_w) - 3.70 \ln\left(\frac{\sigma'_v}{P_a}\right) + 0.05FC + 16.85 + 2.70\Phi^{-1}(P_L)}{13.32} \right]$$

(2.1)

$$P_L(N_{1,60}, CSR_{eq}, M_w, \sigma'_v, FC) = \Phi \left(- \frac{N_{1,60}(1+0.004FC) - 13.32 \ln(CSR_{eq}) - 29.53 \ln(M_w) - 3.70 \ln\left(\frac{\sigma'_v}{P_a}\right) + 0.05FC + 16.85}{2.70} \right)$$

(2.2)

where;

P_L = probability of liquefaction in decimals

CSR_{eq} = equivalent uniform CSR not adjusted for magnitude (or duration) or K_σ effects

FC = percent fines content expressed as an integer ($5 \leq FC \leq 35$)

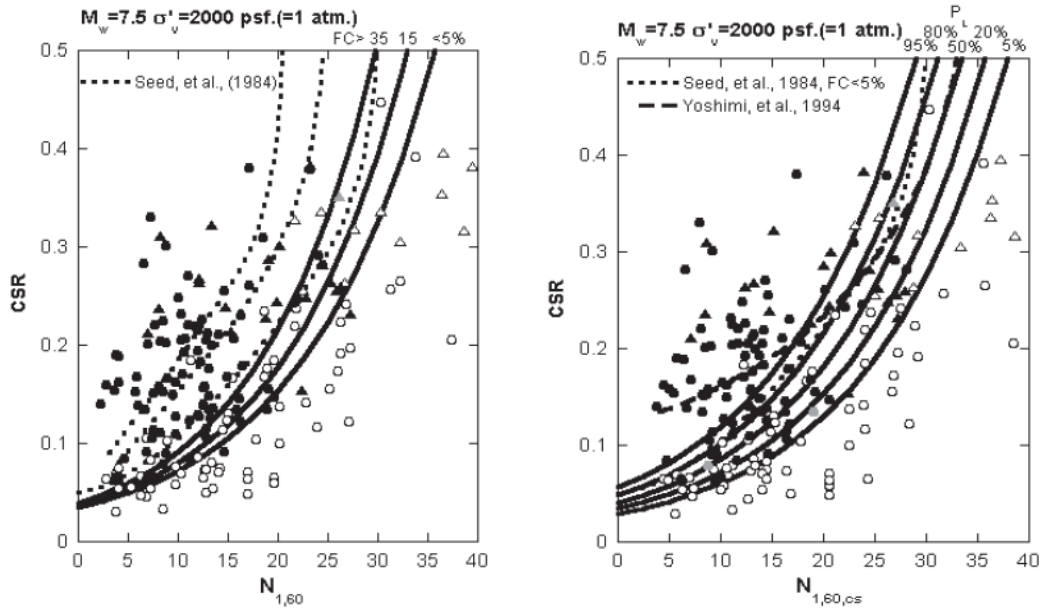
P_a = atmospheric pressure (=1 atm \approx 100 kPa)

Φ = standard cumulative normal distribution

$\Phi^{-1}(P_L)$ = inverse of the standard cumulative normal distribution (i.e., mean=0 and standard deviation=1)

For spreadsheet construction purposes, the command in Microsoft excel for this specific function is “NORMINV($P_L, 0, 1$)”.

Chart solution of deterministic and probabilistic SPT-based liquefaction triggering correlation of Cetin et al. (2004), for $M_w=7.5$ and $\sigma'_v = 1.0$ atm with adjustments for fines content is given in Figure 2.8a and Figure 2.8b. For comparison purposes Seed et al. (1984a)'s deterministic boundary is also shown on the figures.



a) Deterministic Approach

b) Probabilistic Approach

Figure 2.8. SPT-based liquefaction triggering correlation for $M_w=7.5$ and $\sigma_v' = 1.0$ atm with adjustments for fines content (Cetin et al. 2004)

2.3. Cyclic Straining-induced Stiffness Degradation Response

Cyclic loading response of soils is nonlinear and depends on several factors including relative density, in-situ confining pressure, amplitude of loading and number of loading cycles. Earthquake excitation causes shear strains, which lead to an increase in excess pore water pressure and this result in the reduction of soil stiffness. As the soil stiffness is reduced, excess pore water pressure continues to increase with increasing cyclic shear strains, until the end of loading. As revealed by this interaction, modulus degradation response of soils is recognized as an essential part of seismic ground response, and also soil structure interaction problems.

2.3.1. Modulus Degradation and Damping Response of Granular Soils

According to Hashas and Park (2001); “Non-linear hysteretic soil behavior is commonly characterized by an equivalent secant shear modulus and viscous damping. The effect of confining pressure on dynamic properties, which is substantial compared to other soil properties, has been initially recognized by Seed and Idriss (1970) and Hardin and Drnevich (1972a, 1972b). Damping, which is defined as a measure of energy dissipation in a loading cycle, increases with increasing magnitude of cyclic shear strain. Modulus degradation and damping curves for a wide range of soils have been developed by several researchers including Seed et al. (1984) and Vucetic and Dobry (1991). These curves have been extensively used for estimating seismic site response in relatively shallow deposits ($z < 30$ m).”

Seed and Idriss (1970) proposed a simplified equation for shear modulus, G in psf units as given in Equation 2.3 which is function of strain amplitude (γ), effective mean principal stress (σ'_m), and void ratio (e) or relative density D_R . K_2 is a material coefficient, which depends on the relative density and initial shear strain level of the soils, as shown in Figure 2.9. For any sand, this coefficient has a maximum value ($K_{2,max}$) at very low strains (approximately of the order of 10^{-4} %) and be formulized as a function of D_R (Equation 2.4) as recommended by Cetin and Bilge (2014).

$$G = 1000 \cdot K_2 \cdot (\sigma'_m)^{0.5} \quad (2.3)$$

$$K_{2,max} = 0.59 \cdot D_R + 16.47 \quad (2.4)$$

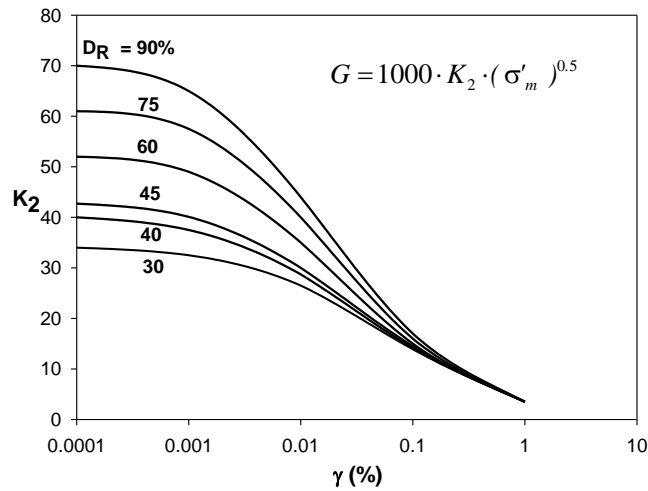


Figure 2.9. Shear Moduli of Sands at Different Relative Densities
(After Seed and Idriss, 1970)

After the work of Seed and Idriss, in the following years various modulus degradation models have been proposed such as Shibata and Soleano (1975), Sherif and Ishibashi (1976), Iwasaki and Tatsuoka (1977), Edil and Luh (1978), Tatsuoka et al. (1978), Kokusho (1980), Khouri (1984). Laird and Stokoe (1993) developed modulus degradation relations by performing torsional shear and resonant column tests. Recently, Matasovic and Vucetic (1993) proposed a constitutive model, which took into account the effect of generation of excess pore water pressure in degradation of shear modulus.

Increase in confining pressure has a significant influence on damping. Small strain damping decreases with an increase in confining pressure due to an increase in number of particle contacts, which is the main factor that dissipates energy at low amplitude strain. Damping is considered to be a measure of the energy dissipation and for practical purposes it is accepted to be composed of two components as hysteretic damping and viscous damping. The majority of the internal damping is due to hysteretic damping. Figure 2.10 and Figure 2.11 show hysteresis loops, for small and large shear strains, respectively, which is obtained by cyclic torsional shear tests.

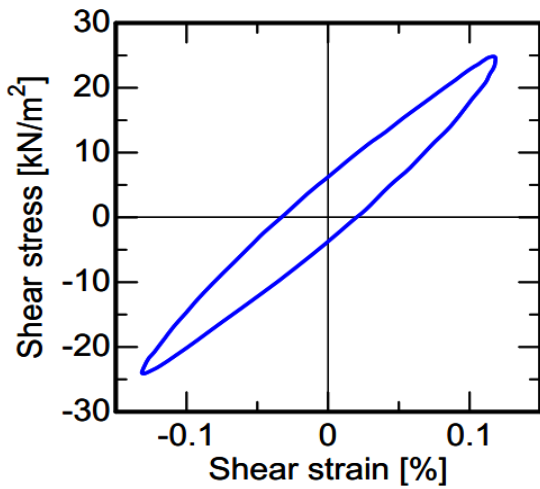


Figure 2.10. Hysteresis loop at smaller strains

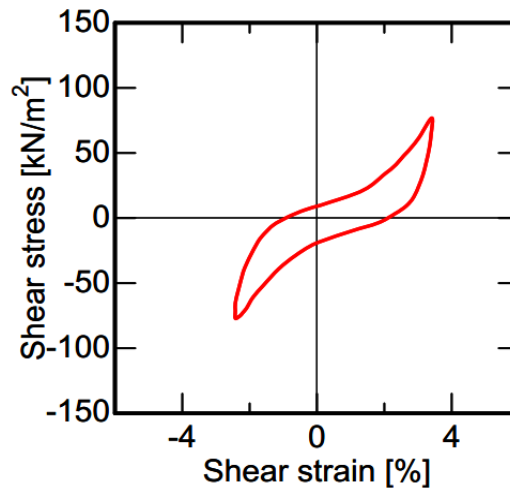


Figure 2.11. Hysteresis loop at larger strain

Shear stiffness, G , is defined by secant modulus at reversal points as shown in Figure 2.12. Hysteretic damping component is generally represented by damping ratio, D . In simpler terms, D is the ratio of the energy dissipated in one cycle of loading (area under the stress-strain loop, W_D) to the maximum strain energy stored during loading cycle. Hysteretic damping D is defined as;

$$D = \frac{1}{4\pi} \frac{A_L}{A_T} \quad (2.5)$$

lim: $0.0\% < D < 100\%$

where A_L and A_T are the area of the hysteresis and the area of the shaded triangular in Figure 2.12.

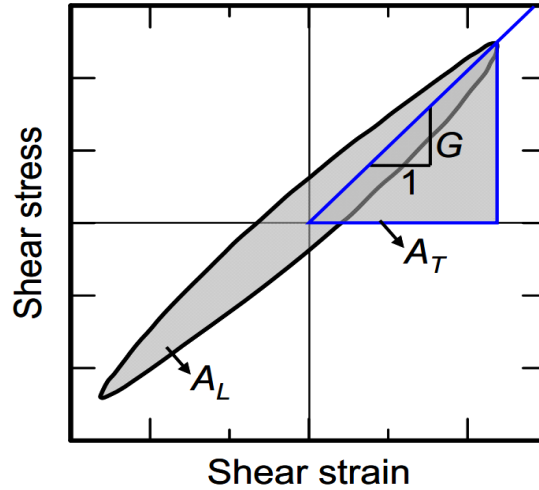


Figure 2.12. Hysteretic stress-strain loop

2.4. Cyclic Straining and Induced Pore Pressure Models

2.4.1. Stress Based Pore Pressure Models

For stress controlled loading, the cyclic shear strain is replaced by the normalized cyclic shear stress and the void ratio. Seed et al. (1975) developed an empirical, closed-form solution to calculate excess pore-water pressure ratio (r_u) on the basis of De Alba et al. (1975) experimental data, which is insensitive to relative density of soil and initial effective confining stress as given in Equation 2.6.

$$r_u = \left\{ \frac{1}{2} + \frac{1}{\pi} \sin^{-1} \left[2 \left(\frac{N}{N_{liq}} \right)^{\frac{1}{\alpha}} - 1 \right] \right\} \quad (2.6)$$

where;

N = number of equivalent uniform loading cycles.

N_{liq} = number of cycles to liquefaction

α = recommended as 0.7 (as a function of soil property)

Liyanapathirana and Poulos (2002) implemented Seed et al.'s (1975) methodology in a finite-element-based model. Moreover, Polito et al. (2008)

improved the methodology as a function of cyclic stress ratio (CSR), fines content (FC), and D_R , given in Equation 2.7.

$$\alpha = 0.01166FC + 0.007397D_R + 0,01034CSR + 0.5058 \quad (2.7)$$

$$\text{lim: } 0 \leq FC \leq 35, \quad 0.73 \leq \alpha \leq 1.14$$

Major limitations of Seed et al. (1975) and later modified approaches are the difficulties in defining and estimating N_{liq} , lack of effective differentiation between cyclic liquefaction and mobility responses, and the need to convert transient earthquake excitations to equivalent harmonic cycles.

2.4.2. Strain Based Pore Pressure Models

For strain controlled cyclic loading, excess pore pressure depends on the number of cycles, the cyclic shear strain and the effective consolidation stresses. According to Martin and Finn (1975), the relation between irrecoverable volumetric strain and cyclic shear-strain amplitude is independent of confining stress. Increase in excess pore pressure relates the increment of volume decrease, $\Delta\varepsilon_{vd}$, to the cyclic shear-strain amplitude, γ (Equation 2.8). The variables \bar{E}_r and $\Delta\varepsilon_{vd}$ are defined in equations 2.9 and 2.10 respectively.

$$\Delta u = \bar{E}_r \Delta\varepsilon_{vd} \quad (2.8)$$

$$\bar{E}_r = \frac{(\sigma'_v)^{1-m}}{m k_2 (\sigma'_{v0})^{n-m}} \quad (2.9)$$

$$\Delta\varepsilon_{vd} = c_1(\gamma - c_2\varepsilon_{vd}) + \frac{c_3\varepsilon_{vd}^2}{\gamma + c_4\varepsilon_{vd}} \quad (2.10)$$

where;

Δu = increase in excess pore-water pressure

\bar{E}_r = tangent modulus of the one-dimensional unloading curve corresponding to the initial effective vertical stress

$\Delta\varepsilon_{vd}$ = the change in volumetric strain corresponding to cyclic shearing

ε_{vd} = accumulated volumetric strain

$c_1, c_2, c_3, c_4, m, n, k_2$ = model coefficients.

Byrne (1991) developed an alternative and relatively simpler model as given in Equation 2.11.

$$\frac{\Delta\varepsilon_{vd}}{\gamma} = c_1 \exp\left(-c_2 \frac{\varepsilon_{vd}}{\gamma}\right) \quad (2.11)$$

where;

$$c_1 = 7,600(D_R)^{-2.5} \quad \text{and} \quad c_2 = \frac{0.4}{c_1} \quad (2.12)$$

Both Finn et al. (1976, 1977) and Byrne (1991) models were subsequently implemented in dynamic coupled stress-flow finite difference software Fast Lagrangian Analysis of Continua (FLAC). The major difficulty to use these models is the requirement of a large number of model parameters. The shear induced volumetric strain for constant amplitude of cyclic shear strain predicted by Equation 2.8 is plotted versus number of cycles in Figure 2.13. This formula predicts an increase in shear-induced (contractive active) volumetric strain with the level of cyclic shear-strain. Also, for a given strain amplitude, the rate of strain accumulation decreases with the number of cycles.

Moreover, Dobry et al. (1982) developed a relationship among r_u , cyclic shear strain amplitude, and the number of loading cycles. A threshold shear strain level of 10^{-2} %, below which applied shear strains do not trigger significant excess pore-water pressures, was proposed. This model was subsequently used by Matasovic (2006) and Hashash (2009) in their effective-stress-based nonlinear ground response modeling software D-Mod and Deepsoil, respectively.

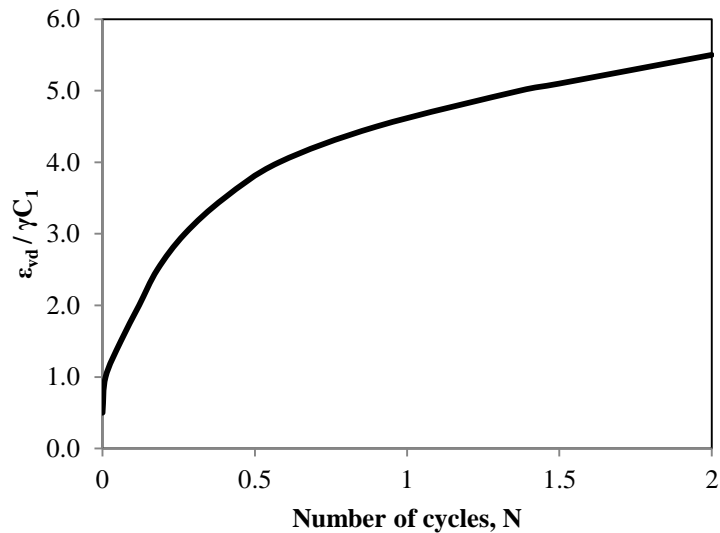


Figure 2.13. Constant, cyclic shear-strain amplitude proposed by Byrne (1991)

2.4.3. Other Pore Pressure Generation Models

Some research studies have evolved in strain-energy concepts such as Law et al. (1990), Wang et al. (1997), Green et al. (2000) and Davis and Berrill (2001). These studies are based on the change in excess pore pressure to the energy dissipated per unit volume of soil during the same cycle of loading and mostly focusing on the development of empirical models benefiting from experimental data.

Moreover, a number of researchers were studied on the theory of plasticity, developed effective stress-based models capable of predicting cyclic excess pore pressure response. (e.g.: Wang et al., 1990; Ishihara, 1993; Elgamal et al., 2003; Park and Byrne, 2004). These models have been increasingly implemented in various finite element/finite difference based commercial software. However, model input parameters should be obtained from adequate laboratory or field test data which are missing generally for common projects.

2.4.4. Probabilistic Models for Cyclic Straining and Induced Pore Pressure

In this study constitutive modeling of the stress- strain behavior of cohesionless soils and induced pore pressure under dynamic loadings are based on the correlations given by Cetin et al. (2009) and Cetin and Bilge (2012) respectively.

Cetin et al. (2009) and Cetin and Bilge (2012) studies were based on cyclic laboratory test results composed of 524 maximum shear strain, γ_{\max} , and 76 volumetric strain, ε_v data points. The various testing conditions, such as sand type, test procedure, rate of loading and confining stress of different databases were minimized through a series of correction factors, as shown in Equations 2.13 to 2.16. $CSR_{\text{test},20}$ is defined, conventionally, as the ratio of half of the deviatoric stress, $\sigma_d/2$, to initial confining stress ($CSR_{\text{test},20} = \sigma_d/2\sigma'_c$), and the ratio of cyclic shear stress to initial vertical effective stress ($CSR_{\text{test},20} = \tau_c/\sigma'_v$), respectively.

$$CSR_{SS,20,1D,1atm} = CSR_{\text{test},20} K_{\sigma} K_{mc} \quad (2.13)$$

$$K_{\sigma} = \left(\frac{\sigma'_{v0}}{P_a} \right)^{f-1} \quad f = 1 - 0.005D_R \quad (2.14)$$

$$K_{mc} = -3 \times 10^{-5} D_R^2 + 0.0048 D_R + 0.7222 \quad (2.15)$$

$$K_r = 1.0 \text{ for } K_0 = 1.0 \quad (2.16)$$

Cetin and Bilge (2009) state that “By these equations, $CSR_{\text{test},20}$ values, corresponding to one-dimensional, 20 uniform loading cycles were converted to simple shear CSR values, again corresponding to one-dimensional, 20 uniform loading cycles, under a confining pressure of 100 kPa (=1 atm) designated by $CSR_{SS,20,1D,1atm}$. K_{σ} corrections as recommended by Youd et al. (2001) were applied to $CSR_{\text{test},20}$ values to eliminate the effects of varying confining stress

conditions on the cyclic strain response of tested soil samples. Similarly, membrane compliance effects in cyclic simple shear tests and shearing of incorrect plane in cyclic triaxial tests were corrected through K_{mc} and K_r correction factors, respectively, as recommended by Wu et al. (2003) and Seed (1976).”

Cetin et al. (2009) probabilistic model is developed by selecting a limit state expression that captures the essential parameters of the problem. Consistent with the maximum likelihood methodology, model coefficients are estimated by maximizing the likelihood functions. The final form of the resulting proposed models for maximum cyclic shear strain, (γ_{max}) and post cyclic volumetric strain (ε_v) are presented in Equations 2.17 and 2.18 along with as \pm one standard deviation of model error.

$$\ln(\gamma_{max}) = \ln \left[\frac{-0.025N_{1,60,CS} + \ln(CSR_{SS,20,1D,1atm}) + 2.613}{0.004N_{1,60,CS} + 0.001} \right] \pm 1.880 \quad (2.17)$$

$$lim: 5 \leq N_{1,60,CS} \leq 40, 0.05 \leq CSR_{SS,20,1D,1atm} \leq 0.60, 0\% \leq \gamma_{max} \leq 100\%$$

$$\ln(\varepsilon_v) = \ln \left[1.879 \ln \left[\frac{780.416 \ln(CSR_{SS,20,1D,1atm}) - N_{1,60,CS} + 2,442.465}{636.613N_{1,60,CS} + 306.732} \right] + 5.583 \right] \pm 0.689 \quad (2.18)$$

$$lim: 5 \leq N_{1,60,CS} \leq 40, 0.05 \leq CSR_{SS,20,1D,1atm} \leq 0.60, 0\% \leq \varepsilon_v \leq 5\%$$

The mean boundary curves for different cyclically induced maximum shear and post cyclic volumetric strain levels developed by using these equations are presented in Figure 2.14 and Figure 2.15, respectively.

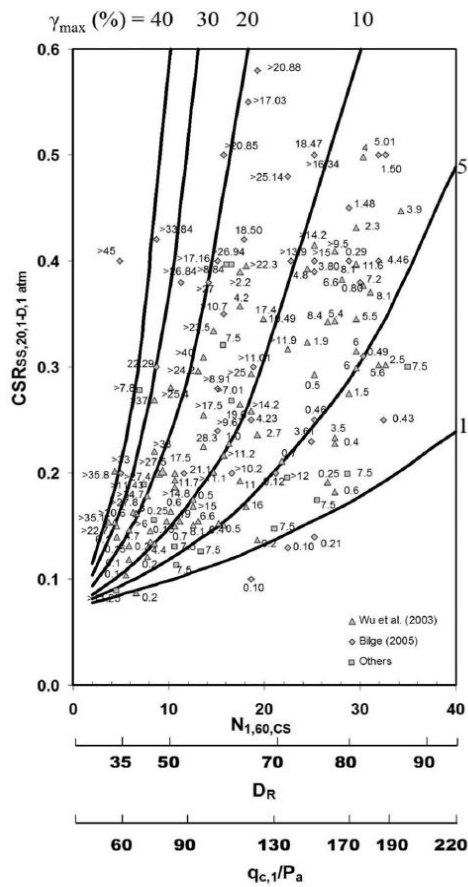


Figure 2.14. Recommended maximum double amplitude shear strain boundary curves (Cetin et al., 2009)

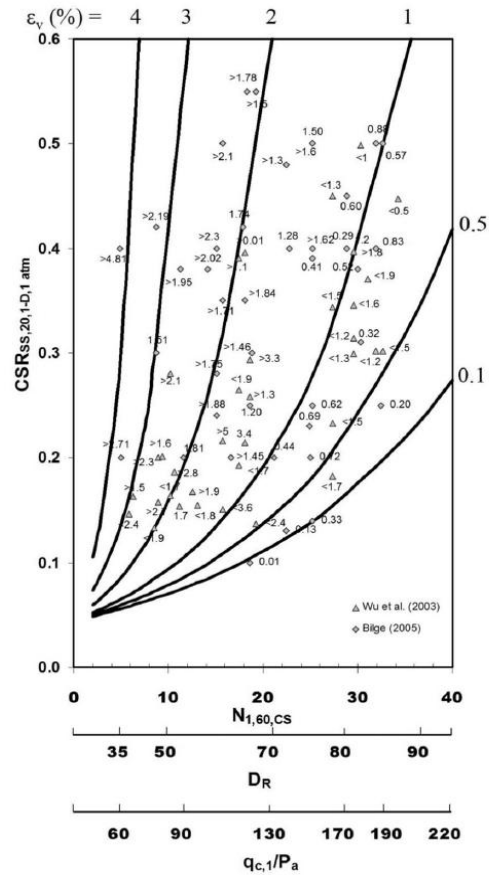


Figure 2.15. Recommended post cyclic volumetric strain boundary curves (Cetin et al., 2009)

According to Cetin and Bilge 2012; “Similarly, semi-empirical probabilistic models are described to assess cyclic large strain and induced excess pore-water pressure responses of fully saturated clean sands. For this purpose, available cyclic simple shear and triaxial tests were compiled and studied. The resulting r_u versus γ , and γ versus N databases are composed of 101 and 84 cyclic test data, respectively. Key parameters of the proposed r_u and γ models are defined as critical shear strain, relative density, effective confining stress, and equivalent number of loading cycles. Consistent with the maximum likelihood methodology, model coefficients were estimated by maximizing the likelihood function. The

final forms of the resulting proposed models are presented in Equation 2.19 along with \pm one standard deviation of the model error term.”

$$\ln(r_{u,N}) = \ln \left(1 - \exp \left(- \frac{-0.407\gamma_{\max,N}}{-0,486+0,025\ln\sigma'_{v,0} - (\frac{D_R}{100})} \left(\frac{0.620}{1+\gamma_{\max,N}} + 1 \right) \right) \right) \pm \sigma_{\varepsilon\ln(r_{u,N})} \quad (2.19)$$

and $\sigma_{\varepsilon\ln(r_{u,N})}$ is the standard deviation as follows

$$\sigma_{\varepsilon\ln(r_{u,N})} = \frac{1}{(\gamma_{\max,N})^{1.375} + 1.889} \quad (2.20)$$

where $\gamma_{\max,N}$, defined as the maximum double-amplitude cyclic shear strain at the end of n^{th} loading cycle.

Proposed r_u versus $\gamma_{\max,N}$ approach is also given in Figure 2.16.

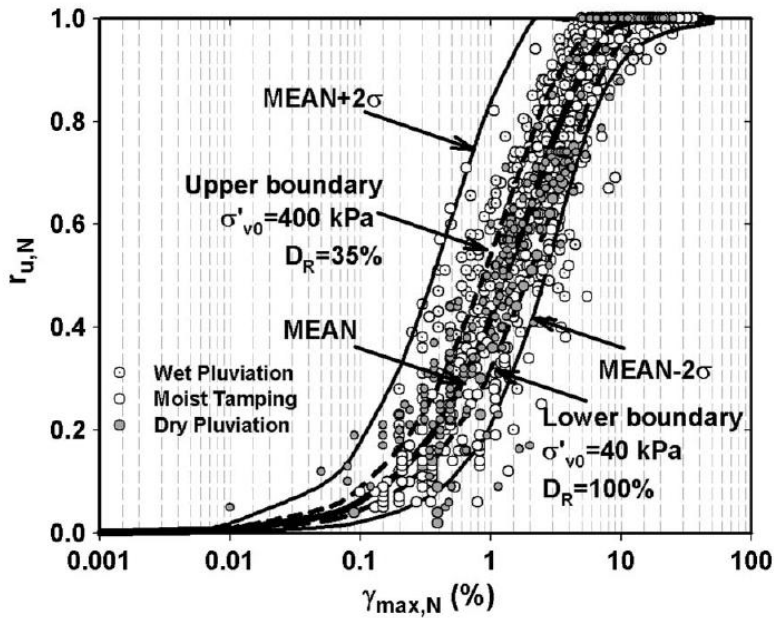


Figure 2.16. Proposed r_u versus $\gamma_{\max,N}$ model along with test results used in Cetin and Bilge (2012)

2.5. Comprehensive Liquefaction Constitutive Models

The constitutive modeling of soil has achieved certain degree of success in the past decade by using different versions of elasto-plastic formulations. Advanced plasticity models depends on their density and confining pressure level, in which sand behavior could be dramatically different (such as generalized plasticity model of Pastor et al., 1990). As a result, according to plastic sand models, a large number of state parameters are required in analyzing the sand of varying densities when subjected to different confining pressures.

Beatty and Perlea (2011) describes constitutive models as follows: “Constitutive models have strengths and weaknesses. Many work well only for the specific material types or load paths for which they were developed. The following features should commonly be considered when selecting and using a constitutive model for an advanced analysis;

- i) the formulation of the constitutive model should adequately address the key features of the anticipated soil behavior. These may include the relationship between shear stiffness and strain, stress-level dependence, generation of pore pressures, and strain softening.
- ii) it should have a sound theoretical basis,
- iii) it should reasonably model the stress-strain and pore pressure generation in monotonic and cyclic laboratory tests. Direct comparisons should be available between numerical simulations and laboratory test data (site specific and/or relevant published information),
- iv) when appropriate, the model should reasonably capture the behavior represented by the empirical relationships for liquefaction triggering and post-liquefaction behavior,
- v) the selection of input parameters should be reasonably transparent, particularly in cases where direct calibration to laboratory data is not possible,

- vi) successful use of the model should be documented through back-analysis of case history response.”

There are several ways to include the liquefaction behavior in numerical methods, ranging from total-stress based empirical schemes to estimate liquefaction conditions such as the UBCTOT model (Beaty and Byrne, 2000), to simple effective-stress shear-volume coupling schemes such as the Finn model (Martin et al., 1975) and the “Roth” model (Dawson et al., 2001), to more comprehensive constitutive models such as the UBCSAND model (Beaty and Byrne, 2011); PM4Sand model (Boulangier et al., 2012), and Wang (1990) bounding surface model.

2.5.1. Total Stress-Based Models

Total stress based models are a relatively simpler class of constitutive models which simulate the softening of liquefiable elements. In the simplest formulations, the timing and the extent of liquefaction should be externally controlled by the users. More sophisticated models use cycle counters based on laboratory data and theoretical formulations to predict the evolution of liquefaction on an element by element basis. UBCTOT constitutive model, described by the Beaty and Byrne (2000) combines the three steps of the standard practice approach (triggering, flow slide and estimate of liquefaction-induced displacements) into one single analysis. It is implemented to FLAC software, which assumes undrained behavior, uses a (two-dimensional) total-stress approach to perform liquefaction analysis. Although pore pressures are not directly predicted in a true total stress model, the element stiffness may be decreased prior to liquefaction in relation to the anticipated change in pore pressure. UBCTOT uses Mohr- Coulomb elasto-plastic scheme with zero friction and a value of cohesion equal to the undrained shear strength, in combination with Rayleigh damping. The models have the advantage of being simple, while still incorporating critical aspects of liquefaction in the analysis.

Some of the limitations of the model are summarized as follows;

- i) the model is not iterative, and appropriate values of modulus reduction, factor and damping are selected at the start of the seismic analysis,
- ii) the use of equivalent modulus ratio that may not capture the pre-liquefaction phase well,
- iii) the cyclic shear stresses are accounted for on the horizontal plane only,
- iv) the simplified manner in which the undrained shear strength is specified,
- v) pore pressure is not taken into account explicitly,
- vi) liquefaction due to monotonic loading is not considered.

2.5.2. Loosely Coupled Effective Stress-Based Models

Effective stress-based models are used primarily for soils subject to changes in effective stresses due to cyclic loading. Loosely-coupled models do not directly predict the volumetric strains that lead to pore pressure changes but instead use an independent pore pressure generator. The Roth model (Dawson et al., 2001) is defined as a loosely coupled effective stress-based constitutive model to generate pore pressure from shear stress cycles using Seed's cyclic stress approach. This model is implemented in FLAC standard Mohr-Coulomb model. The two-dimensional model counts shear stress cycles by tracking the shear stress acting on horizontal planes (τ_{xy}) and looking for stress reversals. The cyclic stress ratio (CSR) of each cycle is measured, and it is used to compute the incremental "damage" that is then translated into an increment of excess pore pressure. The procedure is "loosely-coupled" because pore pressures are only computed after each 1/2 cycle of strain or stress as the analysis proceeds.

Some of the limitations of the model are summarized as follows;

- i) liquefaction-induced consolidation settlements are not captured,
- ii) pore pressure generation through contraction of the soil skeleton is not incorporated,
- iii) it is applicable to problems, where slope movements due to reduced shear strength are the main concern, while shaking-induced consolidation settlements are of secondary importance.

Loosely-coupled models may be based on complex non-linear models (e.g., Finn et al., 1986). Other examples of loosely coupled models include TARA-3 and TARA-3FL programs (Finn and Yogendrakumar, 1986)

2.5.3. Fully Coupled Effective Stress-Based Models

The most sophisticated type of continuum models are the fully-coupled effective stress models. These models directly predict the tendency of soil to dilate or contract in response to each load increment. This results in the generation or reduction of pore pressure depending on whether the strain is contractive or dilative. These models are often the most difficult to calibrate and verify, since the stiffness and pore pressure response of these models depend on the accurate prediction of volumetric strains at each load increment. The effects of pore water flow can often be considered when using a fully-coupled model. Although coupling groundwater flow and dynamic mechanical response requires an extremely complex analysis procedure, the effects of pore pressure migration or dissipation can be significant in some cases. Some well-known models implemented in FLAC software will be summarized in the following pages.

2.5.3.1. WANG (1990) Model

The WANG model is a fully coupled effective stress, bounding-surface hypo-elasticity model for (cohesionless) soil that is capable of reproducing, in detail, typical monotonic and cyclic, drained and undrained, hardening and softening behavior observed in classical laboratory tests on initially dense and loose soils (Wang, 1990). The model formulation includes a non-circular pyramidal failure (bounding) surface, a loading surface, a surface of phase transformation (at which contractive behavior changes to dilative during shearing), and a critical state surface (defining an ultimate state in which the sand deforms at constant volume under constant stress).

Some of the limitations of the model are summarized as follows;

- i) the three-dimensional effective-stress model requires the specification of 15 constants for given sand,
- ii) model calibration is a difficult task because most model constants are not related to soil properties which are familiar by the users and the body of available parameter data is not yet sufficiently developed,
- iii) comparison to state-of-practice analysis is not straightforward. Assistance of the model developer may be required for model calibration, interpretation of results, and support on possible issues with numerical implementation.

2.5.3.2. NTUA-SAND Model

The NTUA-SAND model is a fully coupled effective stress, bounding-surface model for loose and dense sand that is based on critical state elasto-plasticity (Papadimitriou et al., 2001 and Papadimitriou and Bouckovalas, 2002). The model applies to monotonic as well as cyclic loading (in two and three dimensions) of non-cohesive soils under small and large strains. The model uses a kinematic

hardening non-circular cone as the (loading) yield surface. In addition to bounding and dilatancy (marking the transition between contractive and dilatants behavior) surfaces, the model also contains a critical-state surface (defining an ultimate state in which the sand deforms at constant volume under a constant shear and confining stress).

The model has the capability to model degradation of shear modulus and increase of hysteretic damping with cyclic shear strain amplitude, the shear and volumetric strain accumulation at a decreasing rate with increasing number of cycles, and the increase in liquefaction resistance with density.

Some of the limitations of the model are summarized as follows;

- i) the model contains a total of 14 parameters: 11 of the parameters can be derived from in-situ and laboratory tests, while the remaining three must be derived indirectly via trial-and-error simulations of drained and undrained laboratory tests,
- ii) model calibration requires a test database not readily available in most cases,
- iii) long computational time required for the solution of practical problems,
- iv) application of the model to study boundary-value problems at the field scale is not recommended,
- v) comparison to standard practice is not straightforward. Assistance of the model developer is required for model calibration, interpretation of results and numerical implementation.

2.5.3.3. UBCSAND Model (2009, 2012)

This model was developed at the University of British Columbia and is outlined in multiple references (e.g.: Puebla et al., 1997; Byrne et al., 2004; Beaty and Byrne, 2011). UBCSAND is an incremental elastic-plastic model, which is controlled by

changes in the effective stress ratio. The model was developed based on plasticity theory and observations from laboratory tests on sands. The model is currently in use on multiple large scale projects, such as the evaluation of liquefaction potential at Success Dam (Perlea et al., 2008). The version of the model used here is 904aR as described by Beaty and Byrne (2011). One major change with the new version is that reloading cycles, which do not follow a stress reversal, behave plastically as opposed to remaining elastic as predicted by previous versions. This allows plastic strains to be accumulated without having full stress reversals. This model is formulated for plane strain conditions and depends only on the shear and normal effective stress.

Elastic Response: The elastic strains for this model are a function of changes in either the shear or normal effective stress. The relationship between stresses and strain is controlled by the shear and bulk moduli. Both moduli are isotropic and non-linear, meaning they are a function of the current mean stress, which are mentioned in Equations 2.21 and 2.22 respectively.

$$G^e = K_e^G P_a \left(\frac{\sigma'_m}{P_a} \right)^{n_e} \quad (2.21)$$

$$\text{lim} : 500 \leq K_e^G \leq 2000, \quad 0.4 \leq n_e \leq 0.6$$

$$B^e = \alpha G^e \quad (2.22)$$

$$\text{lim} : \frac{2}{3} \leq \alpha \leq \frac{4}{3} \quad \text{or} \quad \alpha \approx 1$$

where;

K_e^G = A shear modulus number (depends on the density of the sand)

B^e = the elastic bulk modulus

σ'_m = the mean stress in the plane of loading

P_a = Atmospheric pressure in the chosen units.

n^e = An elastic exponent (approximately 0.5)

α = A constant depends on the elastic Poisson's ratio

Yield Surface: The yield surface for a model controls the boundary between elastic and plastic behavior. For UBCSAND, the yield surface can be described as radial lines which extend outward from the origin at a constant stress ratio. At the onset of loading the current stress ratio is very small so each increment of loading produces an elastic-plastic response. The yield surface is illustrated schematically in Figure 2.17.

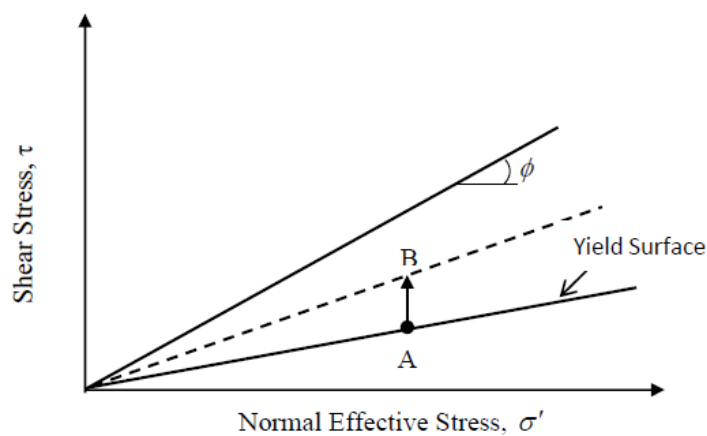


Figure 2.17. Yield surfaces for UBCSAND (Beatty and Byrne, 2011)

Plastic Flow: As the stress ratio of the soil moves outside the yield surface plastic strains will develop. This model utilizes a non-associated flow rule, meaning that the direction of plastic strains is not dependent on the current slope of the yield surface. Plastic shear strains are computed from the current stress ratio ($n = \tau / \sigma_v'$) through a hyperbolic relationship as shown in Figure 2.18. The magnitude of the plastic volumetric strains is coupled to the shear strain through the angle of dilation. Volumetric strains can either be contractive or dilative and this is determined by the relation of the soil to the critical state line as defined by the constant volume friction angle. Soils at a stress ratio below the constant volume friction angle will undergo contractive behavior, while soils above will tend to

dilate. Soils at the critical state line will not experience volumetric strains. This is consistent with critical state theory and is illustrated in Figure 2.19.

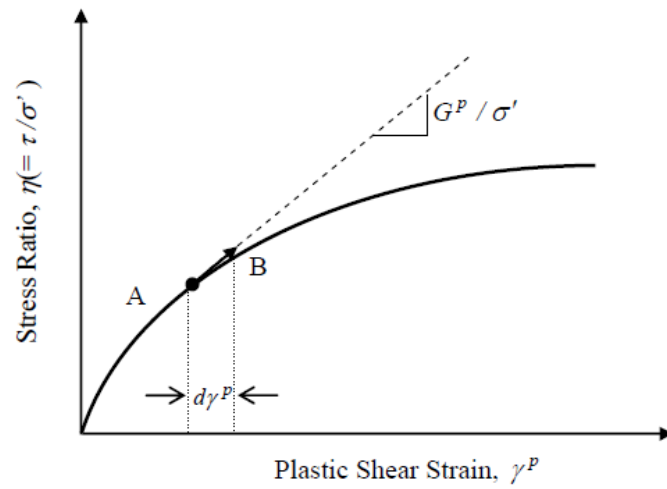


Figure 2.18. Relationship between stress ratio and plastic shear strains for UBCSAND (Beaty and Byrne, 2011)

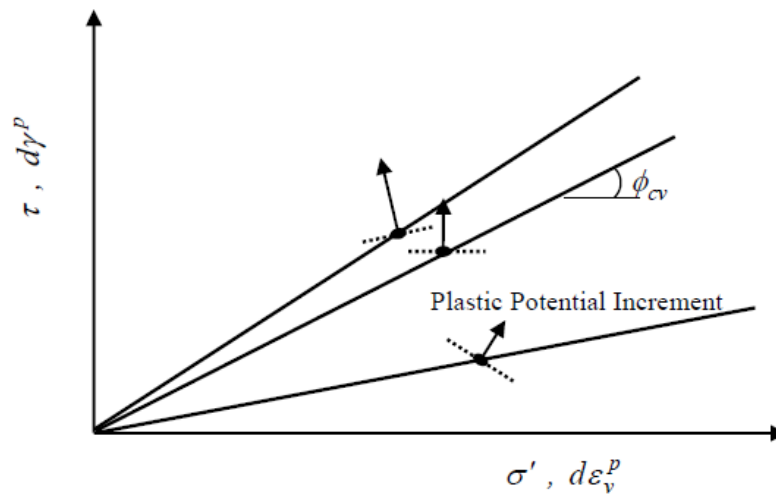


Figure 2.19. Direction of plastic shear strains for UBCSAND (Beaty and Byrne, 2011)

The plastic shear modulus relates the shear stress and the plastic shear strain ($d\gamma^P$) and is assumed to be hyperbolic with stress ratio as shown in Figure 2.18, and can be expressed as in Equation 2.23.

$$d\gamma^P = \frac{1}{G^P / \sigma'} d\eta \quad (2.23)$$

where;

G^P = Plastic shear modulus

The associated plastic volumetric strain increment, $\Delta\varepsilon_v^P$, is obtained from the dilation angle ψ , which is estimated by laboratory test data and energy considerations;

$$\Delta\varepsilon_v^P = \Delta\gamma^P \sin(\psi) \quad (2.24)$$

The plastic properties used by the model are the peak friction angle ϕ^P , the constant volume friction angle ϕ_{cv} , and plastic shear modulus G^P ;

$$G^P = G_i^P \left(1 - \frac{\eta}{\eta_f} R_f \right)^2 \quad (2.25)$$

where;

lim: $\eta_f = \sin\phi_f$ and $0.70 \leq R_f \leq 0.98$

G_i^P = Plastic modulus at a low stress ratio level ($\eta=0$)

η_f = the stress ratio at failure

ϕ_f = the peak friction angle;

R_f = the failure ratio, decreases with increasing relative density.

Note that R_f is used for truncating the best fit hyperbolic relationship and prevent the over prediction of strength at failure.

It has been useful to relate G_i^P to G^e and relative density D_R through the approximate relationship;

$$G_i^P = 3.7 (D_R)^4 G^e + P_a \quad (2.26)$$

Hardening Laws: The yield surface begins as a small radial line extending from the origin, but the yield surface “opens” as the soil is plastically sheared as shown in Figure 2.17. The maximum and minimum stress ratios seen by the soil are tracked separately, so the hardening law is tracked independently for positive and negative stress ratios. If the soil is unloaded it will behave elastically until the sign of the shear stress reverses. At this point the soil will be “reloading” until it reaches its previous maximum or minimum stress ratio. Reloading does generate plastic strains, but with a shear modulus that is significantly stiffer than the first time or virgin loading.

Input Parameters: Input parameters of the model are briefly described as follows:

- i) *Clean Sand SPT blow count* – The corrected SPT blow count after considering the effect of fines on the measured penetration resistance. The correction proposed by Idriss and Boulanger (2008) was used in this paper. UBCSAND is internally calibrated to the Youd et al. (2001) relationship for calculating the CRR for a given soil from the clean sand blow count, so this blow count directly affects the number of cycles to cause liquefaction.
- ii) *Constant Volume Friction Angle* – The constant volume or critical state friction angle controls the direction of the plastic flow for UBCSAND as shown in Figure 2.19.
- iii) *Elastic Shear Modulus Number* – The elastic shear modulus number represents the small-strain shear stiffness, G_{max} , for a given soil and is used in the non-linear relationship between the shear modulus and mean confining stress. This is an optional input parameter, but to maintain consistency between the two models it was set. G_{max} is based on the equivalent shear wave velocity as correlated from the blow counts and the density of the material.

- iv) *Elastic Bulk Modulus Number* – The elastic bulk modulus number was set for similar reasons to the elastic shear modulus number. This number is related to G_{max} through Poisson’s ratio.

2.5.3.4. PM4Sand Model (2012)

The model is a bounding surface plasticity model for sand presented by Boulanger et al. (2012). PM4Sand was modified from a model proposed by Dafalias and Manzari, (2004), to improve its ability to predict the soil behavior important to geotechnical earthquake engineering, as seen in empirical and case history based correlations. This model was modified at the equation level to better predict the response of sandy soils to laboratory testing and to fit published design relationships and correlations. It is formulated for plane strain problems and is controlled by the current stress ratio (q/p').

Critical State: The soil response is compatible with critical state soil mechanics through the use of the relative state parameter ξ_r and the critical state line formulate by Bolton (1986) given in Figure 2.20.

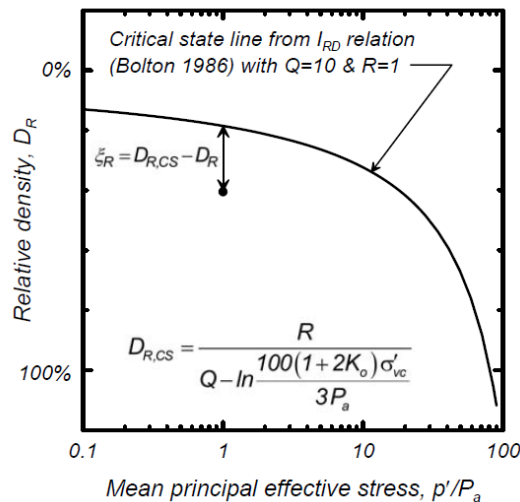


Figure 2.20. Critical state line and relative state parameter used in PM4Sand (Boulanger et al, 2012)

Elastic Response: The elastic shear modulus, G in the model is dependent on the mean effective stress as follows;

$$G = G_0 p_A \left(\frac{p}{p_A} \right)^{1/2} C_{SR} \quad (2.27)$$

and

$$C_{SR} = 1 - C_{SR,0} \left(\frac{M}{M^b} \right)^{m_{SR}} \quad (2.28)$$

where;

G_0 = shear modulus constant,

p_A = atmospheric pressure (101.3 kPa)

C_{SR} = factor that accounts for stress ratio effects

Yield Surface: The yield surface for PM4Sand is a tiny cone in stress-space whose center is defined by a term called the back-stress ratio. The yield surface along with bounding and dilatancy surfaces, described below, are illustrated schematically in Figure 2.21 and Figure 2.22.

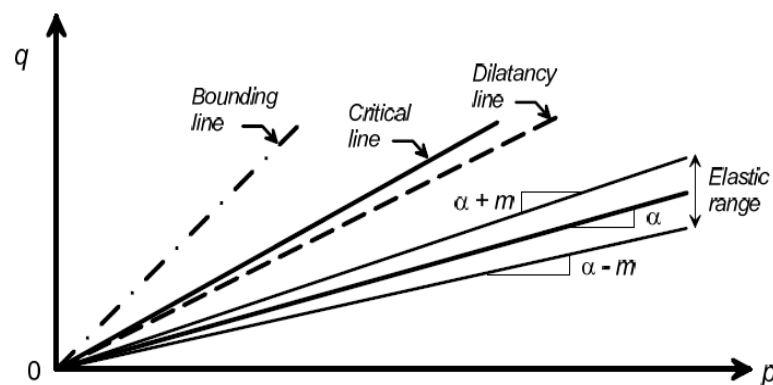


Figure 2.21. Schematic of yield, critical, dilatancy, and bounding lines in q - p space (After Dafalias & Manzari, 2004)

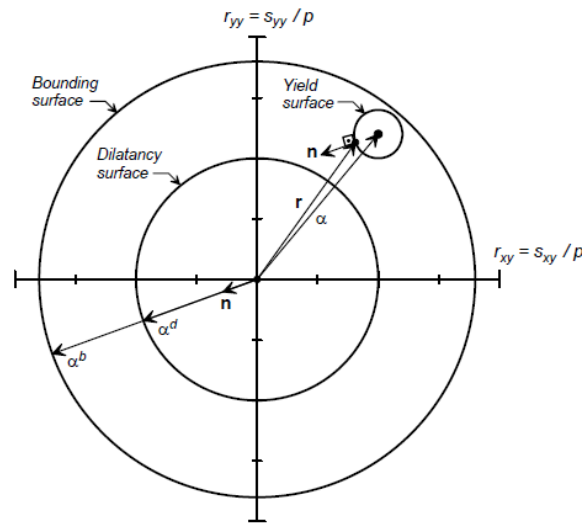


Figure 2.22. Schematic of the bounding, dilation, and yield surfaces
(after Dafalias & Manzari, 2004)

Plastic Flow: The flow rule for PM4Sand is non-associated and is separated into deviatoric and volumetric component. Deviatoric strains are computed based on the plastic modulus, which is based on the distance from the current stress state to the bounding surface. The location of the bounding surface is related to the relative state of the soil, so as the soil is sheared the bounding surface will also move towards the critical state line. Volumetric strains are related to the deviatoric strains through the dilation term. The sign of the dilation term is controlled by the distance to the dilatancy, or phase transformation, line. If the soil lies above the line, it will become dilative and if it is below the line then the soils will be contractive. Accumulation of strains is affected in this model by a fabric dilatancy tensor. The fabric tensor modifies the plastic modulus and the dilation response of the soil to better predict the accumulation of shear strains with additional cyclic loading and the effects of sustained static shear stresses.

Hardening Laws: This model accounts for hardening and softening by kinematic rotation of the yield surface in the stress space. This rotation is accomplished by updating the back-stress ratio which defines the center of the yield surface. The

rate of hardening is controlled by the distance to the bounding surface and the plastic modulus, so it will also be affected by the fabric tensor.

Input Parameters: The model parameters are grouped into two categories; a primary set of five parameters (three properties, one flag, and atmospheric pressure) that are most important for model calibration, and a secondary set of parameters that may be modified from their default values in special circumstances.

- i) *Relative Density (D_R)* : The relative density of the material is the primary input variable for PM4SAND and determines the dilatancy and stress-strain response of the soil and SPT-N based penetration resistances correlation, used by Idriss and Boulanger (2008) is recommended:

$$D_R = \sqrt{\frac{N_{1,60}}{c_d}} \quad (2.29)$$

where $c_d=46$.

- ii) *Shear Modulus Coefficient (G_0)*: Primary variable controlling the small strain shear modulus, G_{max} which should be chosen to match estimated or measured shear wave velocities according to $G_{max} = \rho V_s^2$
- iii) *Contraction rate parameter (h_{p0})*: Primary variable that adjusts contraction rates and hence can be adjusted to obtain a target cyclic resistance ratio, as commonly estimated based on CPT or SPT penetration resistances and liquefaction correlations.
- iv) *Poisson's Ratio* – This number is used to calculate the small-strain bulk modulus based on the shear modulus.

- v) The secondary input parameters (16 in total) which default values have been developed that will generally produce reasonable agreement with the trends in typical design correlations

2.6. Conclusion

In this chapter, a brief overview of the previous studies on liquefaction definitions and mechanisms, liquefaction susceptibility of cohesionless soils and liquefaction triggering procedures were briefly discussed. Moreover, cyclic straining and induced pore pressure models, stiffness reduction response of the soils under dynamic loadings were also presented. There are several ways liquefaction behavior can be modeled by numerical methods, ranging from total-stress empirical schemes to simple effective-stress shear-volume coupling schemes. In this chapter, available comprehensive liquefaction constitutive models were discussed in order to distinguish their strengths and weaknesses. In the next chapter, the proposed effective stress based simplified constitutive model and its implementation procedure is discussed in detail which constitutes the basis of this dissertation.

CHAPTER 3

THEORETICAL BASIS OF THE PROPOSED CONSTITUTIVE MODEL AND ITS NUMERICAL IMPLEMENTATION

3.1. Introduction

A fully-coupled effective stress based constitutive model, METUSAND was developed for modeling cyclic response of fully saturated cohesionless soils. The proposed constitutive model is composed of two major components corresponding to pre-liquefaction and post-liquefaction responses.

Within the proposed constitutive model framework, the cyclic straining and induced pore pressure responses are modeled as described in Cetin et al. (2009), Cetin and Bilge (2012, 2014). Hysteretic modulus degradation and damping responses are confirmed with widely available modulus degradation and damping curves. This nonlinear and plastic response until the onset of failure is referred to as *pre-liquefaction phase*. As described in Cetin and Bilge (2012), soil system stiffness is reduced with increasing cyclic shear strain and pore pressure. This results in a zero effective stress state, which is referred as “*initial liquefaction*”. Beyond the onset of initial liquefaction, the response during the *post-liquefaction phase* is governed by large deformations which are assessed by the constitutive relations given by Shamoto et al. (1998). Schematic illustration of METUSAND is given in Figure 3.1

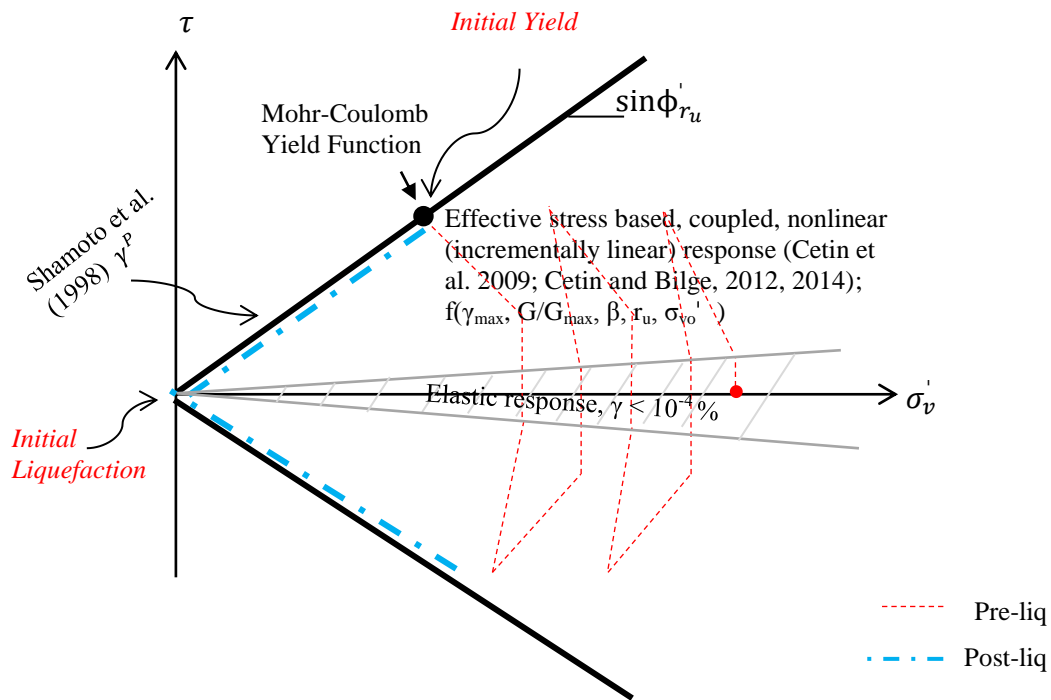


Figure 3.1. Schematic illustration of METUSAND

3.2. Description of Proposed METUSAND Model

METUSAND is a simplified effective stress-based nonlinear constitutive model which assesses the response of the fully saturated cohesionless soils subjected to dynamic loading. The response of the pore fluid is coupled to the soil response through the bulk modulus of the fluid. It is based on the recent semi-empirical cyclic straining and excess pore water pressure assessment models of Cetin et al. (2009), Cetin and Bilge (2012, 2014) and Shamoto et al. (1998).

Proposed model is implemented into elastic-perfectly plastic constitutive model with Mohr-Coulomb failure criterion already built-in FLAC (ITASCA 2012) software, which accounts for strain-based modulus degradation behavior applicable for plane strain conditions. The plastic response generates plastic strains, and pore pressure generation is a function of plastic shear strain. Unloading is assumed to be linear, using reduced shear modulus which is also a

function of mean effective stress ($\sigma'_{m,0}$). The parameters associated with the proposed constitutive model are grouped into three categories: i) elastic stress-strain behavior, ii) plastic stress-strain behavior and pore pressure generation under cyclic loading, iii) post liquefaction stress-strain response.

3.2.1. Elastic Response

In general, initial conditions are composed of the initial i) configuration of geometry, ii) ground water conditions and iii) effective stress state. In order to calculate cyclic response of a soil, first of all, stress state under gravitational loading should be defined. The initial elastic component of response is assumed to be isotropic and based on Hooke's law, which mathematically expresses the linear relationship of the strains in terms of the stresses. There are four material parameters, two of which are required to fully specify the elastic material response. Bulk modulus K^e , shear modulus G^e and initial earth pressure constant K_0 are expressed as a function of elastic modulus E , and Poisson's ratio ν , as follows;

$$G^e = \frac{E}{2(1+\nu)} \quad (3.1)$$

$$K^e = \frac{E}{3(1-2\nu)} \quad (3.2)$$

$$K_0 = \frac{\nu}{(1-\nu)} \quad (3.3)$$

The principal stresses and principal directions according to FLAC are evaluated from the stress tensor components, and ordered as follows;

$$\sigma_1 \leq \sigma_2 \leq \sigma_3 \quad (3.4)$$

The corresponding principal strain increments $\Delta\varepsilon_1$, $\Delta\varepsilon_2$, $\Delta\varepsilon_3$ are decomposed as shown in equation 3.5 where the superscripts e and p refer to elastic reversible and

plastic irreversible parts, respectively, and the plastic components are nonzero only during plastic phase.

$$\begin{aligned}
 \Delta\varepsilon_1 &= \Delta\varepsilon_1^e + \Delta\varepsilon_1^p \\
 \Delta\varepsilon_2 &= \Delta\varepsilon_2^e + \Delta\varepsilon_2^p \\
 \Delta\varepsilon_3 &= \Delta\varepsilon_3^e + \Delta\varepsilon_3^p
 \end{aligned}
 \tag{3.5}$$

The incremental expression of Hooke's law is given in Equation 3.6 in terms of the principal stresses and strains.

$$\begin{aligned}
 \Delta\sigma_1 &= \alpha_1\Delta\varepsilon_1 + \alpha_2(\Delta\varepsilon_2 + \Delta\varepsilon_3) \\
 \Delta\sigma_2 &= \alpha_1\Delta\varepsilon_2 + \alpha_2(\Delta\varepsilon_1 + \Delta\varepsilon_3) \\
 \Delta\sigma_3 &= \alpha_1\Delta\varepsilon_3 + \alpha_2(\Delta\varepsilon_1 + \Delta\varepsilon_2)
 \end{aligned}
 \tag{3.6}$$

where

$$\alpha_1 = K^e + \frac{4}{3}G^e \text{ and } \alpha_2 = K^e - \frac{2}{3}G^e
 \tag{3.7}$$

Initial shear modulus, G_{\max} is a user defined input parameter, which should to be selected at reference stress condition of $\sigma'_{vo} = 100$ kPa. For cohesionless soils, shear modulus is assigned to each element which changes nonlinearly with vertical effective stress according to Equation 3.8.

$$G^e = G_{\max} \sqrt{\frac{\sigma'_{vo}}{100}}
 \tag{3.8}$$

In METUSAND model, elastic response is applicable up to maximum shear strain levels of 10^{-4} %.

3.2.2. Effective-stress Based Nonlinear (Incrementally Linear) Soil Response

When maximum shear strain levels exceed 10^{-4} %, and before yield criterion is fulfilled, stress-strain response is defined as given herein. The model implementation in dynamic analyses is a modified form of the built-in elastic-plastic model with Mohr-Coulomb failure criterion (referred to as Mohr-Coulomb model in FLAC) in FLAC software. Mohr-Coulomb model, unfortunately cannot incorporate, strain (or effective stress) induced modulus degradation and corollary damping responses. Hence, in METUSAND, a modification to Mohr-Coulomb was implemented to take into account: i) effective stress based definition of G_{\max} , ii) excess pore pressure generation as a function of shear straining, iii) strain (and effective stress) compatible shear modulus degradation by G/G_{\max} relationships as defined by Cetin and Bilge (2014), iv) unloading and corresponding stiffer modulus response and v) strain compatible hysteretic damping. Plastic strains are controlled by the modulus degradation and unloading response. The Mohr-Coulomb criterion (shear yield function) with tension cutoff (tensile yield function) is adopted to define the failure envelope for the proposed model. The nonlinear modulus degradation behavior results in plastic strains and pore pressure generation is defined as a function of maximum shear strains. The subroutine is applicable in pre-liquefaction phase until the system reaches to the initial liquefaction state.

3.2.2.1. Yield Criterion

Yielding (and failure) takes place in the soil mass when mobilized (actual) shear stress at any plane becomes equal to shear strength (τ_f) which is given by:

$$\tau = c' + \sigma'_v \tan\phi' = \tau_f \quad (3.9)$$

where c' and ϕ' are strength parameters; c' is referred the cohesion and ϕ' is referred the angle of internal friction. τ and σ' are the shear and effective vertical stresses acting on the plane where failure occurs (through a shearing effect).

Mohr-Coulomb criterion in the space of principal stresses (according to the order given in Equation 3.4) can be expressed as;

$$\sigma_1 - \frac{1+\sin\phi'}{1-\cos\phi'}\sigma_3 - 2\frac{\cos\phi'}{1-\sin\phi'}c' = 0 \quad (3.10)$$

In METUSAND, internal friction angle is decreasing with increasing excess pore pressure as follows;

$$\phi'_{ru} = (\phi' - \phi_{ss})x(1 - r_u) + \phi_{ss} \quad (3.11)$$

where;

r_u = excess pore pressure ratio

ϕ'_{ru} = reduced friction angle in dynamic condition

ϕ_{ss} = steady state friction angle of cohesionless soils (taken as 28°)

Stress states are updated incrementally according to excess pore water increase, Δu , in each stress increment as;

$$-\Delta u = (r_u^N - r_u^O)\sigma'_{v0} \quad (3.12)$$

$$\begin{aligned} \sigma_{11}^N &= -\Delta u + \sigma_{11}^O + \alpha_1^p \Delta \epsilon_{11} + \alpha_2^p (\Delta \epsilon_{22} + \Delta \epsilon_{33}) \\ \sigma_{22}^N &= -\Delta u + \sigma_{22}^O + \alpha_1^p \Delta \epsilon_{22} + \alpha_2^p (\Delta \epsilon_{11} + \Delta \epsilon_{33}) \\ \sigma_{33}^N &= -\Delta u + \sigma_{33}^O + \alpha_1^p \Delta \epsilon_{33} + \alpha_2^p (\Delta \epsilon_{11} + \Delta \epsilon_{22}) \\ \sigma_{12}^N &= \sigma_{12}^O + \beta \gamma_{12} \\ \sigma_{13}^N &= \sigma_{13}^O + \beta \gamma_{13} \\ \sigma_{23}^N &= \sigma_{23}^O + \beta \gamma_{23} \end{aligned} \quad (3.13)$$

where;

$$\alpha_1^p = K + \frac{4}{3}G, \alpha_2^p = K - \frac{2}{3}G, \beta = 2G \quad (3.14)$$

Plastic component is referred to by the superscript “p”. New and old stress states are referred to by the superscripts “N” and “O”, respectively.

3.2.2.2. Modulus Degradation and Damping Response

Cyclic response of saturated cohesionless soils is governed by the *initial shear modulus (stiffness) parameter*, which should be determined carefully. There exist a number of methods for calculating initial stiffness of the soil based on site specific field tests and/or laboratory tests results. However, stress dependency and strain compatibility also affect the stiffness response.

In this research, semi-empirical shear modulus degradation model, which is developed by Cetin and Bilge (2014), is used to define the modulus degradation response of granular soils during cyclic loading. Cetin and Bilge (2014) followed an experimental approach to deal with the modulus degradation and hysteretic damping responses of fully saturated clean sands by taking into account the coupled shear strain accumulation and excess pore water pressure generation responses. For this purpose, a database was compiled including resonant column, simple shear and cyclic triaxial tests performed on different types of clean sands. On the basis of these laboratory test results, a probabilistically-based semi-empirical model is introduced by Cetin and Bilge (2014).

Modulus degradation is expressed by the ratio of the shear modulus, G , which is given in Equation 3.18, corresponding to various strain amplitudes to the maximum shear modulus, G_{\max} . For all practical purposes, G_{\max} is accepted to be the G value at small strain threshold level of $\gamma=10^{-4}\%$. By using maximum likelihood methodology, Equation 3.15 was developed which presents shear

modulus as a function of maximum single amplitude cyclic shear strain (γ_N) and the corresponding excess pore water pressure ratio ($r_{u,N}$) at any loading cycle, N. Moreover, effective stress-based modulus degradation relations are developed and introduced in Equation 3.16 and model parameters are given in Table 3.1.

$$G = \frac{\theta_1 \cdot D_r + \theta_2}{1 + \theta_3 \cdot (\gamma_N)^{\theta_4}} \cdot \left[(1 - r_{u,N} + \theta_5) \cdot 0.0479 \cdot \sigma'_{m0} \right]^{0.5 + \theta_6 \cdot \gamma_N} \pm \sigma_\varepsilon \quad (3.15)$$

$$\frac{G}{G_{\max}} = \frac{G}{G_{\gamma=10^{-4}\%}} = \frac{1 + \theta_3 \cdot (10^{-4})^{\theta_4}}{1 + \theta_3 \cdot (\gamma_N)^{\theta_4}} \cdot \frac{\left[(1 - r_{u,N} + \theta_5) \cdot 0.0479 \cdot \sigma'_{m0} \right]^{0.5 + \theta_6 \cdot \gamma_N}}{\left[(1 + \theta_5) \cdot 0.0479 \cdot \sigma'_{m0} \right]^{0.5 + \theta_6 \cdot 10^{-4}}} \pm \sigma_\varepsilon \quad (3.16)$$

where;

γ_N = maximum single amplitude cyclic shear strain at Nth loading cycle

$r_{u,N}$ = excess pore water pressure ratio at Nth loading cycle

σ'_{m0} = effective initial mean principal stress

Table 3.1 Model Coefficients of Modulus Degradation Model (Cetin and Bilge, 2014)

θ_1	θ_2	θ_3	θ_4	θ_5	θ_6	σ_ε
528.64	11910.89	37.1	1.06	0.05	0.01	1.55

Stress-strain behavior of the model is given in Figure 3.2 for soil relative density of 60 %, and initial vertical effective stress of 100 kPa in isotropic condition.

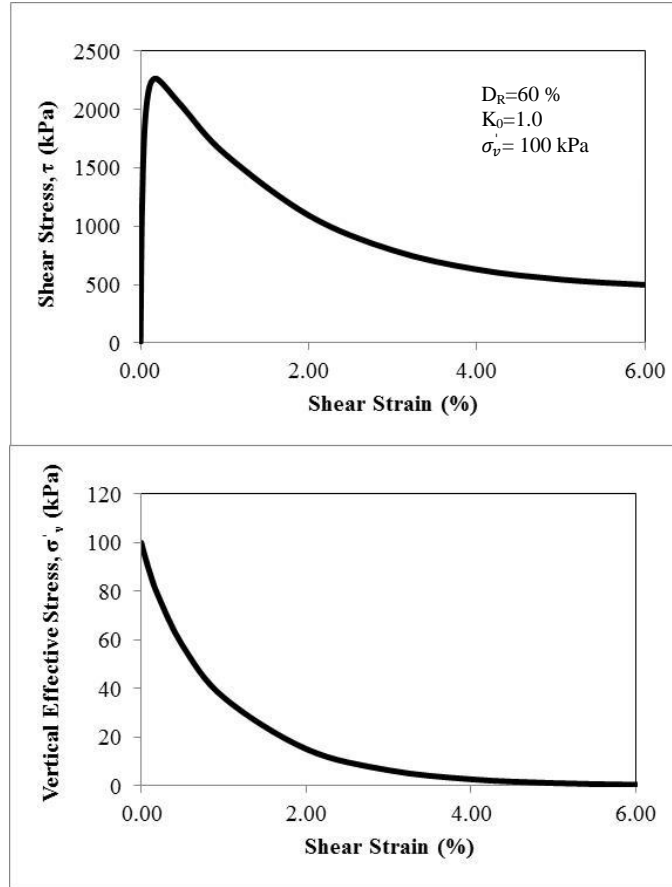


Figure 3.2. Stress-Strain Relationship (Cetin and Bilge, 2014)

Similarly, to model the hysteretic damping response, a model was introduced by Cetin and Bilge (2014) as a function of maximum single amplitude cyclic shear strain (γ_N), initial mean effective stress (σ'_{m0}), excess pore water pressure ratio ($r_{u,N}$) at N^{th} loading cycle, and relative density of sand, D_R . Equation 3.17 is adopted for the prediction of D in percentage at any n^{th} loading cycle (i.e.: D_N) and model parameters are given in Table 3.2.

$$D = (1 - \exp\left(\frac{\theta_1 \cdot \gamma_N^{\theta_4}}{\theta_2 + \theta_3 \cdot \ln[\sigma'_{m0} \cdot (1 - r_{u,N} + \theta_5)] - D_R / 100}\right)) \pm \sigma_\varepsilon \quad (3.17)$$

Table 3.2 Model Coefficients of Damping Model (Cetin and Bilge, 2014)

θ_1	θ_2	θ_3	θ_4	θ_5	σ_ε
3.220	-2.690	0.010	0.594	0.010	0.145

Modulus degradation and damping relations of Cetin and Bilge (2014) (for $D_R=60$ %, $\sigma'_{m0} = 100$ kPa and $r_u=0.0$) are compared with widely-used relations of Seed et al. (1984) (the average curve corresponding to the stress range of 1 to 3 tsf) and Vucetic and Dobry (1991) (PI=0 % curve) in Figures 3.3 and 3.4, respectively.

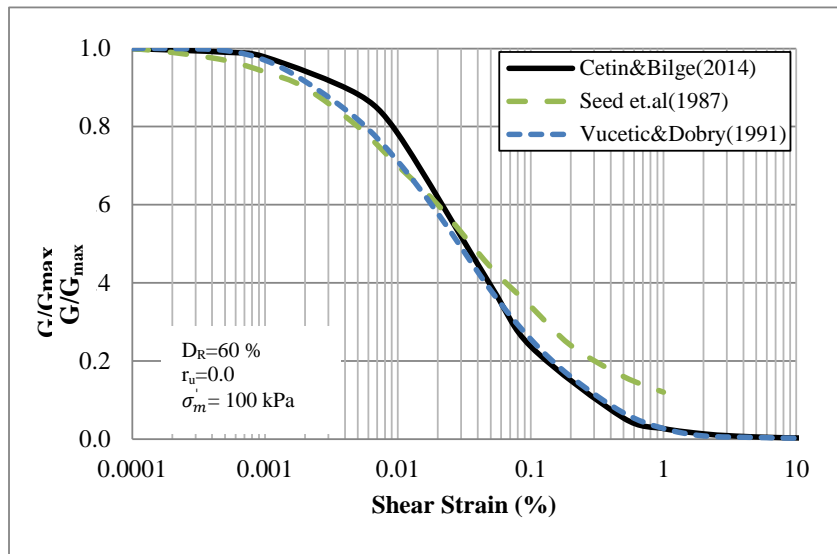


Figure 3.3. Comparison of effective stress-based modulus degradation relationships (Cetin and Bilge, 2014) with existing models

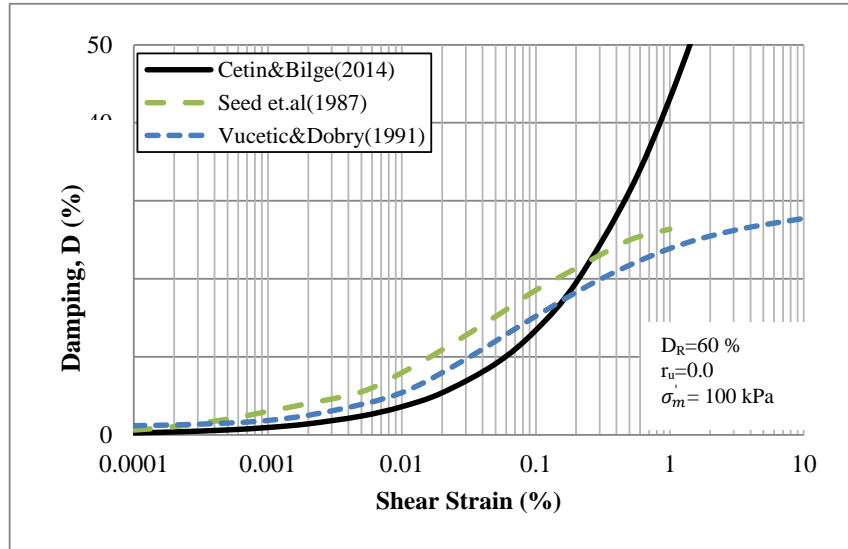


Figure 3.4. Comparison of effective stress-based damping model (Cetin and Bilge, 2014) with existing models

As presented in Figure 3.3, the proposed model yields very similar results with the existing studies at small strain range, especially up to 0.04 % shear strain; whereas beyond this strain level the proposed model yields smaller G/G_{max} values, which reveals the significance of pore water pressure generation. During undrained cyclic shearing, excess pore water pressure generates and it significantly alters the dynamic response of saturated soils compared to response of dry soils.

The METUSAND model presented herein follows the basic framework of accumulation of the cyclically induced plastic shear strain as a result of degradation of soil stiffness and strength reduction. Soil stiffness is adjusted at each loading cycle; due to increase in excess pore pressure, and accumulation of shear strain.

It is a common approach to assess modulus degradation and damping responses in a combined manner, while assessing the nonlinear soil response under cyclic loading conditions. A major advantage of the proposed model is that damping is mainly hysteretic and both modulus degradation and damping is intrinsically

assessed. Hence no additional damping such as viscous or Rayleigh damping needs to be specified. Hysteretic damping is appropriate to the level of excitation at each point in time and space.

Figure 3.6 presents the shear stress - shear strain response of a saturated sand specimen having D_R of 44% and isotropically consolidated ($K_0 = 1$) under an effective vertical stress (σ_{v0}') of 100 kPa. In this simulation, CSR (τ/σ'_{v0}) is increased from 0.001 to 0.19 step by step in each loading cycle (Figure 3.5). Hysteretic damping values, which was described in Section 2.3.1 was estimated from the area under the each stress-strain loop. It is clear that the area under the stress strain loop is changing with increasing strain levels. Unloading modulus is selected as the 2.5 times of loading modulus of each cycle to obtain a compatible damping value with damping relationships available in the literature. Estimated damping values are given in Figure 3.7, which is compatible with existing shear strain-damping relations.

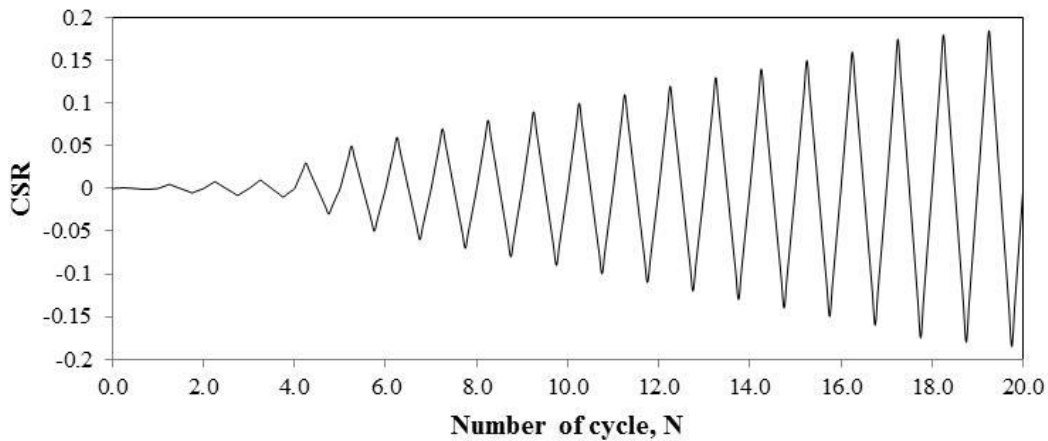


Figure 3.5. Applied CSR (τ/σ'_{v0}) increased step by step in each loading cycle

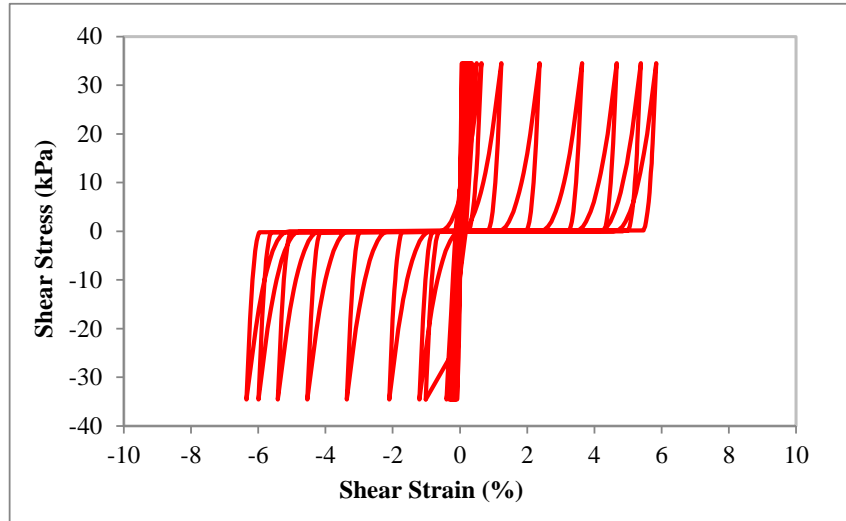


Figure 3.6. Shear stress-shear strain loop for increasing τ/σ'_{v0}

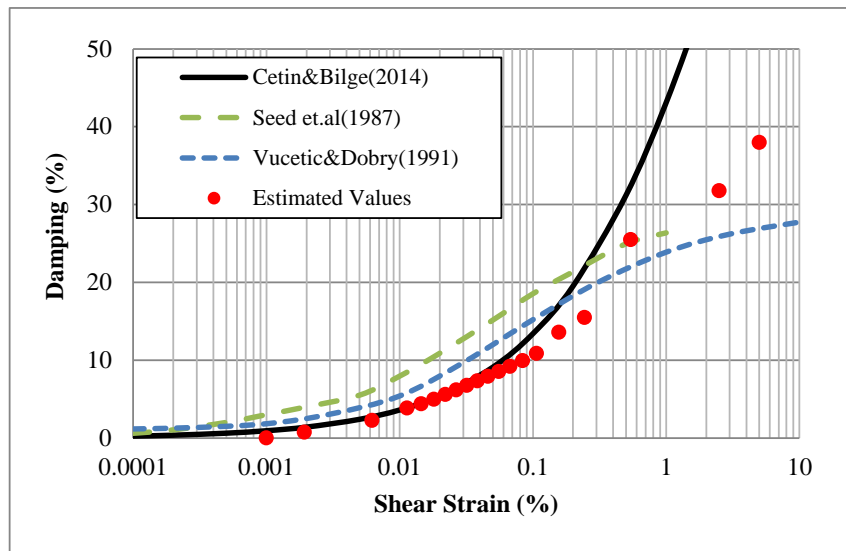


Figure 3.7. A comparison of the intrinsically developed damping values of METUSAND with existing strain dependent damping relations

3.2.2.3. Loading and Unloading Definitions and Plastic Shear Straining

Plastic straining as a result of modulus degradation in each cycle of dynamic loading is illustrated in Figure 3.8. Consistent with increasing excess pore pressure, plastic strains are observed to be accumulated.

Shear modulus during loading, G is a function of single amplitude shear strain, γ_N relative density, D_R of the soil, excess pore pressure ratio, r_u and, initial mean effective stress, $\sigma'_{m0} \left(\frac{\sigma_x + \sigma_y + \sigma_z}{3} \right)$ as given in Equation 3.15.

Single amplitude shear strain, γ_N , is defined as the half of maximum double amplitude cyclic shear strain level observed at N^{th} loading cycle;

$$\gamma_N = \frac{\gamma_{max,N}}{2} \quad (3.18)$$

Unloading shear modulus $G_{\text{unloading}}$ is constant and calculated as a function of reduced loading modulus of the corresponding cycle;

$$G_{\text{unloading}} = G * \left(\theta - \frac{G}{G_{\text{max}}} \right) \quad (3.19)$$

θ is an adjustment parameter which is selected as 2.5 to have strain-compatible hysteretic damping values with damping relationships available in the literature as shown in Figure 3.7.

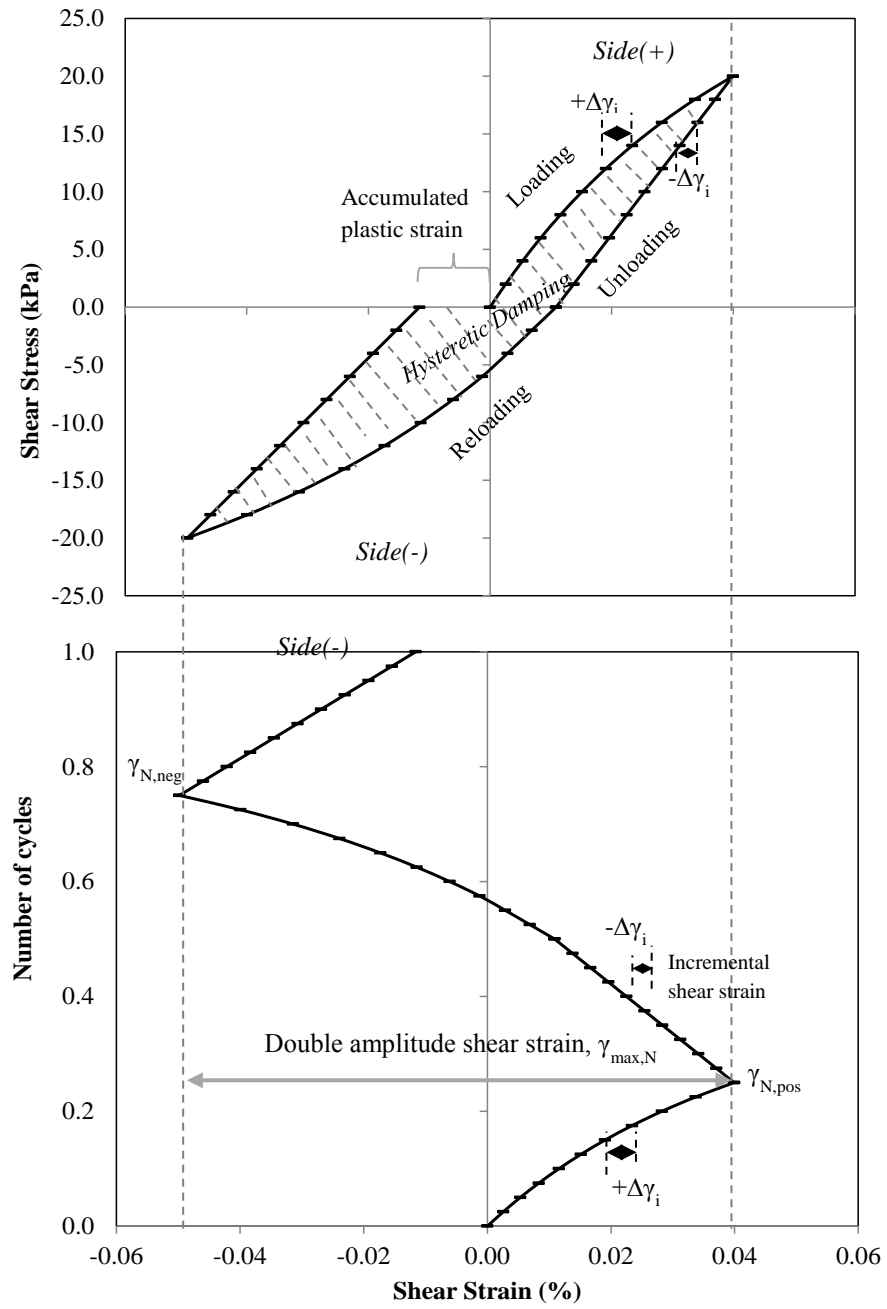


Figure 3.8. Single Loading-Unloading cycle of the proposed model

3.2.2.4. Excess Pore Pressure Generation

Excess pore pressure ratio, r_u , is defined as a function of maximum double amplitude cyclic shear strain at N^{th} cycle ($\gamma_{\max,N}$), relative density, D_R , of the soil and initial vertical effective stress, σ'_{v0} in METUSAND and given in Equation 3.20.

$$r_u = f(\gamma_{\max,N}, \sigma'_{v0}, D_R) = \left[1 - \exp \left(- \frac{-0.407 * \gamma_{\max,N}}{-0.486 + 0.025 \ln(\sigma'_{v0}) - \left(\frac{D_R}{100}\right)} \left(\frac{0.620}{1 + \gamma_{\max,N}} + 1 \right) \right) \right] \quad (3.20)$$

Estimation of $\gamma_{\max,N}$ is equated in Equation 3.21 and shown schematically in Figure 3.8.

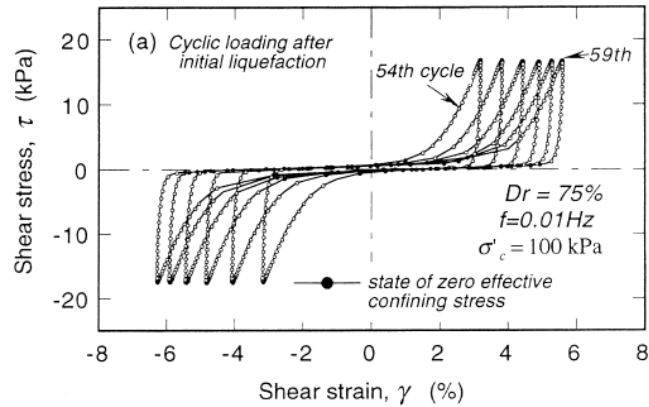
$$\gamma_{\max,N} = \gamma_{N,\text{pos}} - \gamma_{N,\text{neg}} \left\{ \begin{array}{l} \gamma_{N,\text{pos}} = \max(\gamma_{N-1,\text{pos}}, \gamma_{N,\text{pos}}) \\ \gamma_{N,\text{neg}} = \min(\gamma_{N-1,\text{neg}}, \gamma_{N,\text{neg}}) \end{array} \right\} \quad (3.21)$$

$\gamma_{\max,N}$ is the memory parameter updating the excess pore pressure ratio and shear modulus if $(\gamma_{N,\text{pos}} - \gamma_{N,\text{neg}}) > (\gamma_{N-1,\text{pos}} - \gamma_{N-1,\text{neg}})$.

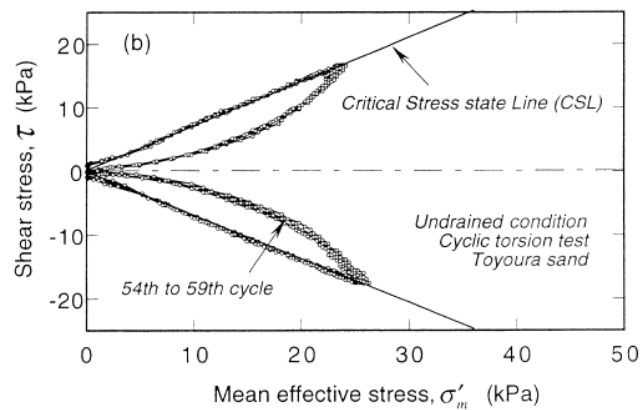
3.2.3. Post-Liquefaction Soil Response

The first occurrence of zero effective stress state was defined as “*liquefaction initiation*” and it separates the pre- and post-liquefaction stages. METUSAND adopted the constitutive relations presented by Shamoto et al. (1998) to define the response in post liquefaction phase. Large deformations occur after initial liquefaction, and, in particular, can develop when the effective confining stress

goes through zero during undrained shearing. Figure 3.9 shows typical post-liquefaction stress–strain hysteresis curves observed in a cyclic undrained torsional shear test.



(a) Shear stress–shear strain relationship;



(b) Effective stress path.

Figure 3.9. Two post-liquefaction shear strain components observed in a typical cyclic undrained torsional shear test (Shamoto et al., 1998)

The post-liquefaction stress–strain relationship shown in Figure 3.9 is described schematically in Figure 3.10, which corresponds to two completely different physical states of soil referred as granular and perfectly plastic materials.

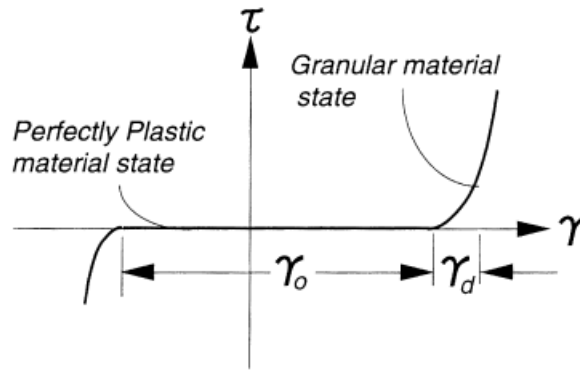


Figure 3.10. Post liquefaction physical states during undrained shear
(Shamoto et. al, 1998)

Two shear strain components exist during post-liquefaction cyclic undrained loading;

- γ_0 is induced at zero effective confining stress state and soil behaves as a perfectly plastic material,
- γ_d occurs during non-zero effective confining stress behaves as a hardening material

These two components constitute post-liquefaction shear strain γ^p as;

$$\gamma^p = \gamma_0 + \gamma_d \quad (3.22)$$

Shamoto et al. (1998) defined this constitutive relationship as; “For saturated sand subjected to post-liquefaction undrained shear, it always behaves as a perfectly plastic material for the time interval that γ_0 occurs and as a granular material for the time that γ_d occurs. The two physical states repeatedly alternate with each other in a process of post-liquefaction cyclic undrained shear. Apparently, saturated sand behaves as a fluid, in the time interval of zero effective confining stress within which γ_0 appears. Under post-liquefaction undrained shear, the existence of the two physical states and their causes of formation are related to the changes in volumetric strain. Two types of volumetric strain components exist due to dilatancy during the application of shear: a reversible dilatancy component $\epsilon_{vd, re}$

and an irreversible dilatancy component $\varepsilon_{vd,ir}$. The former is characterized by its reversibility and dependency on the magnitude and direction of the current shear strain, and the latter by its irreversibility and dependency on past shear history. For a soil element subjected to a general loading application, its volumetric strain may also be induced by the change in mean effective confining stress. Such a volumetric strain component is denoted here as $\varepsilon_{vc,ir}$. For a saturated, completely consolidated sand subjected to the application of shear, no volume change occurs in an undrained condition or, $\varepsilon_v=0$.”

Thus, the total volumetric strain, ε_v , is defined in Equation 3.23 (Shamoto et al., 1998).

$$\varepsilon_v = \varepsilon_{vd} + \varepsilon_{vc} = \varepsilon_{vd,re} + \varepsilon_{vd,ir} + \varepsilon_{vc} = 0 \quad (3.23)$$

The rearrangement of soil particles before and after the initial liquefaction in undrained condition is shown in Figure 3.11.

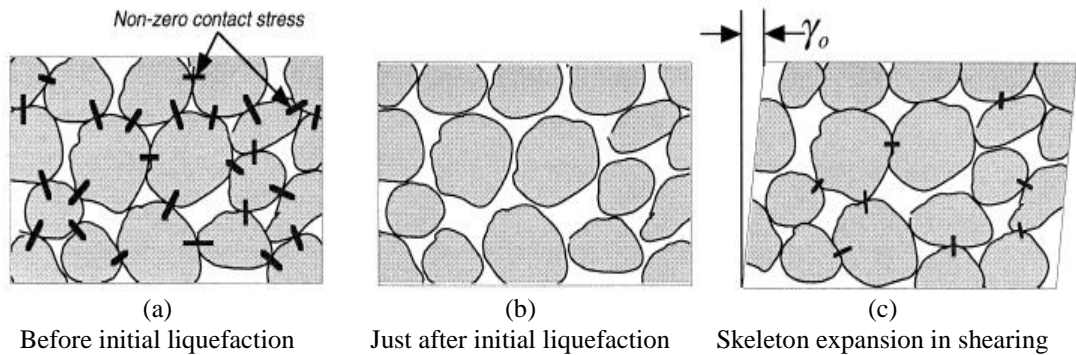


Figure 3.11. Probable arrangement of sand particles during pre- and post-liquefaction undrained shearing (Shamoto et al., 1998)

Before the initial liquefaction shown in Figure 3.11a, any increase in $\varepsilon_{vd,ir}$ can always be absorbed by a decrease in $\varepsilon_{vd,re}$ and $\varepsilon_{vc,0}$, thereby satisfying Equation 3.26.

“At the initial liquefaction state, following condition is satisfied $\varepsilon_{vc} = \varepsilon_{vc,0}$. A further shear application following the initial liquefaction leads to $\varepsilon_{vd,ir} > -\varepsilon_{vc,0}$ as shown in Figure 3.11b. At this instant, there will not be any change in effective stress dependent shear strain component (γ_d). Similarly, no change occurs in $\varepsilon_{vc,0}$ either since effective stress remains constant. In this situation, an increase in $\varepsilon_{vd,ir}$ is balanced by a reduction in $\varepsilon_{vd,re}$ induced by shear strains occurred during the state of zero effective confining stress. It is the shear strain component (γ_0) independent of effective stress, referred as perfectly plastic material state, which defined in Equation 3.27” (Shamoto et al., 1998).

$$\gamma_0 = \frac{R'_0}{M_{CS,0}} \frac{e_0 - e_{\min}^*}{1 + e_0} (\gamma_{\max,N} - \gamma_{\text{entry}})^m \quad (3.24)$$

“During this time interval, $\varepsilon_{vd,ir}$ continues to increase, and the γ_0 value accordingly needs to increase, thereby causing a sufficient decrease in $\varepsilon_{vd,re}$ as shown in Figure 3.11(c). In this interval, sand behaves as a perfectly plastic material with a nearly zero shear resistance. The corresponding stress– strain response to such shear at zero effective confining stress has been illustrated in Figure 3.10. With the further development of shear strain γ , the rate of decrease rate of $\varepsilon_{vd,re}$ can exceed that of the increase in $\varepsilon_{vd,ir}$, and eventually an increase in ε_{vc} is required to retain the condition $-(\varepsilon_{vd,re} + \varepsilon_{vc}) = \varepsilon_{vd,ir}$, thereby causing an increase in effective confining stress. The shear strain ($\gamma - \gamma_0$) induced at the non-zero effective confining stress state is (γ_d) defined by Equation 3.28. At this time, sand behaves as a granular material” (Shamoto et al., 1998).

$$\gamma_d = \frac{\alpha K}{M_{CS} - M_0} \left(\frac{p'_i}{P_a} \right)^A \left(\frac{q}{M_{CS} p'_i} \right)^B \quad (3.25)$$

where R'_0 , m , A and B are material constants .

The component γ_0 depends on maximum double amplitude shear strain history $\gamma_{\max,N}$, the minimum shear strain triggering initial liquefaction, γ_{entry} , the critical deviator–isotropic stress ratio, M_{CS} , initial and reference minimum void ratios of the corresponding sand. γ_{entry} , is the transition parameter between effective stress based nonlinear (incrementally linear) phase to post liquefaction phase. γ_{entry} , is the double amplitude maximum shear strain occurred at the initiation of liquefaction. ($\gamma_{\text{entry}} = (\gamma_{\max,N})_{\text{at initial liquefaction}}$).

Conversely the component γ_d is dependent on the state of current effective stress as defined by the stress state parameters p' and q as follows;

$$p' = \frac{1}{3}(\sigma'_1 + \sigma'_2 + \sigma'_3) \quad (3.26)$$

$$q = \frac{1}{\sqrt{2}}\sqrt{(\sigma'_1 - \sigma'_2)^2 + (\sigma'_2 - \sigma'_3)^2 + (\sigma'_3 - \sigma'_1)^2} \quad (3.27)$$

Volumetric strain components corresponding to these phase are defined in Shamoto et al. (1998) as follows;

$$\varepsilon_v = \varepsilon_{\text{vd, re}} + \varepsilon_{\text{vd, ir}} + \varepsilon_{\text{vc}} = 0 \quad (3.28)$$

$$\varepsilon_{\text{vd, ir}} = \frac{\Delta e}{1+e_0} = \frac{e_0 - e_{\min}^*}{1+e_0} R'_0 (\gamma_{\max,N})^m \quad (3.29)$$

$$\varepsilon_{\text{vd, re}} = -M_{\text{CS.o}} \int_0^{\gamma_0} d\gamma_0 - \frac{M_{\text{CS}} - M_0}{\alpha} \int_0^{\gamma_d} d\gamma_d = -M_{\text{CS.o}} \gamma_0 - \frac{M_{\text{CS}} - M_0}{\alpha} \gamma_d \quad (3.30)$$

$$\varepsilon_{\text{vc}} = K \left(\frac{p'_i}{p_a} \right)^A \left(\frac{p'}{p'_i} \right)^B \quad (3.31)$$

According to Shamoto et al., (1998) approach; “When drained conditions are allowed to occur in the sand after a post-liquefaction undrained loading, the

excess pore pressure Δu tends to dissipate, thereby leading to an increase in ε_v . If the values of γ_0 and γ_d remaining at $\Delta u = 0$ are respectively denoted as γ_{0r} and γ_{dr} , then the residual shear strain after post-liquefaction drained consolidation γ_r^p , is equal to their sum.”

$$\gamma_r^p = \gamma_{0r} + \gamma_{dr} \quad (3.32)$$

“The residual post-liquefaction shear and volumetric strains are dependent on each other and their magnitudes depend strongly on irreversible dilatancy. The residual post-liquefaction ground settlement and lateral spreading are therefore independent of each other. Both the residual post-liquefaction volumetric and shear strains, ε_{vr} and γ_r^p , reaches its maximum value at $\gamma_r^p = 0$ or $\varepsilon_{vr} = 0$ for a given value of $\varepsilon_{vd,ir}$ and thus $\gamma_{max,N}$, ε_{vr} and γ_r^p can be calculated as given in Equation 3.33 and 3.34” (Shamoto et al., 1998)

$$\varepsilon_{vr(@\gamma_r^p=0)} = \varepsilon_{vd,ir} = \frac{e_0 - e_{min}^*}{1 + e_0} R'_0 (Y_{max,N})^m \quad (3.33)$$

$$\gamma_r^p (@\varepsilon_{vr}=0) = \frac{\varepsilon_{vd,ir}}{M_{CS,o}} = \frac{e_0 - e_{min}^*}{1 + e_0} \frac{R'_0}{M_{CS,o}} (Y_{max,N})^m \quad (3.34)$$

Detailed model parameters with their description are given in Table 3.3. There are eleven constant coefficients determined by shear tests. Some of these values (A, B, K, e_{max} , e_{min} , e_{min}^*) are given specifically for Tayoura sand.

As a result, post liquefaction deformations are difficult to estimate yet this model gives reasonable estimations of large deformations in a range of $\frac{1}{2}$ to 2.0 of the actual deformation. As stated by Shamoto et al. (1996, 1997 and 1998), the proposed framework was validated by using field case histories after 1995 Hyogoken-Nanbu earthquake.

Table 3.3. Shamoto et al. (1998) post liquefaction constitutive relation parameters

Description	Symbol	Value
initial effective confining stress	p'_i	
barametric pressure	p_a	100 kPa
Coefficients for Toyoura Sand when $\frac{p'_i}{p_a} = 1$	A	1
	B	0.44
	K	0
Constant related to dilatancy	α	$\alpha = \frac{3\sqrt{3}}{2}$ (Toyoura Sand)
The slope of critical state line CSL based on the Mohr Coulomb's Failure Creation	M_{cs}	$M_{cs} = \left(\frac{q}{p'}\right)_{max}$
The deviator– isotropic stress ratio at zero dilatancy is constant, about 31° for clean quartz sands	M_o	$\tan(31^\circ)$
Constants independent of type of sand	R_0'	2
	m	0.76
Depends on critical stress ratio, M_{cs}	$M_{cs.o}$	$M_{cs.o} = a \cdot M_{cs}$
	a	0.142
Minimum shear strain triggering initial liquefaction	γ_{entry}	
Void Ratio $e_0 = e_{max} - D_R(e_{max} - e_{min})$ $e_{min}^* = e_{max} - 1.3 \times (e_{max} - e_{min})$	e_0	
	e_{max}	0.973 (Toyoura Sand)
	e_{min}	0.635 (Toyoura Sand)
	e_{min}^*	0.533 (Toyoura Sand)

3.3. Numerical Implementation

The METUSAND model includes an improved numerical implementation and coding as a user defined material in a dynamic link library (DLL) for use with the commercial program FLAC (Itasca 2011). The simulations presented in this study were prepared using the DLL module *modelMetusand003.dll* and would be available for the users. Note that a DLL must be compiled using Microsoft Visual Studio 2005 (or later) for operation in *FLAC*.

FLAC is an explicit finite difference program, which uses time steps equal to or smaller than the minimum time required for waves to travel between any pair of nodes. This approach ensures that physical information does not propagate faster than numerical information. FLAC computes a default time step based on the properties of the model (e.g., element size, material stiffness, permeability, and damping). Users may specify a time step that is smaller than the default value. The implementation of a complex constitutive model in FLAC requires special attention to the way stresses and strains are handled under FLAC's mixed discretization scheme. During each time step, FLAC calls the constitutive model *once per triangular subzone* (four times per zone). The isotropic components of the stress outputs from the four subzones are then averaged internally by FLAC according to the Mixed Discretization scheme (Constitutive Model Manual, FLAC, 2011).

Class specification for METUSAND model is developed from Mohr-Coulomb elastic/plastic model contained in files “Model example” in FLAC software. Detailed information for the implementation of the code could be obtained from the instruction “*Writing new constitutive model*” available in FLAC software manual.

Member functions for initialization (**initialize()**) and execution (**run()**) is controlled by *ini-static* input parameter, which should be assigned as 0 for initial

phase to develop initial stress condition and convert to 1 to execute for dynamic analyses.

In the FLAC software, dynamic analyses are carried out in the time domain with full coupling between groundwater flow and mechanical loading. The FLAC DLL code for METUSAND is given in Appendix 3A.

3.4. Single Element Behavior of METUSAND

The first step of assessing the model performance is the determination of single element response predicted by METUSAND constitutive model. A series of numerical analyses were performed by FLAC-METUSAND to simulate an idealized Simple Shear (DSS) laboratory test. Unit size FLAC model element is shown in Figure 3.12. The two bottom nodes of the element are fixed both in x and y direction, whereas the top nodes are constrained in the vertical direction, so that horizontal movements of the top two nodes are identical. Stress controlled loading is imposed by applying a horizontal velocity to the top nodes in positive and negative direction to simulate cyclic loading condition. A generic simple shear test input for METUSAND is given in Appendix B.

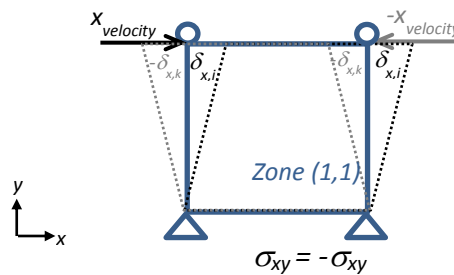


Figure 3.12. Simple Shear Test (DSS) Simulation Model in FLAC

The advantage of this model is that an assumption either on the basis of excess pore pressure generation or shear strain is not necessary to define initial liquefaction. Instead, liquefaction is assumed to be triggered when the effective stress state touches the updated Mohr-Coulomb failure envelope. Depending on initial shear stiffness of the model, excess pore pressure ratio r_u and the maximum shear strain γ_s vary in the ranges of 0.7 to 1.0 and 1.0 % to 4.0 %, respectively, at the time of initial liquefaction. r_u , defined as the ratio of increase in pore pressure to initial effective stress, where r_u equals 0 if pore pressure does not accumulate (i.e.: drained loading), and r_u equals 1, when effective stresses become zero.

The response of the model is illustrated by presenting simulation results for a set of input parameters, which is summarized in Table 3.4. Undrained cyclic responses of fully saturated sands with relative densities of 29%, 39 %, 57%, 66% and 74% (corresponding to SPT- N_{160} values of approximately 4, 7, 15, 20 and 25) are assessed. Maximum shear modulus is selected according to Cetin and Bilge (2014) methodology. For the purpose of defining effective-stress based failure envelope, friction angle values are selected as recommended by Peck et al. (1974) relation. Simulations were performed for isotropic ($K_0=1.0$) and $K_0=0.5$ consolidation conditions. Mean effective stresses are chosen as 100 and 65 kPa. Shear stresses corresponding to CSR ratios varying in the range of 0.19 to 0.39 were applied to the specimens.

Cyclic stress ratio (CSR) is defined as the ratio of the shear stress applied to initial effective vertical stress (τ/σ_{v0}'). Liquefaction-induced failure is observed to be a sudden phenomenon which occurs unexpectedly when CSR (τ/σ_{v0}') values exceed certain the threshold limits (i.e.: CRR) as reported in Table 3.4. CRR and number of cycle, N, to liquefaction depends mostly on the initial shear modulus of the soil samples.

Table 3.4. Input parameters for the illustrative elemental responses

No	$D_R(\%)$	$(N_1)_{60}$	σ_{m0}'	K_0	G_{max} (Cetin-Bilge 2014) (GPa)	Friction Angle, ϕ°	CSR
1	29	4	100	1.0	61.5	28	0.195
2	39	7	100	1.0	72.8	29	0.245
3	57	15	100	1.0	94.2	32	0.320
4	66	20	100	1.0	104.6	34	0.355
5	74	25	100	1.0	113.8	36	0.390
6	29	4	65	0.5	49.6	28	0.165
7	39	7	65	0.5	58.6	29	0.190
8	57	15	65	0.5	76.0	32	0.25
9	66	20	65	0.5	84.3	34	0.28
10	74	25	65	0.5	91.8	36	0.305

METUSAND simulation for a loose sand with relative density of 39%, which is isotropically consolidated ($K_0=1.0$) under vertical effective stress (σ_{v0}') of 100 kPa (Simulation No.2 of Table 3.4) is presented in Figure 3.13 until the initiation of liquefaction in the form of 4-way plots. The upper left plot presents effective mean stress reduction with increasing number of shear stresses during cyclic loading. The upper right plot shows the stress-strain relationship and stiffness degradation of the specimen. Hysteretic damping values can be estimated from this graph. The lower right plot presents the accumulation of shear strain with loading cycles. On the other hand, the lower left plot shows how excess water pressure ratio changes with loading cycles pore.

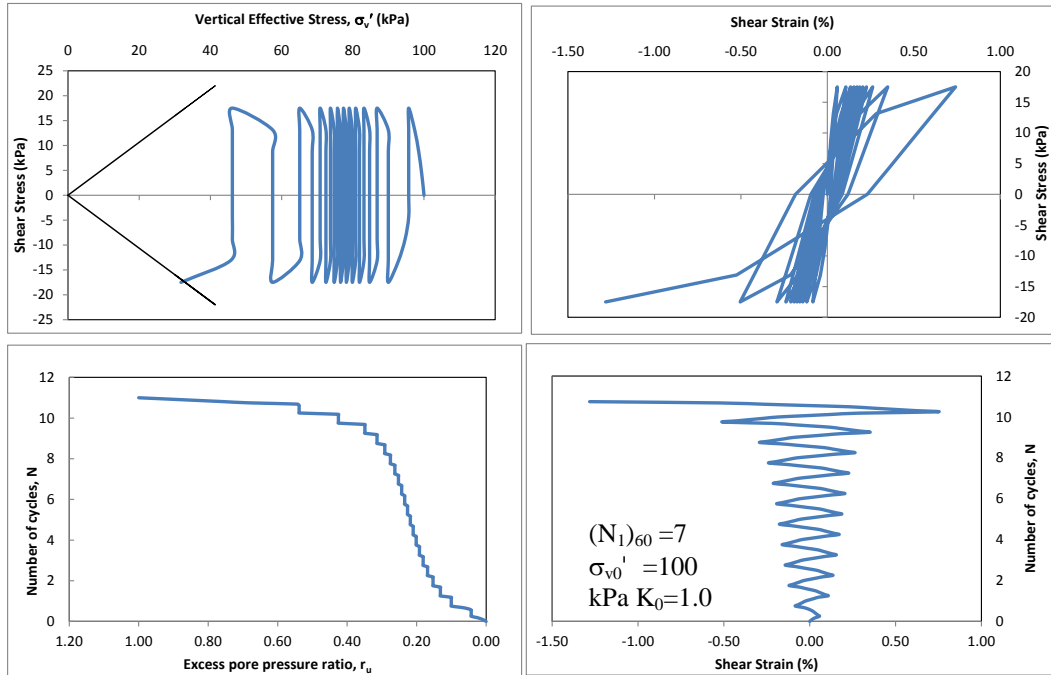


Figure 3.13. Simulation of METUSAND *pre-liquefaction* behavior ($(N_1)_{60} = 7$, $\sigma_{v0}' = 100$ kPa, $K_0 = 1.0$)

Further application of shear stresses following the initial liquefaction leads to post liquefaction phase. At zero effective stress crossings a dramatic increase in shear strain (γ_0) is observed. Cyclic liquefaction type soils responses can also be observed when “banana loops” are formed in the upper right plot. At the time of dilation-contraction cycles, a stiffer response accompanied with shear strain (γ_d) is expected. The post liquefaction phase simulation of the model is presented in Figure 3.14.

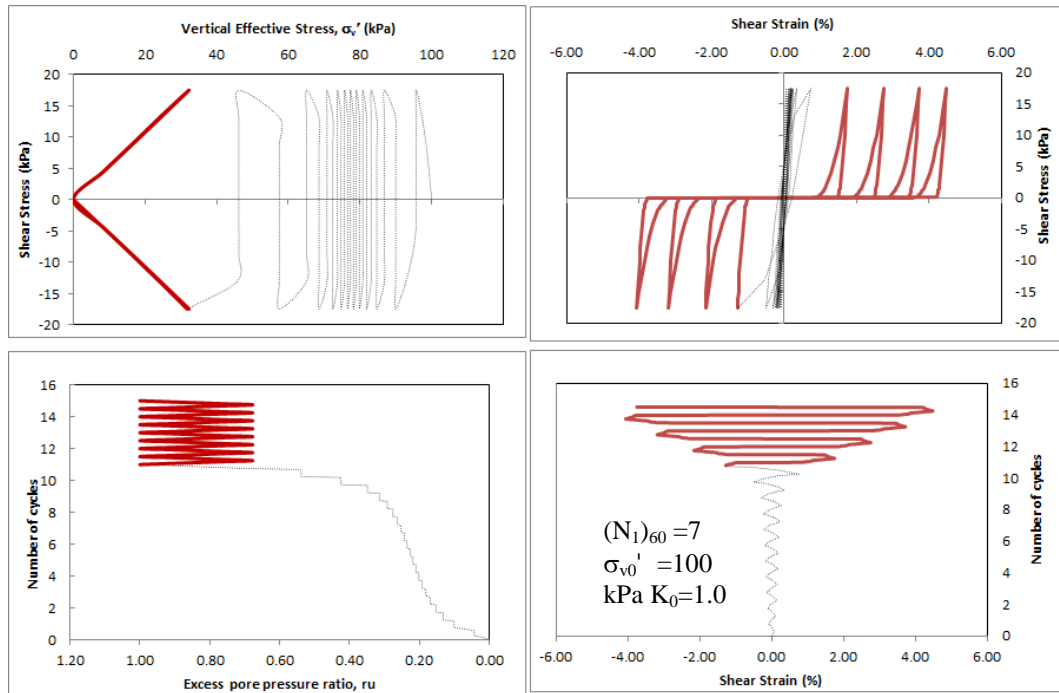


Figure 3.14. Simulation of METUSAND *post-liquefaction* behavior
 $((N_1)_{60} = 7, \sigma'_{v0} = 100 \text{ kPa}, K_0 = 1.0)$

3.4.1. Comparison with Cyclic DSS Tests

METUSAND model predictions in the elemental sense are compared with a series of stress-controlled cyclic triaxial and simple shear tests performed on laboratory reconstituted sand specimens. Details of the cyclic triaxial and simple shear test results used for comparison and calibration purposes can be found in Cetin et al. (2009), Cetin and Bilge (2012) and Shamoto et al. (1998).

Figure 3.15 and 3.16 compares the results of METUSAND simulations with the experimental data corresponding to specimens K_0 -consolidated ($K_0 = 0.5$) under a vertical effective stress of 100 kPa with D_R values of 39 and 66 %. As revealed by these figures, METUSAND produces reasonably good matches with the experimental data.

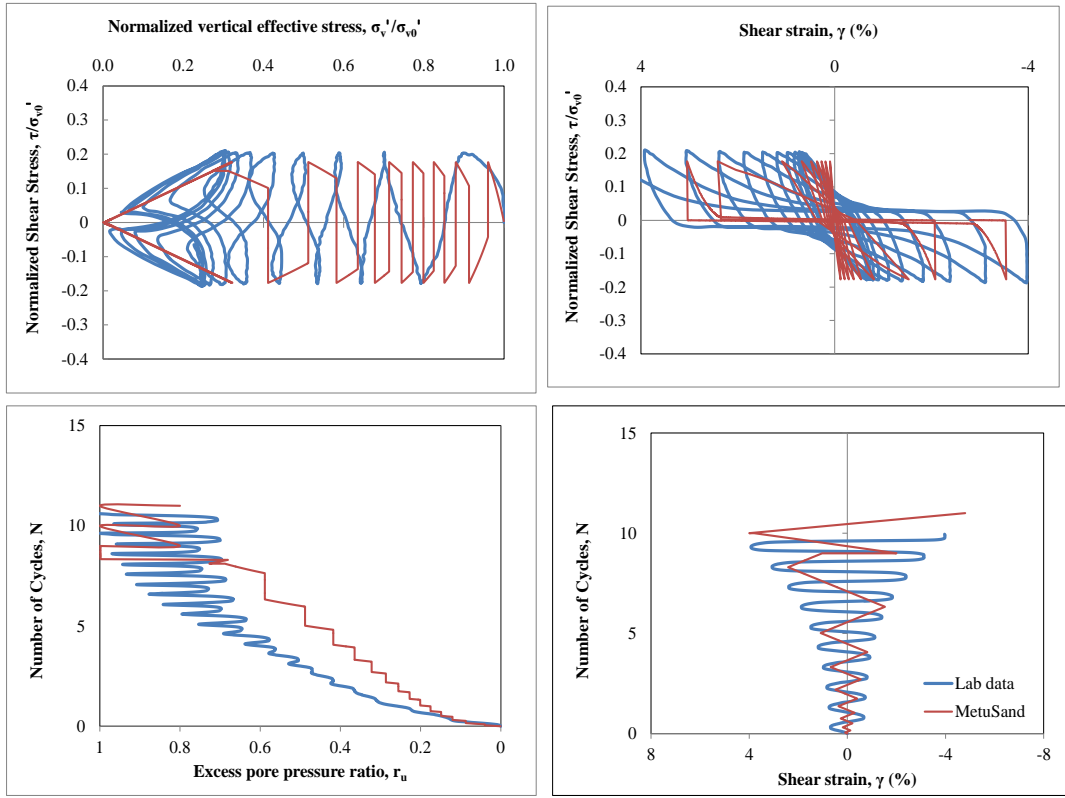


Figure 3.15. Laboratory DSS and METUSAND response on undrained cyclic loading condition

($D_R = 39\%$, $\alpha = 0.0$, $\sigma_{v0}' = 100 \text{ kPa}$, $K_0 = 0.5$, $CSR = 0.177$ (Monterey sand) Cetin and Bilge 2009).

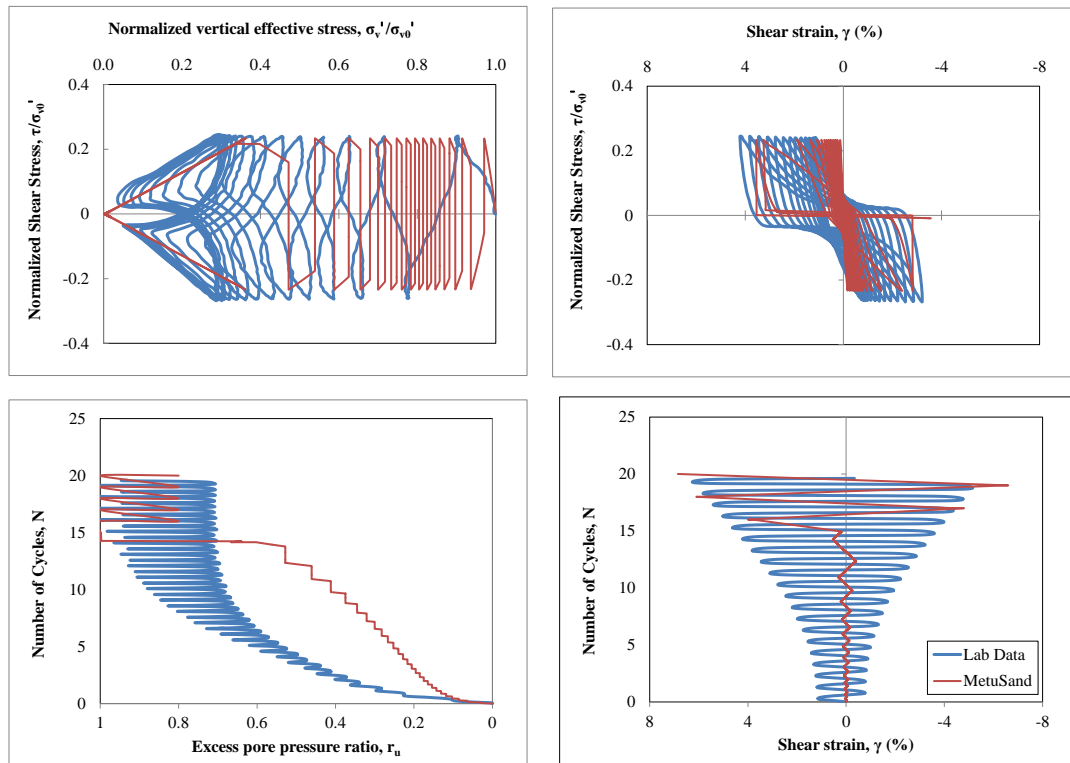


Figure 3.16. Laboratory DSS and METUSAND response on undrained cyclic loading condition

($D_R = 60\%$, $\alpha = 0.0$, $\sigma_{v0}' = 100$, $K_0 = 0.5$, $CSR=0.234$ (Nevada sand) Cetin and Bilge 2009)

3.4.2. Comparisons with Semi-Empirical Liquefaction Triggering Relationships

Site specific laboratory-based assessment of liquefaction triggering is often not possible due to sample disturbance problems. It is common practice, therefore, to rely on empirical “Seed type” (Seed et. al. 1984, NCEER 1997; Cetin et al. 2004, Idriss and Boulanger, 2006) empirical liquefaction triggering charts given as a function of penetration test data METUSAND predictions are compared with the prediction of the semi-empirical liquefaction chart solutions.

A correction factor is adopted to convert CSR_{field} value to equivalent $CSR_{SS,20,1D,1atm}$, as presented in Equation 3.36;

$$CSR_{SS,20,1D,1atm} = \frac{CSR_{\text{field}}}{K_{\sigma}K_{M_w}K_{md}} \quad (3.35)$$

K_{σ} correction is applied for confining stress other than the reference state of 100 kPa. The duration magnitude correction K_{M_w} factor, as proposed by Cetin et al. (2004), is given in Equation 3.39.

$$K_{M_w} = \frac{87.1}{M_w^{2.217}} \quad (3.36)$$

K_{md} correction is used to convert multi-directionally applied CSR_{field} value to the value of a unidirectional applied laboratory CSR. Wu et. al.(2003), correction factor for multidirectional shaking effects K_{md} is given as a function of relative density, as shown as follows:

$$K_{md} = 0.361 \ln(D_R) - 0.579 \quad (3.38)$$

A single undrained soil element is simulated in FLAC with METUSAND, for which the procedure is given as follows:

- i) An undrained single element model is set up in FLAC and initialized with the representative vertical and horizontal effective confining pressures, small strain shear modulus, G_{max} and $(N_1)_{60\text{-CS}}$.
- ii) A series of simulations is carried out to obtain a cyclic shear stress (τ_{xy}) compatible with a cyclic resistance ratio (CRR) in 20 number of cycle that initiates liquefaction.
- iii) CRR values to trigger liquefaction corresponding to $(N_1)_{60\text{-CS}}$ are reported and compared with semi-empirical charts of NCEER 1997 workshop and Cetin et. al. (2004) for $M_w=7.5$ and $\sigma_{v0}' = 100$ kPa for fines content, $FC < 5\%$ (SPT clean sand curves).

Figure 3.17 compares METUSAND element data to empirical triggering charts of NCEER (1997) and Idriss and Boulanger (2006) and Cetin et al. (2004). In order to make a reasonable comparison, CRR values obtained by FLAC simulations are corrected for multidirectional shaking effects, as given in Equation 3.16. The liquefaction initiation curves generated by METUSAND are in reasonable agreement with the curve developed by NCEER (1997) and Cetin et al. (2004) relationship.

The key parameter of METUSAND model is the small strain shear modulus G_{max} . In the literature, there exist a number of approaches to obtain G_{max} values, which gives a range of values within a factor of almost 2. In order to emphasize the effect of G_{max} value to the results, FLAC simulations were repeated for G_{max} values selected from Japan Road Association Design Specifications of Highway Bridges Part V: Seismic Design (JRA, 2002), Seed et. al (1970), Andrus and Stoke 1997, Juang 2002 approaches (Figure 3.18). CRR corresponding to $(N_1)_{60-CS}$ are given in Figure 3.19. Note that depending on the G_{max} value adopted, a perfect or a poor match is quite possible.

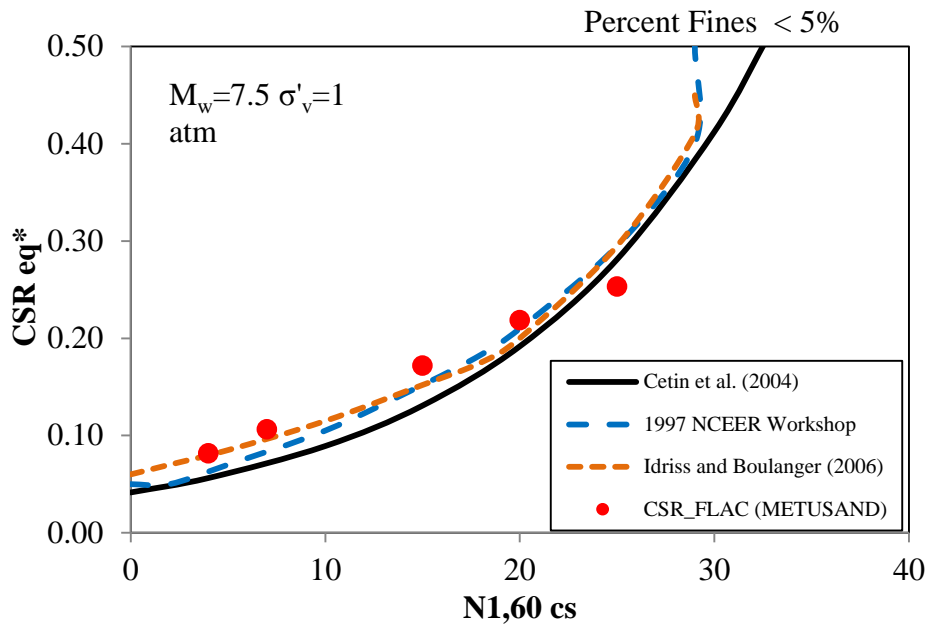


Figure 3.17. Values of CRR predicted by METUSAND and compared to probabilistic semi-empirical relationships

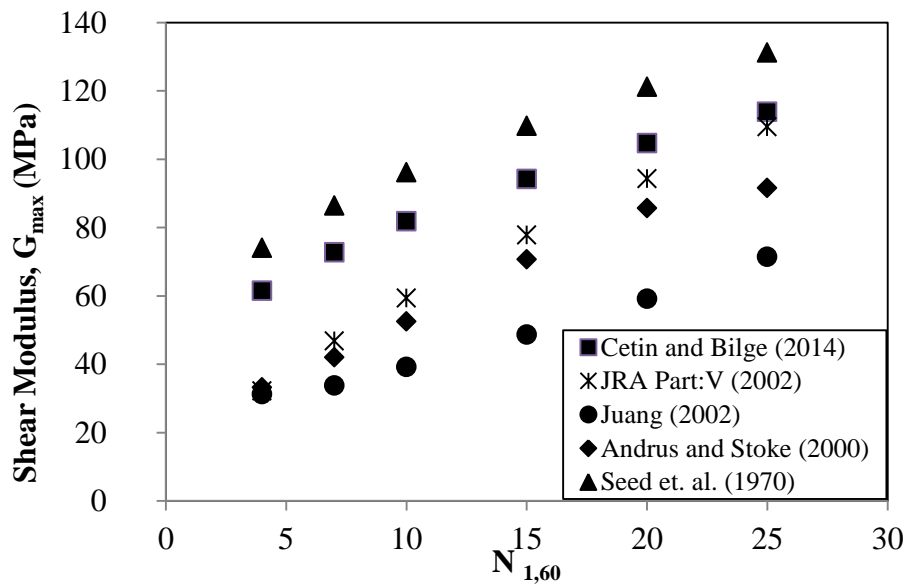


Figure 3.18. Initial shear modulus, G_{max} obtained from different methods

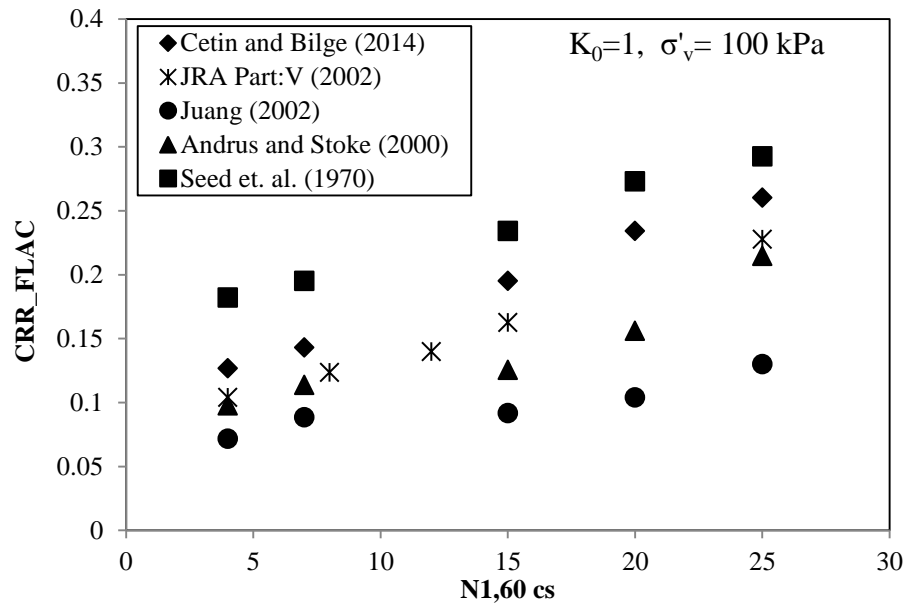


Figure 3.19 Values of CRR predicted by METUSAND by using G_{max} obtained from different methods

3.5. METUSAND Model Limitations and Challenges

METUSAND is a simplified constitutive relationship developed for modeling saturated cyclic response of cohesionless soils. The framework is capable of modeling i) stress dependent initial modulus, ii) elastic response at shear strain ranges smaller than the threshold level of $10^{-4}\%$. iii) excess pore water generation as function of induced shear strains, iv) strain compatible modulus degradation and corollary hysteretic damping and v) post liquefaction shear flow at zero effective stress crossings as well as dilation and contraction cycles.

However, following responses cannot be reliably modeled by METUSAND;

- i) Plastic strains which are controlled by the flow rule
- ii) Strain hardening response based on hyperbolic relation between stress ratio and plastic shear strain

- iii) Shear induced plastic expansion or dilation and plastic volumetric strains related to plastic deviatoric strains through the dilatancy, D
- iv) Stress-ratio controlled, critical state compatible, bounding surface plasticity based model response

The limitations of the model are as follows;

- v) Some constants of Shamoto et al.(1998) post liquefaction constitutive relation were adopted for Tayouro sand
- vi) METUSAND model is very sensitive to the small strain shear modulus G_{\max} and a perfect or a poor match is quite possible depending on the G_{\max} value adopted. In the literature, there exist a number of approaches to obtain G_{\max} values, which gives a range of values within a factor of almost 2.

CHAPTER 4

VERIFICATION OF METUSAND MODEL

4.1. Introduction

Damage due to seismic loading is often directly correlated to local site conditions. This correlation was evident during recent earthquakes in the form of intensity amplification and/or liquefaction induced ground deformations (e.g., Mexico City, Seed et al. 1987; San Francisco, Seed et al. 1990; Kobe, Mizuno and Hirade, 1995; Bardet et al. 1995, Comartin et. al. 1995, Sitar 1995). The associated mechanisms of ground response are being increasingly documented through a growing worldwide network of sites instrumented with downhole seismic arrays, especially in the United States, Mexico, Japan, and Taiwan.

Constitutive relation presented in this study is based on semi-empirical cyclic straining and excess pore water pressure assessment models of Shamato et al. (1998), Cetin et al. (2009), Cetin and Bilge (2012). The model prediction is developed on the basis of series of stress-controlled cyclic triaxial and simple shear tests, which were performed on laboratory reconstituted sand specimens. Detailed model prediction responses are given in the Shamato et al. (1998), Cetin et al. (2009), Cetin and Bilge (2014). Hence, for only illustration purposes, 1D comparison between the numerical model and cyclic laboratory data in DSS was presented in Chapter 3. Due to the fact that element-wise validation of the models was done by Shamato, 1998, Cetin et al. (2009), Cetin and Bilge (2012), it is not going to be repeated. However, the constitutive model, METUSAND, which was founded on these semi-empirical models, will be calibrated with well documented

field case histories. For this purpose, first well documented field case history Wildlife Liquefaction Site, Imperial Valley, California, shaken by 1987 Superstition Hills earthquake will be used. Secondly, dynamic site response of Port Island Array, Kobe site shaken by 1995 Hyogo-ken Nanbu Earthquake, is numerically investigated by using METUSAND constitutive model. Site response of these sites in the form of variation of ground motion intensity characteristics, excess pore pressure, and shear straining with depth will be presented and compared.

4.2. Verification of the METUSAND Model Response with Wildlife Site Case History

4.2.1. Site Description, Instrumentation and Seismic Records

Wildlife site is located on the west side of the Alamo River in Imperial County in Southern California. The site was instrumented in 1982 by the United States Geological Survey to monitor ground and pore-pressure responses during earthquakes. These data could then be used to analyze the relations between ground motion, pore-water-pressure buildup and stiffness and strength loss at the site (Bennett et al. 1984). Many significant and insightful investigations of the Wildlife recordings have been conducted such as Hushmand et al., 1992; Gu et al., 1994; Zeghal and Elgamal, 1994; Glaser, 1996; Bonilla et al., 2005; Youd and Carter, 2005.

The location map of Wildlife Array is shown in Figure 4.1. The magnitude of 6.6, 6.2, and 5.9 earthquakes shown in the figure are the Superstition Hills, Elmore Ranch, and Westmorland earthquakes.

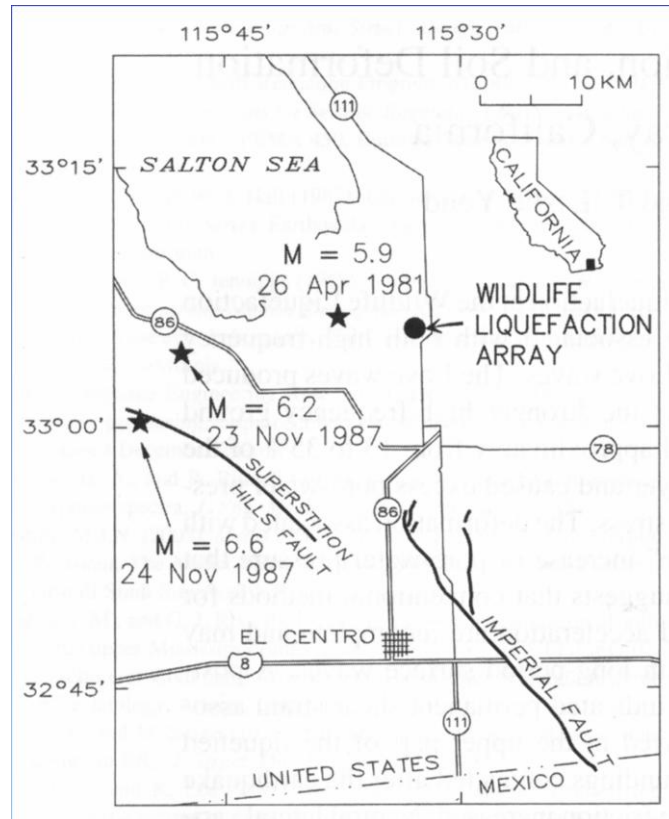


Figure 4.1. Location Map of Wildlife Array (Holzer & Youd, 2007)

Site was instrumented with two accelerometers, SM1 at -7.5 m depth below ground surface, and SM 2 at ground surface; and with six piezometers (P1 to P6) at depths ranging between -2.9 m and -12.0 m.

In-situ and laboratory investigations (Bennett et al., 1984) showed that a layer of approximately 2.5-m-thick layer of lean clay to silt (CL-ML) overlies the 4.3 m of liquefiable silty sand layer. The upper 1 m of the liquefiable layer is actually sandy silt (ML) with an average fines content of 78%. The lower 3.3 m is silty sand (SM) with an average fines content of 36%. Liquefiable layer lies above a 5 m thick layer of stiff clay. Of the six piezometers, five were placed in the silty sand layer. The ground water table was located at a depth of approximately 1.2 m. The downhole accelerometer (SM1) was positioned near the upper surface of the stiff clay. Schematic cross section is presented in

Figure 4.2.

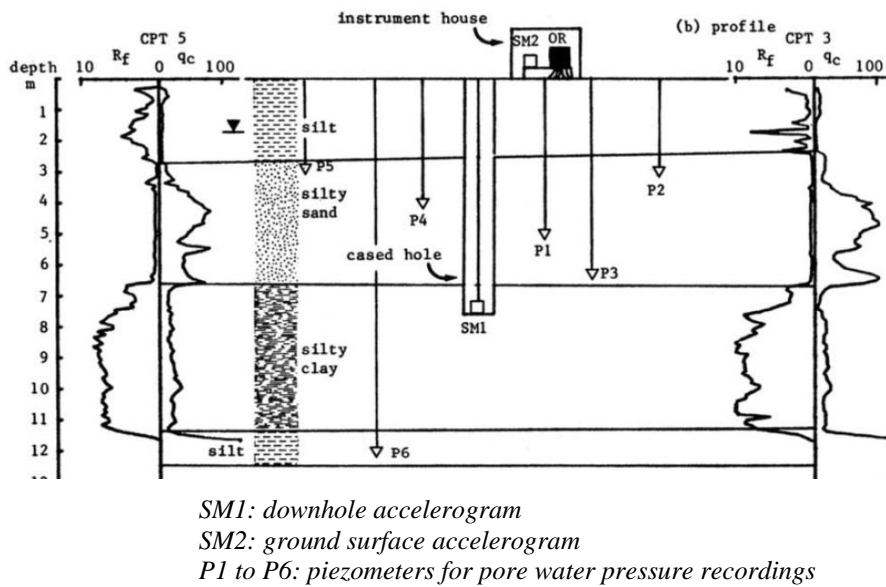


Figure 4.2. Schematic cross section through Wildlife Liquefaction Array
(Bennett et al., 1984)

The key element of instrumentation and surface effects on the area were mapped by Holzer et al. (1989a) after the earthquake, as shown in Figure 4.3. In the figure, it is indicated that most of the sand boils were occurred above and around the instrumentation and was concentrated along a couple of major cracks. Secondary cracks, further away from the instrumented site, were developed parallel to Alamo River. Lateral movements and spreading above the instruments occurred predominantly in the north-east direction, perpendicular to major ground cracking (Youd and Bartlett, 1988).

In November 1987, two earthquakes occurred near Wildlife site within a period of 12 hours. The first was the 6.2 magnitude Elmore Ranch earthquake, which was named after foreshock event located approximately 23 km west from Wildlife site. The peak measured acceleration at the ground surface was measured as 0.13g. None of the field piezometers indicated significant pore pressure increase during the Elmore Ranch event.

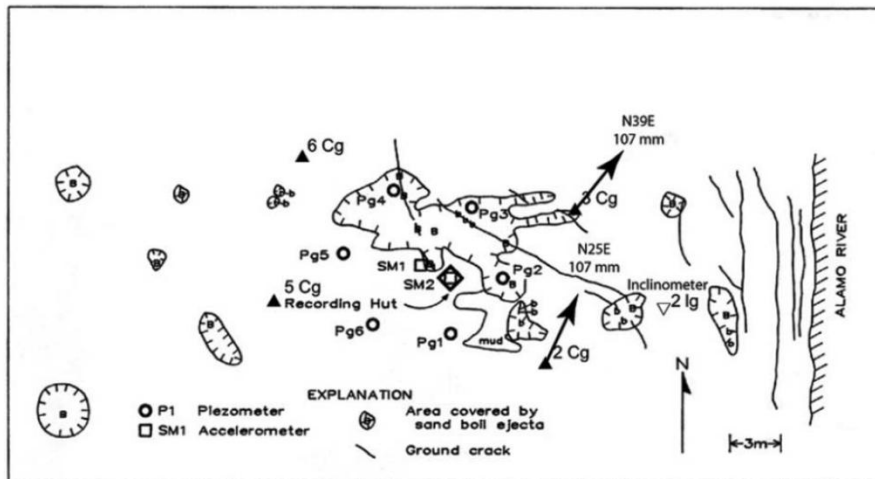


Figure 4.3. Map of liquefaction effects caused by Superstition Hills earthquake, instrumentation, and CPT soundings (modified from Holzer et al., 1989a). Piezometers are labeled as Pg and CPT soundings as Cg. Displacements of control points are from Youd and Bartlett (1989). No displacements were measured at 5Cg and 6Cg.

The main shock was the magnitude 6.6 Superstition Hills earthquake (05:15 Pacific Standard Time (PST), November 24, 1987), located approximately 31 km to the west and south from Wildlife. At the ground surface the peak measured acceleration was 0.21g.

Figure 4.4 and Figure 4.5 show the measured accelerations from Superstition Hills event at Wildlife in north-south and east-west direction. Complete records from the array were published by Holzer et al. (1989b). Pore pressure and acceleration records at Wildlife Site were obtained from Holzer and Youd (2007). The peak horizontal acceleration at the ground surface was 0.21 g in the North- South record at roughly 13.6s after triggering. The peak acceleration at the -7.5 m depth was 0.17g, also in the North- South record at roughly the same time.

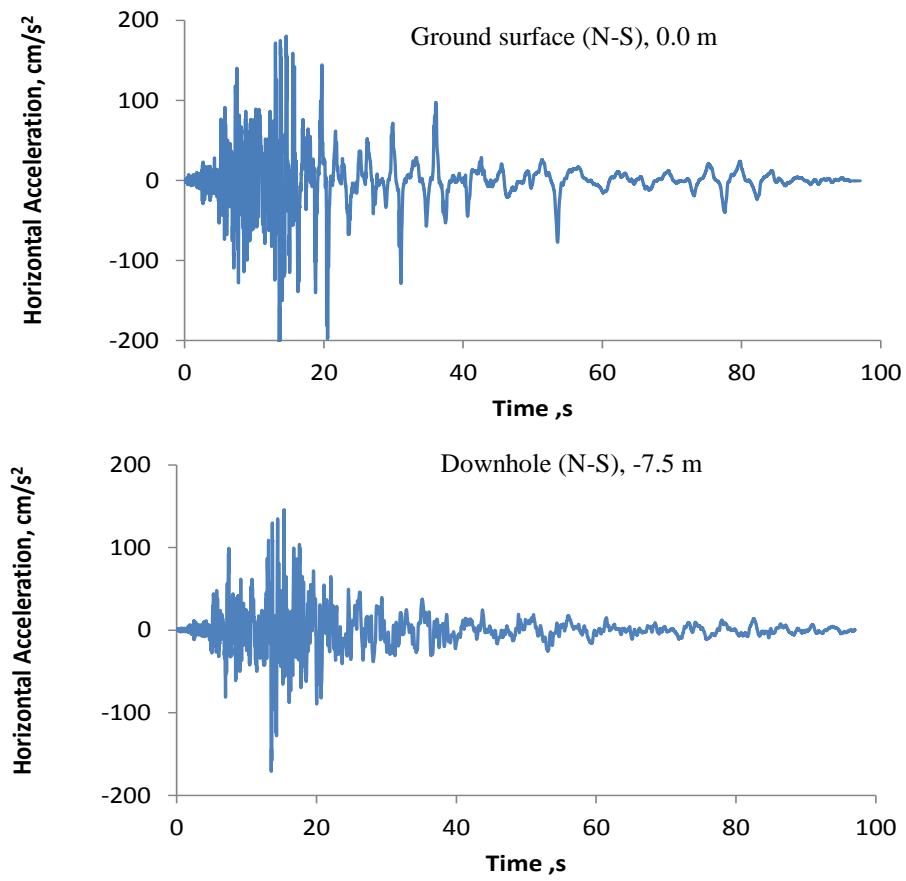


Figure 4.4. Measured accelerations from Superstition Hills earthquake: North-South data (Holzer and Youd, 2007)

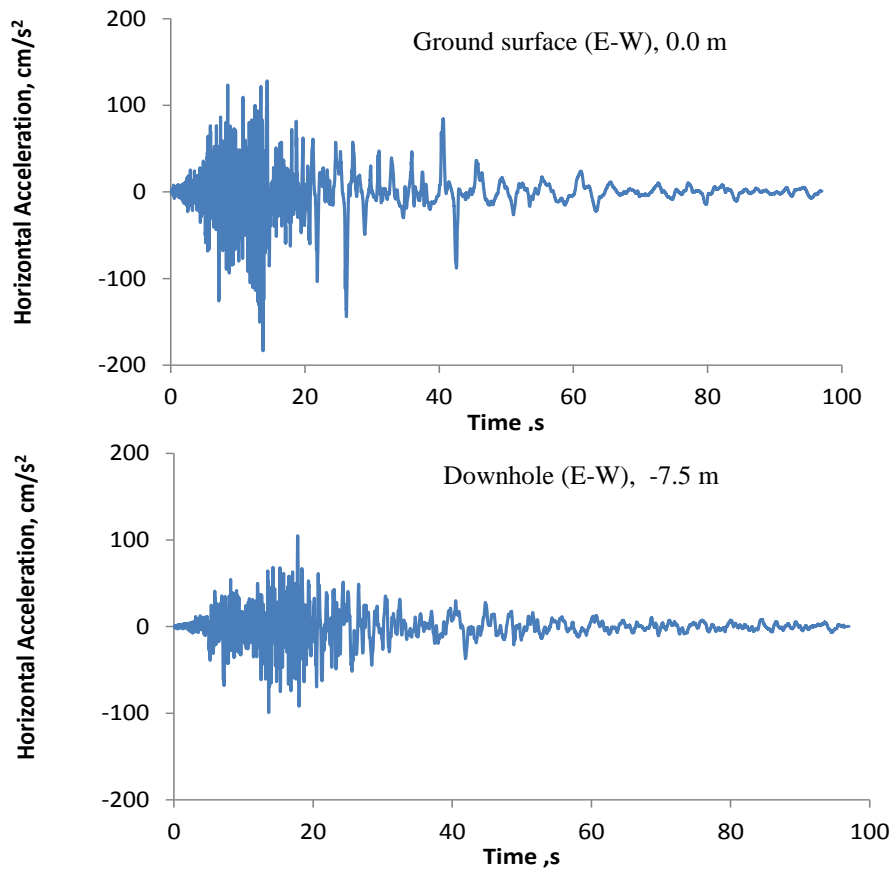


Figure 4.5. Measured accelerations from Superstition Hills earthquake: East-West data (Holzer and Youd, 2007)

During this event, site response was monitored by a surface and a down-hole accelerometers, as well as pore-water pressure transducers. Field investigations after the earthquake provided evidence of liquefaction and minor permanent lateral ground displacement (Holzer et al., 1989b).

Figure 4.6 shows the absolute excess pore-water pressures recorded by P1, P2, P3 and P5. Piezometer P4 in the silty sand did not function properly and Piezometer P6 was located in deeper soil below the liquefying layer. According to Holzer and Youd (2007), a delay in the buildup of pore-water pressure in all the functioning piezometers was observed in the liquefied layer. The buildup began simultaneously at 13.6 sec at each of the piezometers. Figure 4.6 shows the

absolute excess pore-water pressure values recorded by all of the piezometers. Note that these recordings were not corrected for drift. Excess pore-water pressure at each piezometer ultimately reaches the approximate static effective overburden stress at 97 sec, which is shown on each recording in Figure 4.6. Excess pore-water pressure ratio was computed by dividing observed excess pore-water pressure by the value measured at 97 second, which is given in Figure 4.7.

The 1987 surface and downhole acceleration, and pore water pressure records were used to estimate of Wildlife site average seismic shear stress-strain and effective stress-path histories. These histories provided valuable insight into the site seismic behavior during liquefaction and associated loss of soil stiffness.

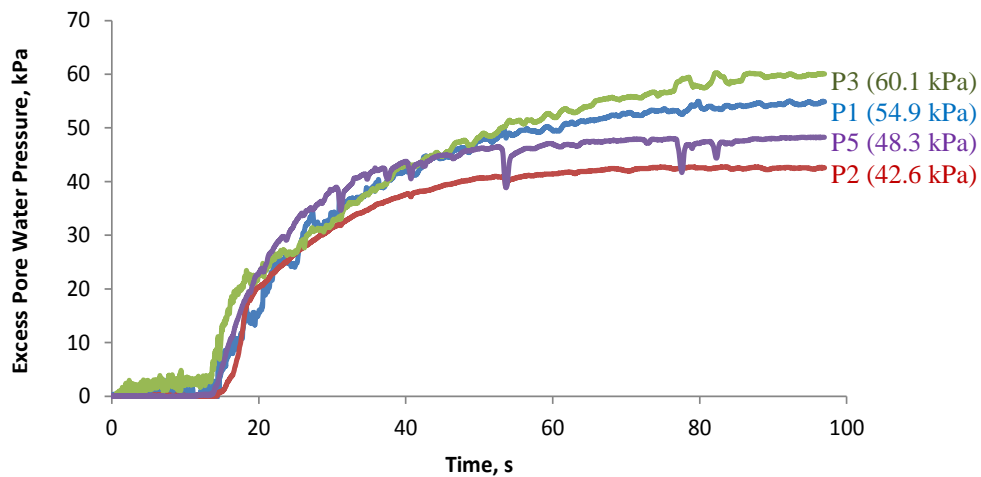


Figure 4.6. Pore water pressure time histories recorded during the 1987 Superstition Hills Earthquake (Holzer and Youd, 2007)

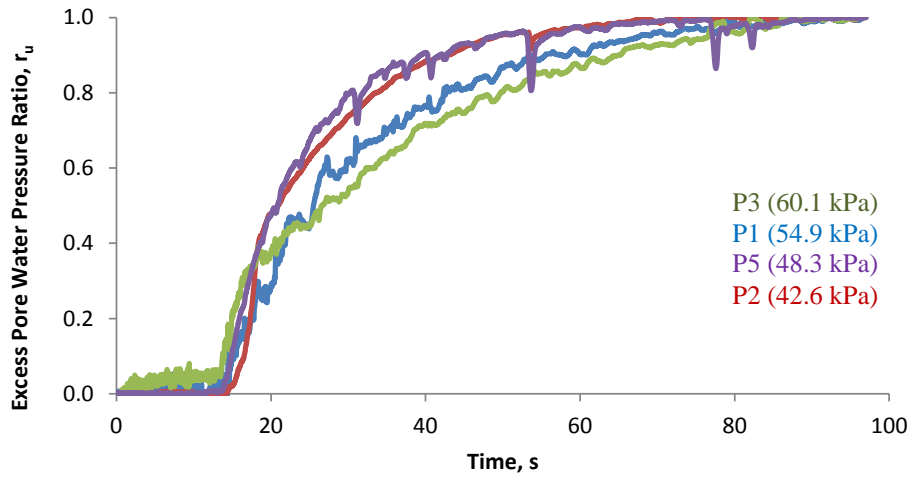


Figure 4.7. Excess pore pressure ratio, r_u at each piezometer (Holzer and Youd, 2007)

Zeghal and Elgamal (1994) were the first to demonstrate that the buildup of pore-water pressure at Wildlife Site at low levels of shaking was accompanied by strain softening. They calculated time histories of transient shear stress and average seismic strain from the recordings of the horizontal accelerometers. Horizontal shear stress at depth z was estimated by Equation 4.1. Average seismic shear strain, γ , from the surface to a depth of 7.5 m was estimated with Equation 4.2.

$$\tau = \frac{1}{2} \rho z (a_s + a_z) \quad (4.1)$$

$$\gamma = \frac{d_{DH} - d_s}{7.5} \quad (4.2)$$

$$a_z = a_s + (a_{DH} - a_s) \left(\frac{z}{7.5} \right) \quad (4.3)$$

where;

ρ = soil density, assumed to be 2000 kg/m^3

a_s = horizontal acceleration recorded at the surface

a_z = horizontal acceleration at depth z evaluated by linear interpolation using Equation 4.3

a_{DH} = horizontal acceleration recorded by the downhole accelerometer at 7.5m

Shear stress- shear strain history of North-South components of Superstition Hills 1987 Earthquake is shown in Figure 4.8. As the pore pressure increases due to seismic excitation, site stiffness is observed to gradually decrease.

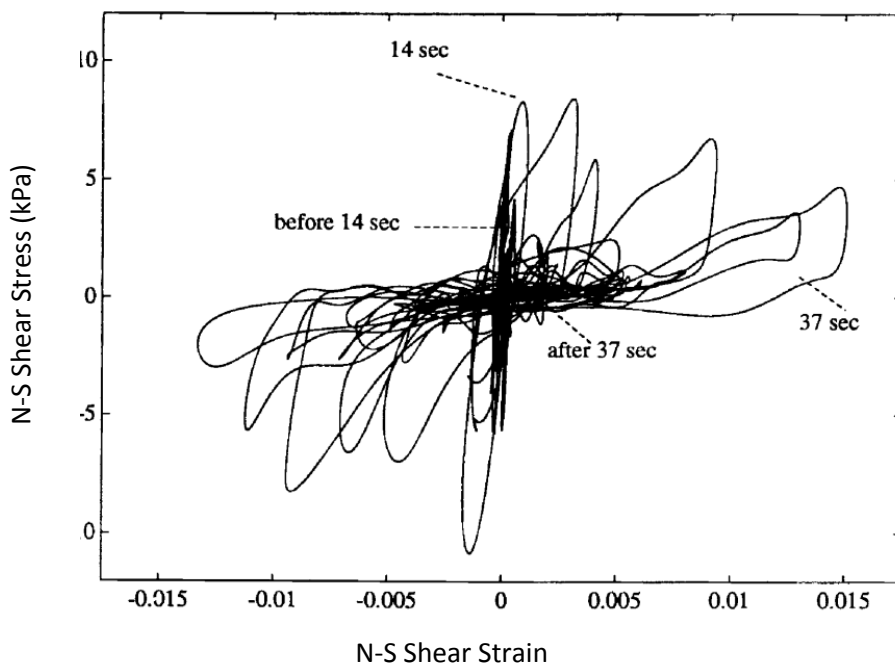


Figure 4.8. North-South shear stress-strain history at the Wildlife Site during liquefaction (Zeghal and Elgamal 1994)

4.2.2. Idealized Soil Profile used in Finite Element Analyses

Subsurface conditions and geotechnical properties of sediment at the Wildlife array site are described by Bennett et al. (1984) and are summarized in Table 4.1. The table is based on samples from borings drilled immediately next to the instrumented area.

An idealized soil profile with shear wave velocities increasing with depth as 99,116, 141,168 m/s were generated for effective stress based 2-D finite element/difference analyses (Figure 4.9). Initial (maximum) shear modulus is estimated as defined by Cetin and Bilge (2014). Generic input parameters necessary for finite element analyses are summarized in Table 4.2.

Table 4.1. Geotechnical properties of Wildlife array instrumented site
(Holzer and Youd, 2007)

Depth (m)	q_c (MPa)	R_f (%)	D_{50} (mm)	Fines <75 μ m (%)	Clay <5 μ m (%)	V_s (m/sec)	wc (%)	Atterberg Limits (%)		USGS Soil Type
								LL	PL	
0-2.5	0.6 \pm 0.36	3.41 \pm 4.72	0.025	93 \pm 8	25 \pm 16	99	32 \pm 4.8	30 \pm 4.6	22 \pm 2.7	CL-ML
2.5- 3.5	1.87 \pm 1.00	0.87 \pm 0.75	0.055	78 \pm 6	8 \pm 3	116	-	-	-	ML
3.5- 6.8	5.68 \pm 2.26	1.01 \pm 0.67	0.091	36 \pm 12	5 \pm 3	-	-	-	-	SM
6.8- 12	2.04 \pm 1.30	7.14 \pm 5.29	0.005	98 \pm 2	60 \pm 19	168	28 \pm 2.2	59 \pm 13.4	30 \pm 7	CH
12- 17.5	9.38 \pm 1.69	2.38 \pm 0.45	0.027	94 \pm 6	18 \pm 10	-	28 \pm 3.3	35 \pm 10.8	24 \pm 2.1	CL, ML,SM

**Note: q_c is tip resistance; R_f is friction ratio; D_{50} is median grain-size diameter; V_s is shear-wave velocity; wc is water content; LL is liquid limit; PL is plastic limit; and USCS is Unified Soil Classification System.*

Table 4.2. Geotechnical properties of idealized soil properties of Wildlife site

	Material Model	Depth (m)	Spt-N	D_R (%)	V_s (m/s)	PI (%)	ρ (kg/m^3)	G_{max} (kPa)	ϕ ($^\circ$)	c (kPa)
Silt	Mohr-Coulomb	2.5	2	21	99	10	1.8	41375	0	15
Silty Sand 1	MetuSand	3.5	4	29	116	-	1.9	49616	30	0
Silty Sand 2	MetuSand	7	6	36	141	-	1.9	55937	30	0
Silty Clay	Mohr-Coulomb	12	11	49	168	30	2.0	68131	0	35

*Note: D_R : relative density, V_s : shear wave velocity, PI: plasticity Index, ρ : density, G_{max} : initial (small strain) shear modulus, ϕ : friction angle, c : cohesion

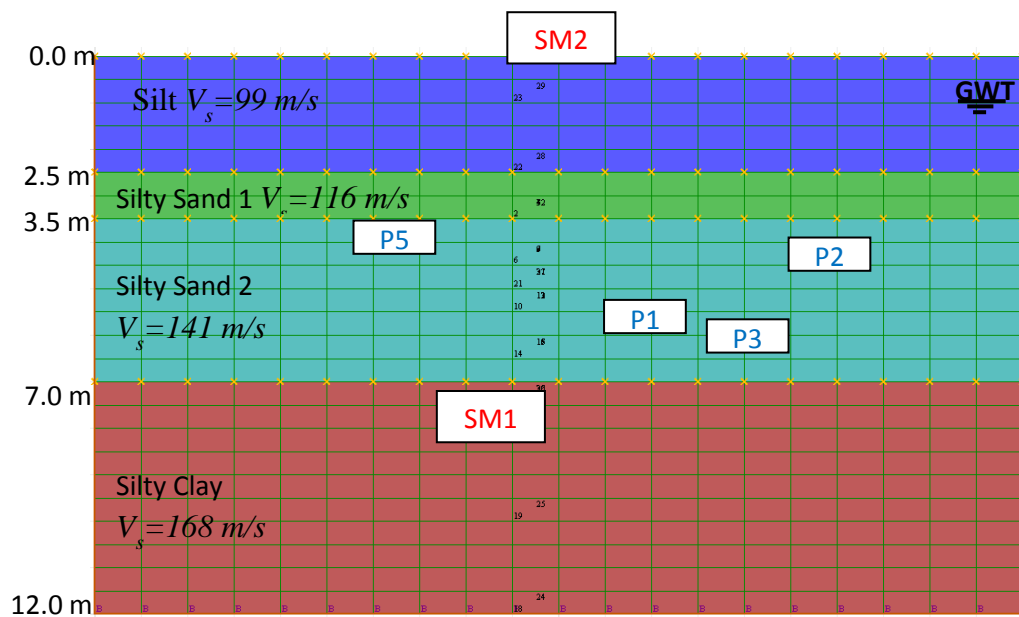


Figure 4.9. Finite element/difference mesh and idealized soil profile

4.2.3. Numerical Static Analyses

“FLAC-2D Version 7.0 Finite Difference Software” is used in the analyses of the idealized profile of the Wildlife site array. At the first stage, static analyses were

performed with elastic-perfectly plastic constitutive model with Mohr –Coulomb failure criterion.

The material properties used in the static analysis, including stiffness, density, and strength, were based primarily on field and laboratory test data as summarized in Table 4.2. Finite element mesh with initial boundary conditions is presented in Figure 4.10 and distribution of initial i) effective vertical stress, ii) horizontal effective stress and iii) pore water pressure is shown in Figures 4.11 - 4.13.

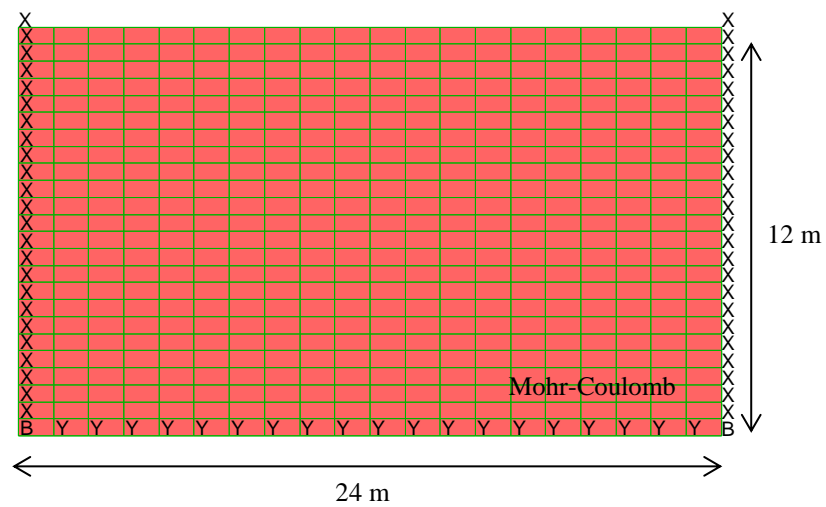


Figure 4.10. Finite element mesh and initial boundary condition

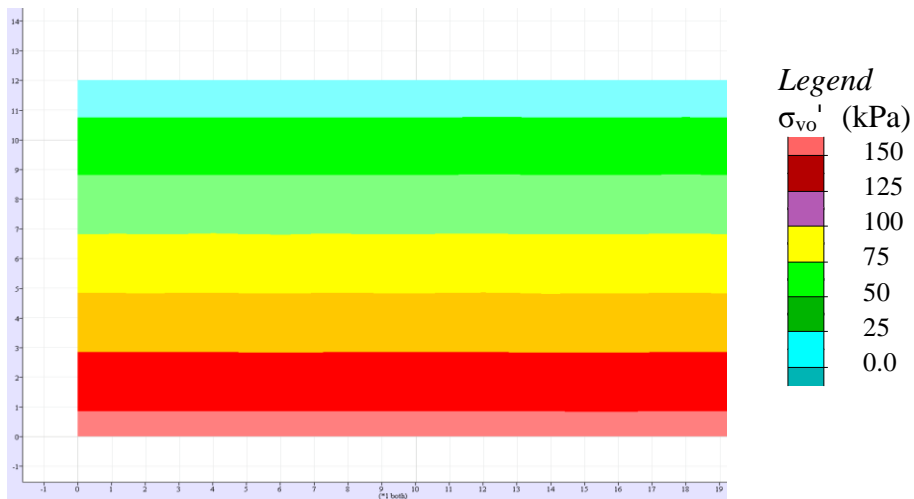


Figure 4.11. Initial vertical effective stress distribution of Wildlife site

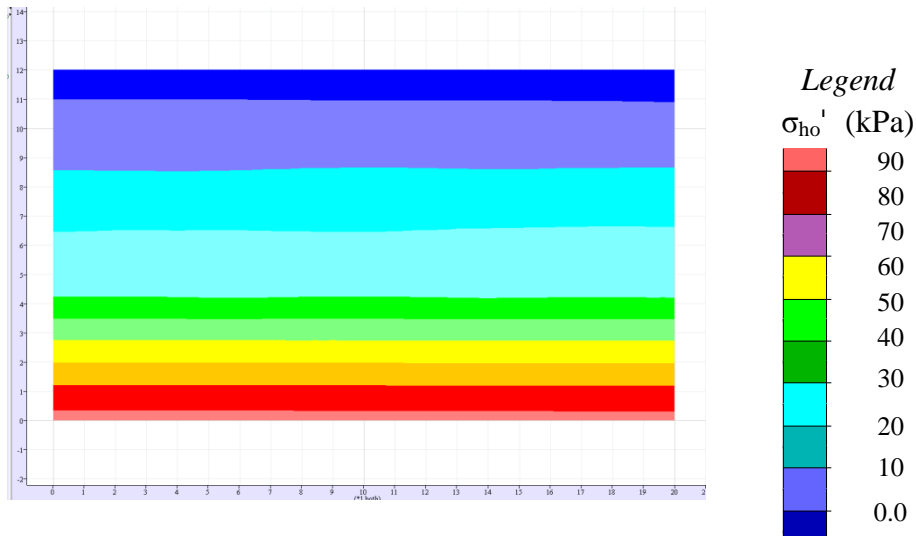


Figure 4.12. Initial horizontal effective stress distribution of Wildlife site (kPa)

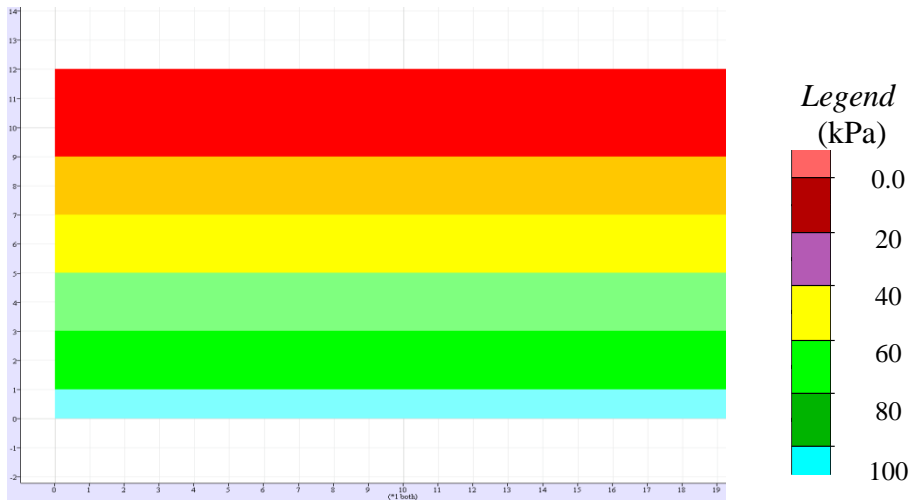


Figure 4.13. Initial pore water pressure distribution of Wildlife site (kPa)

4.2.4. Effective Stress-based Dynamic Response Analyses

The seismic analysis, including liquefaction response and deformations, was performed in FLAC by using METUSAND liquefaction model for silty sand layer and, elastic-perfectly plastic constitutive model with Mohr-Coulomb failure criterion for top silt and bottom silty clay layers.

Upper 1m of liquefiable silty sand layer is modeled as a layer with relative density of 29 %, and lower 3.5 m sand is assumed to have a relative density of 36%. According to METUSAND model, excess pore pressure starts to build up after shear strains exceeding the threshold shear strain of 10^{-4} % METUSAND model is shown to accurately model both modulus reduction and hysteretic damping responses, consistent with available degradation curves. So that, no additional Rayleigh or viscous damping is needed.

The input motion selected for this analysis is the most critical component of 1987 Superstition Hills earthquake with peak ground acceleration of 202 cm/sec^2 in North-South direction (Figure 4.4). The corresponding downhole (SM1) MHA was 171 cm/sec^2 . The outcrop input seismic motion was converted to “within” motion that was estimated by site response analyses (i.e.: SHAKE-91 analysis), and then applied to a compliant boundary at the base. Static boundary conditions were converted to FLAC free-field boundary for dynamic analyses (Figure 4.14).

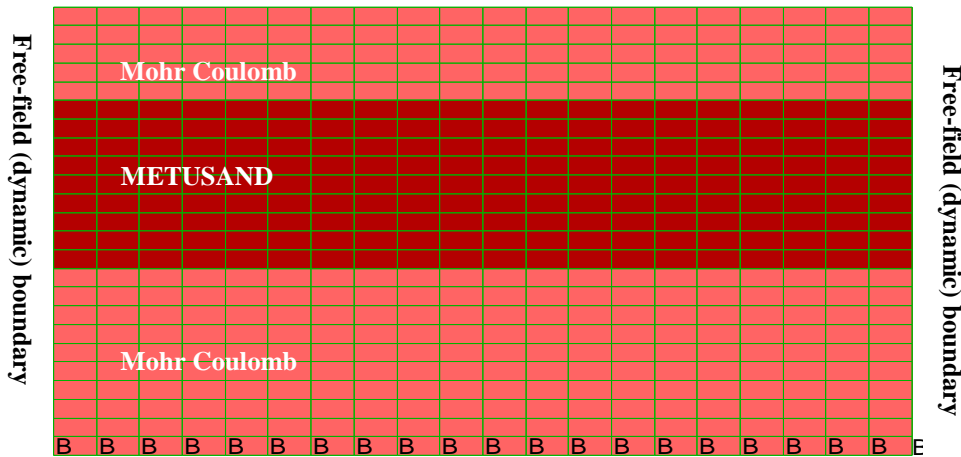


Figure 4.14. Material models and dynamic boundary condition

4.2.5. Computed Dynamic Response and Comparison with Field Data

Figure 4.15 shows a comparison between the computed and recorded acceleration time histories at the ground surface and at 7.5 m depth, which corresponds to the location of instrumented accelerometers, SM2 and SM1 respectively. Similarity between the computed and recorded acceleration time histories both at early and late stages of shaking is remarkable. This close match confirms hysteretic degradation and damping nature of the METUSAND model.

Distribution of the maximum excess pore pressures ratio, r_u contours at dynamic time $d_t=7.5$ sec, 20 sec, and 40 sec are given in Figure 4.17 to Figure 4.19 respectively.

Figure 4.20 shows that excess pore pressure increases during seismic loading at locations of piezometer P1, P2, P3 and P5. This pore pressure response was associated with maximum shear strains of 3 - 4 % as shown in Figure 4.21 at time of the initiation of liquefaction. This value is comparable with the Zeghal and Elgamal (1994)'s empirically estimated shear strain values changing with shear stresses, as presented in Figure 4.8.

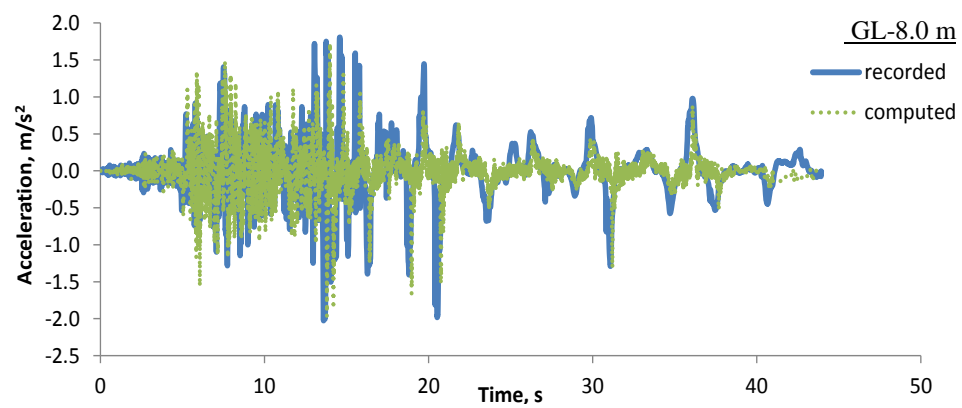
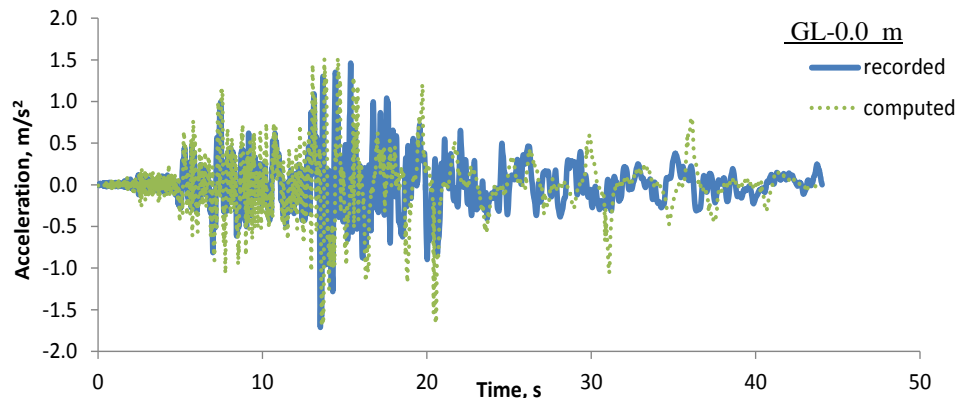


Figure 4.15. Computed and recorded acceleration time histories for ground surface and at 8 m depth

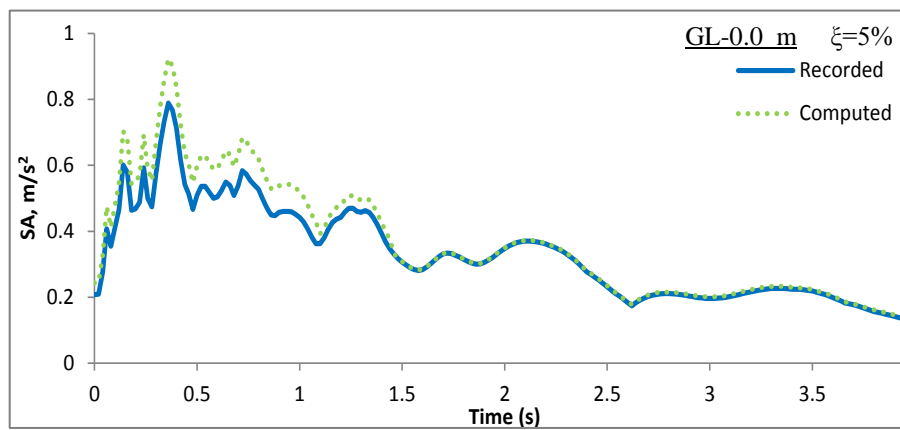


Figure 4.16. Computed and recorded response spectra for %5 damping at ground level

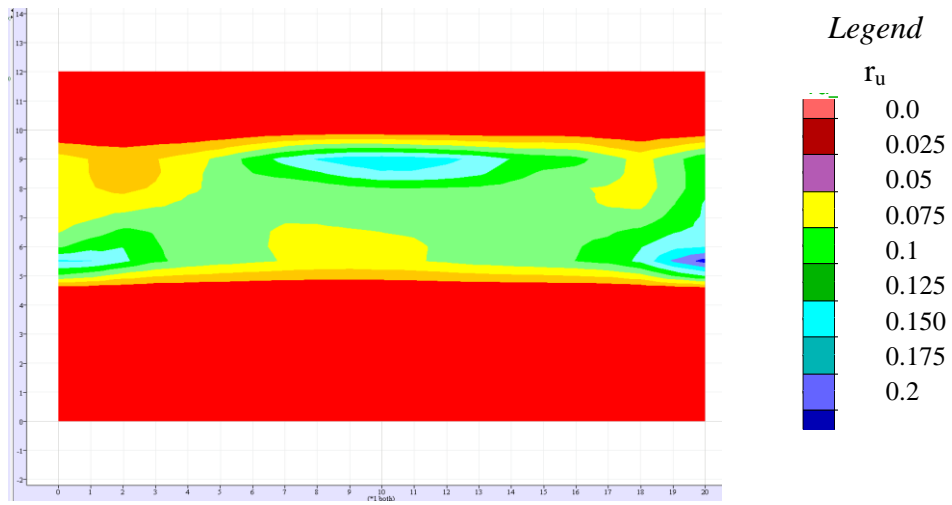


Figure 4.17. Excess pore pressure distribution, r_u , at $t=7.5$ sec

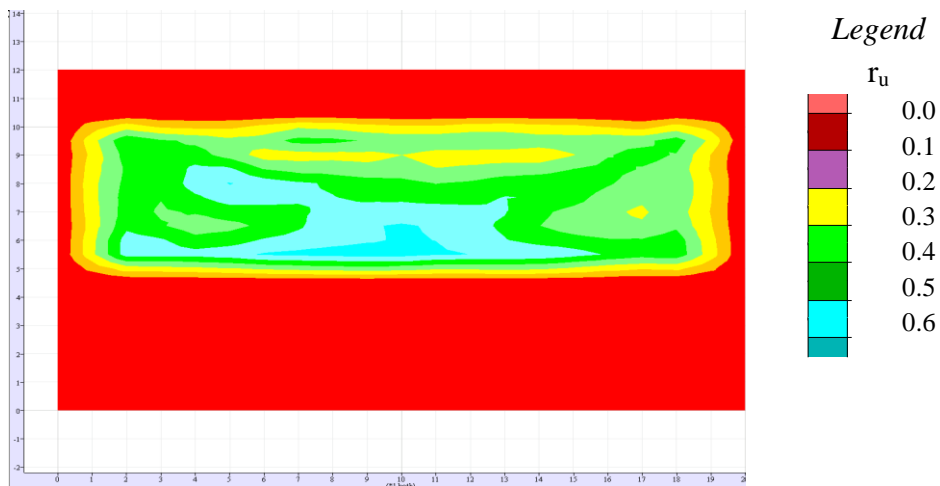


Figure 4.18. Excess pore pressure distribution, r_u , at $t=20$ sec

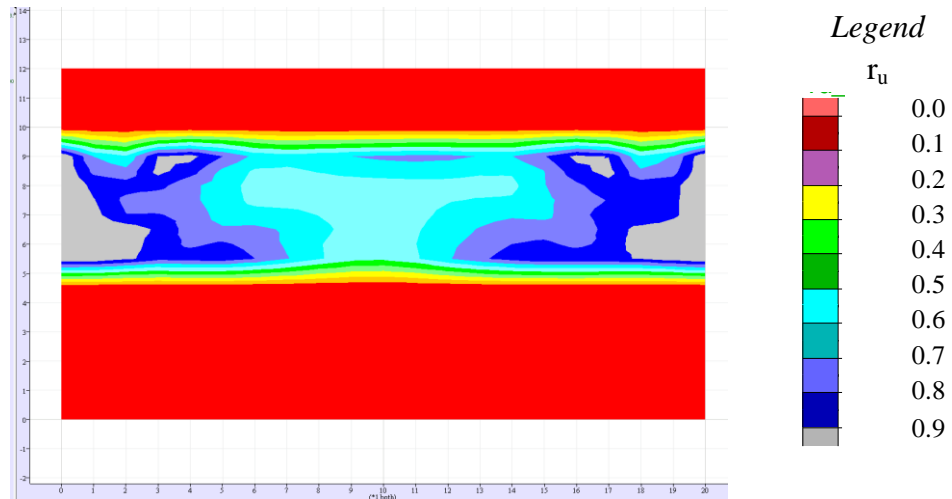


Figure 4.19. Excess pore pressure distribution, r_u , at $t=40$ sec

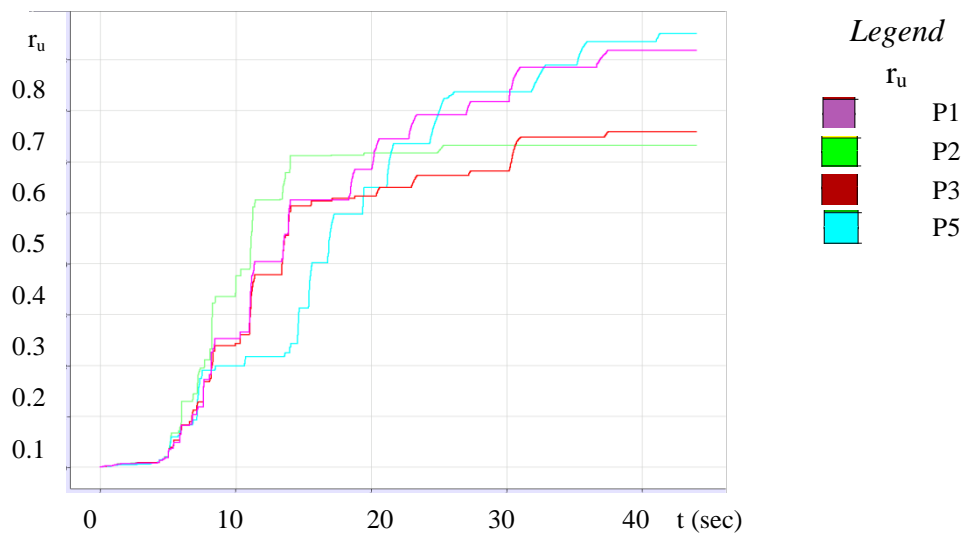


Figure 4.20. Excess pore pressure ratio vs dynamic time at location of field piezometers P1, P2, P3 and P5 at $t=40$ sec

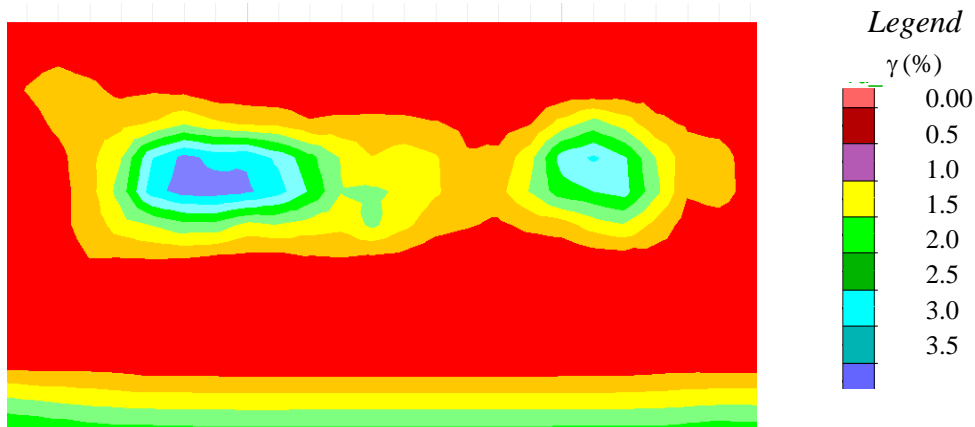


Figure 4.21. Shear strain distribution, γ (%) at $t=40$ sec

As mentioned earlier, measurements of excess pore water pressures in field piezometers has a delay, which was taken into consideration while presenting the computed and recorded response of the excess pore pressure response, as shown in Figure 4.22.

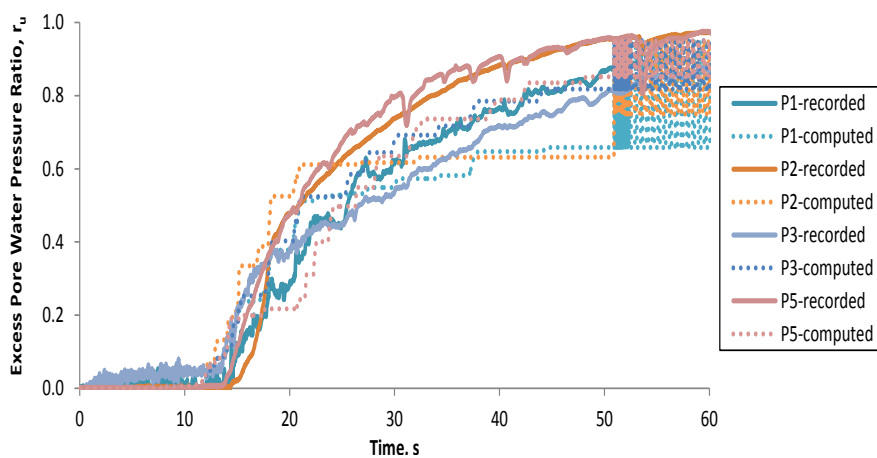


Figure 4.22. Computed and recorded excess pore pressure ratio, r_u response

More specifically, as mentioned before, a recent in situ effort to calibrate the piezometers showed that the P5 pore-pressure transducer responded consistently similar to an employed reference transducer (Hushmand et al., 1992). As a result of comparisons with P5 (Figure 4.23) by METUSAND it is concluded that

effective stress based numerical assessment of Wildlife site liquefaction array produces similar response with field data.

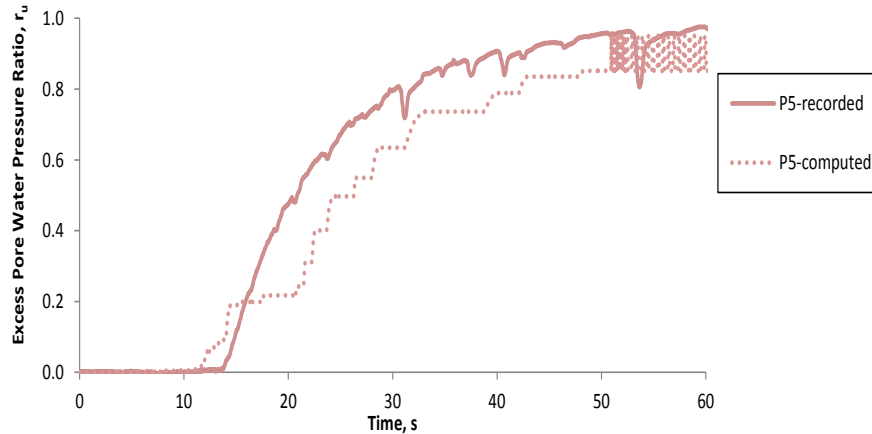


Figure 4.23. Computed and recorded excess pore pressure ratio, r_u response for piezometer P5

As a summary, well-documented Wildlife site case history is simulated with effective stress based, fully coupled nonlinear METUSAND constitutive model. The shallow model analyses clearly demonstrate a governing influence of the excess pore pressures on the ground response, and thus emphasize the need for effective stress analysis of soils that are susceptible to liquefaction. Another important result from the presented analyses is that the excess pore pressure, as a scalar quantity, has to be associated with the characteristics of cyclic shear strain occurred as a result of degradation of the soil stiffness.

The pore pressure response recorded in the field has been delayed; however numerical model instantly react the cyclic softening occurred during dynamic loading. It is apparent that, in order to make a reasonable comparison with respect to dynamic time, this recorded delay should be take into consideration and after this a very good agreement between the computed and the recorded excess pore water pressure response is obtained.

4.3. Prediction of Seismic Response of Port Island/Kobe Site

Widespread seismic soil liquefaction was occurred in Kobe, Japan, during the 1995 Hyogoken-Nanbu earthquake. Liquefaction-induced damage was particularly extensive and severe in the reclaimed lands of the two largest man-made islands, Port Island and Rokko Island. The observed liquefaction response was also evident in acceleration records from a downhole seismic array at the Port Island. As no excess-pore water pressure data were available at Port Island, a simulation was conducted to assess the corresponding mechanisms of excess pore pressure generation.

4.3.1. Site Description, Instrumentation and Seismic Records

The earthquake that shook the southern Hyogo Prefecture in Japan on January 17, 1995, commonly known as the Kobe earthquake ($M_w=7.2$) was the most devastating earthquake to strike Japan since the Kanto earthquake, in 1923. Within the southern Hyogo Prefecture, most of the damage was inflicted on the city of Kobe, including its Chuo, Nada, and Higashinada wards, and on the neighboring cities of Ashiya and Nishinomiya. Figure 4.24 shows the location map of the earthquake area. Most damaged areas are along a narrow band straddling the trace of fault rupture, extending from the southwest towards the north-east.

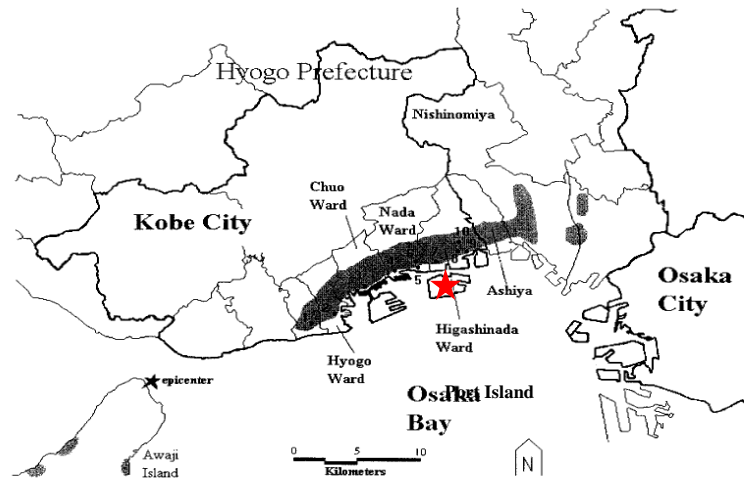


Figure 4.24. Areas of Damage in Hyogoken-Nanbu Earthquake of January, 1995
(Azizinamini et. al., 1997)

Port Island is a man-made island, with an area of 436 ha, constructed in the period between 1966 and 1981. The map of reclaimed areas completed by 1981 is given in Figure 4.24. A downhole accelerometer array was installed at the north-west corner of Port Island in 1991, as shown in Figure 4.25. It consists of four sets of accelerometers located at the ground surface and at depths of 16m, 32m and 83 m. Each set has three accelerometers, oriented in N-S, E-W and U-D directions, respectively (Figure 4.26).

Soil profile characteristics of the down-hole array site including SPT N-values, shear wave velocities, material types and location of the accelerometers along the depth of the profile are shown in Figure 4.26. As shown in the Figure 4.26a, the soil profile consists of five distinct layers down to a depth of about 83 m. The reclaimed layer is decomposed weathered granite known as Masado (Masa-soil) with grain sizes ranging from gravel and cobble-sized particles to fine sand (2 mm mean particle size, with silt-sized particles or smaller of less than 10% by weight). 19m thick reclaimed Masado overlies the original sea-bed layer of alluvial clay layer between 18 and 27m in depth and an alluvial gravelly sand layer underneath, at about 36m depth. Below these layers lies diluvial gravelly sand with a 22 m thickness and diluvial clay layer with a 23 m thickness to a

depth of about 82 m. It is to be noted that both gravelly sand layers are interlayered with silt. The water table is located approximately at 4m depth. Soil properties are summarized in Table 4.3.

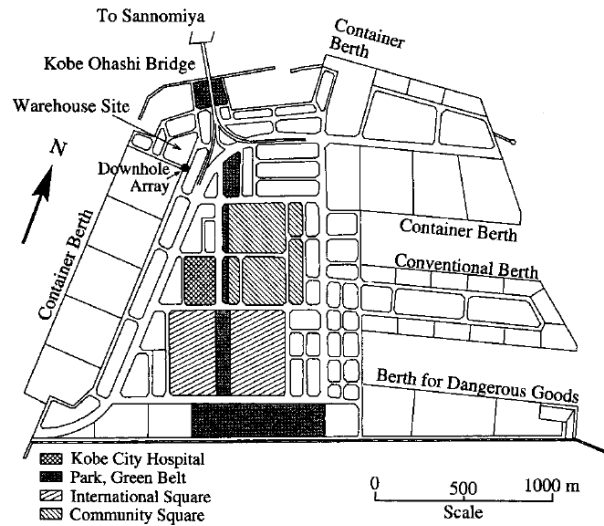


Figure 4.25. Port Island Map after Nakakita and Watanabe (1981)
(Elgamal et. al., 1996)

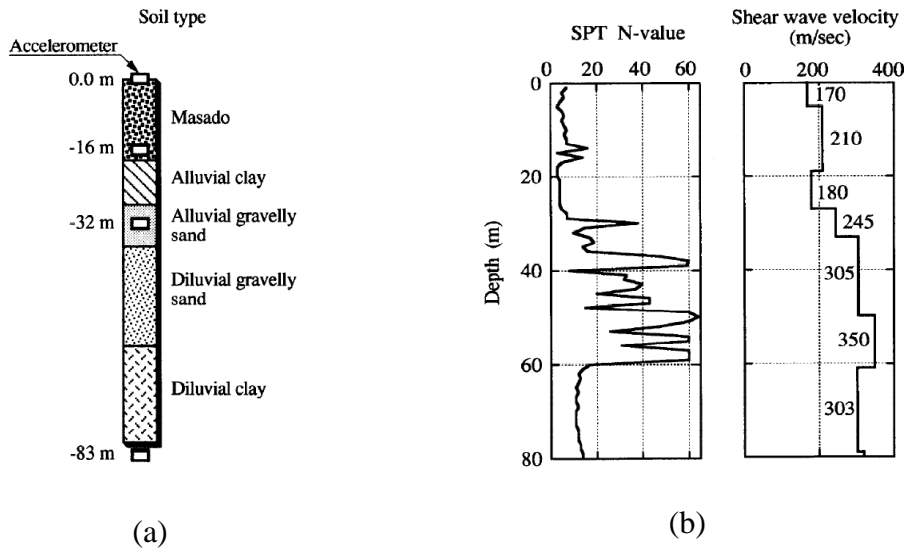


Figure 4.26. Soil profile of the seismic array site at Port Island
(Cubrinovski et. al 1996)

Table 4.3. Soil Properties (after Nakakita and Watanabe 1981)

Layer (1)	Depth (m) (2)	Mass density (kg/m ³) (3)	Water content (%) (4)	Shear strength (kPa) (5)
Fill layer	0-19	1.800-2.100	-	-
Alluvial clay	19-27	1.450-1.550	70-100	0-98
Upper clay	27-61	1.850-2.000	20-40	98-294
Diluvial clay	61-82	1.650-1.850	40-55	147-540
Lower clay	82-	1.850-2.000	20-40	98-294

The reclaimed Masado fill was constructed mainly by bottom dumping from barges with no compaction except for the upper few meters above the ground-water table (Sitar 1995). As shown in Figure 4.26b, in this layer, SPT blow counts are very low as average uncorrected N-values of about 6 blows/ft. Such low values in a granular fill are indicative of high liquefaction susceptibility (Seed et al. 1983).

During the Hyogoken-Nanbu Earthquake massive liquefaction occurred in the area of the down-hole array site at Port Island resulting in an average settlement of 30-40 cm and a 15-20 cm thick layer of sand and mud littered on the ground surface due to sand boiling. Horizontal acceleration vs. time records of the main shock of the quake recovered with the down-hole array accelerometers are given in Figure 4.27 (Cubrinovski et. al 1996).

Shaking was severe during the Hyogoken-Nanbu earthquake lasted for about 20 second. From 3 to 13 second, peak horizontal accelerations exceed the level of 0.5 g throughout the depths 16-83 m. However, soil liquefaction at shallower depths appears to cause de-amplification at the surface and acceleration levels decreases below 0.15-0.20g. No piezometer was available, so the intend of numerical simulations is to re-produce the recorded acceleration time history response of the site.

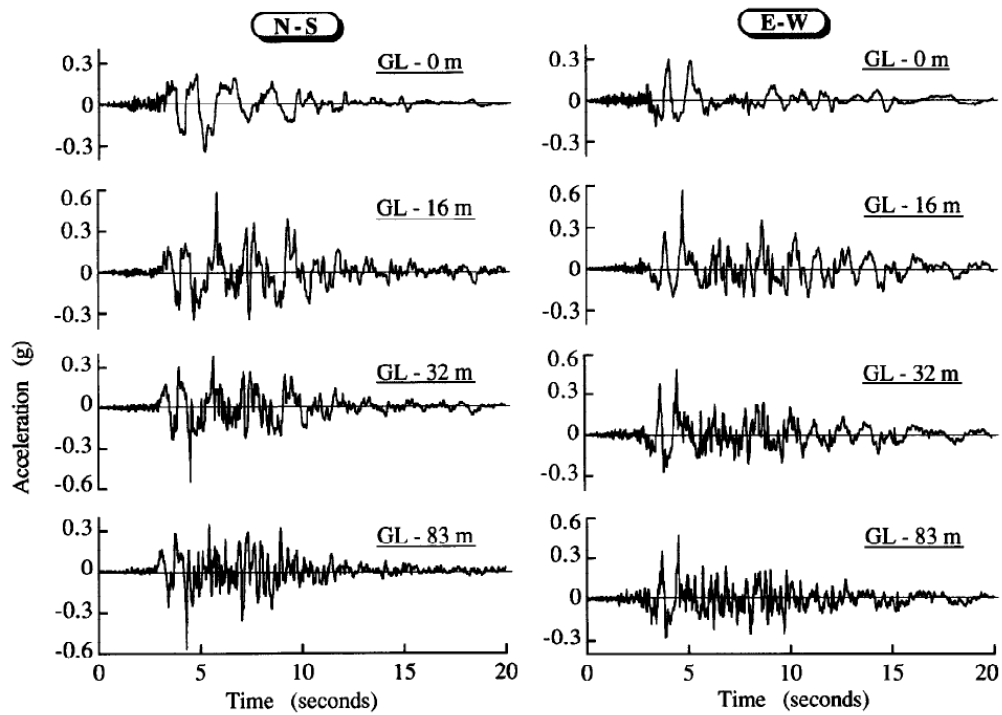


Figure 4.27. Recorded horizontal accelerations with the down-hole array at Port Island (Cubrinovski et. al 1996)

4.3.2. Idealized Soil Profile Used in Finite Element Analyses

An idealized soil profile with shear wave velocities increasing with depth as 170, 210, 180 and 245 m/s were developed for effective stress based 2-D finite element/difference analyses through the downhole accelerometer array of 32 m (Figure 4.28). Initial shear modulus is estimated as defined by Cetin and Bilge (2014) approach. Generic input parameters necessary for finite element analyses is summarized in Table 4.4.

Table 4.4. Geotechnical properties of idealized soil properties of Port Island Array

	Material Model	Depth (m)	Spt-N	D_R (%)	V_s (m/s)	PI	ρ (kg/m ³)	G_{max} (kPa)	ϕ (°)	c (kPa)
Masado	METUSAND	5	10	47	170	-	2.0	65960	30	0
Masado	METUSAND	18	18	63	210	-	2.0	81150	33	0
Alluvial Clay	Mohr-Coulomb	28	11	50	180	30	2.0	68131	30	15
Alluvial gravelly sand	Mohr-Coulomb	32	29	79	245	-	2.0	97221	36	0

D_R : relative density, V_s : shear wave velocity, PI : plasticity Index, ρ : density, G_{max} : initial (small strain) shear modulus, ϕ : friction angle, c : cohesion

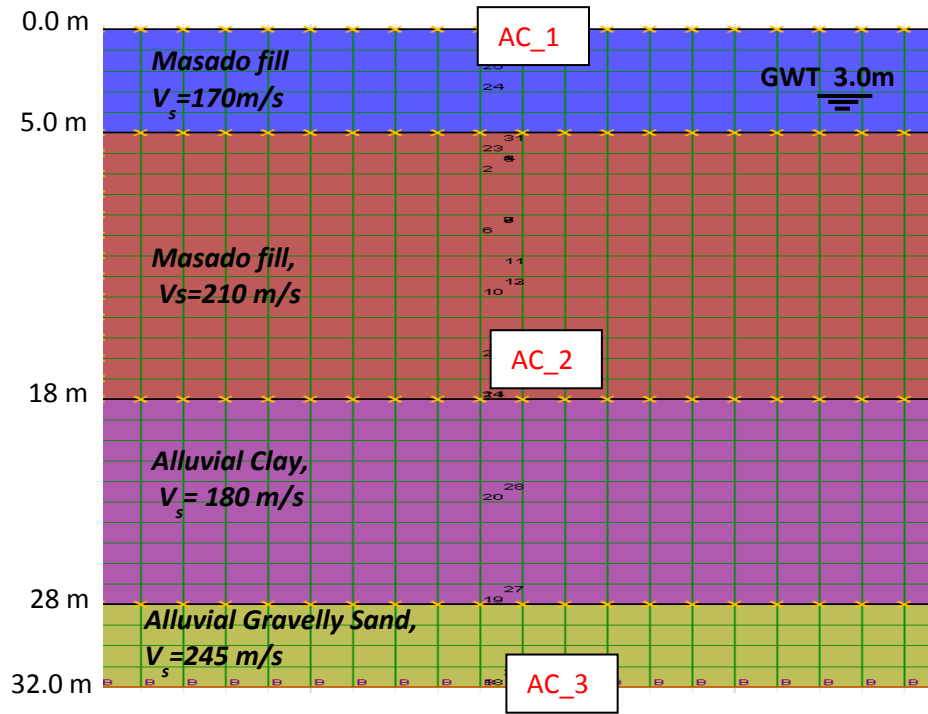


Figure 4.28. Finite element/difference mesh and idealized soil profile

4.3.3. Initial Conditions and Static Analyses

Similar to Wildlife site, static analyses were performed with elastic-perfectly plastic constitutive model with Mohr Coulomb failure criterion. Numerical simulation model parameters are given in Table 4.4. The variation of initial i)

effective vertical stress, ii) horizontal effective stress and iii) pore water pressure is given in Figure 4.29 through Figure 4.31, respectively.

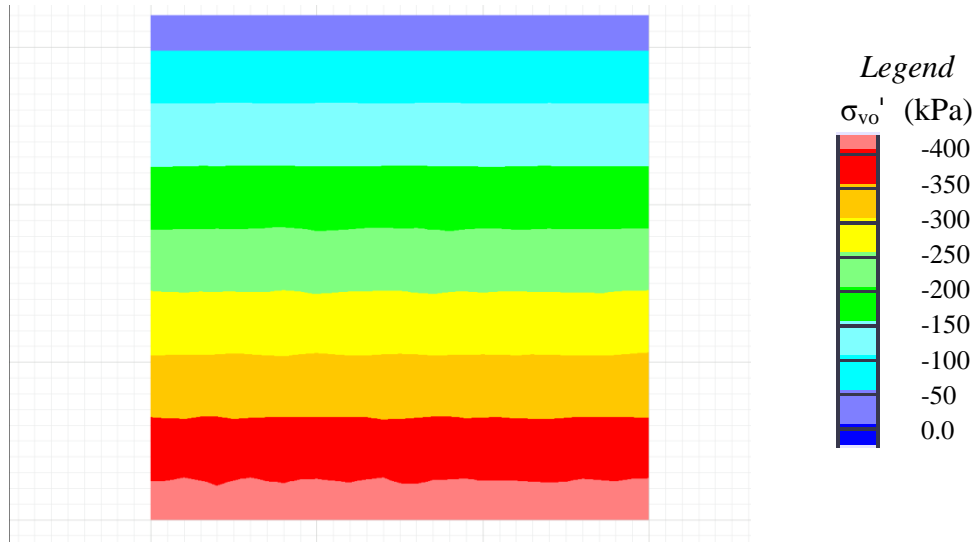


Figure 4.29. Initial Vertical Effective Stress Distribution of Port Island Site (kPa)

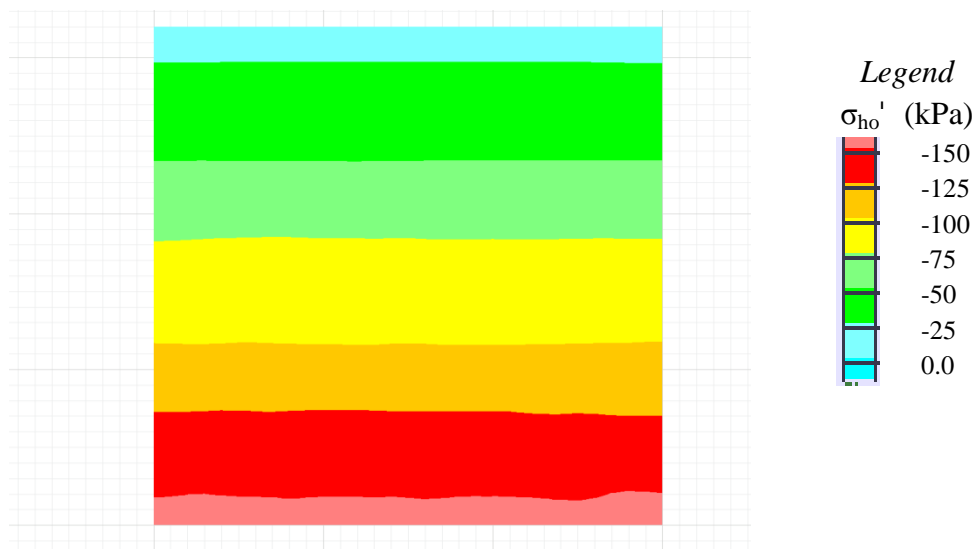


Figure 4.30. Initial Horizontal Effective Stress Distribution of Port Island Site (kPa)



Figure 4.31. Initial Pore Water Pressure Distribution of Port Island Site (kPa)

4.3.4. Effective Stress Based Dynamic Analyses

In order to closely investigate the ground response associated with the recorded accelerations shown in Figure 4.27, the input motion selected for this analysis is obtained from PEER strong motion database. Data is recorded at Port Island CEOR station, at ground surface. Closest distance to the fault is 3.3 km. The most critical component of 1995 Kobe Earthquake recorded at Port Island site has a peak ground acceleration of 308 cm/sec^2 in North-South direction (Figure 4.31). The outcrop input seismic motion was converted to “within” motion which was estimated by site response (i.e.: SHAKE-91) analysis. Then it was applied to a compliant boundary at the base. The horizontal within motion at 32 m is developed and maximum horizontal acceleration (at the location of AC_3, as shown in Figure 4.28) was estimated as 502.7 cm/sec^2 . Static boundary conditions were converted to FLAC free-field boundary for dynamic analyses (Figure 4.14). Input motion that was used in the numerical analyses is given in Figure 4.32.

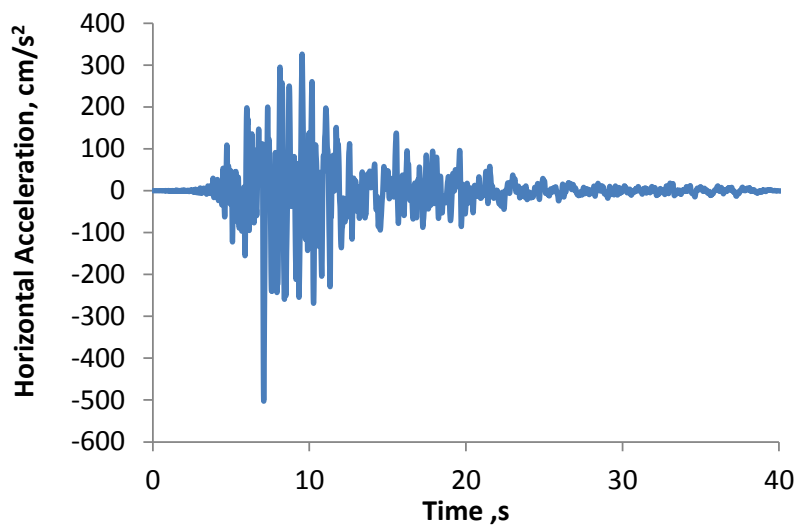


Figure 4.32. Input motion used in numerical analyses

Upper reclaimed 10 m of Masado layer is assumed to be liquefiable; hence it was modeled with METUSAND. The upper 5m thick soil layer has a relative density of 47%, and lower 5 m fill is assumed to have a relative density of 63%. According to METUSAND model, excess pore pressure starts to build up after shear strains start to exceed the threshold shear strain level of $10^{-4}\%$. METUSAND model is shown to accurately model both modulus reduction and hysteretic damping responses, consistent with available degradation curves. So that, no additional Rayleigh or viscous damping is needed.

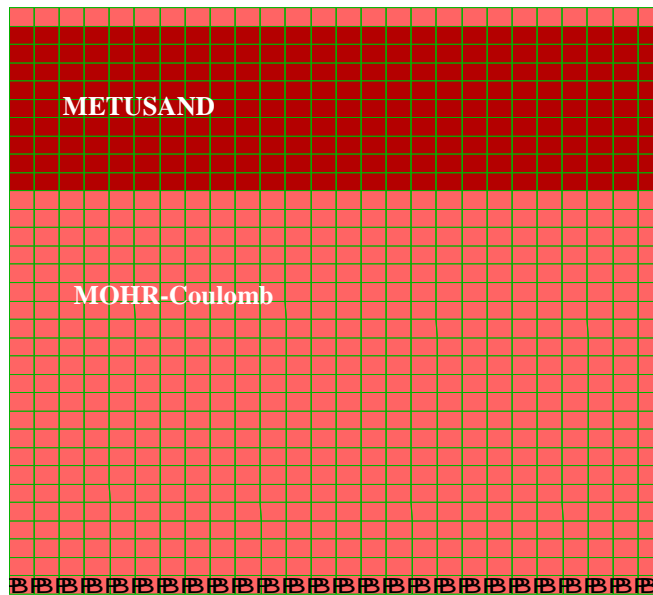


Figure 4.33. Material models and dynamic boundary condition

4.3.5. Computed Dynamic Response and Comparison with Field Data

Figure 4.34 shows a comparison between the computed and the recorded acceleration time histories at the ground surface and at the base (at depth 32m which input motion is given) for the maximum shaking intensity direction N-S which are the location of instrumented accelerometers AC_3 and AC_1 respectively. Apparently, there is a very good agreement between the computed and the recorded accelerations at both depths. Surface accelerations are seen to be de-amplified after 7.5 second of the main shock also indicating that the top soil layer is liquefied. Due to the dilation response of the model, an extreme peak acceleration response at ground level was computed at 20 sec as seen in Figure 4.34. Comparison between computed and recorded spectral acceleration time history at the ground level is given in Figure 4.35.

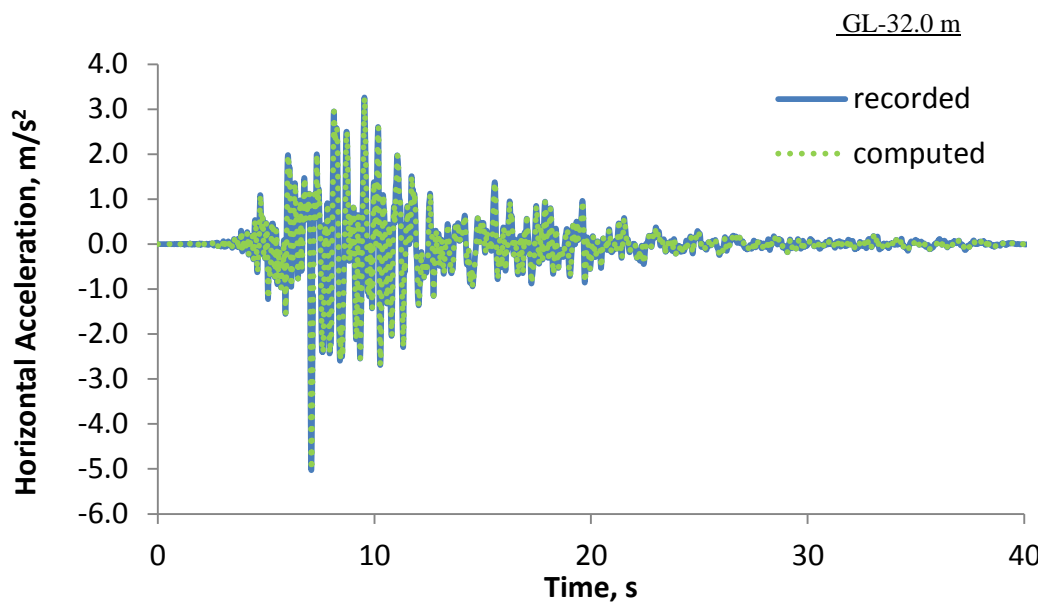
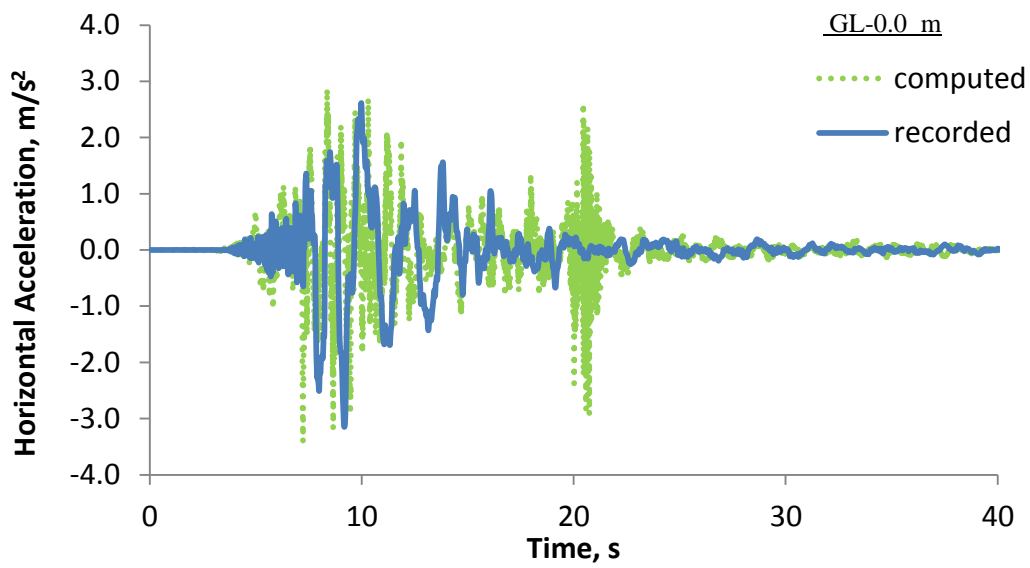


Figure 4.34. Computed and recorded acceleration time histories for ground surface and at 32 m depth

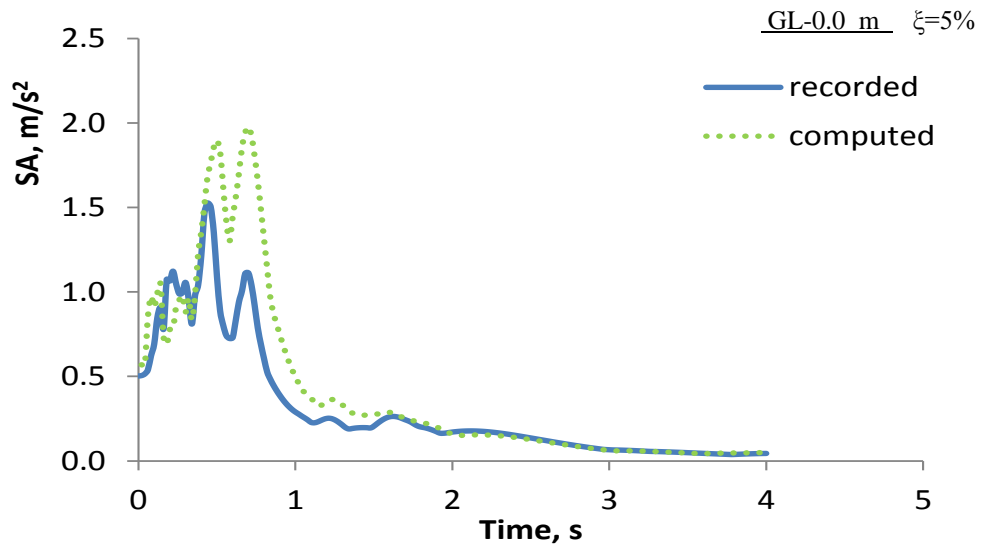


Figure 4.35. Computed and recorded response spectra for %5 damping at ground level

Distribution of the maximum excess pore pressures ratio, r_u contours at dynamic time $t_i=8$ sec, 20sec, and 40 sec are given in Figure 4.36-Figure 4.38.



Figure 4.36. Excess pore pressure distribution, r_u , at $t=8.0$ sec

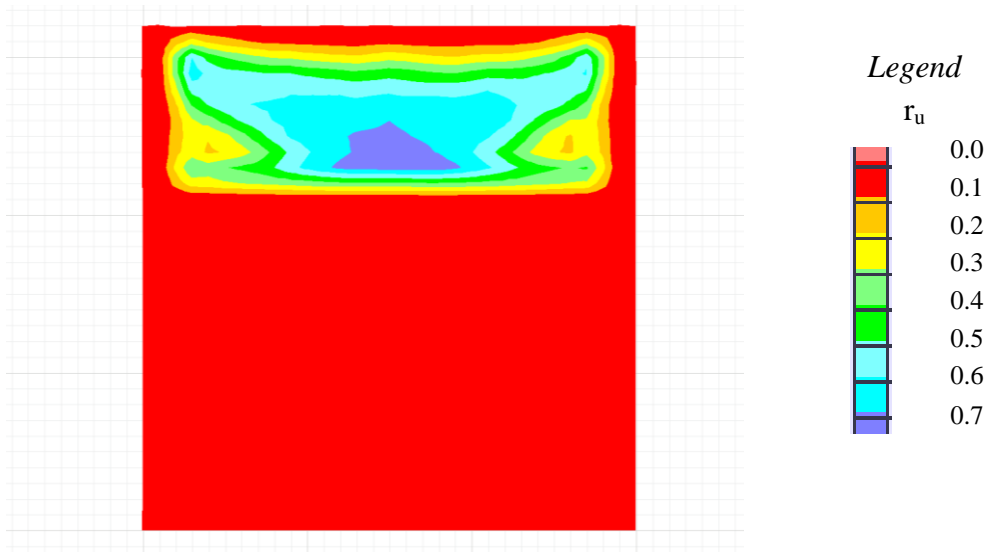


Figure 4.37. Excess pore pressure distribution, r_u , at $t=20$ sec

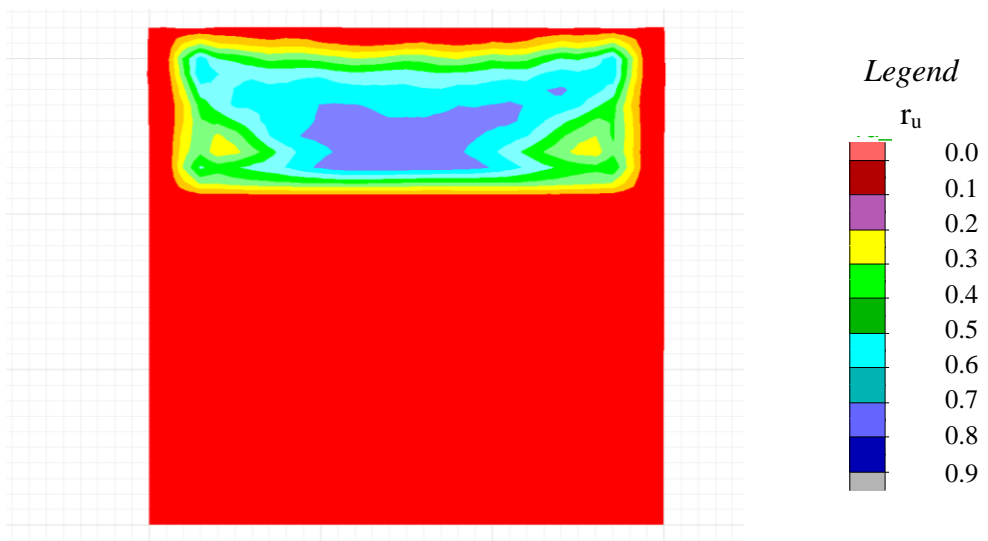


Figure 4.38. Excess pore pressure distribution, r_u , at $t=40$ sec

Distribution of the maximum excess pore pressures and the maximum shear strains computed during dynamic loading at liquefied Masado layer are shown in Figure 4.39 and Figure 4.40. These results reveal that the most heavily liquefied layers were the part of the Masado layer extending from 5 m to 10 m depth. In this layer, the excess pore pressure reached to the initial effective vertical stress,

and a cyclic softening due to liquefaction occurred after only one and a half to two cycles of intensive shaking. This pore pressure response was associated with maximum shear strain levels of 3-4 %.

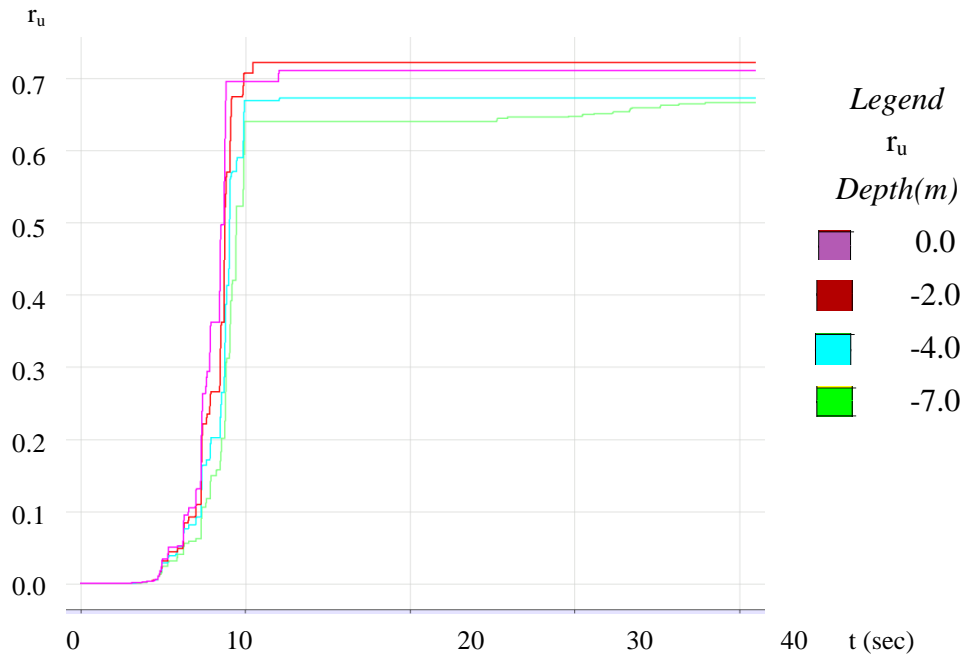


Figure 4.39. Excess pore pressure ratio vs dynamic time at depth 0.0m, 2.0 m, 4.0m and 7.0 m at $t=40$ sec

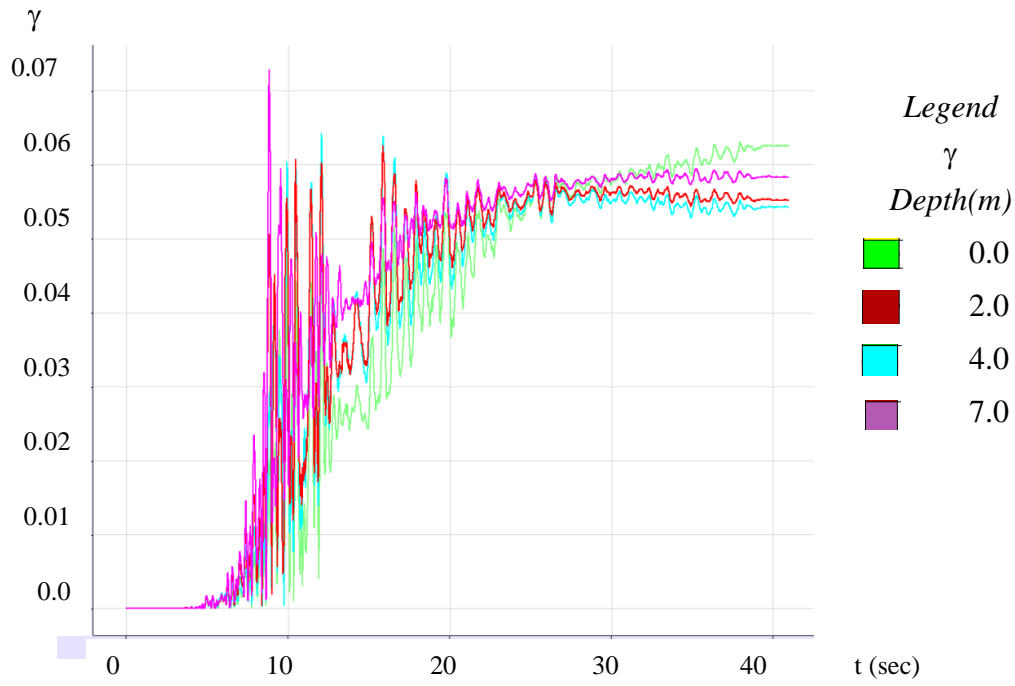


Figure 4.40. Shear strain vs dynamic time at depth 0.0m, 2.0 m, 4.0m and 7.0 m at t=40 sec



Figure 4.41. Shear strain distribution, γ (%) at t=40 sec

4.4. Conclusion

In this chapter, well documented field case histories of Wildlife Liquefaction Site, Imperial Valley, California, shaken by 1987 Superstition Hills earthquake was used to validate the proposed effective stress based constitutive model, METUSAND. “FLAC-2D v7.0 Finite Difference Software” along with METUSAND constitutive model was used for dynamic response of the idealized Wildlife site array profile. Pore pressure and acceleration records at Wildlife Site were obtained from Holzer and Youd (2007), and compared with FLAC-2D computed values. Comparisons in general revealed that both the amplitude and the frequency content of the acceleration time histories were comparable. Additionally, a very similar match to recorded excess pore pressure response is also observed. Secondly, a fully coupled effective stress analysis of the Port Island down-hole array site was performed in order to simulate the acceleration records and to clarify the characteristics of the ground response at this fully liquefied site. Port Island Site, Kobe shaken by 1995 Hyogo-ken Nanbu Earthquake is numerically modeled and estimated response of the site is compared with the actual response. Hence no piezometric data was available; comparisons could only be made on the basis of recorded within and outcropping motions. Simulation results revealed that a close match between the recorded and simulated acceleration time histories was achieved. Also, simulated site response by METUSAND model confirmed that liquefaction was likely to trigger at 8 seconds.

As a conclusion , on the basis of comparisons with well documented site response of liquefied case history sites of Wildlife and Port Island, it was shown that METUSAND model can reliably simulate effective stress-based coupled response of pore pressure generation and cyclic shear straining. Additionally, closely matching outcropping acceleration time histories at liquefied site also confirmed that the modulus degradation and damping responses could be reliably simulated by METUSAND in the wide range of very small to large strains.

CHAPTER 5

REVIEW ON METHODS FOR ASSESSMENT OF LATERALLY LOADED PILES RESPONSE

5.1. Introduction

Piles are slender structural elements used to transfer loads from structures into deeper bearing strata below the ground level. It should withstand various types of loads including axial, lateral loads and moments. Although piles are usually used to carry axial loads, they may be subjected to lateral loads due to earthquakes, high winds, wave action, ship impact, liquefaction, and slope failure. The load transfer mechanism for a laterally loaded pile is very complex especially when it is subjected to cyclic loads.

In the design of such pile foundations, not only the ultimate loads but also the deflections shall be estimated to ensure the serviceability requirements. Hansen (1961) developed the ultimate lateral resistance of rigid piles based on earth pressure theory which is applicable for short piles. Matlock and Reese (1960) developed a generalized iterative solution method for rigid and flexible laterally loaded piles embedded in soils with two forms of varying modulus with depth. Davisson and Gill (1963) presented the case of a laterally loaded pile embedded in a layered soil system with a constant (but different) modulus of subgrade reaction in each layer. Broms (1964a, b) method is also based on earth pressure theory with simplifying assumption for distribution of ultimate soil resistance along the pile length and this method is applicable for both short piles and long piles. More recently, Yang and Jeremic (2002) carried out finite element analyses on the

behavior of a single pile in elastic-plastic soils, for single as well as double layer composed of both sand and clays, and generated p-y curves. Zamri et al. (2009) have assessed the lateral load behavior under combined vertical and lateral loads considering the variation of water table elevations.

Case histories of collapsed pile-supported structures founded on liquefiable soils during earthquakes are presented in Figure 5.1. Figure 5.1a shows the failure of pile supported pier of the Salinas Bridge during the 1906 San Francisco Earthquake. Figure 5.1b presents “Miles Glacier Bridge (also known as Million Dollar Bridge) damage after 1964 Alaska earthquake: Span 4 fell into the river and Pier 3 was badly damaged. The view of the Showa bridge in Nigata is given in Figure 5.1c, showing the damage caused by 1964 Nigata earthquake. Liquefaction led to the collapse of two piers and the span between them. The free displacement made allowed at one end of each span caused the remaining spans to drop into the river. Tilted tank on piled foundation at the Karumojima tank farm is shown in Figure 5.1d, which is caused by Kobe, Japan earthquake, Jan. 17, 1995. Note the ground cracking due to lateral spreading in the foreground

Analyzing piles under seismic loading is much more complex and involves the assessment of soil structure interaction, and shall account for kinematic and inertial interactions which are obtained by performing ground response analysis. Seismic lateral response of piles in liquefying soil was analyzed by Liyanapathirana and Poulos (2005a). However their approach is very complex and difficult to implement for pile designers. A pseudo-static approach was proposed by Liyanapathirana and Poulos (2005b), which can be more frequently used by the designers.

In the present study, the aim is defined as to develop a semi-empirical model to assess cyclic response of piled foundations.



(a)

Failure of pile supported pier of the Salinas Bridge during the 1906 San Francisco Earthquake
 (Source: NISEE, Berkeley)



(b)

“Million Dollar Bridge damaged after 1964 Alaska Earthquake (Source: Mceer and Wikipedia)



(c)

Damage of Showa bridge in Nigata by the earthquake in 1964. (Source: USGS page on 1964 Niigata earthquake)



(d)

Tilted tank on piled foundation at the Karumojima tank farm which is caused by Kobe, Japan earthquake, Jan. 17, 1995. (Source: NISEE Earthquake Engineering Online Archive)

Figure 5.1. Collapse of some pile-supported structure during earthquakes

5.2. Laterally Loaded Piles

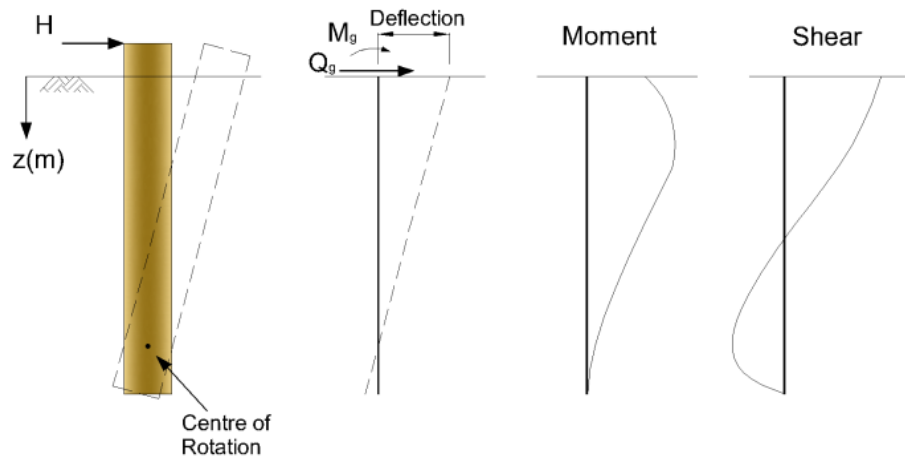
Determining the response of a single pile to an applied load is a difficult analytical problem. A vertical pile resists lateral load by mobilizing the reacting pressure in the soil surrounding it. The degree of distribution of the soil reaction depends on
 i) the strength and the stiffness of the pile, b) the strength and the stiffness of the

soil and iii) external forces and boundary conditions. In general, laterally loaded piles can be divided into two major categories as free or fixed headed, which are also further classified as short-rigid and long- flexible piles.

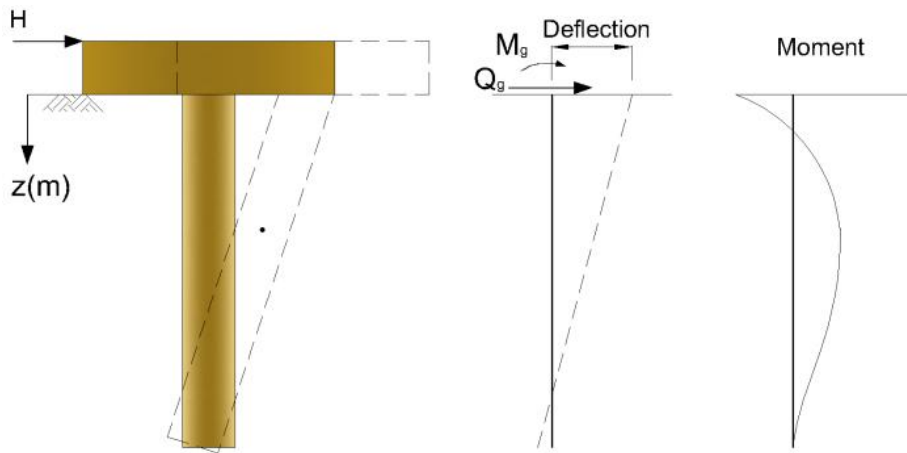
The failure mechanism of short rigid piles is distinguished by the rotation of the pile around a pin-point at a depth, z , below the ground soil surface for free head loading conditions (Figure 5.2a). Whereas, rigid body translational lateral displacements occurs on the fixed head piles, as shown in Figure 5.2b.

The failure mechanism for long piles is characterized by the formation of a plastic hinge at a depth z below the ground surface for free head loading conditions, as shown in Figure 5.3. If the pile is uniform maximum bending moment is observed at the plastic hinge location.

Many procedures have been proposed, which enable some approximation to true pile behavior without requiring detailed analyses. The analytical approaches developed for a single pile and pile group under lateral load can be divided into two main categories i) methods of calculating ultimate lateral resistance and ii) methods of calculating acceptable deflection at applied lateral load. Some of these widely used methods will be discussed next in detail.

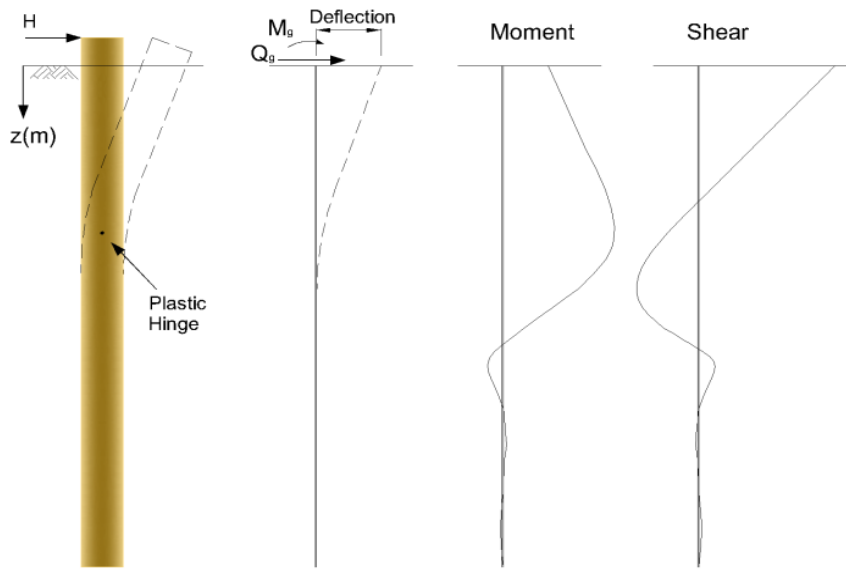


a) Free Head- Short (rigid) pile

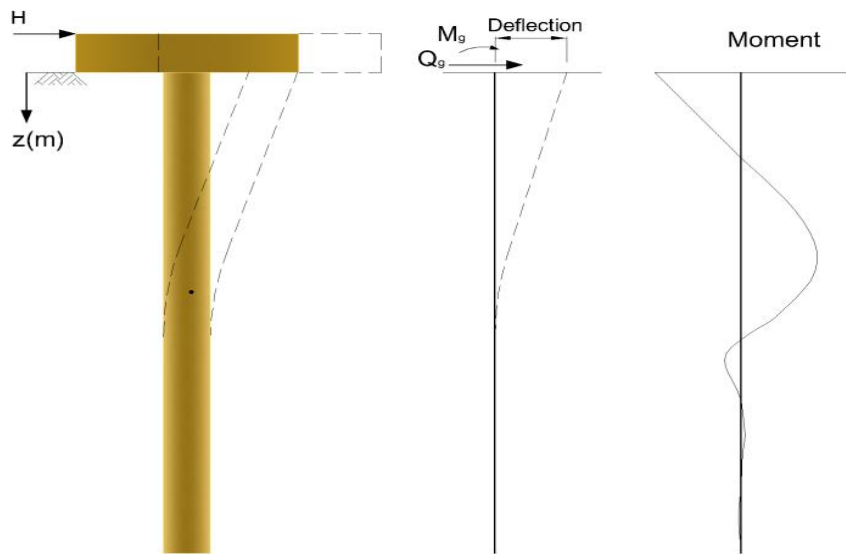


b) Fixed Head - Short (rigid) pile

Figure 5.2. Short (rigid) pile failure mechanism and the nature of variation of pile deflection, moment and shear force



a) Free Head- Long (elastic) pile



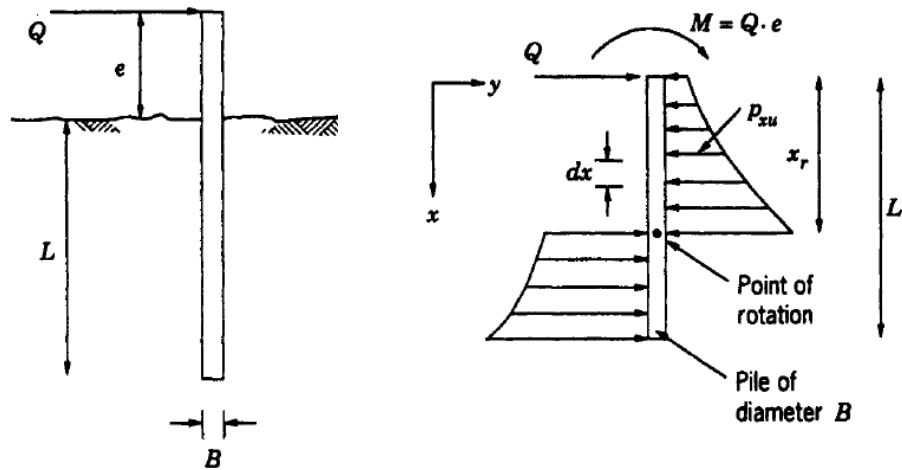
b) Fixed Head – Long (elastic) pile

Figure 5.3. Long (elastic) pile failure mechanism and nature of variation of pile deflection, moment and shear force

5.3. The Ultimate Lateral Resistance of Laterally Loaded Piles

The response of piles subjected to lateral loads has been frequently analyzed by limit equilibrium methods. These methods assume that the soil exhibits a rigid, perfectly plastic stress-strain behavior (i.e.: no strain until the constant yield stress is reached). When a pile is subjected to increasing lateral loads, failure will be manifested by a rapid increase in the deflection of the top of the pile. This excessive deflection may result from the failure of the soil surrounding the pile element or from failure of the pile itself. By making reasonable assumptions regarding the distribution of soil reaction along the length of the pile at failure, ultimate lateral load capacity can be calculated from simple static equilibrium requirements (Kramer, 1988).

The ultimate resistance that the soil can provide per unit length is usually considered to be constant with depth. Figure 5.4 shows the mechanism in which the ultimate soil resistance is mobilized to resist a combination of lateral force Q and moment M applied at the top of a free-head pile.



Laterally loaded pile

Soil resistance on pile caused by lateral load

Figure 5.4. Mobilization of lateral soil resistance on pile caused by lateral load for a free-head rigid pile (Prakash and Sharma, 1990)

The ultimate lateral resistance, Q_u , and the corresponding moment, M_u , can then be related with the ultimate soil resistance, p_u , by considering the equilibrium conditions as follows;

$$Q_u = \int_{x=0}^{x=x_r} p_{xu} B dx - \int_{x=x_r}^{x=L} p_{xu} B dx \quad (5.1)$$

$$M_u = Q_u e = - \int_{x=0}^{x=x_r} p_{xu} B x dx + \int_{x=x_r}^{x=L} p_{xu} B x dx \quad (5.2)$$

where;

B = width of pile

x_r = depth of point of rotation

If the distribution of ultimate unit soil resistance, p_{xu} , with depth "x" along the pile is known, then the values of x_r (the depth of the point of rotation) and Q_g (the ultimate lateral resistance) can be obtained by Equations 5.1 and 5.2.

Hansen (1961) provides a derivation of the static approach that incorporates a variable soil resistance with depth. Davis (1961) developed a solution for plane strain conditions. Brom's (1964a, b) method considers either free or fixed-head piles in both cohesive and cohesionless soil.

According to Zeevaert (1973), the horizontal displacement of the soil mass at any depth level is called as δ_{si} . The pier is subjected at the top to the horizontal force V_0 , representing the base shear of a structure induced by the seismic movement on the pier head. This inertia force will cause horizontal deflection δ_{pi} in the pier at a distance z from the firm base, opposite to the horizontal displacements δ_{si} of the soil. As the soil moves against the pier, the soil is compressed due to the resistance offered by pier. The structural element will yield to the exerted orce in relation to its flexibility an amount δ_{oi} . Therefore, the pier displacements δ_i due to

the shear force applied at its head and the soil pressure is $\delta_{0i} + \delta_{pi}$. Hence the relative displacement between soil and the pier is equal to $\delta_{si} - (\delta_{0i} + \delta_{pi})$.

Meyerhof et al. (1981), Sastry and Meyerhof (1986), Patra & Pise (2001) and Zhang et al. (2005) are some of the other approaches, which are available in the literature.

5.3.1. Brinch Hansen's Method (1961)

The piles used are usually short; hence have to be treated as rigid piles and the ultimate soil resistance must be considered. Poulos and Davis (1980) imply that for rigid piles, one of the most precise methods to evaluate ultimate lateral resistance is the procedure recommended by Brinch Hansen (1961). It can be demonstrated that the value of the ultimate horizontal loading Q_u , which can be applied in the head of the pile is extremely sensitive to the position of the rotation center x_r (Figure 5.4). Q and M are defined as the limiting values to trigger failure - that is, to mobilize the ultimate soil resistance along the pile. The ultimate soil pressure at any depth x below the soil surface is defined as p_{xu} .

$$p_{xu} = \sigma'_v K_q + c K_c \quad (5.3)$$

where;

σ'_v = vertical effective overburden pressure

c = cohesion of soil

K_c and K_q = factors that are function of ϕ and x/B (Figure 5.5)

The method suffers from the following disadvantages that;

- It is applicable to only short (rigid) piles.
- It requires trial and error solution to locate point of rotation.
- It is applicable to an unrestrained head conditions.
- It neglects elastic deformations observed within the pile.

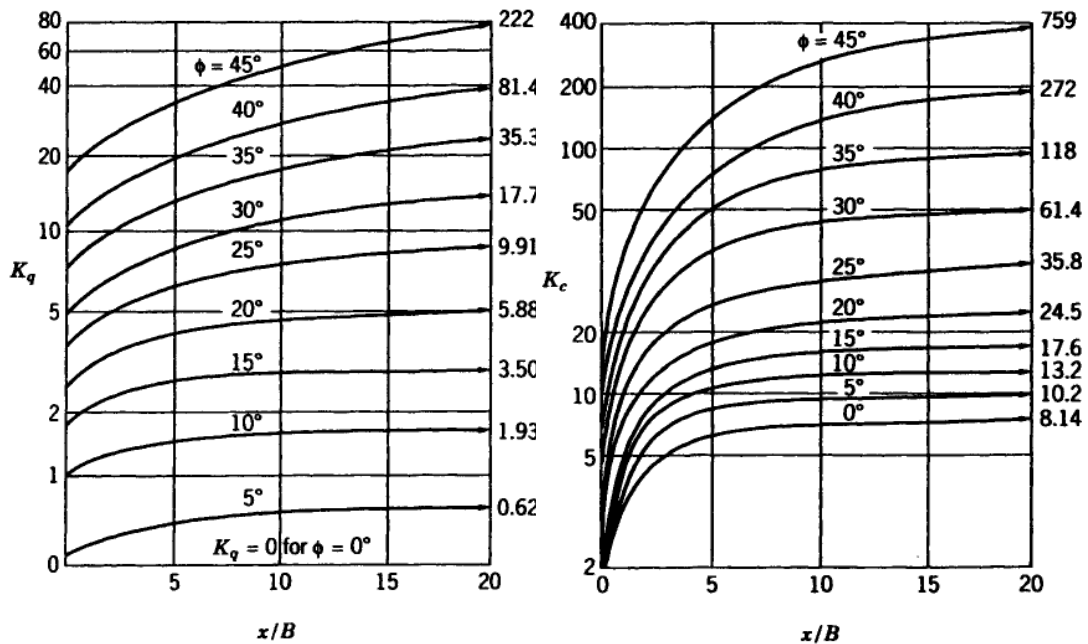


Figure 5.5. Brinch Hansen Method Coefficients K_q and K_c (Hansen, 1961)

5.3.2. Brom's Method (1964)

Brom's (1964a,b) method is also based on earth pressure theory with simplifying assumption for the distribution of ultimate soil resistance along the pile length. The method is applicable for both short and long piles. It is used for assessing the ground surface deflections of fixed and free head piles and is based on the use of modulus of subgrade reaction theory as suggested by Terzaghi (1955).

Rigid piles were considered to fail by rigid body rotation due to failure of the surrounding soil. Long, flexible piles were assumed to fail when the maximum bending moment exceeded the bending capacity of the pile, resulting in the formation of a plastic hinge at some depth below the ground surface. Broms assumed a distribution of ultimate lateral soil resistance along the pile to determine the ultimate capacity.

The criterion defined by Brom's for rigid and flexible piles is as follows;

$$\begin{aligned} L/T \leq 2 & \dots\dots\dots \text{short rigid piles} \\ L/T \geq 4 & \dots\dots\dots \text{long flexible piles} \end{aligned} \quad (5.4)$$

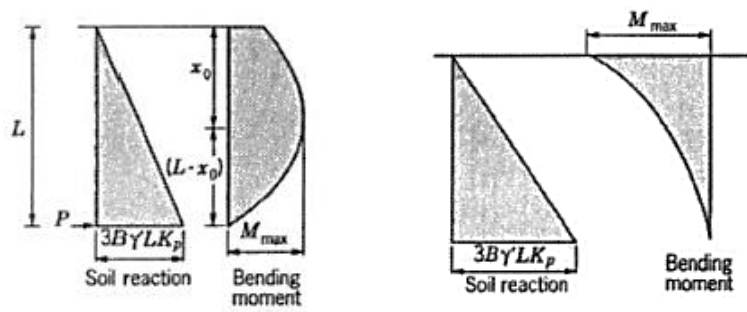
where;

L= length of pile

T= relative stiffness factor (which will be discussed later in the chapter)

For cohesionless soils, the ultimate soil reaction was considered to be three times the maximum Rankine passive pressure, considering the arching effects around the pile. Simple beam theory allows calculation of the induced bending moment along the pile at failure.

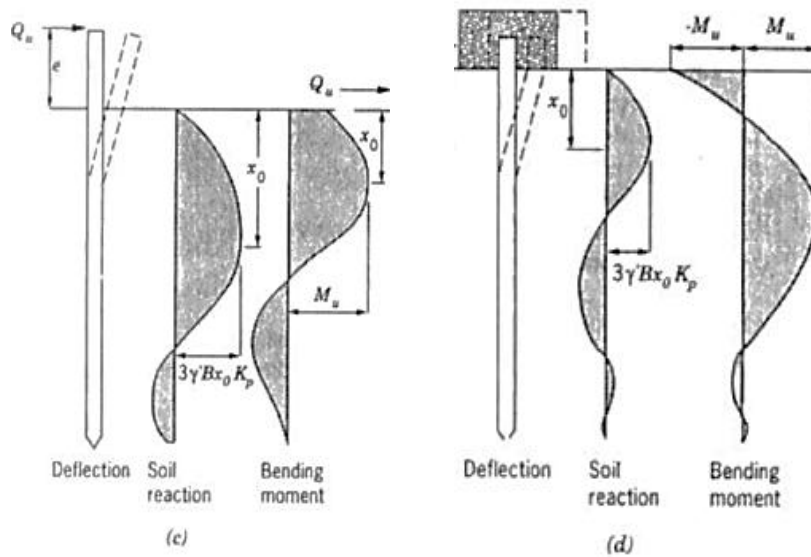
For cohesive soils, the ultimate lateral resistance was estimated, on the basis of a plasticity analysis of a cylinder moving laterally through a plastic medium. The resistance was estimated to be nine times the undrained strength of the soil excluding the upper 1.5 pile diameters. Soil reaction bending moment for free head and fixed head piles is shown in Figure 5.7.



Free Head

Fixed Head

a) Short piles

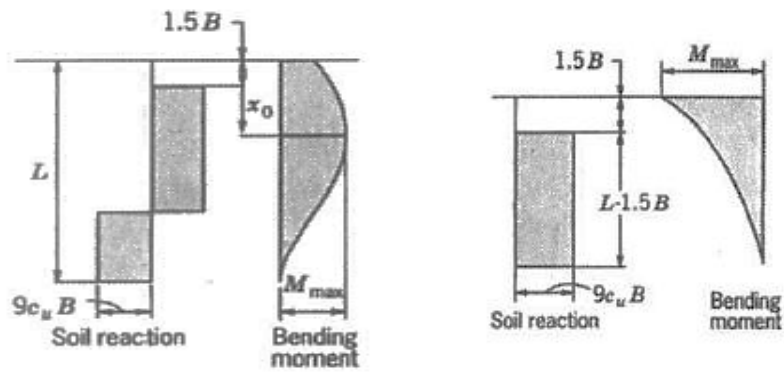


Free Head

Fixed Head

b) Long piles

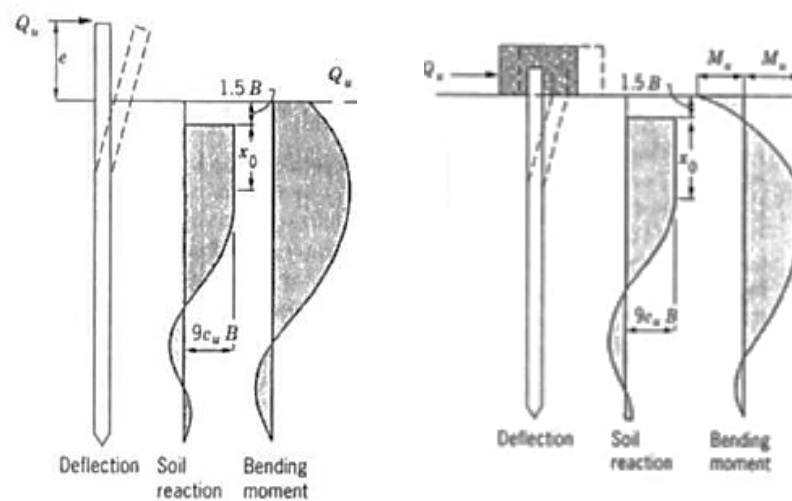
Figure 5.6. Soil reaction and bending moments on piles in cohesionless soils (Broms 1964a)



Free Head

Fixed Head

a) Short piles



Free Head

Fixed Head

b) Long Piles

Figure 5.7. Soil reaction and bending moments on piles in cohesive soils (Broms 1964b)

The ultimate lateral load, Q_u , can be estimated by using the equations or chart solutions given in Table 5.1 and

Table 5.2. Ultimate lateral load capacity of short and long piles in cohesive soils (Broms, 1964b).

for cohesionless and cohesive soils respectively. One should enter the relevant graph through the x-axis by calculating the length to diameter ratio, L/B . Then,

the relevant graph should be selected based on the fixation at the ground line and the ratio between the eccentricity of the load and the diameter of the pile. Then, the value at the y-axis can be determined related to the embedded length and ultimate resistance moment for short and long piles respectively.

According to Broms method, lateral deflections can be calculated at the horizontal working loads, which are approximately 0.5 – 0.3 times the ultimate lateral resistance. It is based on linear portion of subgrade reaction approach, which is discussed in the following sections.

Table 5.1. Ultimate lateral load capacity of short and long piles in cohesionless soils (Broms, 1964a).

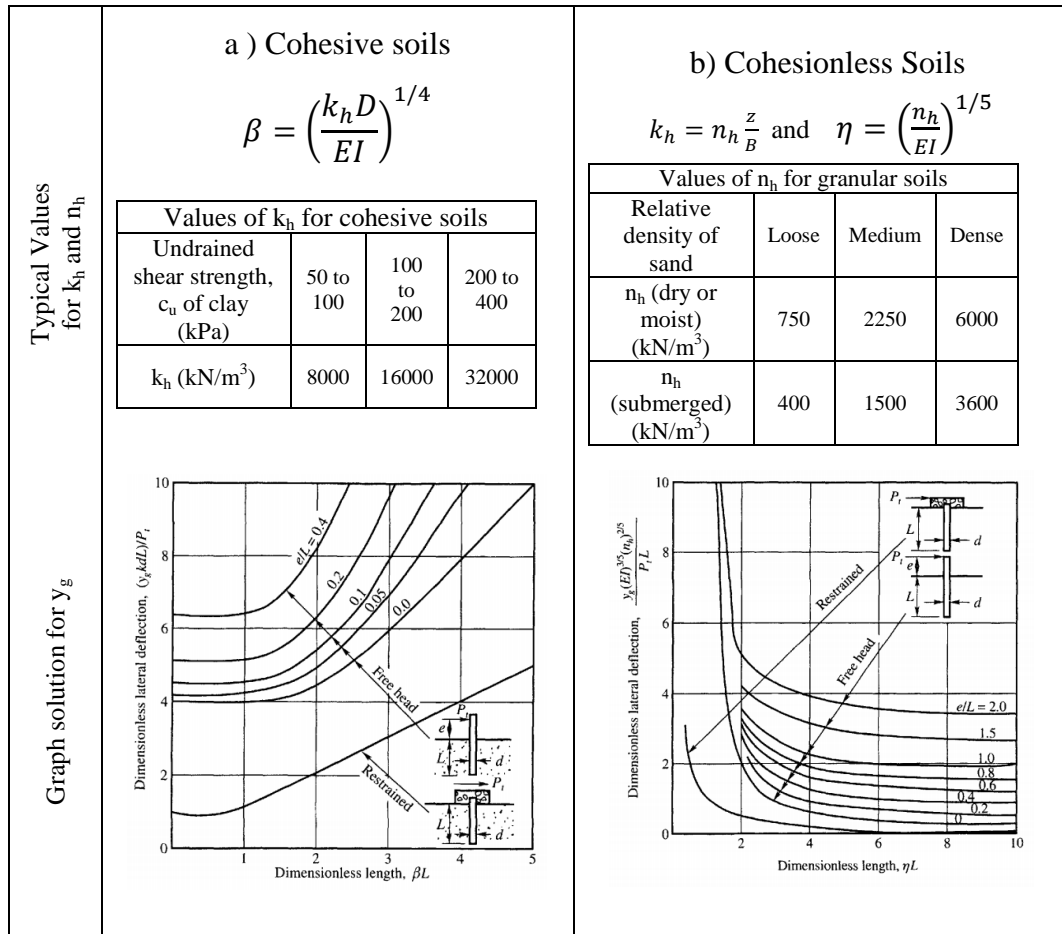
	<i>a) Short piles</i>		<i>b) Long piles</i>	
	Free Head	Fixed-Head	Free Head	Fixed-Head
Ultimate Lateral Resistance, Q_u	$Q_u = \frac{0.5\gamma' L^3 B K_p}{e + L}$	$Q_u = 1.5\gamma' L^2 B K_p$	$Q_u = \frac{M_u}{e + 0.54 \left(\frac{Q_u}{\gamma' B K_p} \right)}$	$Q_u = \frac{2M_u}{(e + 0.67x_0)}$
Maximum Moment, M_{max}	$M_{max} = Q_u(e + 1.5x_0)$	$M_{max} = \gamma' L^3 B K_p$	$M_{max} = Q_u(e + 0.67x_0)$	$M_{max} = Q_u(e + 0.67x_0)$
Depth of Max. Moment, x_0	$x_0 = 0.82 \left(\frac{Q_u}{\gamma' B K_p} \right)$	-	$x_0 = 0.82 \left(\frac{Q_u}{\gamma' B K_p} \right)$	$x_0 = 0.82 \left(\frac{Q_u}{\gamma' B K_p} \right)$
Graphical solution for Q_u				

Table 5.2. Ultimate lateral load capacity of short and long piles in cohesive soils (Broms, 1964b).

	<i>a) Short piles</i>		<i>b) Long piles</i>	
	Free Head	Fixed (Restrained)-Head	Free Head	(Restrained)-Head
Ultimate Lateral Resistance, Q_u	$Q_u = \frac{M_{max}}{(e + 1.5 B + 0.5 x_0)}$	$Q_u = 9c_u B(L - 1.5B)$	$Q_u = \frac{M_{max}}{(e + 1.5 B + 0.5 x_0)}$	$Q_u = \frac{2M_u}{(1.5B + 0.5x_0)}$
Maximum Moment, M_{max}	$M_{max} = 2.25 B c_u (L - x_0)^2$	$M_{max} = 4.5 c_u B(L^2 - 2.25B^2)$	$M_{max} = Q_u(e + 1.5 B + 0.5 x_0)$	$M_{max} = Q_u(e + 1.5 B + 0.5 x_0)$
Depth of Max. Moment, x_0	$x_0 = \left(\frac{Q_u}{9c_u B}\right)$	-	$x_0 = \left(\frac{Q_u}{9c_u B}\right)$	$x_0 = \left(\frac{Q_u}{9c_u B}\right)$
Graphical solution for Q_u				

Horizontal subgrade reaction can be assumed to be constant with depth for cohesive soils, whereas it increases linearly with depth in cohesionless soil. Lateral deflections, y_0 at the ground surface can be found as a function of the dimensionless lengths βL and ηL , as shown in Table 5.3.

Table 5.3. Lateral deflection at ground surface for piles (Broms, 1964 a,b)



5.4. Methods of Calculating Mobilized Deflections

5.4.1. Elastic Continuum Method

Poulos (1971) presents an elastic solution for a single pile subjected to lateral loading. Poulos assumed that the soil is an elastic, homogeneous, isotropic half space with a constant Young's modulus and Poisson's ratio. The pile is divided into equal length segments of constant width and stiffness. Each segment of the pile is considered to be a small vertical footing. The footings are linked together through the stiffness (or flexibility) of the pile. Poulos and Davis (1980) provided means to account for the variation in modulus with depth. Their method also allows a distinction to be made between free-head and socketed piles.

Theoretical basis for the elastic continuum approach solution is given as follows:

- i) As shown in Figure 5.8, the pile is assumed to be a thin rectangular vertical strip of width, B , length, L , and constant flexibility, EI . The pile is divided into $(n + 1)$ elements of equal lengths except those at the top and tip of the pile, which are of length $(\delta/2)$.
- ii) To simplify the analysis, possible horizontal shear stresses developed between the soil and the sides of the pile are not taken into account.
- iii) Each element is assumed to be under a uniform horizontal force P , which is assumed to be constant across the width of the pile.
- iv) The soil is assumed to be a homogeneous, isotropic, semi-infinite elastic material, having a Young's modulus, E_s , and Poisson's ratio, ν_s , which are unaffected by the presence of the pile.

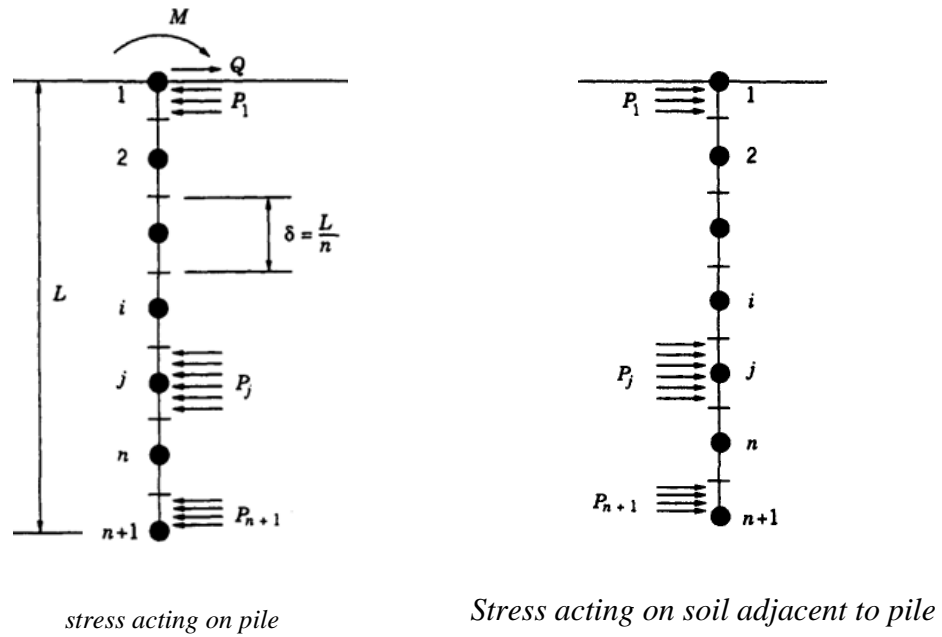


Figure 5.8. Elastic Continuum Model approach (Poulos, 1971)

Although this approach is theoretically more advance compared to empirical approaches, one of the major obstacles in its application to practical problem is the realistic determination of soil modulus E_s . Also, the approach needs more field verification and calibration by applying the theoretical concept to practical problems.

5.4.2. Subgrade Reaction Method

The historical development of subgrade reaction method begins with Winkler (1867) modeling a beam on soil and subsequently adopting it to model embedded piles (Figure 5.9). Winkler (1867), Hetenyi (1946), Terzaghi (1955) methodologies are based on a series of simplifying assumptions regarding the variation of the subgrade modulus with depth, and that the soil response can be modeled as linearly elastic.

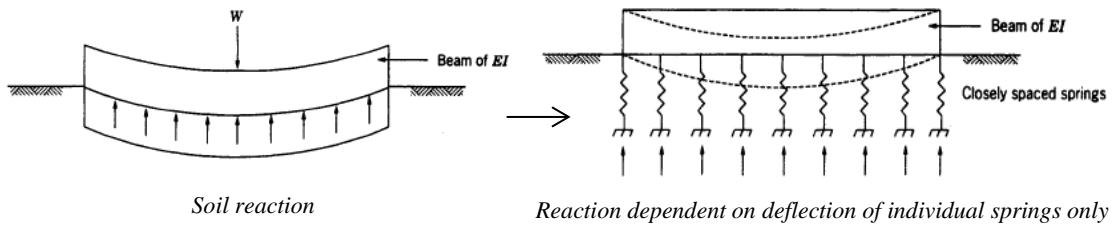


Figure 5.9. Winkler idealization approach

Two issues need to be resolved to obtain the response of a given pile subjected to a lateral load:

- i) The soil resistance must be known as a function of depth, pile deflection, pile geometry, and nature of loading; and
- ii) The equations must be solved that yield pile deflection, bending moment, and shear.

The theory of subgrade reaction that the soil around a laterally loaded pile, can be replaced by a series of discrete springs as shown in Figure 5.10. (Reese and Matlock 1956)

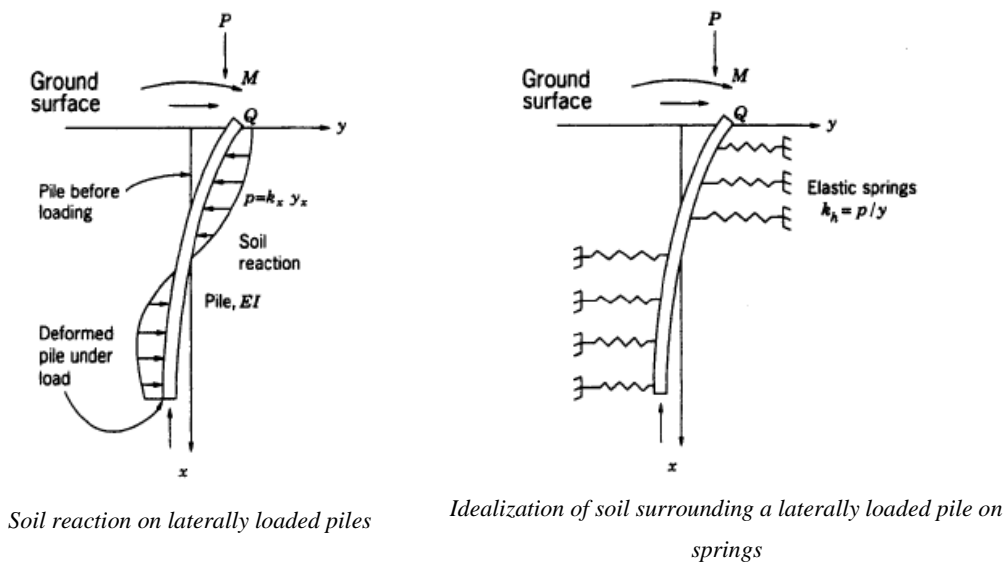


Figure 5.10. Reese and Matlock (1956) approach

In the model, the soil reaction per unit length of pile (p) and corresponding deflection at a point (y) is related by a horizontal modulus of subgrade reaction (k_h) in units force/length²;

$$k_h = \frac{p}{y} \quad (5.5)$$

The stiffness of the spring (or modulus of subgrade reaction) would depend on the modulus of the soil. Early models of this nature could only accept a fixed, linear value for each spring stiffness because of the slow-speed calculators available at that time. However, the soil reaction-deflection relationship for a real soil is nonlinear and Winkler's idealization would require modification.

More recent approaches to design laterally loaded piles, such as by Reese 1977, have introduced the *p-y curves approach*. Soil reaction on laterally loaded piles is modeled as a non-linear spring, which models the highly non-linear nature of soils more accurately.

The behavior of a pile can, thus, be analyzed by using the equation of an elastic beam supported on an elastic foundation and is given by the following equation:

$$EI \frac{d^4y}{dx^4} + p = 0 \quad (5.6)$$

where;

E=modulus elasticity of pile

I=moment of inertia of pile section

Equation 5.6 can be rewritten as follows:

$$\frac{d^4y}{dx^4} + \frac{k_h y}{EI} = 0 \quad (5.7)$$

Solutions to the above equations may be obtained analytically or numerically. Analytical solutions are available only for uniform k_h along pile depth. For over consolidated clays usually this assumption is valid. However k_h is nonlinearly changed with depth in case of cohesionless soils and normally consolidated clays.

The linear variation of k_h , with depth is expressed by the following relationship:

$$k_h = \eta_h x \quad (5.8)$$

where;

η_h = the constant of modulus of subgrade reaction

x = any point along pile
depth

5.4.3. P-y Curve Method

McClelland and Focht (1956) introduced the concept of the *nonlinear* soil resistance deflection curve, “*p-y*” curve, which can be used to obtain depth-varying values of the soil modulus. The concept of a p-y curve can be defined graphically by considering a thin slice of a pile and surrounding soil. The earth pressures, which act against the pile without applying lateral loads, are assumed to be uniform, whereas earth pressure distribution after lateral loading is non-uniform and a net soil reaction will be obtained upon integrating the pressures as shown in Figure 5.11. This process can be repeated in concept for a series of deflections resulting in a series of forces per unit length of pile, which may be combined to form a p-y curve. In a similar manner, p-y curves may be generated for a number of depths.

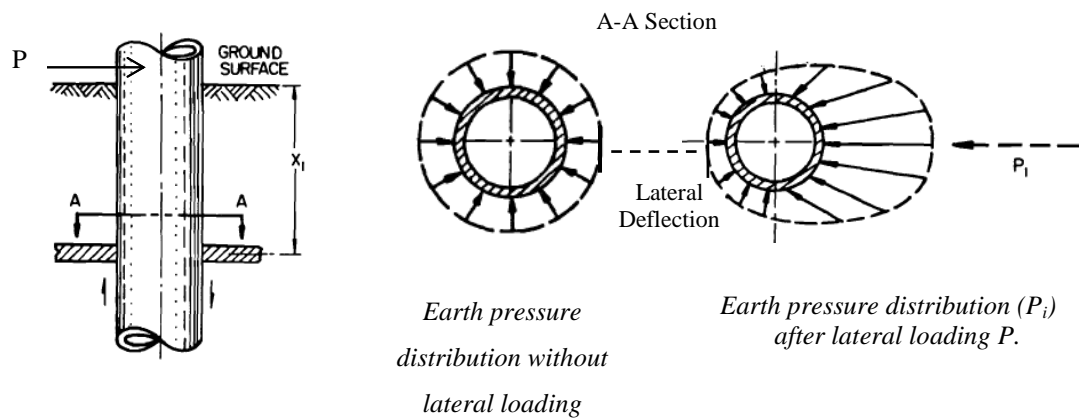


Figure 5.11. Graphical definition of P and Y (Reese and Welch, 1975)

Generally, p-y curves are nonlinear, in which case the modulus of soil response, E_s , can be taken as the secant modulus to a point on the p-y curve as shown in Figure 5.11. The direction which the pile deflects is opposite to the direction of the soil reaction. Characteristic shape of p-y curves is given in Figure 5.12.

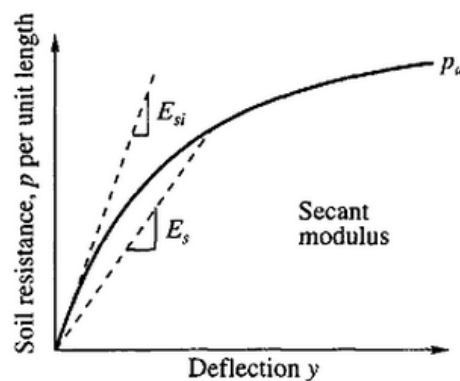


Figure 5.12. Characteristic shape of p-y curves

The soil modulus will vary with deflection and depth, as shown in Figure 5.13; therefore, iterative techniques must be employed to obtain a correct solution to solve Equation 5.7. Typical p-y characteristic shape for sand is given in Figure 5.14.

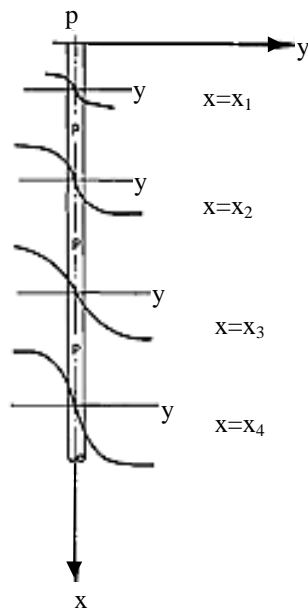


Figure 5.13. Variation of p-y curves with depth
(Reese and Cox, 1968)

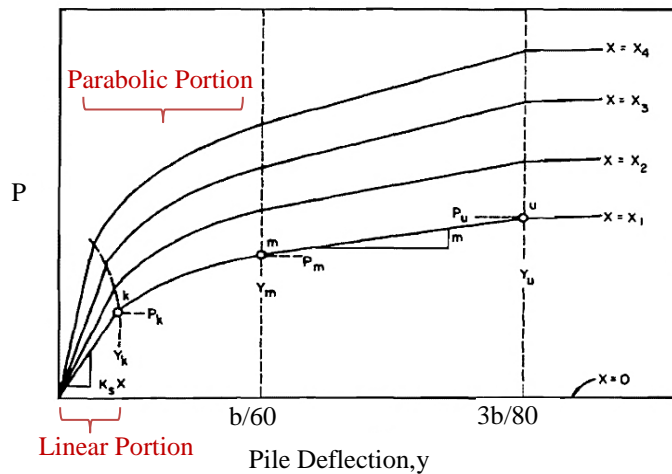


Figure 5.14. p-y curve characteristic shapes in sands
(Reese et al., 1974)

The finite difference method of analysis is very useful in solving the problem of a laterally loaded pile. A solution can be obtained using difference equations when the soil modulus varies with both depth and lateral deflection. The effects of applied axial load and variations in the pile stiffness with depth can also be taken

into consideration (Parker and Cox, 1969). A computer program should be capable of handling the different boundary conditions and should employ an iterative method on account of the nonlinear soil behavior.

5.5. The Application of Subgrade Reaction Approach in Cohesionless Soil

Methods which have been suggested to obtain p-y curves for piles in cohesionless soils are Kubo (1967), Gill and Demars (1970), Parker and Reese (1970) and Reese et al. (1974). Kubo (1967) based on model tests, presented a parabolic equation expressing the variation of the soil resistance with deflection, but a solution for obtaining an ultimate soil resistance as a function of depth was not presented. Parker and Reese (1970) also performed tests on model piles to determine a method suitable for predicting the behavior of full scale piles. Their criteria do not treat, in sufficient detail, the effect of changes in pile width on the deflection at which the ultimate soil resistance is mobilized. Presently, the most widely accepted method for analyzing the behavior of piles in sand is by Reese et al. (1974). The Reese method presents the only published criteria for piles in a cohesionless soil, which takes the effect of cyclic loading into consideration and it will be employed to predict the response of piles which have been tested in a predominately cohesionless media.

5.5.1. Reese et al. (1974) Methodology

Reese et al. (1974), presented procedures for the development of p-y curves for sand on the basis of two field lateral load tests on 24-inch-diameter, 80-foot-long steel pipe piles embedded 69 feet into the ground. The soil at the site of the load tests consisted of a uniformly graded fine sand. This procedure has been incorporated into American Petroleum Institute – Recommended Practice 2A (API RP-2A) for design of offshore pile foundations.

The p-y curves proposed by Reese consist of an initial linear segment for which the unit soil resistance is proportional to the pile deflection, a parabolic segment, a linear segment with positive slope, and a flat segment at the ultimate soil resistance, which is mobilized at relatively large pile deflections. The ultimate resistance is adopted as the lesser of that provided by a passive wedge failure mechanism or a (horizontal) plane strain flow mechanism as postulated by Matlock and Reese (1960). The ultimate resistance, P_u is assumed to be mobilized at pile deflections greater than $3b/80$, where b is the diameter of the pile. At a pile deflection of $b/60$, the unit soil resistance, P_m is equal to an empirically determined fraction of the ultimate soil resistance. The slope of the initial linear segment is characterized by a modulus of subgrade reaction given in tabular form as functions of relative density for sands above and below the water table. The parabolic segment of the p-y curve spans between the initial linear segment and the other linear segment.

The piles may be subjected to either static or cyclic loading. To determine how accurately this method can predict the behavior of laterally loaded piles, it is necessary to compare analytical results obtained by using these criteria with the measured results from load tests.

5.5.2. Method of Obtaining Soil Properties

The constant of subgrade reaction is necessary to establish the initial portion of the p-y curve. In performing the analysis of Reese et. al (1974) approach, the most reasonable assumptions were made in selecting soil properties which are based on Standard Penetration Test, SPT-N results. All of the available information was carefully analyzed, and the best estimate of the in-situ soil properties was made. Relative density of soil is estimated by Bazarra, (1967) method as follows;

$$D_r = \left(\frac{N}{20(1+2\sigma'_v)} \right)^{0.5} \quad \text{for } \sigma'_v \leq 1.5 \text{ kip/ft}^2$$

$$D_r = \left(\frac{N}{20(3.25+0.5\sigma'_v)} \right)^{0.5} \quad \text{for } \sigma'_v > 1.5 \text{ kip/ft}^2 \quad (5.9)$$

where;

N= SPT blow count (blows/ft.)

σ'_v = effective overburden pressure (kips/ft²)

The angle of internal friction was determined from correlations with D_R and effective overburden pressure as shown in Figure 5.12 which is proposed by Touma (1972).

The submerged unit weight was calculated using a degree of saturation, S_r , of 100%, and the total unit weight was calculated using a S_r of 50 %. K_0 is used as 0.4 in the analyses.

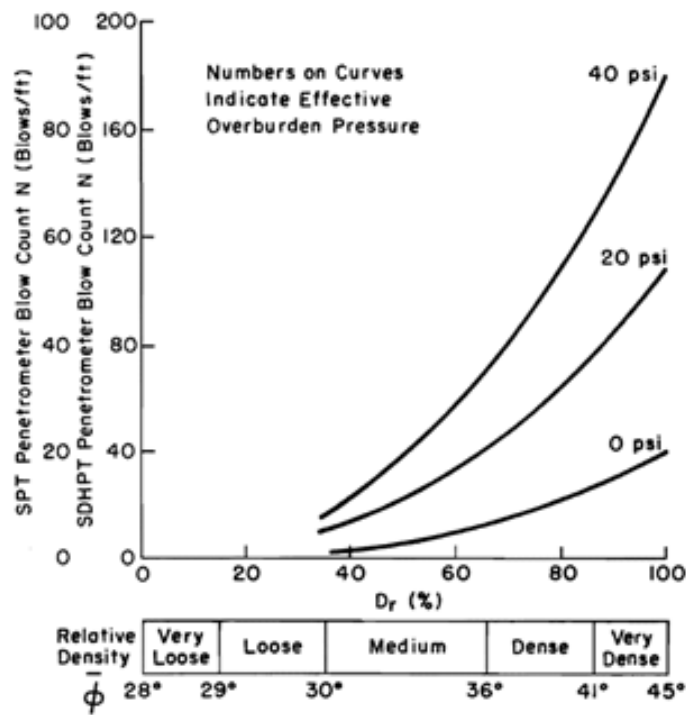


Figure 5.15. Relation between SPT –N values and the friction angle (Touma, 1972)

Values of k , as a function of the general classifications of loose, medium, and dense, have been reported by Reese (1975) and are shown in Table 5.4 for sands below the water table and above the water table. The values of k are also given as a function of D_R , in Figure 5.16.

Table 5.4 Recommended values of subgrade reaction constant k , for sands (Reese et al., 1974)

Relative Density		Loose	Medium	Dense
Recommended k values (lb/in ³)	below water table	20	60	125
	above water table	25	90	225

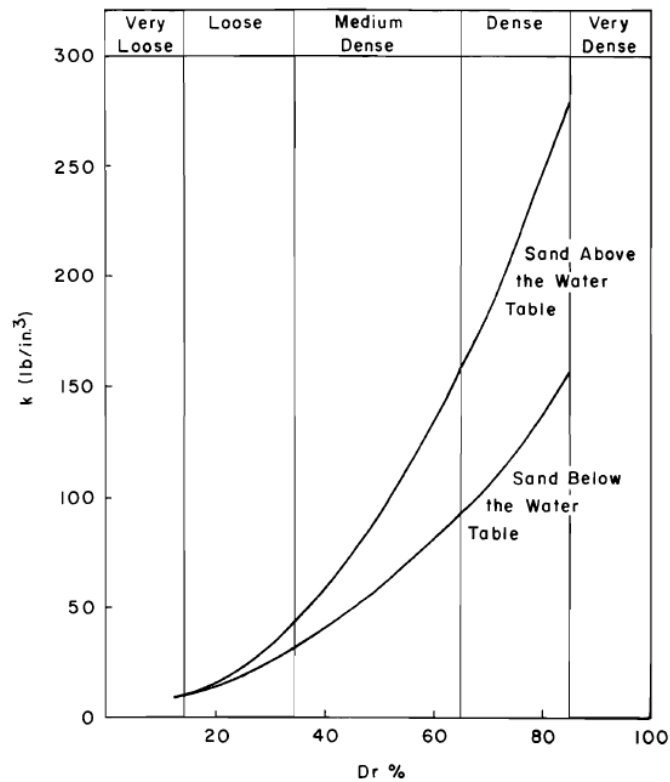


Figure 5.16. Variation of subgrade reaction constant with depth (Reese et al. 1974)

Figure 5.2 and Figure 5.3 show the distribution of pile deflection, δ , moment and shear along the pile length due to a lateral load P , and a moment M , applied at the pile head. In general, the solution for this equation can be expressed by the following variables:

$$\delta = f(z, T, L, k_h, EI, P, M) \quad (5.10)$$

where;

z = depth below ground surface

T = relative stiffness factor

L = pile length

k_h = is the modulus of horizontal subgrade reaction increases linearly with depth

B = pile width

EI = pile stiffness

P = lateral load applied at the pile head

M = the moment applied at the pile head

Elastic behavior can be assumed for small deflections relative to the pile dimensions. For such a behavior, the principle of superposition may be applied. By utilizing the principle of superposition, the effects of lateral load P , on deformation δ_P , and the effect of moment M , on deformation δ_M can be considered separately. Then the total deflection, δ , at depth x can be given by the following:

$$\delta = \delta_P + \delta_M \quad (5.11)$$

where;

$$\frac{\delta_P}{Q_g} = f_1(x, T, L, k_h, EI) \quad (5.12)$$

$$\frac{\delta_M}{M_g} = f_2(x, T, L, k_h, EI) \quad (5.13)$$

f_1 and f_2 are two different functions of the same terms. In equations 5.12 and 5.13 there are six terms and two dimensions; force and length are involved. Therefore, Matlock and Reese (1962) used five independent non-dimensional terms.

Referring to the basic differential Equation 5.5 of beam on elastic foundation and utilizing the principle of superposition,

$$\frac{d^4y}{dx^4} + \frac{k_h \delta_P}{EI} = 0 \quad (5.14)$$

$$\frac{d^4y}{dx^4} + \frac{k_h \delta_M}{EI} = 0 \quad (5.15)$$

Reese and Matlock (1956) obtained the solutions of Equations 5.14 and 5.15 by using finite difference method.

5.5.3. Method of Calculating Non-dimensional Terms

The non-dimensional terms to calculate laterally loaded pile deformation and stresses are defined in Naval Facilities Engineering Command (NAVFAC) “Foundation and Earth Structures Design Manual 7.02, (1986)” as given in Table 5.5.

Table 5.5. Non-dimensional terms of Matlock and Reese, (1962) approach

Deflection coefficient for lateral load, P	$F_{\delta(P)} = \frac{\delta_p EI}{P T^3}$
Deflection coefficient for moment, M	$F_{\delta(M)} = \frac{\delta_M EI}{M T^2}$
Depth coefficient	$\frac{x}{T}$
maximum depth coefficient (short piles: $\frac{L}{T} = 2.0$ medium piles: $\frac{L}{T} = 3.0$ long piles: $\frac{L}{T} = 4.0 - 10.0$)	$\frac{L}{T}$
T is defined as relative stiffness factor in meter	$T = \left(\frac{EI}{f}\right)^5$

f is defined as coefficient of variation of lateral subgrade reaction with depth (defined also as n_h in literature) which depends on soil stiffness as given in Figure 5.17.

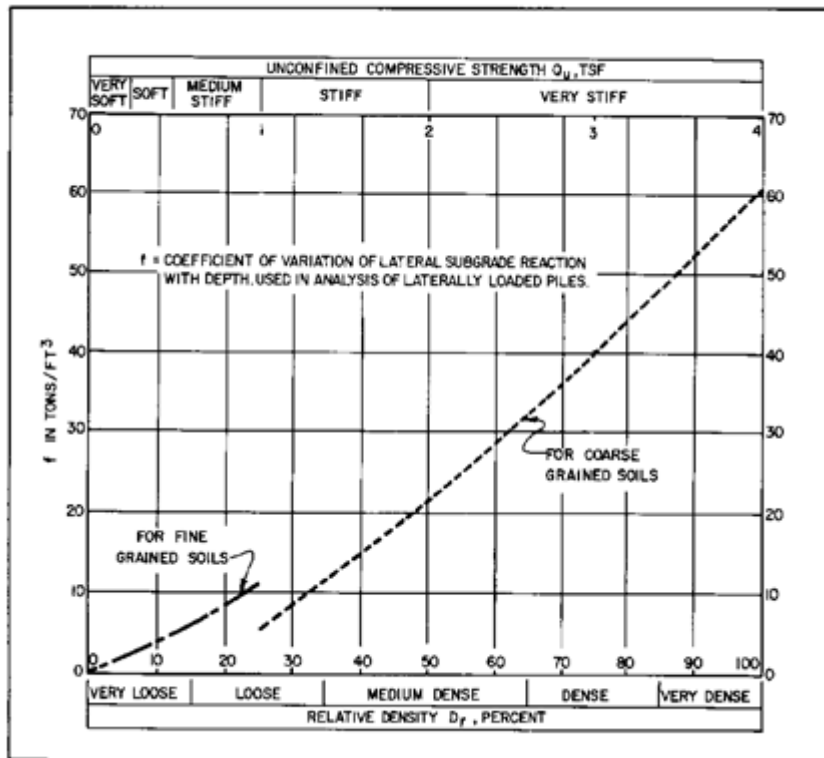


Figure 5.17. Coefficient of variation of subgrade reaction (NAVFAC, 1986)

Reese and Matlock (1956) state that;

“The two basic approaches presented below depend on utilizing the concept of coefficient of lateral subgrade reaction, f ;

- i) It is assumed that for granular soil and normally to slightly over-consolidated cohesive soils; pile deformation can be estimated assuming that the coefficient of subgrade reaction, k_h , increases linearly with depth. For heavily over-consolidated hard cohesive soils, the coefficient of lateral subgrade reaction can be assumed to be constant with depth.
- ii) It is assumed that the lateral load does not exceed about 1/3 of the ultimate lateral load capacity.”

Two principal loading conditions are illustrated with the design procedures in Figure 5.10, using the influence diagrams of Figure 5.18 and Figure 5.19.

CASE 1 defines as *pile with flexible cap or hinged end condition*. The moment and thrust are applied at the top, which is free to rotate. Then, obtain total deflections moment, and shear induced along the pile by algebraic sum of the effects of thrust and moment from the diagrams given in Figure 5.18.

CASE 2 define as *pile with rigid cap fixed against rotation at ground surface*. Thrust is applied at the top, which must maintain a vertical tangent. Then, obtain deflection and moment from influence values of Figure 5.19.

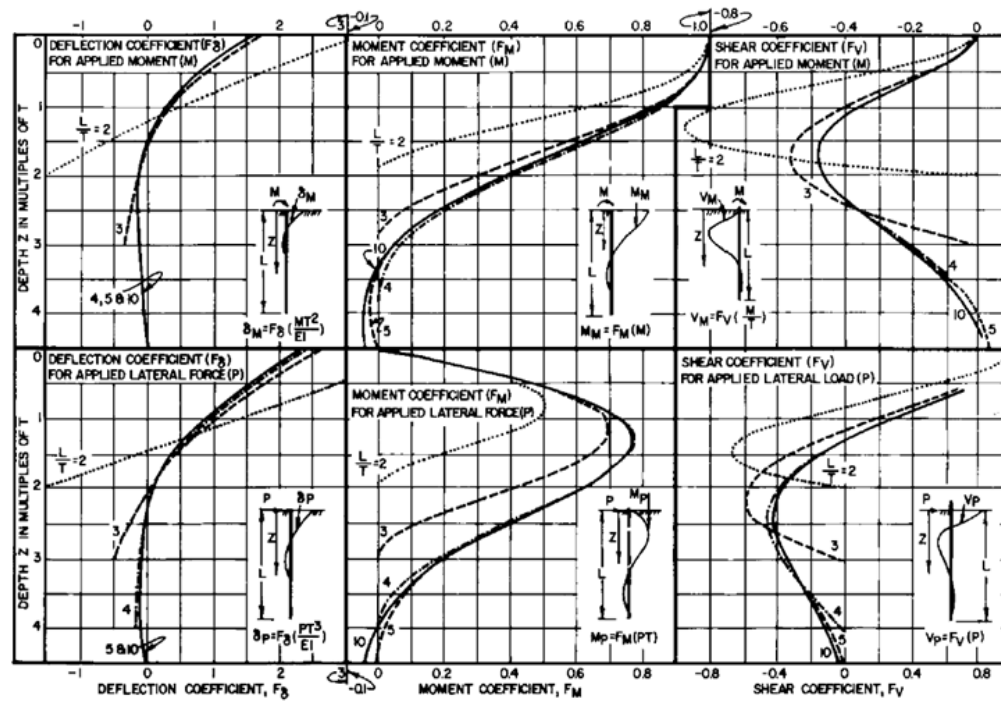


Figure 5.18. Case I: Influence values for laterally loaded pile (NAVFAC, 1986)
(Flexible head or hinged end condition)

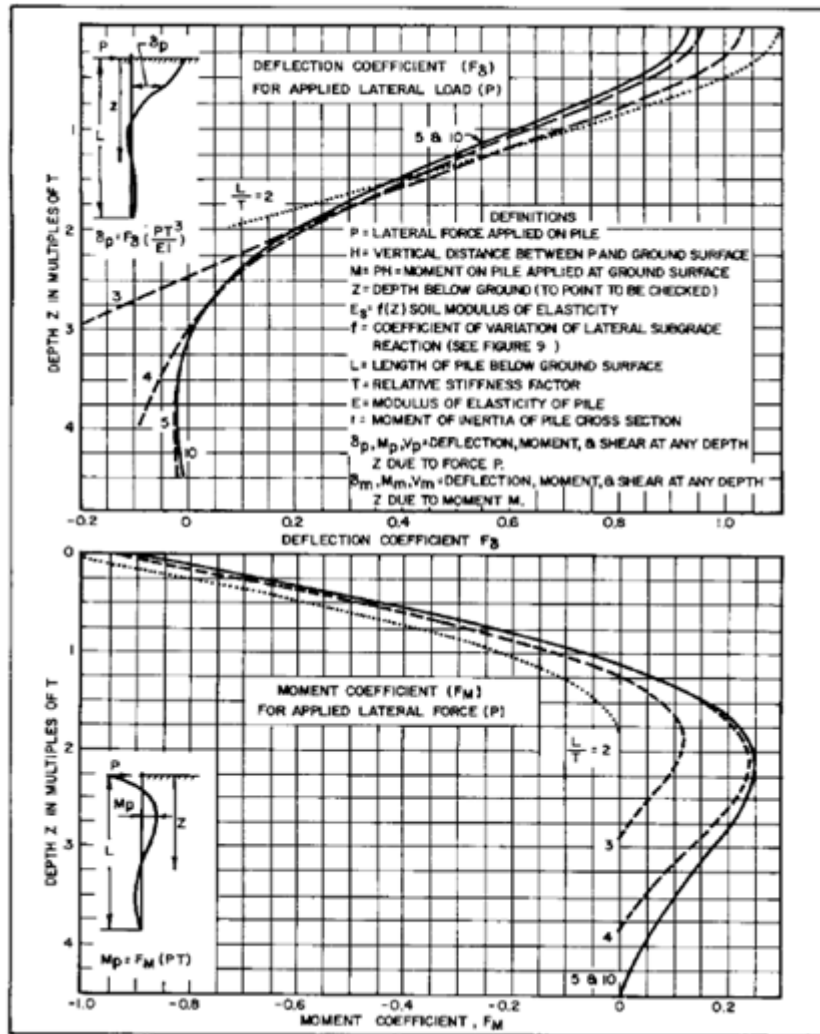


Figure 5.19. Case II: Influence values for laterally loaded pile (NAVFAC, 1986)
(Fixed head against rotation at ground surface condition)

5.5.4. Characteristic Load Method (CLM) (Duncan et al., 1994)

This method is developed by Evans and Duncan (1982), and is based on the results of nonlinear p-y analyses. It was developed by performing nonlinear p-y analyses for a wide range of free-head and fixed-head piles and drilled shafts in clay and in sand, and representing the results in the form of closely approximated relationships among dimensionless variables. The method can be used to determine ground-line deflections due to lateral load and moments applied as well as maximum moment and the location of the maximum moment for free-headed and fixed headed piles. The dimensionless variables are the lateral load divided by a characteristic load, P_c and the applied moment divided by the characteristic moment, M_c . The deflections are divided by the pile width. There are separate design graphs for cohesive soils and cohesionless soils. The use of dimensionless variables makes it possible to represent a wide range of real conditions by means of a single relationship. The dimensionless parameters and graph solution for lateral ground deflections due to lateral load and moments applied at ground line are summarized in Table 5.6.

“Characteristic Load Method is validated with p-y analyses results which are summarized in Table 5.7. The results for clay calculated using the CLM are in close agreement with static p-y results for the soft clay and the stiff clay above water p-y formulations, and the CLM gives a conservative approximation for the static analyses using the stiff clay below water p-y formulation. Moreover, the results for sand calculated using the CLM are in fairly close agreement with the p-y analysis results for both static and cyclic load. The effects of cyclic loading on the p-y results for sand are small, and the CLM approximates the p-y results quite closely. The principal limitation of the CLM is that it is applicable only to piles and drilled shafts that are long enough so that their behavior is not affected to any significant degree by their length. Maximum lengths necessary to satisfy this criterion depend on the relative stiffness of the pile or shaft in relation to the

stiffness of the soil in which it is embedded. Minimum lengths for a number of different conditions are given in Table 5.8” (Duncan et al. (1994).

The method has the following advantages:

1. It can produce quick and simple estimations of the response by incorporating nonlinear soil behavior
2. The results are summarized by non-dimensional graphs that were deduced from numerous p-y analyses.
3. Ground line deflections, maximum moments and the location of the maximum moment can be estimated.

However, the method suffers from the following disadvantages:

1. The soil has to be modeled as a homogeneous layer.
2. The pile must have a constant bending stiffness over the height of the pile
3. The model has a tendency to overestimate the deformations.

Table 5.6. Characteristic Load Method Input Parameters (Duncan et alç 1994)

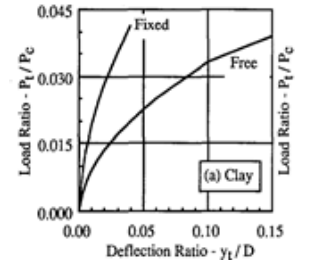
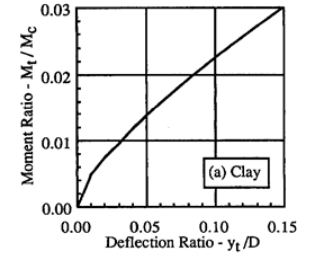
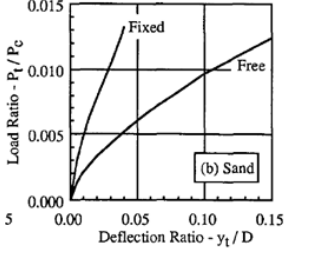
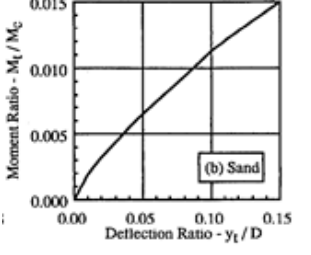
	Characteristic Load, P_c	Characteristic Moment, M_c	Graph Solution for Lateral Load Deflection, y_t at Ground Surface	Deflection y_t Due to Moments Applied at Ground Line
Cohesive Soils	$P_c = 7.34D^2(E_p R_I) \left(\frac{S_u}{E_p R_I} \right)^{0.68}$	$M_c = 3.86D^3(E_p R_I) \left(\frac{S_u}{E_p R_I} \right)^{0.46}$		
Cohesionless Soils	$P_c = 1.57D^2(E_p R_I) \left(\frac{\gamma' D \phi' K_p}{E_p R_I} \right)^{0.57}$	$M_c = 1.33D^2(E_p R_I) \left(\frac{\gamma' D \phi' K_p}{E_p R_I} \right)^{0.40}$		
<p>D = pile or drilled shaft width or diameter (L); E_p = pile or drilled shaft modulus of elasticity (F/L²); R_I = moment of inertia ratio = $\frac{I_{pile}}{I_{circular}}$ S_u = undrained shear strength of clay K_p = Rankine coefficient of passive earth pressure = $\tan^2(45 + \frac{\phi'}{2})$ *Note: S_u, or ϕ' should be averaged over a depth equal to $8D$ below the ground surface.</p>				

Table 5.7. Comparison of Analyses Methods of Characteristic Load and p-y Curves (Duncan et al. 1994)

Method (1)	$P_t = 44.5 \text{ kN (10 kips)}$				$P_t = 89.0 \text{ kN (20 kips)}$			
	y_t		M_{\max}		y_t		M_{\max}	
	mm (2)	in. (3)	kN·m (4)	kip-in. (5)	mm (6)	in. (7)	kN·m (8)	kip-in. (9)
(a) Piles embedded in clay with $S_u = 48 \text{ kPa (1,000 psf)}$								
Characteristic load	6.1	0.24	44	390	20.6	0.81	108	960
p-y, Soft clay, static	5.1	0.20	41	365	21.8	0.86	97	860
p-y, Soft clay, 10,000 cycles	5.1	0.20	41	365	21.8	0.86	97	860
p-y, Stiff clay above water, static	4.3	0.17	40	355	21.3	0.84	101	890
p-y, Stiff clay above water, 100 cycles	5.8	0.23	44	390	37.3	1.47	104	920
p-y, Stiff clay above water, 10,000 cycles	6.9	0.27	47	415	53.6	2.11	105	930
p-y, Stiff clay below water, static	3.8	0.15	39	342	8.6	0.34	84	740
p-y, Stiff clay below water, 100 cycles	Failure indicated	—	Failure indicated	—	Failure indicated	—	Failure indicated	—
(b) Piles embedded in sand with $\phi = 35 \text{ degrees}$								
Characteristic load	5.1	0.20	43	380	13.7	0.54	103	910
p-y, Static	5.1	0.20	44	390	14.0	0.55	105	930
p-y, 100 cycles	5.3	0.21	49	430	15.0	0.59	116	1,030
p-y, 10,000 cycles	5.3	0.21	49	430	15.0	0.59	116	1,030

Table 5.8. Minimum Pile Lengths for CLM Method (Duncan et al., 1994)

Type of soil (1)	Criterion (2)	Minimum length (3)
Clay	$E_p R_t / S_u = 100,000$	6 diameters
Clay	$E_p R_t / S_u = 300,000$	10 diameters
Clay	$E_p R_t / S_u = 1,000,000$	14 diameters
Clay	$E_p R_t / S_u = 3,000,000$	18 diameters
Sand	$E_p R_t / (\gamma' D \phi' K_p) = 10,000$	8 diameters
Sand	$E_p R_t / (\gamma' D \phi' K_p) = 40,000$	11 diameters
Sand	$E_p R_t / (\gamma' D \phi' K_p) = 200,000$	14 diameters

CHAPTER 6

DEVELOPMENT OF SEMI EMPIRICAL MODELS TO ASSESS CYCLIC RESPONSE OF PILED FOUNDATIONS

6.1. Introduction

The response of piles subjected to cyclic lateral loading is governed by the strong nonlinearity of the stress–strain soil behavior that occurs even at low levels of applied load. The problem becomes much more complicated with the appearance of geometric nonlinearities, such as separation of and sliding between pile and soil which is unavoidable under strong excitation.

The methods for lateral pile response assessments are classified into three categories: i) Limit analysis methods: Ultimate soil reaction is predetermined from the assumed deformed shape of the pile at its ultimate state, i.e., after plastic hinge formations (Hansen, 1961; Broms, 1964 a,b), ii) Inelastic continuum-based methods: It is based on boundary-element, finite-element, or finite-difference type numerical formulations (Banerjee and Davies, 1978; Poulos and Davis, 1980), iii) Linear and nonlinear Winkler spring methods: the most successful of which is the p – y method (Matlock, 1970; Reese et al., 1974)

A finite element analysis requires the discretization of the pile and the surrounding soil preferably in three dimensions. Modeling pile–soil separation and gap formation as well as other interface nonlinearities are listed as formidable tasks. In contrast, semi-empirical approaches are simple since the analysis of soil–pile interaction is effectively reduced to a one-dimensional problem.

A brief review of the literature reveals that alteration in pile capacity due to cyclic soil degradation, which is the decrease in stiffness and strength of the soil due to cyclic loading, depends upon the following parameters;

- i) number of loading cycles, and its frequency (cycles per unit time),
- ii) cyclic load level (ratio of cyclic load amplitude to the lateral static ultimate pile capacity),
- iii) cyclic displacement level (ratio of cyclic displacement amplitude applied at the pile head to the external pile diameter),
- iv) excess pore water pressure generated during cyclic loading,
- v) rearrangement of soil particles surrounding the pile surface,
- vi) gradual accumulation of irrecoverable plastic deformations around the pile.

As a result, modulus degradation response and energy dissipation of soils is recognized as an essential part of seismic ground response and also soil structure interaction problems.

Within the confines of this research study, it is intended to modify and improve the original approaches defined in NAVFAC (1986) and Duncan et al. (1994), for the purpose of assessing lateral pile response in liquefiable cohesionless soils. These new semi-empirical approaches are referred to as “*Model I and Model II*” in the remaining sections of this thesis.

Initially, piles were subjected to static lateral loads and the results are compared with the non-dimensional approaches defined in NAVFAC (1986) and Duncan et al. (1994) approaches for calibration purposes. As a second step, when the static lateral load was kept constant, the soil site was subjected to cyclic loading, which may trigger cyclic mobility or full liquefaction. Pile lateral deformation response, as a result of soil degradation and excess pore pressure generation is assessed. Subsequently, the results obtained from numerical analyses are normalized and

probabilistically-based semi-empirical models (Model I and Model II) are obtained to assess cyclic response of piled foundation. Finally, the validity of these simplified frameworks is then confirmed with actual well documented centrifuge model tests.

6.2. Numerical Modeling of Pile Elements in FLAC 7.0 Software

“The pile is a two-dimensional element with 3 degrees of freedom (two displacements and one rotation) at each end node. A pile element segment is treated as a linearly elastic material with no axial yield. However, plastic moments and hinges can be specified. Piles interact with the FLAC grid via shear and normal coupling springs. The coupling springs are nonlinear connectors that transfer forces and motion between the pile elements and the grid at the pile element nodes. The coupling springs associated with FLAC’s pile elements are similar to the load/displacement relations provided by “p-y curves”. However, p-y curves are intended to capture (in a crude way) the interaction of the pile with the whole soil mass, while FLAC’s coupling springs represent the local interaction of the soil and pile elements as shown in Figure 6.1” (FLAC v7.0 Manual).

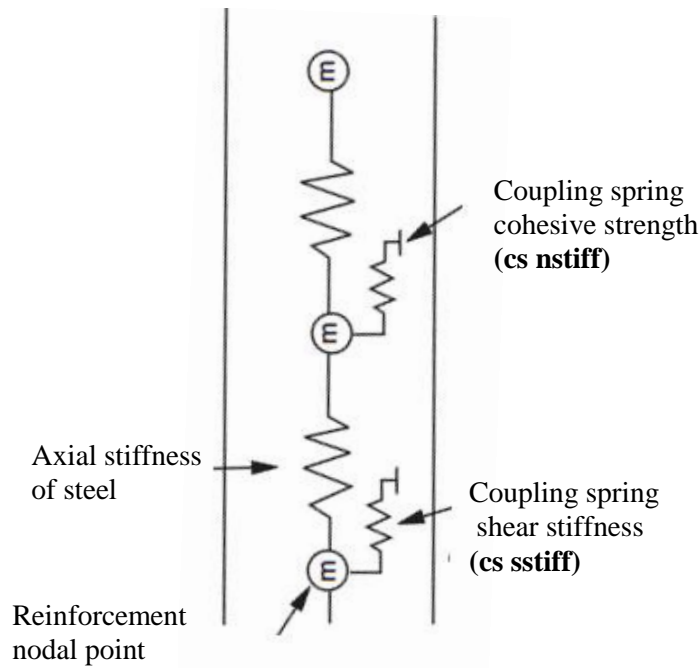
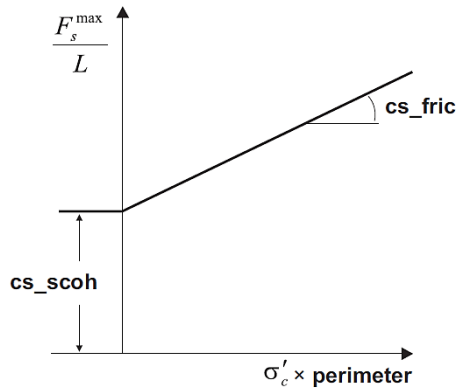


Figure 6.1. Representation of coupling springs on a pile element

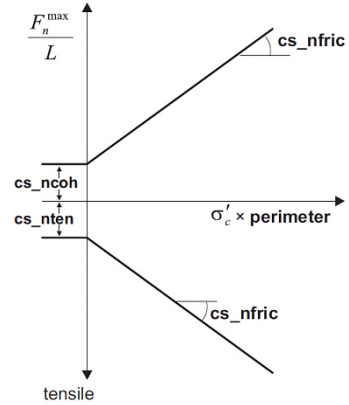
The shear behavior of the interface during relative displacement between the pile nodes and the grid is described numerically by the coupling spring shear stiffness (cs_sstiff) as shown in Figure 6.2. The normal behavior of the pile/grid interface is represented by a linear spring with a limiting normal force that is dependent on the direction of movement of the pile node. The normal behavior during the relative normal displacement between the pile nodes and the grid is described numerically by the coupling spring normal stiffness (cs_nstiff) as shown in Figure 6.2. The values selected for cs_sfric and cs_scoh reflect the roughness of the pile surface.

Shear Coupling Springs

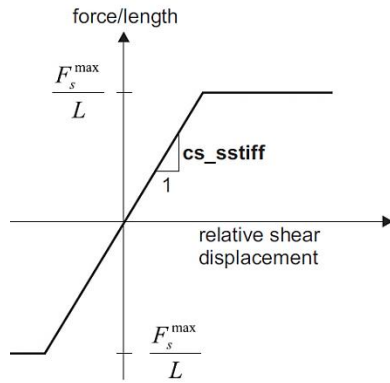


Shear strength criterion

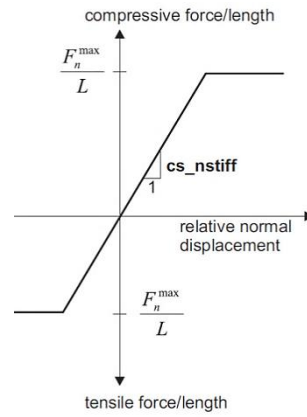
Normal Coupling Springs



Normal strength criterion



Shear force versus displacement



Normal force versus displacement

Figure 6.2. Material behaviors of coupling springs for pile elements (FLAC 7.0 Manual)

where;

F_s^{\max}/L = the maximum shear force that can be developed along the pile/grid interface

cs_{stiff} = coupling spring shear stiffness (cs_sstiff),

cs_{coh} = cohesive strength of the shear coupling spring (cs_scoh),

σ'_c = mean effective confining stress normal to the pile element,

cs_{fric} = friction angle of the shear coupling spring (cs_sfric),

F_n^{\max}/L = the maximum normal force per length of the pile,

cs_{nstiff} = coupling normal shear stiffness (*cs_nstiff*),

cs_{ncoh} = cohesive strength of the normal coupling spring (*cs_ncoh*),

cs_{nfri} = friction angle of the normal coupling spring (*cs_nfri*)

Due to the fact that the pile-soil interactions are very sensitive to coupling normal and shear stiffness's, currently available FLAC 2-D pile element was not used in the assessments. Instead, the pile is defined by four node finite difference elements.

6.3. Numerical Analysis of Laterally Loaded Piles in Static Conditions

For calibration purposes, the numerical analysis results of laterally loaded piles subjected to static loads are compared with the results of non-dimensional approaches defined in NAVFAC (1986) and Duncan et al. (1994) CLM (Characteristic Load Method) .

Piles were modeled in two different ways,

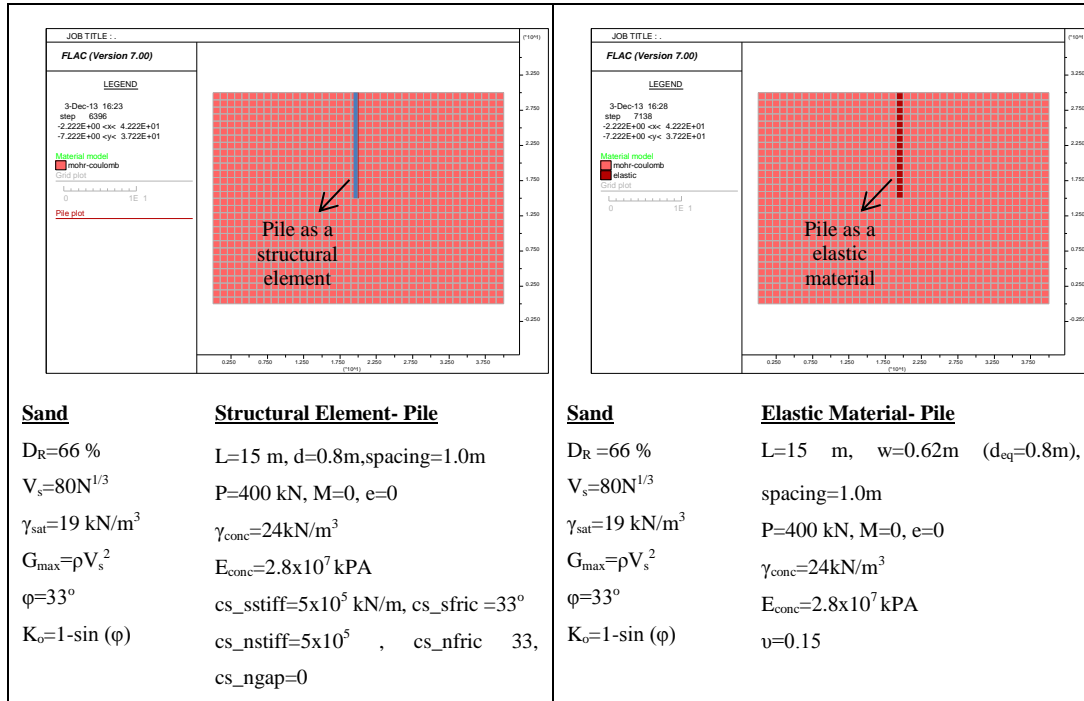
- i) Piles were modeled as two dimensional structural elements, with linearly elastic material response. No yield is possible in the axial direction. Pile elements were composed of segments and each segment is subjected to axial, shear, and bending moments. (*St-1 analyses*)
- ii) Piles were modeled as an elastic material with material properties of reinforced concrete. (*St-2 analyses*)

FLAC models of the two cases are given in Figure 6.3. As an illustration given in Figure 6.4, the soil is selected to be a medium-stiff sand material ($D_R=66\%$) and assumed to behave as elastic-perfectly plastic, with Mohr-Coulomb failure criterion. Friction angle is adopted as 33° , and consistently dilation angle and

tensile strength are assumed to be zero. The bulk and shear moduli are chosen as 233.6 MPa and 89.6 MPa, respectively.

In St-1 analyses, the properties of the coupling springs should be chosen to represent the behavior of the pile/medium interface commensurate with the problem being analyzed. For piles in soil, the pile/soil interaction can be expressed in terms of a shear response along the length of the pile shaft as a result of axial loading (e.g., a friction pile) or in terms of a normal response when the direction of loading is perpendicular to the pile axis. As shown in Figure 6.2 coupling spring parameters of FLAC depend on the relative shear displacement and normal displacement of the piles. However, in many cases, properties needed to characterize the response of pile/soil interaction for piles are not available. Adversely, numerical analyses were performed to assess the response of pile/soil interaction for piles. Hence, the results obtained from the numerical analyses could be off by a factor of 2 if one selects different stiffness parameters for pile-soil interaction response. Another limitation of modeling of structural pile element with FLAC is that coupling spring properties of pile element is defined as *constant values* throughout the pile length. This limitation produced inconsistent and unrealistic results.

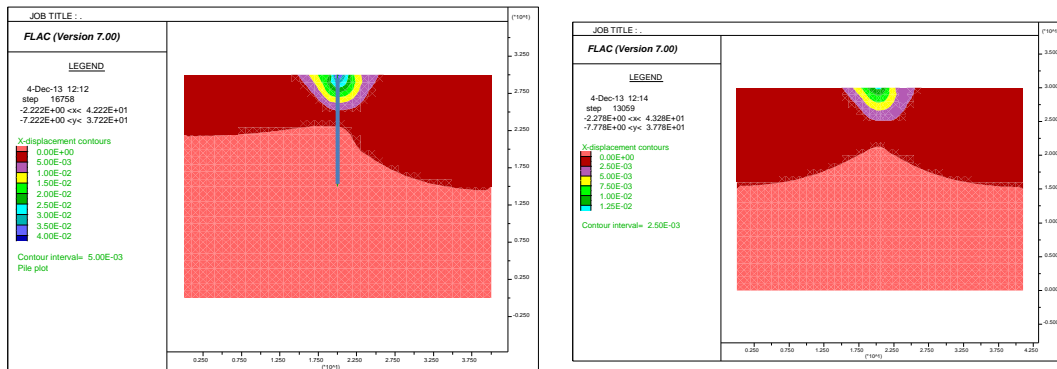
The most suitable values of the coupling spring properties is selected in St-1 analyses and it gives the similar pile response with St-2 analyses results, which directly depends on the soil stiffness as expected (Figure 6.4). Ground deflection obtained from numerical analyses and non-dimensional methods of Duncan CLM and NAVFAC charts, which are consistent with each other, are given in Figure 6.5.



a) St-1 model

b) St-2 model

Figure 6.3. FLAC St-1 and St-2 models of laterally loaded pile



a) St-1 model

b) St-2 model

Figure 6.4. Horizontal displacement contours of FLAC St-1 and St-2 models of laterally loaded piles

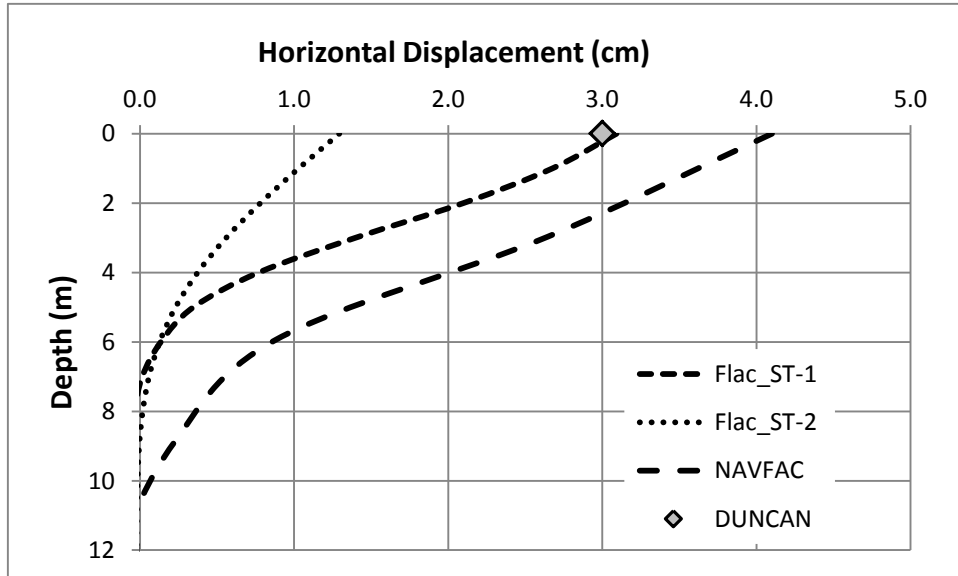


Figure 6.5. Ground deformations estimated by non-dimensional methods and numerical analyses

In order to make a consistent comparison with non-dimensional approaches, elastic modulus is linearly increased without any degradation of soil during FLAC simulations, as recommended by NAVFAC and Duncan CLM methods. Water table is modeled at the ground surface. As shown in Figure 6.6, static numerical analyses are performed for a number of variables given as follows,

- Lateral loads of 150 kN and 400 kN
- Relative density of 42 % and 66 %,
- Free head pile with and without eccentricity,
- Fixed head piles,
- Pile length of 8 m and 20 m,
- Pile diameter of 0.5 m and 1.0 m.

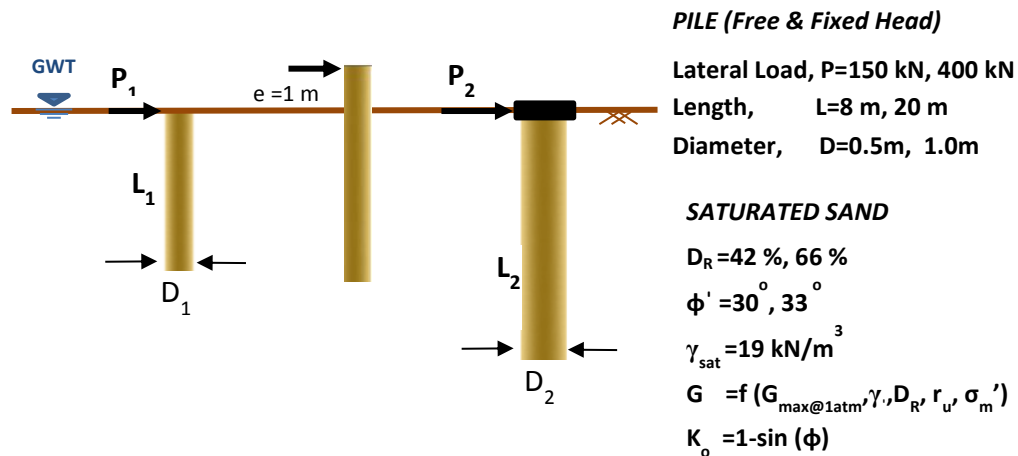
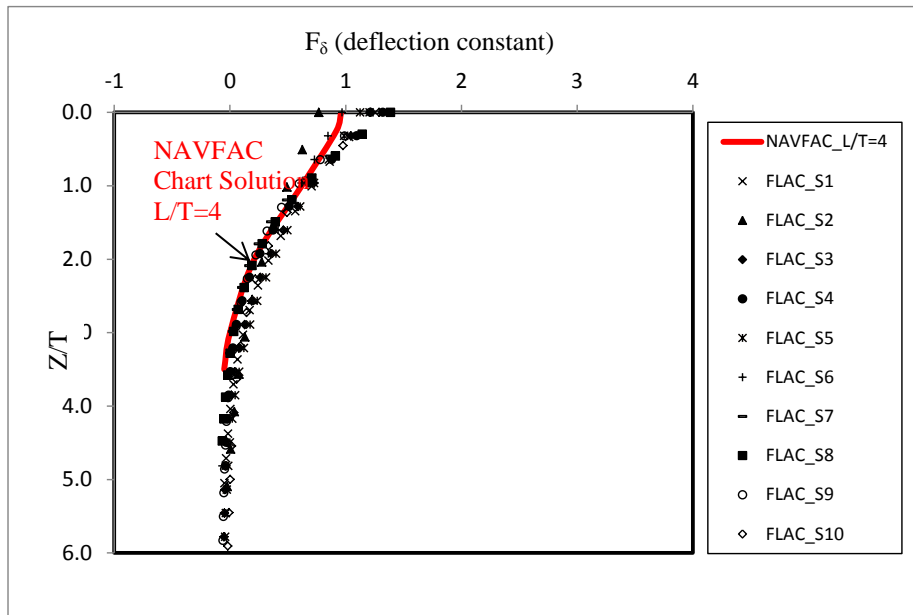


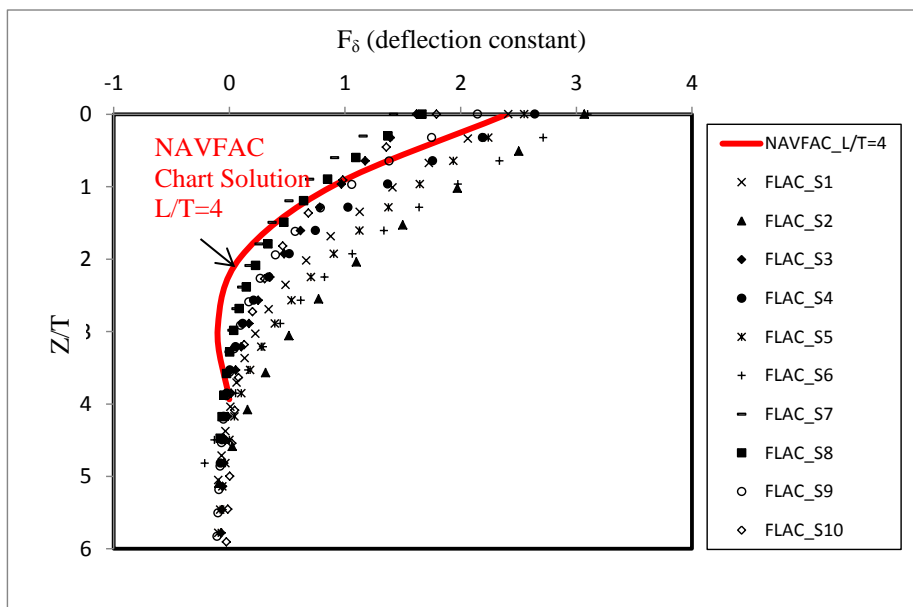
Figure 6.6. Schematic illustration of numerical analysis variables in static loading condition

Figure 6.7 presents static analyses results normalized with NAVFAC (1986) approach, which gives slightly smaller F_δ values, when compared with original NAVFAC chart solutions. The reason is that these analyses were performed with different assumptions. NAVFAC (1986) solution adopted a constant shear modulus with depth, whereas the proposed solution uses effective stress dependent modulus values. Static analyses results normalized with Characteristic Load Method approach are compared with the Duncan et al. (1994) non-dimensional chart solution as given in Figure 6.8 for fixed and free head piles.

As a conclusion, laterally loaded pile response under static loading conditions estimated by empirical methods was successfully compared with numerical analyses results. The model, where piles were modeled as elastic materials (St-2) with the strength and stiffness characteristics of reinforced concrete produced, more robust answer to the problem.

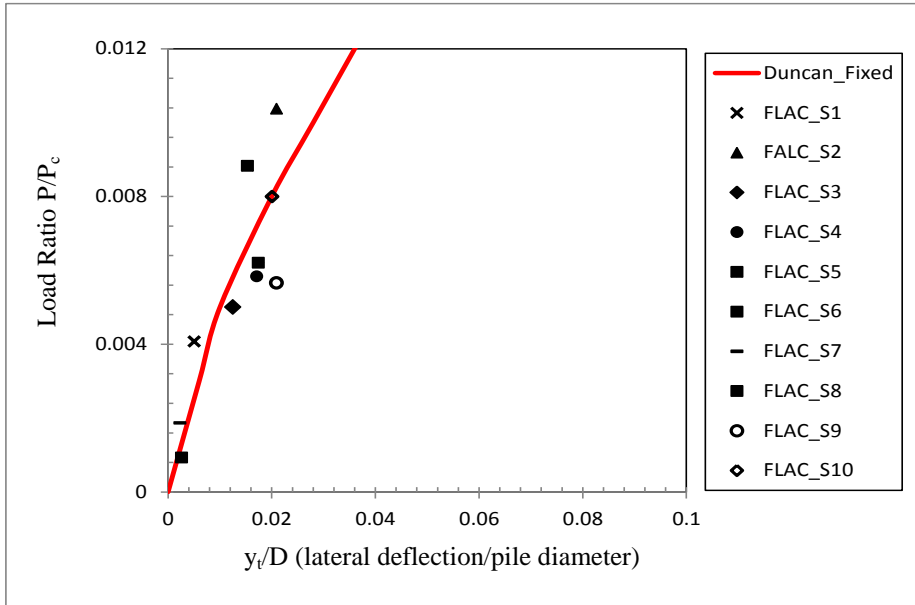


a) Fixed Headed Piles

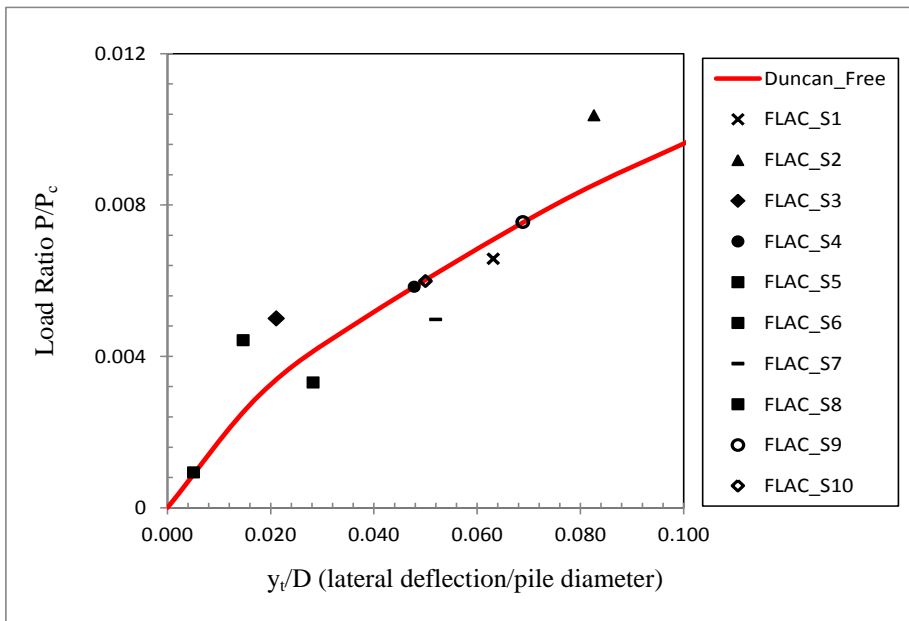


b) Free Headed Piles

Figure 6.7. Comparison of numerical analyses result with NAVFAC (1986) Method in static loading conditions



a) Fixed Headed Piles



b) Free Headed Piles

Figure 6.8. Comparison of numerical analyses result with Duncan et al. (1994), CLM in static loading conditions

6.4. Effective Stress Based Numerical Dynamic Analysis of Laterally Loaded Piles

A maximum likelihood framework for the probabilistic assessment of cyclic response of laterally loaded piles is described in this part of the study.

Series of dynamic analyses were performed to achieve a non-dimensional semi-empirical method to obtain cyclic response of laterally loaded piles in saturated cohesionless soils. Dynamic analyses were performed with semi empirical, effective stress based constitutive model METUSAND implemented in FLAC 2 v.7 software. The advantages of the model are listed below,

- Effective stress dependency in modulus can be reliably assessed
- Strain dependent modulus degradation and increase in damping can be reliably modeled.
- Strain dependent increase in excess pore pressure and in turn decrease in effective stress can be assessed.
- Initial liquefaction response and post liquefaction dilation and contraction responses can be realistically simulated.
- Post liquefaction strength and stiffness, hence deformations can be estimated at large strain levels.

Dynamic analyses were performed for various cases as shown in Figure 6.9 to develop a database, which will establish the basis of non-dimensional semi-empirical approach.

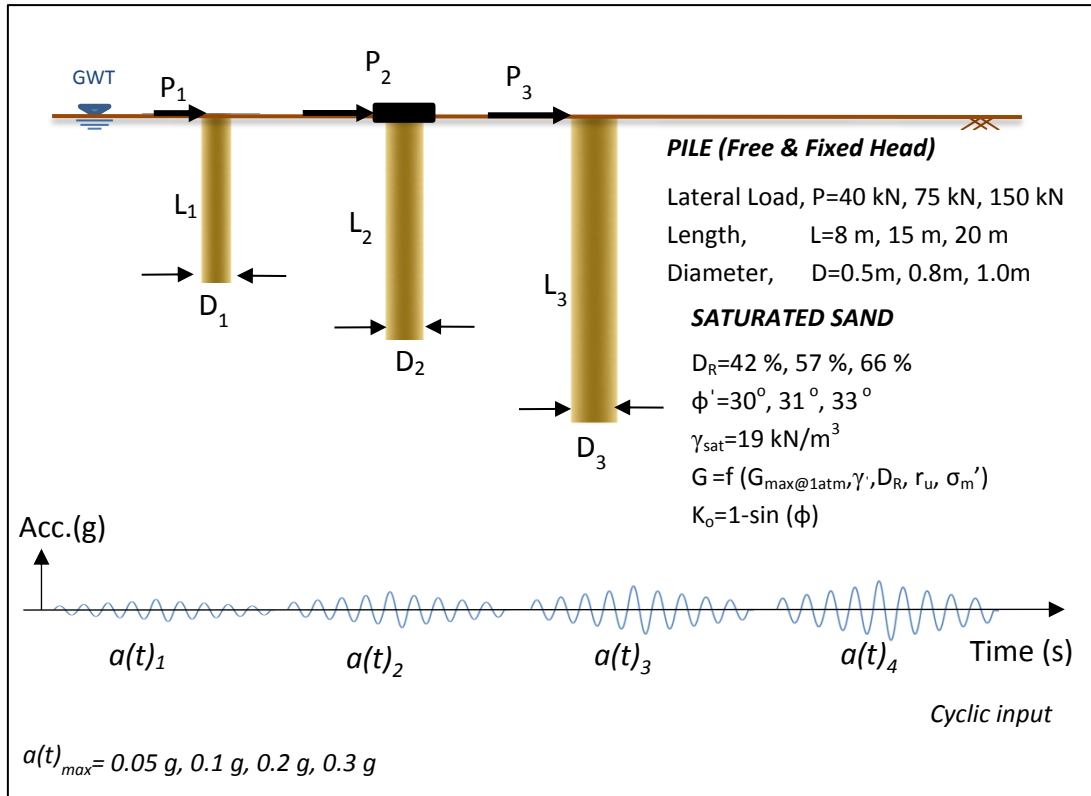


Figure 6.9. Schematic illustration of numerical analysis variables in dynamic condition

Sinusoidal cyclic accelerations with amplitude varying in the range of 0.1g to 0.4g are applied to obtain different levels of excess pore pressure ratio, r_u . Totally 160 analyses were performed by FLAC software by adopting different but realistic combinations of input variables as follows:

- Lateral loads of 40 kN, 75 kN and 150 kN
- SPT-N values of 8, 15 and 20 blows/30 cm,
- Free headed pile without eccentricity
- Fixed headed piles,
- Pile length of 8 m, 15 m and 20 m,
- Pile diameter of 0.5 m, 0.8 m and 1.0 m.
- Excess pore pressure ratio, r_u of 0.2,0.4,0.7 and >0.8

The combinations of the input parameters used for the numerical dynamic analyses are listed in Appendix C.

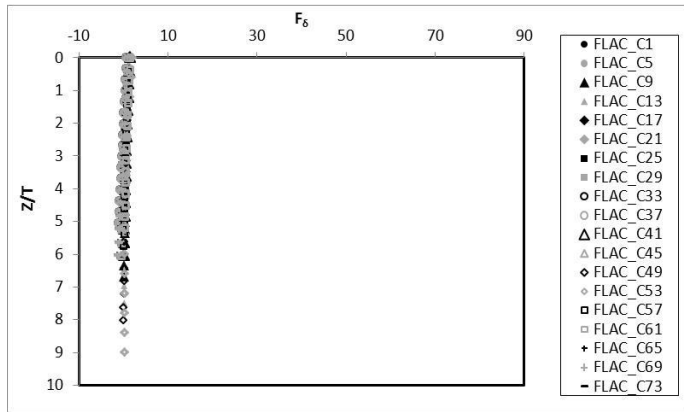
6.5. Development of Semi-Empirical Models to Assess Cyclic Response of Laterally Loaded Piles in Saturated Cohesionless Soils

The next step is the development of semi-empirical models, which can be further used in assessing the effective stress-based dynamic response of laterally loaded piles in liquefied soils. Non-dimensional chart solutions of Reese et.al (1974) and Duncan et. al (1994) given for static lateral loading of piles were modified by considering terms of excess pore pressure ratio, r_u and cyclic shear strain (γ_s) accumulation, responses. The details of these two approaches are discussed in the following sections.

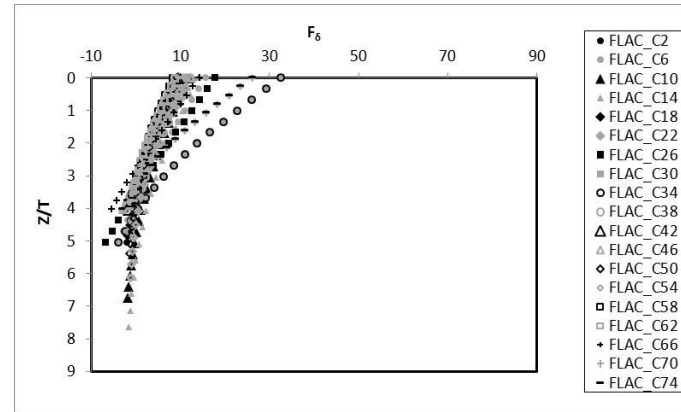
6.5.1. Model I for Dynamic Lateral Loading of Piles in Saturated Cohesionless Soils (Modified NAVFAC, 1986)

The non-dimensional terms to calculate laterally loaded pile deformation and stresses are defined in Naval Facilities Engineering Command (NAVFAC) “*Foundation and Earth Structures Design Manual 7.02, (1986)*” which are based on Reese and Matlock (1956) p-y analyses.

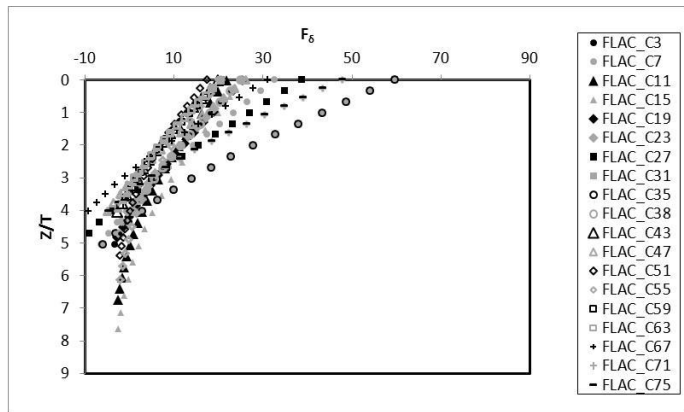
Normalized deflection depth relation, as a result of dynamic analyses is given in Figure 6.10 and Figure 6.11 for free and fixed head piles.



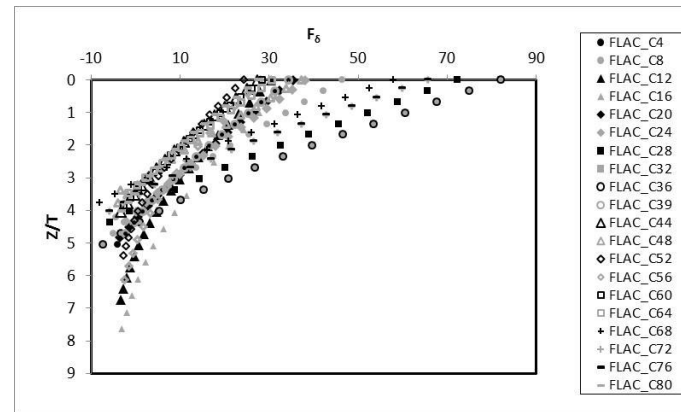
a) $r_u = 0.05-0.10$



b) $r_u = 0.10-0.35$

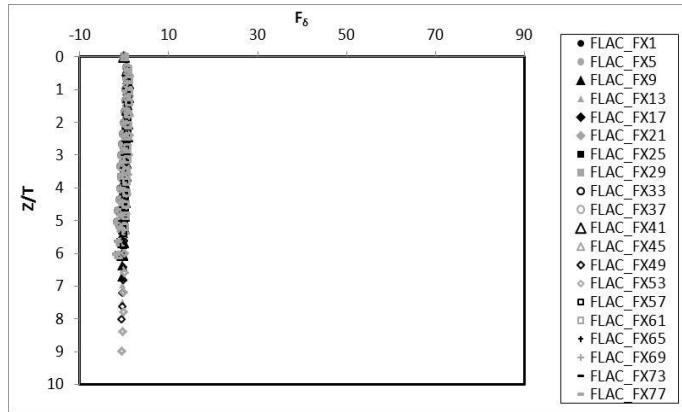


c) $r_u = 0.35-0.65$

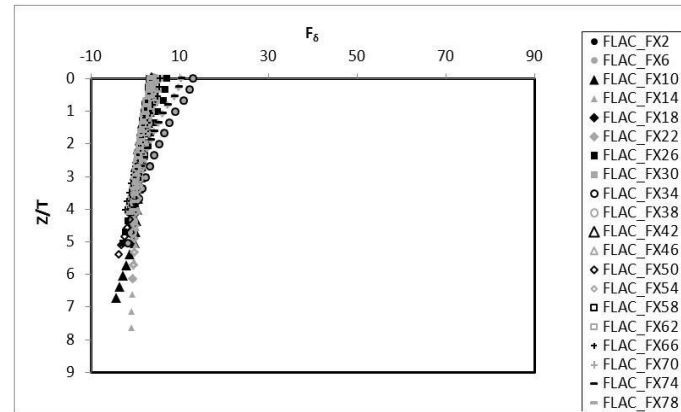


d) $r_u = 0.65-0.80$

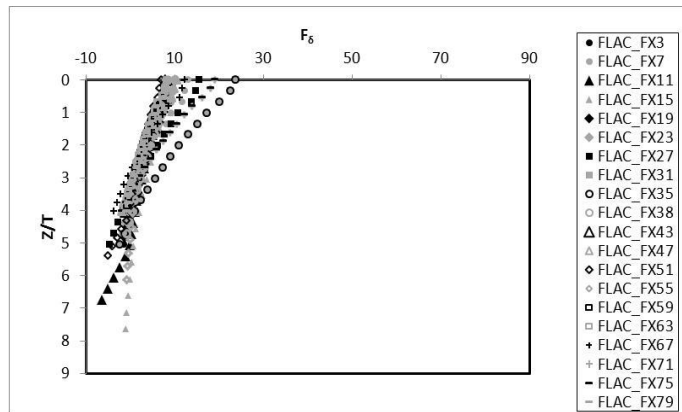
Figure 6.10. Variation of deflection coefficient F_δ in terms of L/T in dynamic analyses for free head piles



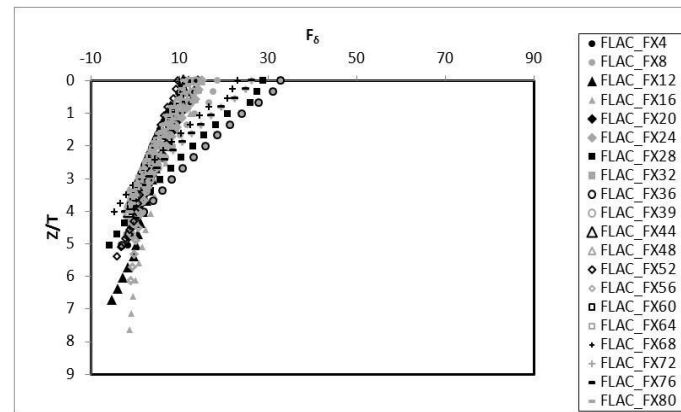
a) $r_u = 0.05-0.10$



b) $r_u = 0.10-0.35$



c) $r_u = 0.35-0.65$



d) $r_u = 0.65-0.80$

Figure 6.11. Variation of deflection coefficient F_δ in terms of L/T in dynamic analyses for fixed head piles

It is observed that F_{δ} values increased with increasing r_u values. With increasing r_u , soil stiffness degrades and initially "long" pile starts to behave as a "short" pile and rotate. Non-dimensional terms basically depend on relative stiffness factor, T and it is clearly seen from Figure 6.10 and Figure 6.11 that T should be modified in terms of soil stiffness to make a reasonable normalization to incorporate dynamic site response and interaction effects.

Coefficient of variation of subgrade reaction, f_{dyn} , depends on the stiffness of the soil, which decreases with increasing excess pore pressure. Passive earth pressure applied on the pile and initial friction angle also decrease, and dynamic coefficient of variation of subgrade reaction, f_{dyn} is defined as given in Equation 6.1,

$$f_{dyn} = f \times (1 - r_u) \times \frac{K_{p,dyn}}{K_p} \quad (6.1)$$

$$\phi_{ru} = (\phi - \phi_{ss}) \times (1 - r_u) + \phi_{ss} \quad (6.2)$$

$$K_{p,dyn} = \tan^2\left(45 + \frac{\phi_{ru}}{2}\right) \quad (6.3)$$

where;

r_u = excess pore pressure ratio

ϕ_{ru} = decreased friction angle in dynamic condition

ϕ_{ss} = steady state friction angle of cohesionless soils (taken as 28°)

$K_{p,dyn}$ = passive earth pressure constant in dynamic conditions

K_p = passive earth pressure constant in static conditions ($=\tan^2\left(45 + \frac{\phi}{2}\right)$)

Coefficient of variation of lateral subgrade reaction, f_{dyn} , values depend on various r_u values and are given in Figure 6.12.

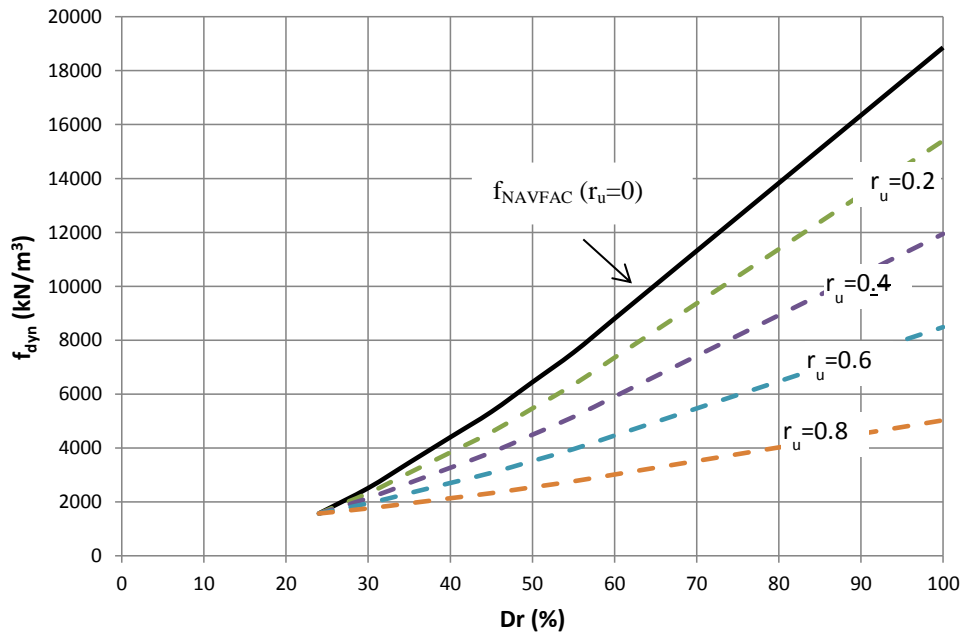


Figure 6.12. Dynamic coefficient of variation of subgrade reaction, f_{dyn} (kN/m^3)

Non-dimensional graphs defined in NAVFAC (1986) are re-normalized with the proposed relative stiffness factor, T_{dyn} . Similarly, dynamic relative stiffness factor is defined as a function of coefficient of variation of subgrade reaction, f_{dyn} as follows,

$$T_{dyn} = \left(\frac{E_{ref} I}{f_{dyn}} \right)^{1/5} \quad (6.4)$$

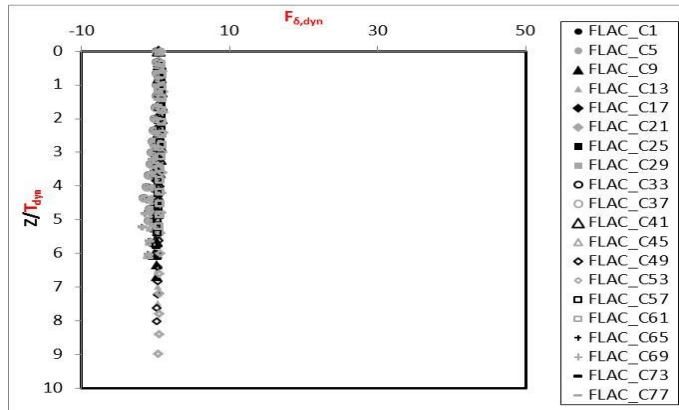
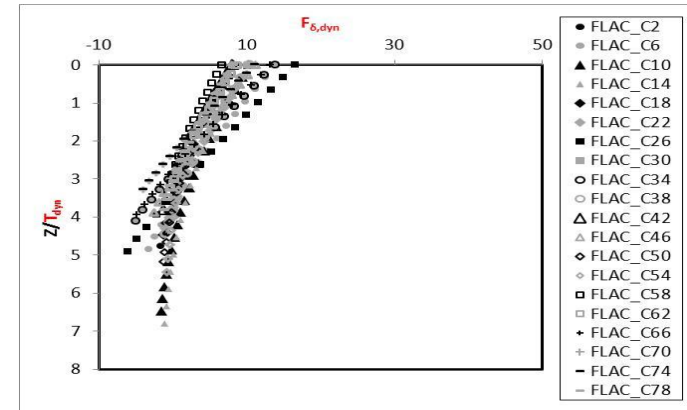
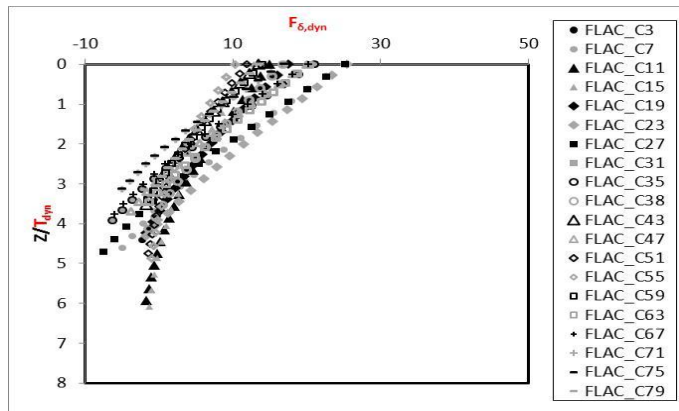
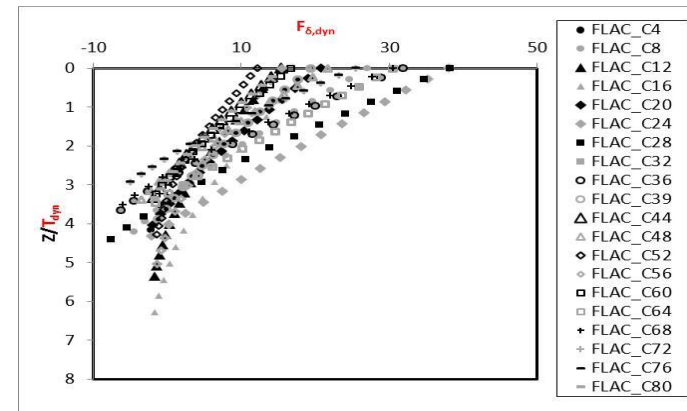
where;

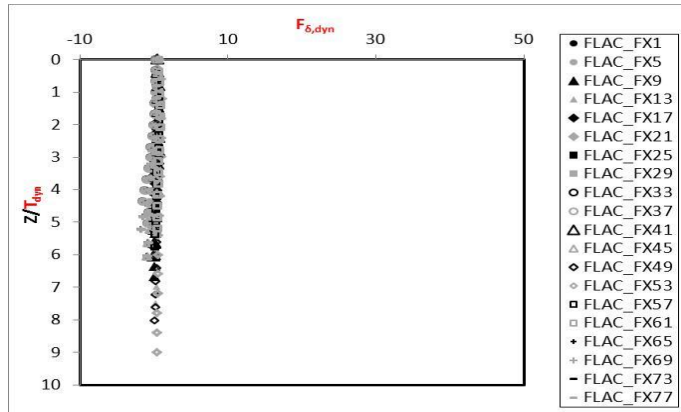
E_{ref} = Elastic modulus of concrete pile, 2.85×10^8 kPa

I = Moment of inertia of pile (m^4)

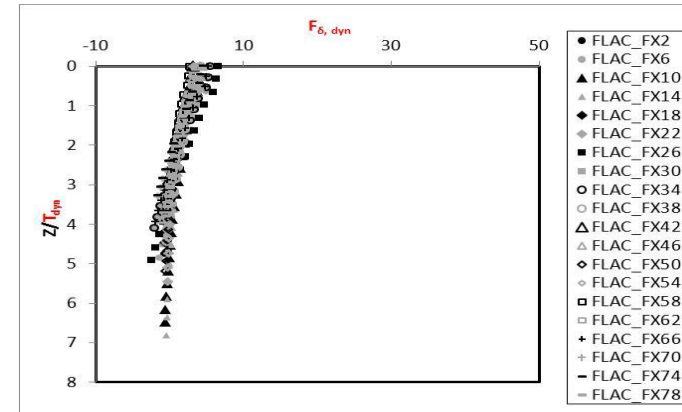
Variation of the lateral deflection constant F_δ in terms of normalized depth obtained by T_{dyn} is given Figure 6.12 and 6.13 for free and fixed head piles respectively. It is clearly understood that r_u values smaller than 0.1 produces similar results with the ones of the static analyses. For $r_u > 0.8$ values, failure occurs as a result of liquefaction and most analyses were not able to be completed

due to extremely large nature of deformations. So, It is assumed that the proposed T_{dyn} is valid within the range of $0.10 < r_u < 0.8$. The range of F_δ is mainly decreases to 10-20 from a value of 10-40 indicating the success of the proposed normalization scheme. Moreover, consistent with the analyses results, maximum depth coefficient L/T (ratio of pile length to relative stiffness factor) is selected as equal or greater than 4 ($L/T_{dyn} \geq 4$), which defines the border to long pile response.

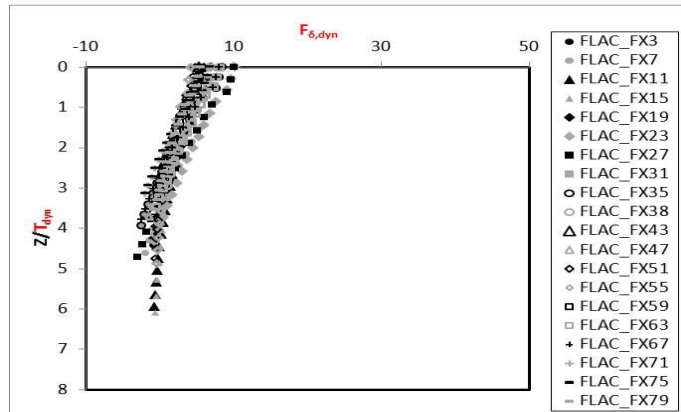
a) $r_u = 0.05-0.10$ b) $r_u = 0.10-0.35$ c) $r_u = 0.35-0.65$ d) $r_u = 0.65-0.80$ Figure 6.13. Variation of deflection coefficient $F_{\delta,dyn}$ in terms of L/T_{dyn} in dynamic analyses for free head piles



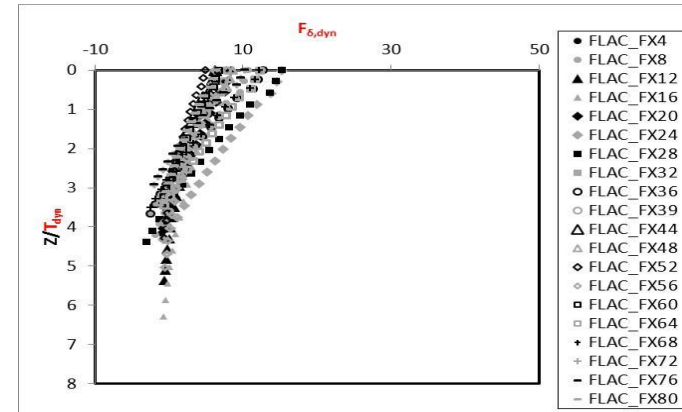
a) $r_u = 0.05-0.10$



b) $r_u = 0.10-0.35$



c) $r_u = 0.35-0.65$



d) $r_u = 0.65-0.80$

Figure 6.14. Variation of deflection coefficient $F_{\delta,dyn}$ in terms of L/T_{dyn} in dynamic analyses for fixed head piles

6.5.1. Maximum Likelihood Framework for the Development of a Semi-Empirical Model: *MODEL I*

Deflection coefficient F_{δ} is expressed by the ratio of pile lateral deflection and pile stiffness corresponding to relative stiffness factor and lateral load applied to the pile head. In this section, a probabilistically based semi-empirical model is proposed for the prediction of F_{δ_dyn} over a very wide range of relative stiffness factor and lateral load, by also considering the effect of excess pore water pressure generation.

As a first step in developing a probabilistic model is to select a limit state expression that captures the essential parameters of the problem. The model for the limit state function has the general form $g = g(x, \Theta)$ where x is a set of descriptive parameters and Θ is the set of unknown model coefficients. Inspired by previous studies and as well as the trends from numerical analyses results, the key components determining the deflection coefficient F_{δ_dyn} are selected as normalized depth (Z/T_{dyn}), excess pore water pressure ratio (r_u) at any loading cycle, maximum depth coefficient (L/T_{dyn}), and lateral load, P , applied to the pile head the following equation is adopted as the limit state function for prediction of F_{δ_dyn} ,

$$g_{F_{\delta,dyn}}(z, T_{dyn}, L, r_u, P, P_{ult}, F_{\delta,dyn}, \Theta) = \ln(F_{\delta,dyn}) - \ln\left[\frac{z}{T_{dyn}} - \left[\theta_1 + \theta_2 \left(\frac{10 - \frac{L}{T_{dyn}}}{4}\right) \frac{L}{T_{dyn}}\right] \left(\frac{z}{T_{dyn}} - \theta_3\right) \left(\frac{\theta_4}{\frac{L}{T_{dyn}}}\right) + (\theta_5(r_u + \theta_{65})x(\ln\left(\frac{P_{ult}}{P}\right) + \theta_7))\right] \pm \varepsilon_{\ln(F_{\delta,dyn})} \quad (6.5)$$

The proposed model includes a random model correction term (ε) to account for the possibilities that i) missing descriptive parameters with influence on modulus degradation may exist, and ii) the adopted mathematical expression may not have the ideal functional form. It is reasonable and also convenient to assume that ε

follows a normal distribution with a mean of zero for the aim of producing an unbiased model (i.e., one that on the average makes correct predictions). The standard deviation of ε , denoted as σ_ε , however is unknown and must be estimated. The set of unknown coefficients of the model, therefore, is $\Theta = (\theta, \sigma_\varepsilon)$.

Assuming that data from simulation results to be statistically independent, the likelihood function for “n” points can be written as the product of possibilities of the observations.

$$L_{F_{\delta,dyn}}(\theta, \sigma_\varepsilon) = \prod_{i=1}^n P \left[F_{\delta,dyn,i} \left(z_i, T_{dyn,i}, L_i, r_{u,i}, P_i, P_{ult,i}, \varepsilon_{F_{\delta,dyn,i}}, \theta \right) = 0 \right] \quad (6.6)$$

Suppose the value of $(r_u)_i$ at the each data point ,is exact, i.e. no measurement error is present, noting that $g(\dots) = \hat{g}(\dots) + \varepsilon_i$ has the normal distribution with mean \hat{g} and standard deviation σ_ε , then the likelihood functions can be written as a function of unknown coefficients as in Equation. 6.7.

In below equation $\varphi[]$ is the standard normal probability density function.

$$L_{F_{\delta,dyn}}(\theta, \sigma_\varepsilon) = \prod_{i=1}^n \varphi \left[\frac{\hat{g}_{F_{\delta,dyn}}(z_i, T_{dyn,i}, L_i, r_{u,i}, P_i, P_{ult,i}, \theta)}{\sigma_{\varepsilon_{F_{\delta,dyn}}}} \right] \quad (6.7)$$

As part of maximum likelihood methodology, the coefficients which are estimated to maximize the likelihood functions given in Equation 6.7 are presented in Table 6.1. The final form of the resulting proposed models are presented in Equation 6.8 along with as one standard deviation of model error.

Table 6.1. MODEL I Parameters

		θ_1	θ_2	θ_3	θ_4	θ_5	θ_6	θ_7	σ_ε
Free Head	Short piles	0.46	0.1	8.05	3.03	1.85	0.03	0.15	0.252
	Long piles	0.35	0.07						
Fixed Head	Short piles	0.6	0.05	9.51	2.57	1.85	0.03	0.15	0.335
	Long piles	0.18	0.02						

$$\ln(F_{\delta,dyn}) = \ln \left[\left(\frac{z}{T_{dyn}} - \left[\theta_1 + \theta_2 \left(\frac{10 - \frac{L}{T_{dyn}}}{4} \right) \right] \frac{L}{T_{dyn}} \right) \left(\frac{z}{T_{dyn}} - \theta_3 \right) \left(\frac{\theta_4}{\frac{L}{T_{dyn}}} \right) + \theta_5 \left((r_u + \theta_6) \times \left(\ln \left(\frac{P_{ult}}{P} \right) + \theta_7 \right) \right) \right] \pm \sigma_{\varepsilon_{F_{\delta,dyn}}} \quad (6.8)$$

Lateral deflection, δ can be defined as,

$$\delta = F_{\delta,dyn} \left(\frac{P (T_{dyn})^3}{E_{ref} I} \right) \cdot c \quad (6.9)$$

where

$$c = \frac{E_{ref}}{E_{pile}} \quad (6.10)$$

E_{ref} =modulus of elasticity of concrete pile, 2.85×10^8 kPa

Figure 6.15 and Figure 6.16 present the normalized lateral deflection data corresponding to normalized depth, for $r_u = 0.25, 0.5$ and 0.75 for free head and fixed head piles respectively. The predicted $F_\delta - Z/T_{dyn}$ pairs are determined by using $L/T_{dyn} = 4$ for short piles and $L/T_{dyn} = 5-10$ for long piles for $P_{ult}/P = 10$.

Predicted and measured F_d values for are paired and shown in Figure 6.16 along with the 1:3 boundaries. Moreover, the differences of predicted and measured F_δ values are shown in Figure 6.17. Pearson's product (R^2), which is a measure of the correlation between compared values, is also calculated as 0.61 and 0.53 for

free and fixed head piles respectively. All of the data pairs fall within the bounds of 1:3 and mostly accumulated along 1:1 line, suggesting an unbiased and accurate model.

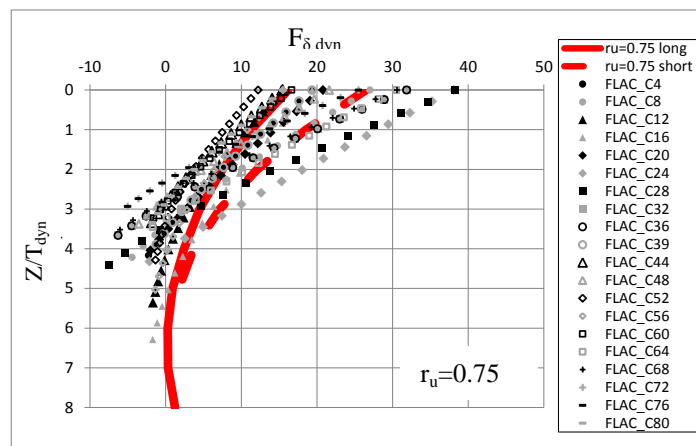
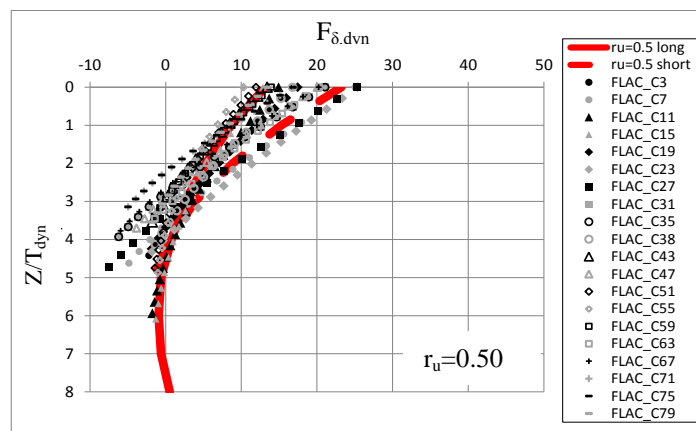
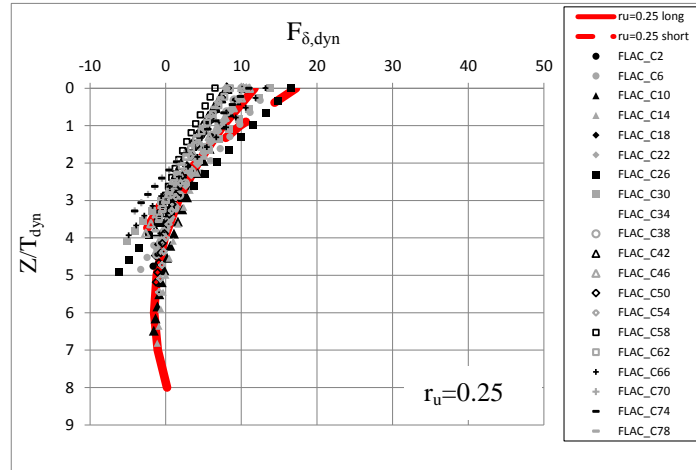


Figure 6.15. Summary of the compiled database in $F_{\delta,dyn}$ vs. L/T_{dyn} domain along with the proposed model for free head piles

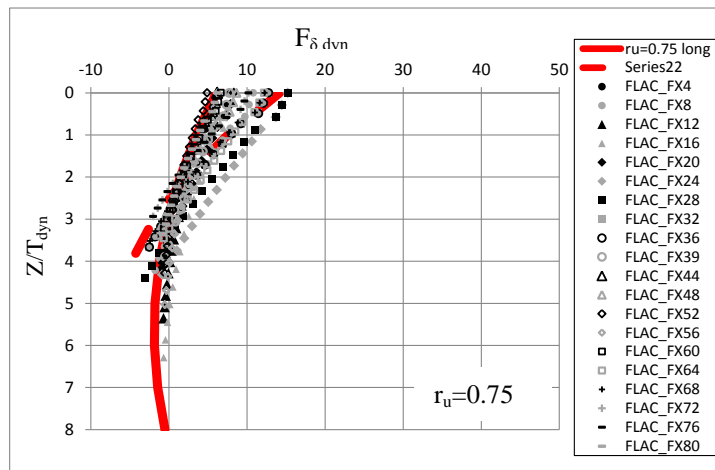
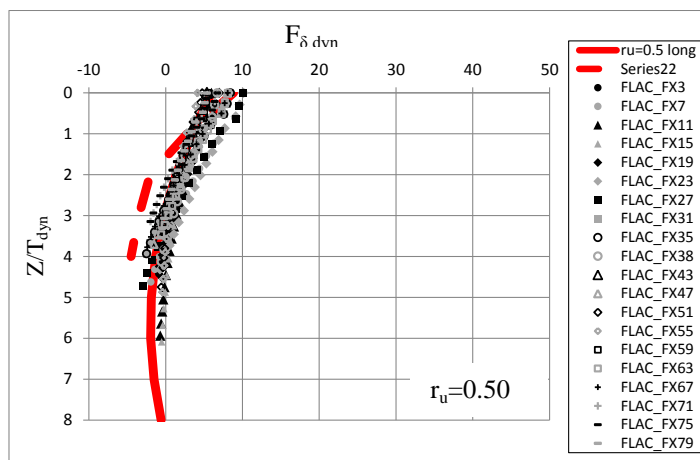
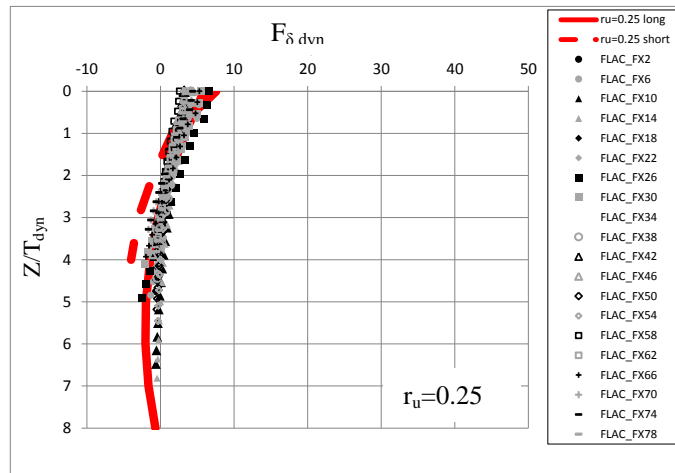
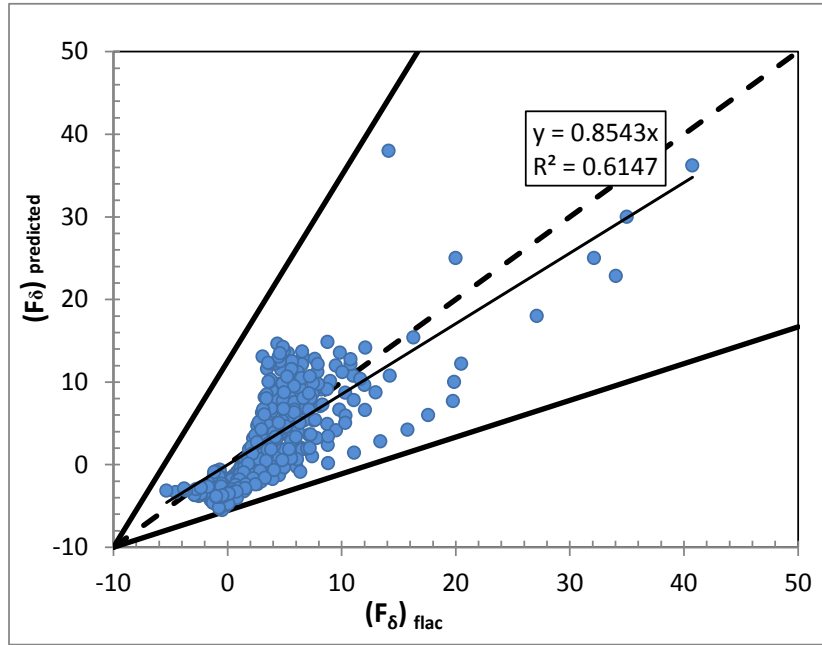
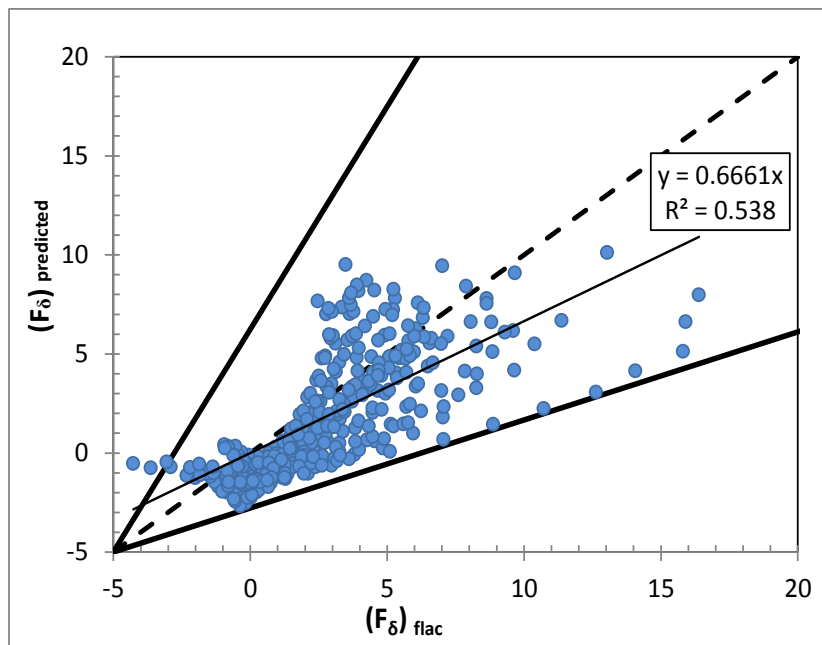


Figure 6 16. Summary of the compiled database in $F_{\delta, dyn}$ vs. L/T_{dyn} domain along with the proposed model for fixed head piles

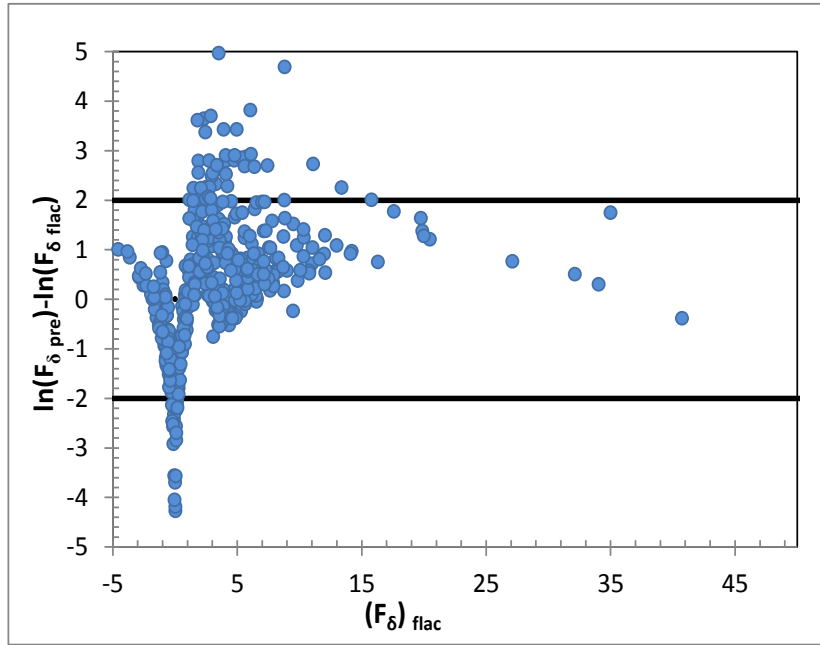


a) Free Head Piles

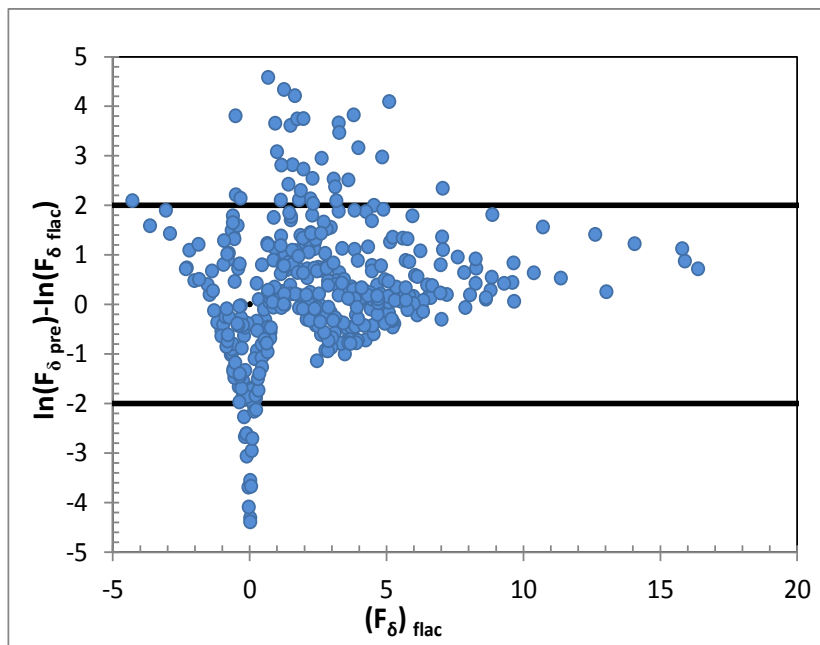


b) Fixed Head Piles

Figure 6.17. Comparison between the measured and predicted $F_{\delta,\text{dyn}}$ values for fixed and free head piles by the proposed methodology



a) Fixed Head Piles



b) Free Head Piles

Figure 6.18. Difference between the measured and predicted $F_{\delta,dyn}$ for fixed and free head piles values by the proposed methodology

6.5.1. Model II for Dynamic Lateral Loading of Piles in Saturated Cohesionless Soils (Modified Duncan et al. 1994)

Duncan et al. (1994) Characteristic Load Method (CLM), which defines approximate relationships among dimensionless variables, was developed on the basis of nonlinear p-y analyses performed for a wide range of free-head and fixed-head.

Characteristic load, P_c , depends on pile diameter D , pile stiffness EI , submerged unit weight, γ' , passive earth pressure constant, K_p , and friction angle, ϕ' of cohesionless soils. Ground deflections obtained from the series of numerical analyses is presented after Duncan normalization in Figure 6.19a and Figure 6.19b for fixed and free headed piles, respectively. It is obvious that characteristic load needs to be modified to obtain dynamic response of laterally loaded piles.

Characteristic load, P_c , is modified for saturated cohesionless soils to consider their excess pore pressure generation potential, and the proposed $P_{c,ru}$ is defined in Equation 6.11.

$$P_{c,ru} = 1.57D^2 (ER_1) \left(\frac{\gamma'_{ru} \times D \times \phi_{ru} \times K_{p,dyn}}{ER_1} \right)^{0.57} \quad (6.11)$$

$$\gamma'_{ru} = \gamma'_{sat} \times (1 - r_u) \quad (6.12)$$

$$\phi_{ru} = (\phi - \phi_{ss}) \times (1 - r_u) + \phi_{ss} \quad (6.13)$$

$$K_{p,dyn} = \tan^2 \left(45 + \frac{\phi_{ru}}{2} \right) \quad (6.14)$$

where;

D = pile diameter

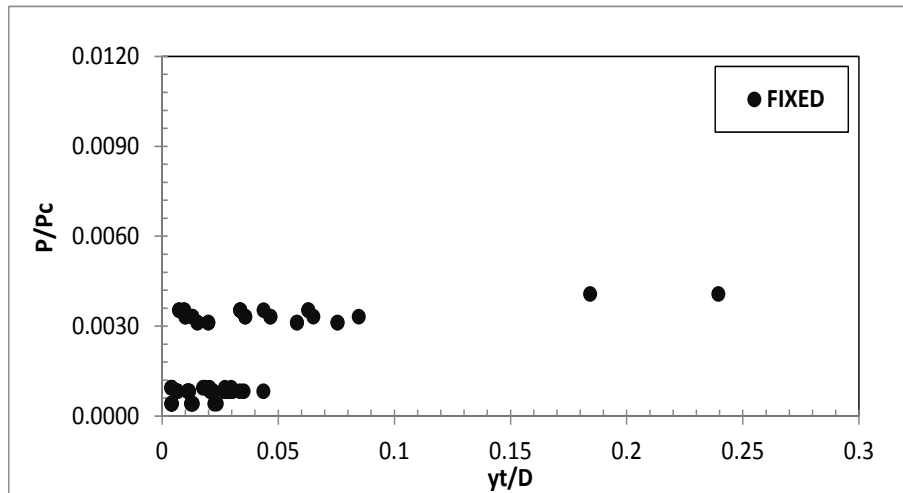
E = Modulus of elasticity pile

R_1 =Moment of inertia ratio ($R_1 = \frac{I_{pile}}{I_{circular}}$)

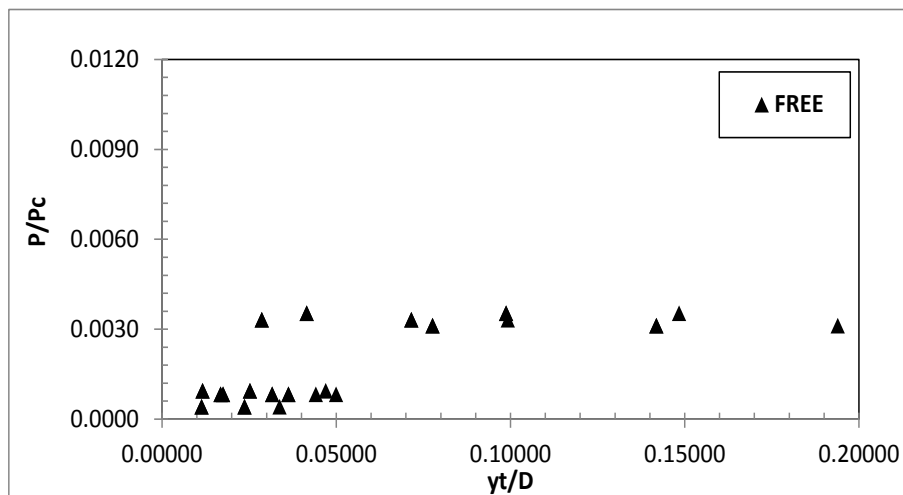
γ'_{ru} = saturated unit weight in dynamic condition

ϕ_{ru} =decreased friction angle in dynamic condition

$K_{p,dyn}$ = passive earth pressure constant in dynamic conditions



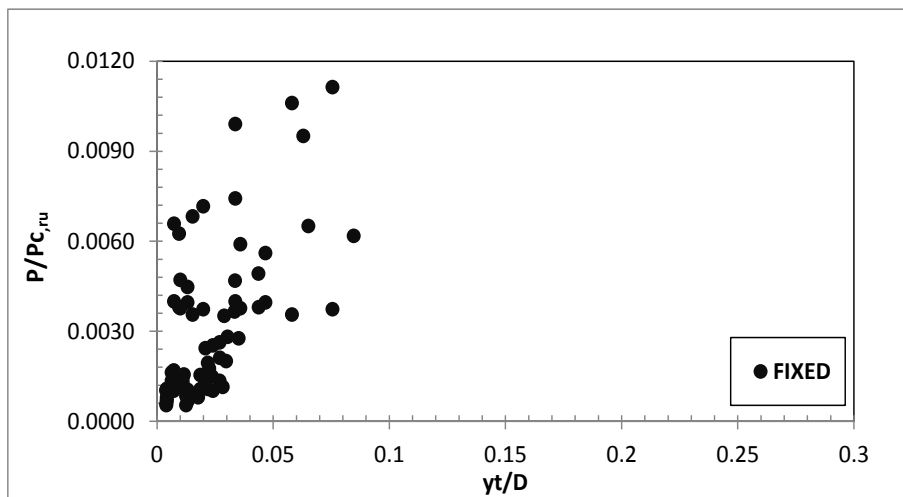
a) Fixed Headed Piles



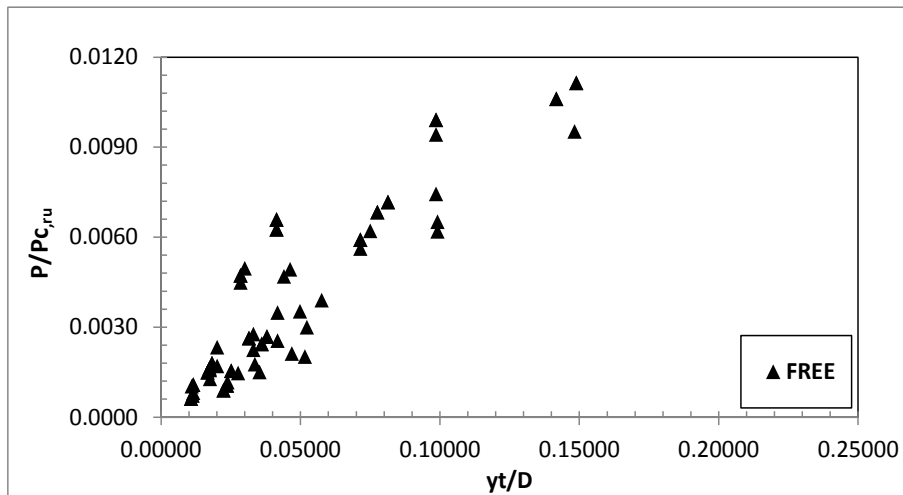
b) Free Headed Piles

Figure 6.19. Dynamic analyses results given in CLM normalized domain

Ground deflections are presented for corresponding load ratio, as shown in Figure 6.20a and Figure 6.20b for fixed and free headed piles respectively. Laterally loaded pile response in liquefiable soils subjected to cyclic loading is affected by the decrease in soil stiffness due to pore water pressure increase and the proposed normalization scheme incorporating the r_u response can capture the observed response better as compared with Figure 6.19.



a)Fixed Headed Piles



b)Free Headed Piles

Figure 6.20. Dynamic analyses results given in modified CLM normalized field

6.5.1. Maximum Likelihood Framework for the Development of a Semi-Empirical Model: *MODEL II*

Characteristic load ratio $P/P_{c,ru}$, is expressed by the ratio of lateral load applied on pile head corresponding to characteristic load $P_{c,ru}$. In this section, a probabilistically-based semi-empirical model is proposed for prediction of $P/P_{c,ru}$ and corresponding lateral deflection ratio y_t/D by considering the effect of excess pore water pressure generation.

The model for the limit state function has the general form $g = g(x, \Theta)$ where x is a set of descriptive parameters and Θ is the set of unknown model coefficients and following equations are adopted as the limit state function for prediction of $P_{c,ru}$ and y_t ,

$$g_{P_{c,ru}}(D, \gamma'_{(ru)}, \phi_{ru}, K_{p,dyn}, P_{c,ru}, \Theta) = \ln(P_{c,ru}) - \ln \left[\theta_1 D^{\theta_2} E_{ref} R_1 \left(\frac{\gamma'_{ru} \times D \times \phi_{ru} \times K_{p,dyn}}{E_{ref} R_1} \right)^{\theta_3} \right] \pm \varepsilon_{\ln(P_{c,ru})} \quad (6.15)$$

$$g_{y_t}(D, P, P_{c,ru}, c, y_t, \Theta) = \ln(y_t) - \ln \left[c \frac{\theta_4 \frac{P}{P_{c,ru}}}{(1 - \theta_5 \frac{P}{P_{c,ru}})} \right] \pm \varepsilon_{\ln(y_t)} \quad (6.16)$$

The proposed model includes a random model correction term (ε) to account for the possibilities that i) missing descriptive parameters with influence on modulus degradation may exist, and ii) the adopted mathematical expression may not have the ideal functional form. It is reasonable and also convenient to assume that ε follows a normal distribution with a mean of zero for the aim of producing an unbiased model (i.e., one that on the average makes correct predictions). The standard deviation of ε , denoted as σ_ε , however is unknown and must be estimated. The set of unknown coefficients of the model, therefore, is $\Theta = (\theta, \sigma_\varepsilon)$.

Assuming the numerical solutions to be statistically independent, the likelihood function for “n” data can be written as the product of possibilities of the observations.

$$L_{P_{c,r_u}}(\theta, \sigma_\varepsilon) = \prod_{i=1}^n P[P_{c,r_u}(D, \gamma'_{ru}, \phi_{ru}, K_{p,dyn}, \theta) = 0] \quad (6.17)$$

$$L_{y_t}(\theta, \sigma_\varepsilon) = \prod_{i=1}^n P[y_t(D, P, P_{c,r_u}, c, \theta) = 0] \quad (6.18)$$

Suppose the value of $(r_u)_i$ at the each data point, is exact, i.e. no measurement error is present, noting that $g(\dots) = \hat{g}(\dots) + \varepsilon_i$ has the normal distribution with mean \hat{g} and standard deviation σ_ε , then the likelihood functions can be written as a function of unknown coefficients as in equation 6.19 and equation 6.20.

In below equation σ_ε is the standard normal probability density function.

$$L_{P_{c,r_u}}(\theta, \sigma_\varepsilon) = \prod_{i=1}^n \varphi \left[\frac{\hat{g}_{P_{c,r_u}}(D, \gamma'_{ru}, \phi_{ru}, K_{p,dyn}, \theta)}{\sigma_{P_{c,r_u}}} \right] \quad (6.19)$$

$$L_{y_t}(\theta, \sigma_\varepsilon) = \prod_{i=1}^n \varphi \left[\frac{\hat{g}_{P_{c,r_u}}(D, P, P_{c,r_u}, c, \theta)}{\sigma_{y_t}} \right] \quad (6.20)$$

As part of maximum likelihood methodology, the coefficients which are estimated to maximize the likelihood functions given in equation 6.15 and equation 6.16 are presented in Table 6.2. The final form of the resulting proposed models are presented in Equations 6.21 and 6.22 along with as one standard deviation of model error.

Table 6.2. MODEL II Parameters

Type	θ_1	θ_2	θ_3	θ_4	θ_5	σ_ε
Fixed Head	2.190	1.255	0.628	5.102	29.020	0.562
Free Head	2.190	1.255	0.628	13.064	19.206	0.318

$$P_{c,ru} = \theta_1 D^{\theta_2} E_{ref} R_1 \left(\frac{Y'_{ru} \times D \times \phi_{ru} \times K_{p,dyn}}{E_{ref} R_1} \right)^{\theta_3} \quad (6.21)$$

$$y_t = c \frac{\theta_4 D \left(\frac{P}{P_{c,ru}} \right)}{\left(1 - \theta_5 \frac{P}{P_{c,ru}} \right)} \pm \sigma_\varepsilon \quad (6.22)$$

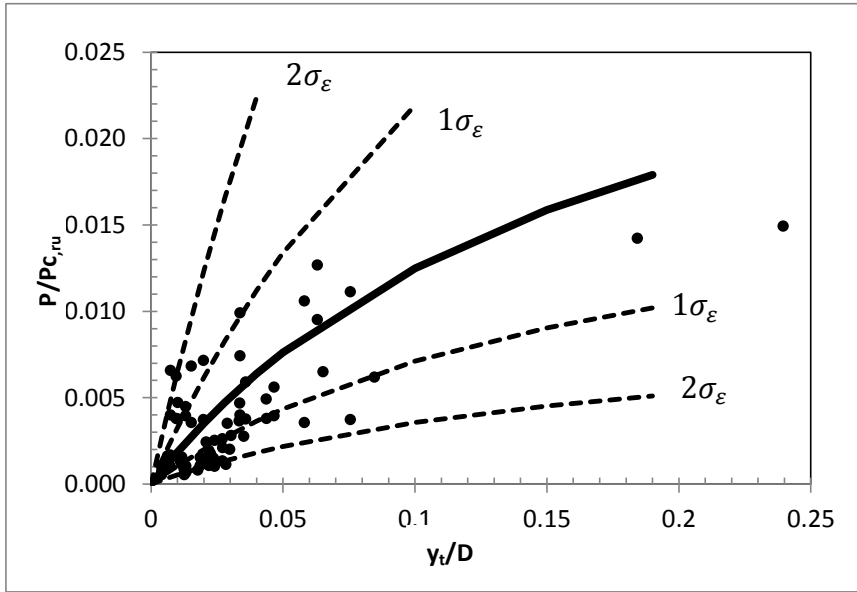
where

$$c = \frac{E_{ref}}{E_{pile}} \quad (6.23)$$

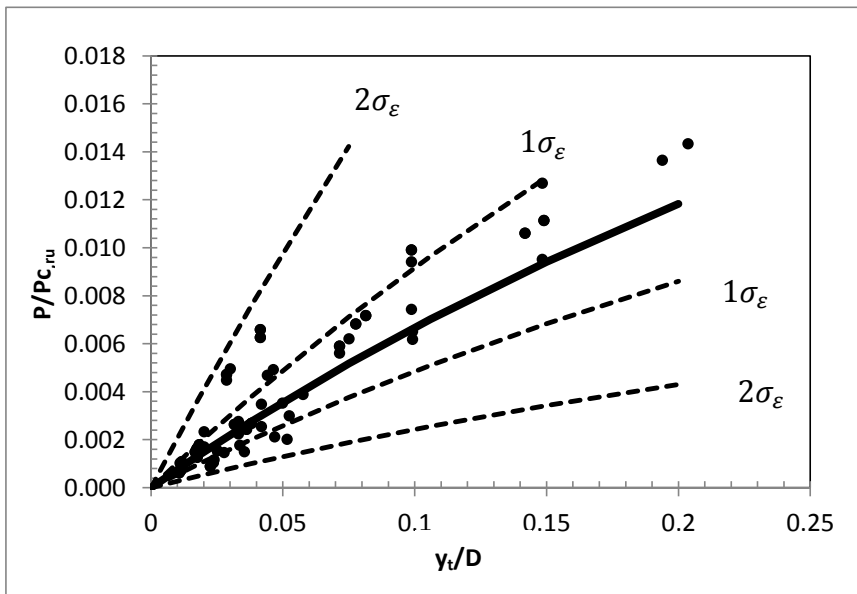
E_{ref} =modulus elasticity of concrete pile= 2.85×10^8 kPa

Figure 6.21 presents the numerical analyses results of lateral ground deflection ratio corresponding to characteristic load ratio. The predicted $y_t/D - P/P_{c,ru}$ pairs are determined and present on the same Figure.

Predicted and measured $P/P_{c,ru}$ values are paired and shown in Figure 6.22 along with the 1:2 boundaries. Moreover, the differences of predicted and measured $P/P_{c,ru}$ values are shown in Figure 6.23. Pearson's product (R^2), which is a measure of the correlation between compared values, is also calculated as 0.52 and 0.87 for fixed and free head piles respectively. All of the data pairs fall within the bounds of 1:2 and mostly accumulated along 1:1 line, suggesting an unbiased and accurate model.

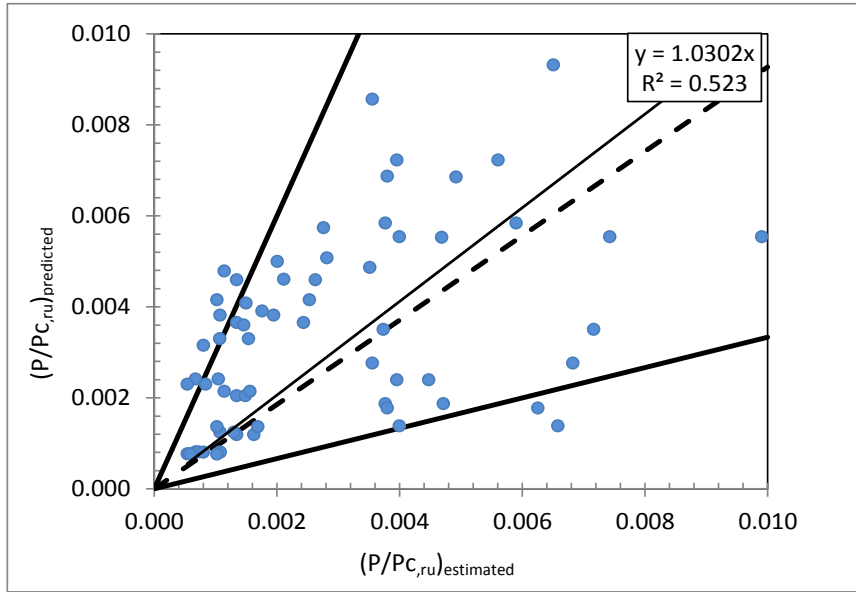


a) Fixed Head Piles

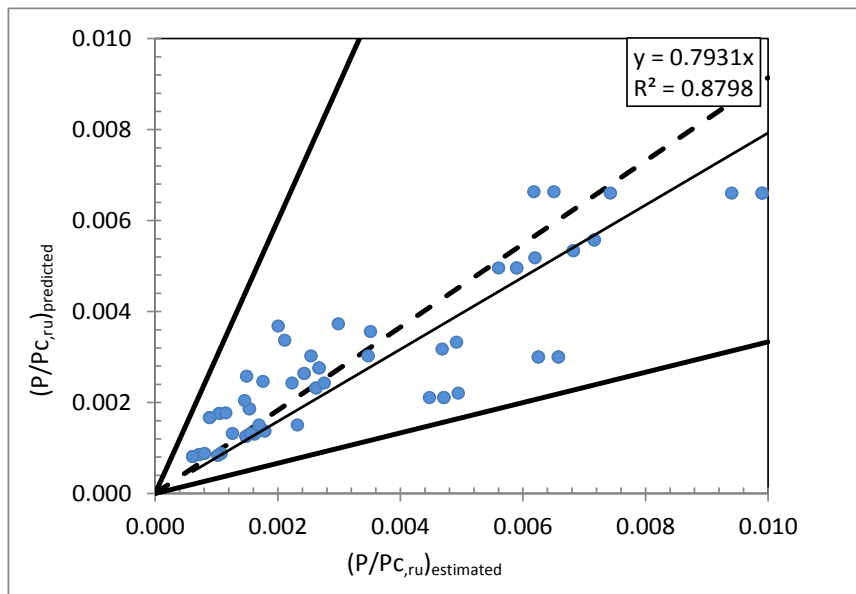


b) Free Head Piles

Figure 6.21. Summary of the compiled database in y_t/D vs. $P/P_{c,ru}$ domain along with the proposed model

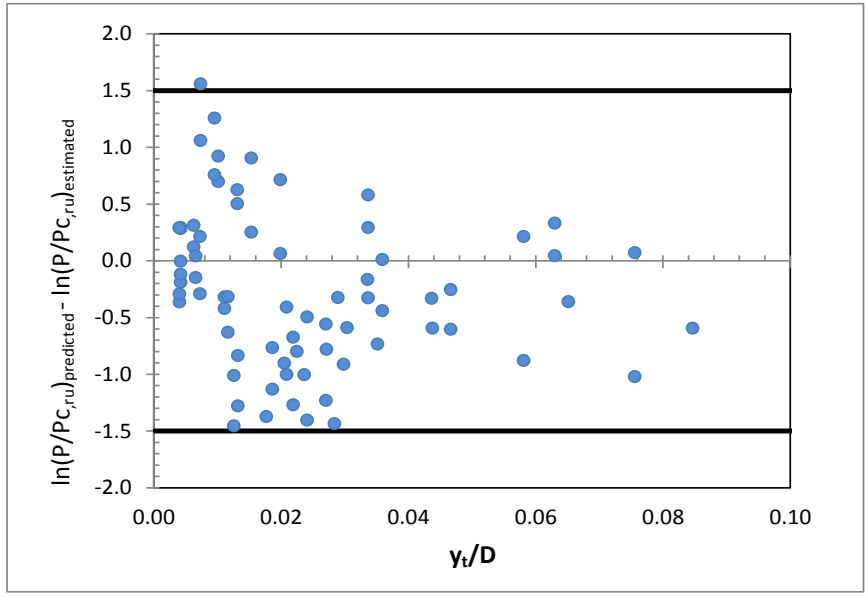


a) Fixed Head Piles

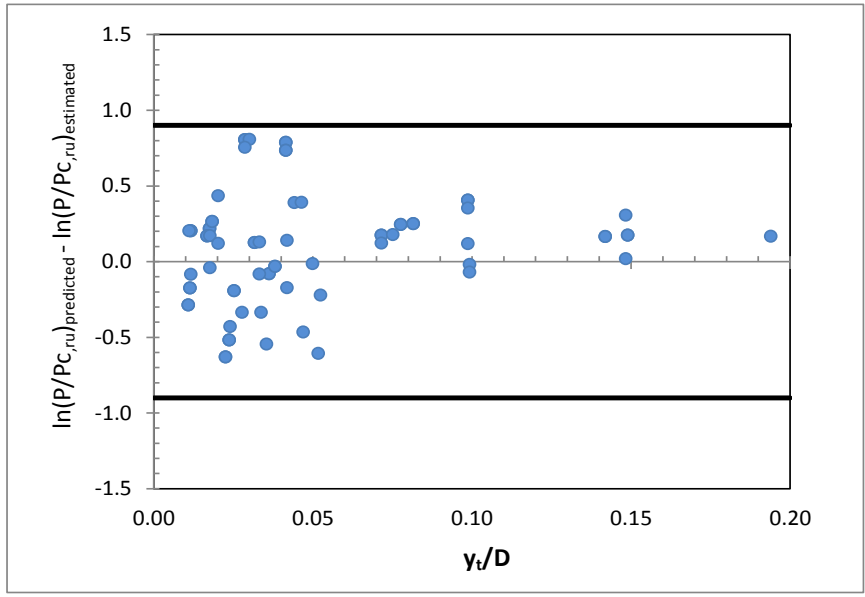


b) Free Head Piles

Figure 6.22. Comparison between the measured and predicted $P/P_{c,ru}$ values for by the proposed methodology



a) Fixed Head Piles



b) Free Head Piles

Figure 6.23. Difference between the measured and predicted $P/P_{c,ru}$ values by the proposed methodology

6.6. Validation of the Semi-Empirical Models through Experimental Investigations

In this section, the proposed model was validated with an actual well documented centrifuge experiments performed to assess the response of piles subjected to lateral loads in liquefiable soils. For this purpose, centrifuge model tests of Abdoun et al. (2003) and Liu et al. (1995), He (2005) and Jakrapiyanun (2002) are compared with the proposed semi-empirical model approaches (Model 1 and Model II). Excess pore pressure response and liquefaction induced ground deformations are presented and discussed in detail.

6.6.1. CASE 1: Validation of the Model with Abdoun et al. (2003)

Study

Abdoun et al. (2003) study presents results of eight centrifuge models of vertical single piles and pile groups subjected to earthquake-induced liquefaction and lateral spreading. Figure 6.24 shows centrifuge pile Model 3, simulating the single piles subjected to earthquake-induced liquefaction and lateral spreading. This experiment was conducted by using the rectangular, flexible-wall laminar box container given in Figure 6.24. In the Model the laminar box and the shaker under it are inclined a few degrees ($\alpha=2^\circ$) to the prototype horizontal direction to simulate an infinite mild slope containing a 6-m-thick prototype layer of liquefiable Nevada sand having a relative density of 40%. A cohesion, $c=5.1$ kPa, and internal friction angle, $\phi=34.5^\circ$, were obtained from the triaxial tests (Abdoun 1997). The prototype single pile is 0.6 m in diameter, 8 m in length, has a bending stiffness, $EI = 8000$ kN-m², and is free at the top. (Dobry et al., 2003). A prototype input accelerogram consisting of 40 sinusoidal cycles of a peak acceleration of 0.3 g was applied to the base (Figure 6.25e).

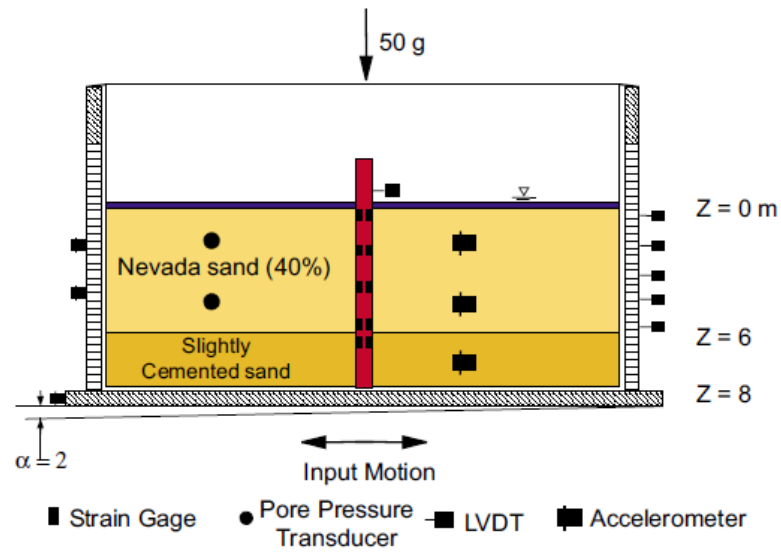


Figure 6.24. Setup of centrifuge model 3 (Abdoun 1997)

The particular results of Model 3 centrifuge test are reported by Abdoun (1997) as follows;

- i) Top layer was liquefied in a couple of cycles and induced a permanent lateral ground surface displacement in the free field of about 0.8 m (Figure 6.25a).
- ii) The pile head displacement (Fig. 6.25b) first increased to a value reaching to a maximum of 27 cm and then decreased to a final permanent value of 15cm.
- iii) The maximum pile bending moment is increased to 110 kN.m at $z = 5.75$ m (Figure 6.25c).
- iv) The pore pressure first increased rapidly and then more slowly. Excess pore pressure ratio reaches to 0.85 (liquefaction occurs) when the pile head deflection reaches to maximum value (Figure 6.25d).

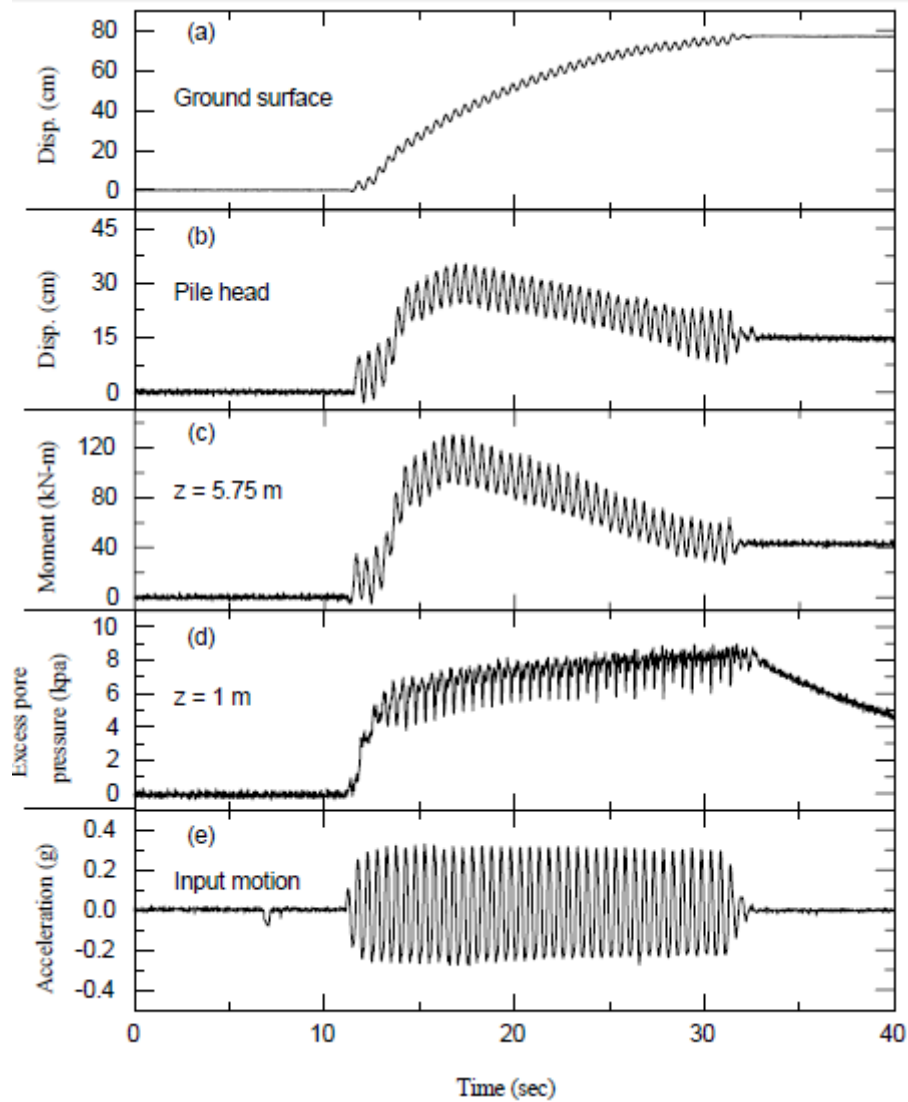


Figure 6.25. Typical Results of Centrifuge Model-3 (Abdoun 1997)

Centrifuge model is idealized as shown in Figure 6.26. Shear stress of 6.4 kPa occurs at the pile head because of 2 °inclination of the model box, which is calculated by finite element modeling of the Model-3. Surface acceleration is reported as 0.5 m/s which cause 0.3 kN lateral load at the pile free head. As a result total lateral load applied to the pile head is calculated as 2.1 kN. Pile is modeled as **free head condition**.

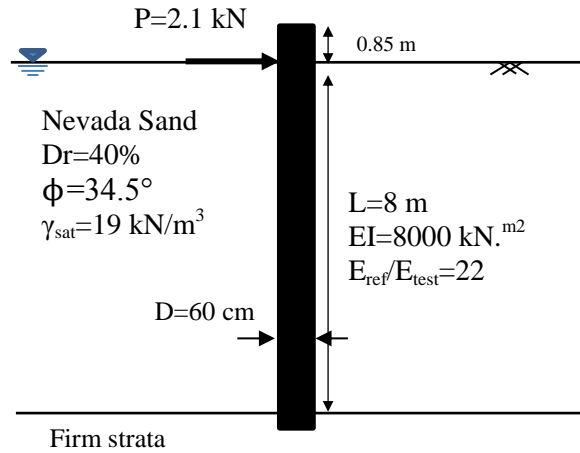


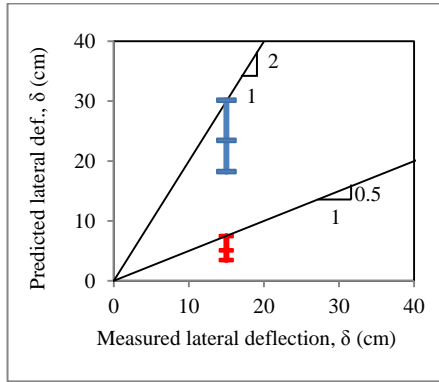
Figure 6.26. Idealized model for semi-empirical approach

Semi-empirical models obtained in this study are based on residual deflections occurred at the pile head. Ultimate lateral pile load capacity P_{ult} is obtained from Broms (1964b) method for free head piles given in Table 5.2. A summary of the assessment inputs of Model 1 and Model II is given in Table 6.3.

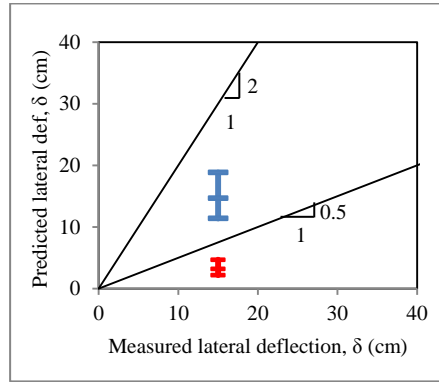
Pile deflections are known to linearly change with the elastic modulus of the pile element. Hence, in order to make a consequent comparison, elastic moduli of the piles in centrifuge test and semi-empirical models should be adjusted. Elastic modulus ratio of the pile between semi-empirical model and centrifuge test model is 22. So that deflections obtained from semi-empirical models should be multiplied with this ratio to compare with the centrifuge results. Predicted and observed lateral deflection for both Model 1 and Model II at pile head are paired and shown on Figure 6.27 for excess pore pressure ratio $r_u=0.7, 0.8$ and 0.9 along with the 1:2 and 1:0.5 boundary lines. Predicted values are given as median and along with $\pm 1\sigma_e$ range. As shown in Figure 6.27, the predicted response for $r_u=0.8$ very nicely matches with the centrifuge test results.

Table 6.3. Summary of the Assessment of the Proposed models parameters for
Case 1 (Abdoun et. al, 1997)

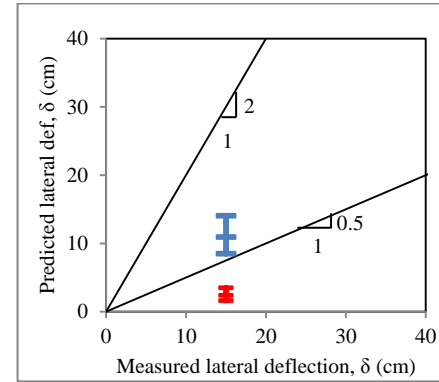
MODEL 1	Static Condition (NAVFAC Approach)		Dynamic Condition (Proposed Model-1)		
Sand ($D_R=40\%$)	r_u	0	r_u	0.80	
	ϕ	34.5 °	ϕ_{ru}	28.8°	<i>Eq.6.2</i>
	K_p	3.61	$K_{p,dyn}$	2.88	<i>Eq.6.3</i>
	f_s	4430 kN/m ³	f_{dy}	716 kN/m ³	<i>Eq.6.1</i>
Pile (free head)	P_{ult}	587 kN	P_{ult}	474 kN	<i>Table 5.2</i>
	P	2.1 kN	P	2.1 kN	
	T	2.10	T_{dyn}	3.0	<i>Eq. 6.4</i>
	L/T	3.8 > 2.0 long pile	L/T_{dyn}	2.6 < 4.0	short pile
	F_δ	2.5	$F_{\delta,dyn}$	20.1	<i>Eq.6.8</i>
	E_{ref}/E_{test}	22.7	E_{ref}/E_{test}	22.7	
	δ_{max} (Horizontal deflection on pile head)	3.2 cm	δ_{max} (Horizontal deflection on pile head)	14.6 cm	<i>Eq.6.9</i>
MODEL 2	Static Condition (Characteristic Load Method)		Dynamic Condition (Proposed Model-II)		
Sand ($D_R=40\%$)	r_u	0	r_u	0.85	
	ϕ	34.5 °	ϕ_{ru}	29.3°	<i>Eq.6.13</i>
	$K_{p(\phi ru)}$	3.61	$K_{p,dyn}$	2.92	<i>Eq.6.14</i>
Pile (free head)	P_c	95859 kN	$P_{c,ru}$	17217 kN	<i>Eq. 6.21</i>
	P	2.1 kN	P	2.1 kN	
	E_{ref}/E_{test}	22.7	E_{ref}/E_{test}	22.7	
	δ_{max} (Horizontal deflection on pile head)	0.03 cm	δ_{max} (Horizontal deflection on pile head)	2.2 cm	<i>Eq.6.22</i>



$r_u=0.90$



$r_u=0.80$



$r_u=0.70$





Legend	
Model 1	Model 2
 +σ	 +σ
 -σ	 -σ

Figure 6.27. Comparison between the measured and predicted pile head displacement by Abdoun et al. (1997)

6.6.2. CASE 2: Validation of the Model with Liu et al. (1995) Study

Liu et al. (1995) assessed on the effect of liquefaction on lateral pile response during the first year of NCEER's Highway Project. The research studies were conducted at Rensselaer Polytechnic Institute by using the geotechnical centrifuge facility. The basic centrifuge model, shown in Figure 6.28, simulates the single pile response subjected to earthquake-induced liquefaction and lateral spreading.

A prototype steel pipe pile is 6.7 m long, 0.381 m outside diameter, and with a bending stiffness of $EI = 2.86 \times 10^4 \text{ kN.m}^2$. Model pile is an end-bearing pile and its tip is fixed to the bottom of the box. During this load test, rotation of the pile is prevented, thus enforcing **a fixed-head condition**. Saturated Nevada No.120 sand having a relative density, $D_R=60\%$ is used in the test. Seismic shaking for a 40-g centrifugal field is applied at the base of the rigid container to induce an excess pore pressure in the sand. At this stage, the pile head is kept locked and the pile moves together with the container during the shaking therefore no relative displacement pile-soil is occurred. Immediately after shaking, and while there are still excess pore pressures in the soil, the pile head is unlocked, and a cyclic (but static) lateral load applied above the ground surface (Liu et. al 1995).

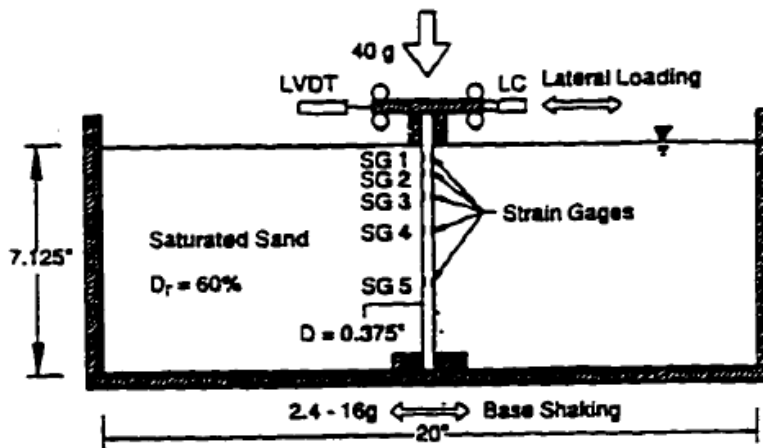
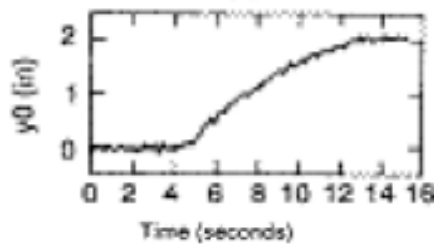


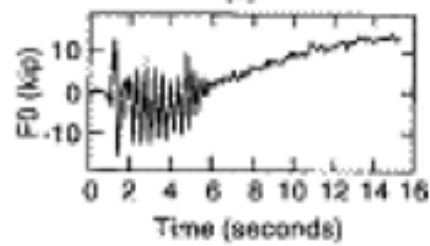
Figure 6.28. Setup of centrifuge model (Liu et al 1995)

The particular results are from test PS07 and are reported by Liu et al. (1995) as follows;

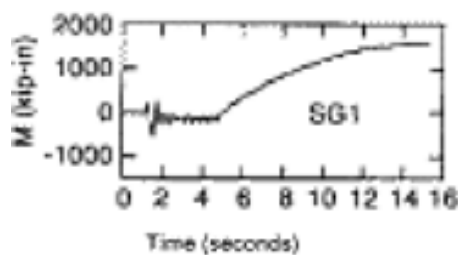
- i) The average amplitude of the input base acceleration in this test was 0.34 g (Figure 6.29d) and the pore pressure ratio r_u reached 100 % very rapidly, as shown in Figure 6.29(d).
- ii) After shaking, statically applied lateral force at the pile head is 44.5 kN (10 kip) (Figure 6.29b).
- iii) The pile head displacement is reaches to permanent value of 5.1 cm (2 inch) as shown in Figure 6.29a.
- iv) The maximum pile bending moment is increased to 1700 kN.m (15000 kip-inch) measured with strain gage at SG1 (Figure 6.29c).



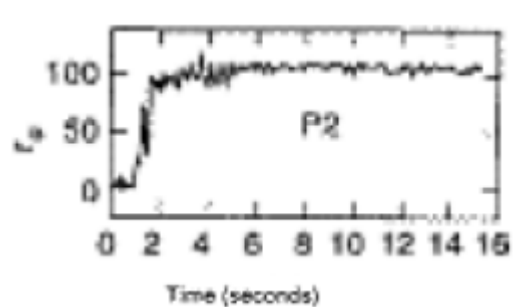
(a) pile head lateral displacement



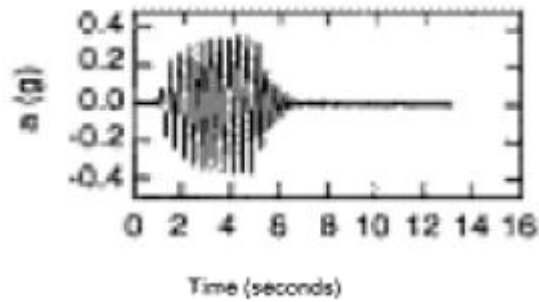
(b) applied force at the pile head



(c) maximum bending moments



(d) excess pore pressure ratio (%)



(e) base acceleration

Figure 6.29. Typical Results of Centrifuge Test PS07 Model-3 (Liu et al. 1995)

Centrifuge model is idealized as shown in Figure 6.30. Friction angle of the sand is taken as 33° estimated from Peck and Hanson (1974) SPT vs. friction angle correlation. Lateral load of 44.5 kPa is applied at the pile head.

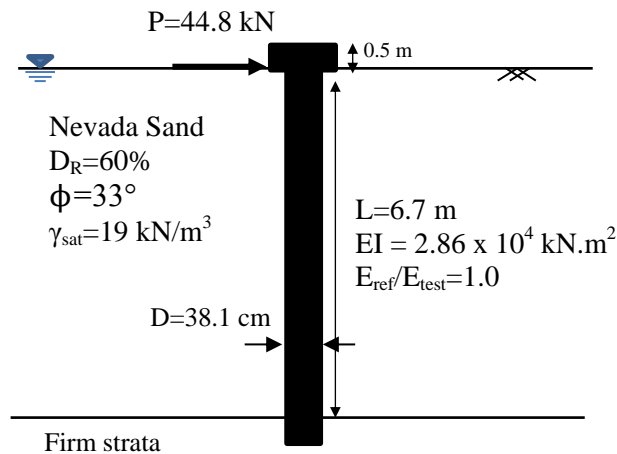


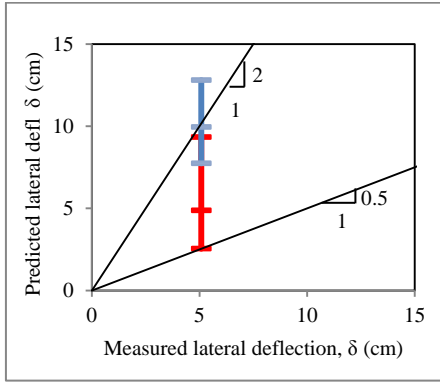
Figure 6.30. Idealized model of Liu et.al (1995) centrifuge model for semi-empirical approach

Summary of the assessments of Model 1 and Model 2 is given in Table 6.4. Ultimate lateral pile load capacity P_{ult} is obtained from Broms (1964b) method for fixed head piles given in Table 5.2.

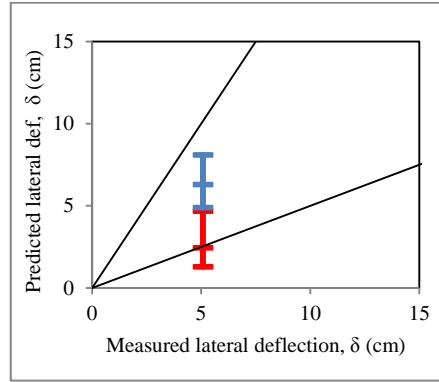
Predicted and observed lateral deflection for both Model 1 and Model II at pile head are paired and shown on Figure 6.31 for excess pore pressure ratio $r_u = 0.7$, 0.8 and 0.9 along with the 1:2 and 1:0.5 boundary lines. Predicted values are given between $\pm 1\sigma_e$. This case of centrifuge testing static lateral load was applied to the pile head and predicted value obtained from Model 1 and Model 2 gives reasonable results compared with observed value.

Table 6.4. Summary of the Assessment of the Proposed models parameters for Case II (Liu et. al 1995)

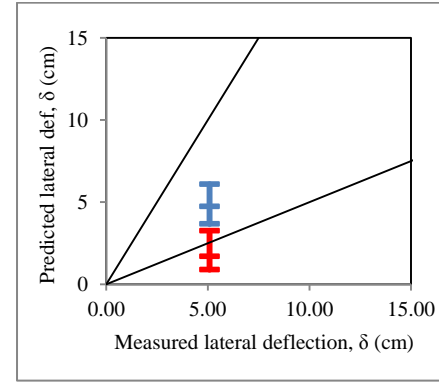
MODEL 1	Static Condition (NAVFAC Approach)		Dynamic Condition (Proposed Model-1)		
Sand ($D_R=60\%$)	r_u	0	r_u	0.80	
	ϕ	33 °	ϕ_{ru}	29.0°	<i>Eq.6.2</i>
	K_p	3.39	$K_{p,dyn}$	2.88	<i>Eq.6.3</i>
	f_s	8784 kN/m ³	f_{dy}	1493 kN/m ³	<i>Eq.6.1</i>
Pile (fixed head)	P_{ult}	243 kN	P_{ult}	206 kN	<i>Table 5.2</i>
	P	44.5 kN	P	44.5 kN	
	T	1.27	T_{dyn}	1.82	<i>Eq. 6.4</i>
	L/T	5.2 > 2.0 long pile	L/T_{dyn}	3.7 < 4.0	short pile
	F_δ	0.95	$F_{\delta,dyn}$	6.9	<i>Eq.6.8</i>
	E_{ref}/E_{test}	1.0	E_{ref}/E_{test}	1.0	
	δ_{max} (Horizontal deflection on pile head)	0.8 cm	δ_{max} (Horizontal deflection on pile head)	6.3 cm	<i>Eq.6.9</i>
MODEL II	Static Condition (Characteristic Load Method)		Dynamic Condition (Proposed Model-II)		
Sand ($D_R=60\%$)	r_u	0	r_u	0.80	
	ϕ	33 °	ϕ_{ru}	28.8°	<i>Eq.6.13</i>
	$K_{p(\phi ru)}$	3.39	$K_{p,dyn}$	2.80	<i>Eq.6.14</i>
Pile (fixed head)	P_c	16532 kN	$P_{c,ru}$	10124 kN	<i>Eq. 6.21</i>
	P	44.5 kN	P	44.5 kN	
	E_{ref}/E_{test}	1	E_{ref}/E_{test}	1	
	δ_{max} (Horizontal deflection on pile head)	0.01 cm	δ_{max} (Horizontal def. on pile head)	1.0 cm	<i>Eq.6.22</i>



$r_u=0.90$



$r_u=0.80$



$r_u=0.70$





Legend	
Model 1	Model 2
 + σ	 + σ
 - σ	 - σ

Figure 6.31. Comparison between the measured and predicted pile head displacement by Liu et al (1995)

6.6.3. CASE 3: Validation of the model with He (2005) Study

The four experiments (Test 1-4) conducted at National Research Institute for Earth Science and Disaster Prevention (NIED) employed a large laminar box, which was inclined at 2° to the horizontal, patterned after Abdoun et al. (2003) and Dobry et al. (2003). Figure 6.32 shows the test setup of Model 4 which consisted of a 5.0 m sand layer with a water table at the upslope ground surface (He, 2005). A prototype steel pipe pile 5.0 m long, 0.381 m outside diameter was selected. In Test 4, two separate single piles with different stiffness's were tested (Elgamal et al., 2006). Model pile is an end-bearing pile and its tip fixed to the bottom of the box. Saturated sand was constructed by the sedimentation method having a relative density about 40%- 50% and saturated density was about 1940 kg/m^3 . The model was instrumented with accelerometers and pore pressure sensors within the soil. The piles were instrumented with strain gages to measure deformation during shaking.

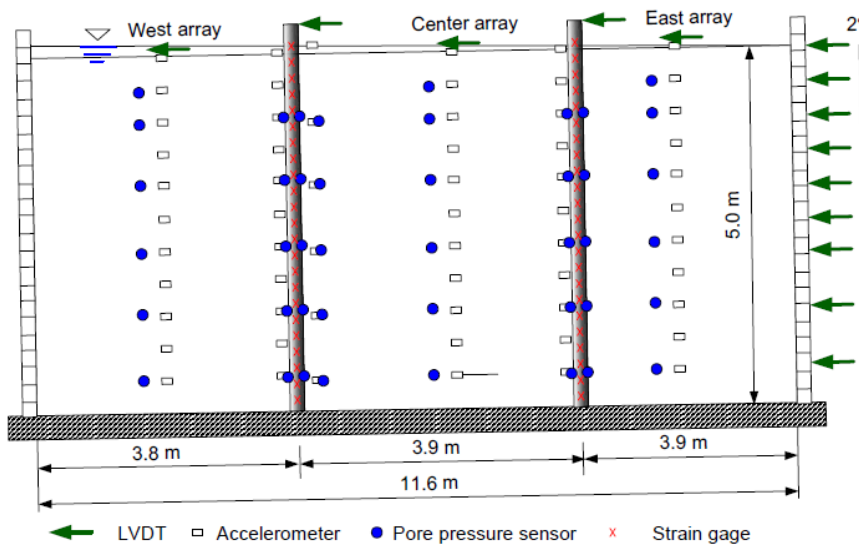
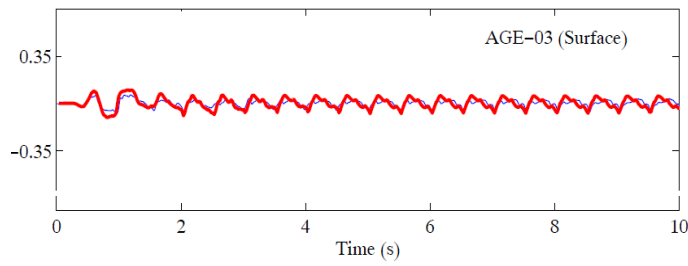


Figure 6.32. Setup of centrifuge model (He, 2005)

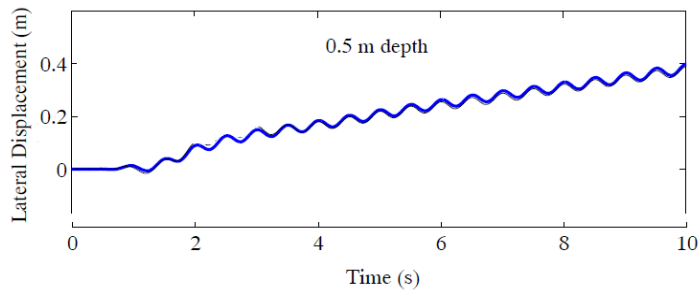
The particular results from Test 4 are reported by He, (2005) as follows;

Shaking of the model was carried out along the 2° sloping direction,

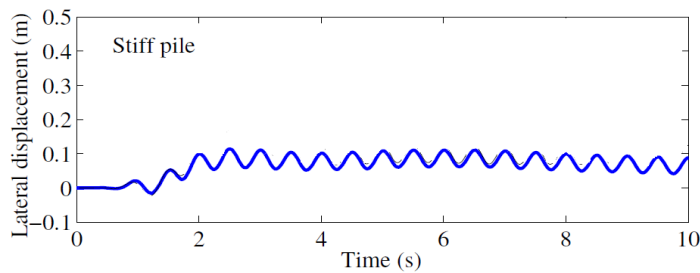
- i) Input motions of the experiment were sinusoidal accelerations with a frequency of 2 Hz, 0.2 g amplitude and with 44 s duration,
- ii) It is stated that the input motion was strong enough to liquefy the soil stratum almost completely,
- iii) Maximum bending moment on pile measured as 132 kN.m,
- iv) Free-field acceleration time histories at surface are given in Figure 6.33a,
- v) Recorded free-field displacement reaches to 40 cm at 0.5 m depth (Figure 6.39b),
- vi) The pile head displacement of relatively stiff pile is reaches to permanent value of 8.5 cm as shown in Figure 6.33c,
- vii) The relatively stiff pile ($EI = 14320 \text{ kN.m}^2$) maximum head deflection is measured as 11 cm whereas relatively flexible pile ($EI = 14320 \text{ kN.m}^2$) head deflection is measured as 21 cm. It is concluded that pile head deflection linearly changed with elastic modulus of the pile.



a) Free-field acceleration time histories in Test 4



b) Recorded and free-field displacement time histories



c) Recorded pile-head displacement time histories

Figure 6.33. Typical Results of Large Size Laminar Box Test Model-4 (He, 2005)

The experimental Model 4 is idealized as shown in Figure 6.34. Friction angle of the sand is taken as 32° . Pile is modeled as free head condition. Surface acceleration is reported about 2.5 m/s which caused 0.3 kN lateral loads at the pile free head. Moreover, lateral load applied on pile head due to the shaking of the model along the 2° sloping direction is obtained from finite element analyses of the idealized model and calculated as 3.4 kN. As a result, in the idealized profile,

total lateral load, which is the sum of lateral load caused by surface acceleration and due to the sloping direction of 2° , 3.7 kN is applied at the pile head.

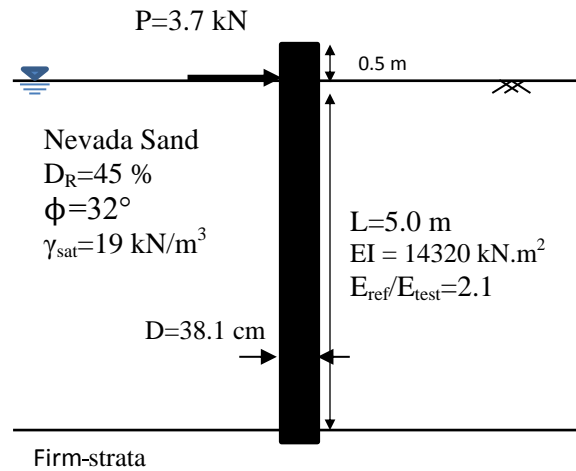


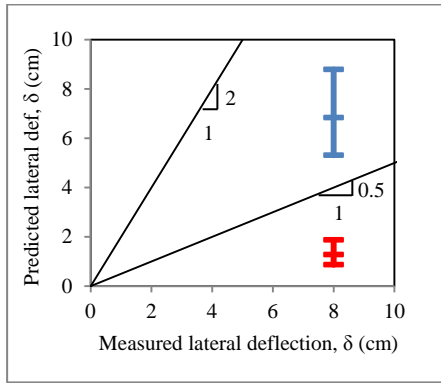
Figure 6.34: Idealized model of He (2005) large size laminar box model for semi-empirical approach

A summary of the assessments of Model 1 and Model 2 is given in Table 6.5. Reference value of elastic modulus of the pile is 2.85×10^8 kPa for semi-empirical approaches so that elastic modulus ratio of the pile between semi-empirical model and experimental model is calculated as 2.1. So that deflections obtained from semi-empirical models was multiplied with this ratio to compare with the experimental results. Ultimate lateral pile load capacity P_{ult} is obtained from Broms (1964b) method for free head piles given in Table 5.2.

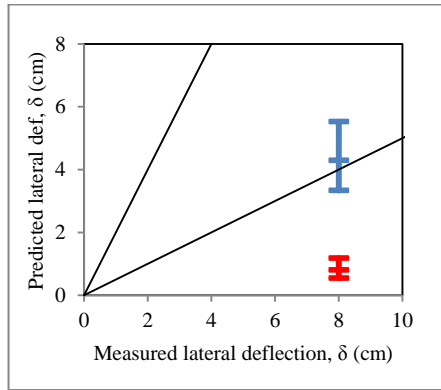
Predicted and observed lateral deflection for both Model 1 and Model 2 at pile head are paired and shown on Figure 6.35 for excess pore pressure ratio $r_u=0.7, 0.8$ and 0.9 along with the 1:2 and 1:0.5 boundary lines. Predicted values are given between $\pm 1\sigma_e$. This case of centrifuge testing, no lateral load was applied to the pile head and predicted value obtained from Model 2 gives smaller deflection results compared with observed value. Model 1 gives reasonable result and comparable with observed values.

Table 6.5. Summary of the Assessment of the Proposed models parameters for
Case 1 (He, 2005)

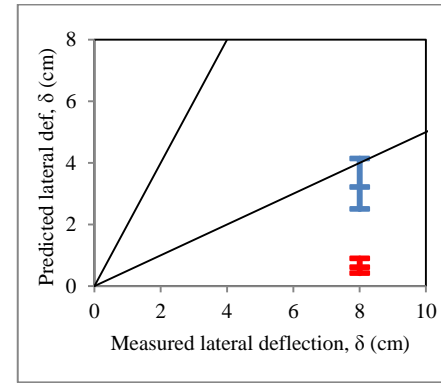
MODEL 1	Static Condition (NAVFAC Approach)		Dynamic Condition (Proposed Model-1)		
Sand ($D_R=45\%$)	r_u	0	r_u	0.80	
	ϕ	32 °	ϕ_{ru}	28.8°	<i>Eq.6.2</i>
	K_p	3.25	$K_{p,dyn}$	2.86	<i>Eq.6.3</i>
	f_s	5478 kN/m ³	f_{dy}	962 kN/m ³	<i>Eq.6.1</i>
Pile (free head)	P_{ult}	139 kN	P_{ult}	122 kN	<i>Table 5.2</i>
	P	3.7 kN	P	3.7 kN	
	T	1.40	T_{dyn}	1.98	<i>Eq. 6.4</i>
	L/T	3.5 > 2.0 long pile	L/T_{dyn}	2.5 < 4.0 short pile	
	F_δ	2.0	$F_{\delta_dynamic}$	20.9	<i>Eq.6.8</i>
	E_{ref}/E_{test}	2.1	E_{ref}/E_{test}	2.1	
	δ_{max} (Horizontal deflection on pile head)	1.0 cm	δ_{max} (Horizontal deflection on pile head)	4.3 cm	<i>Eq.6.9</i>
MODEL 2	Static Condition (Characteristic Load Method)		Dynamic Condition (Proposed Model-2)		
Sand ($D_R =45\%$)	r_u	0	r_u	0.80	
	ϕ	32 °	ϕ_{ru}	28.8°	<i>Eq.6.13</i>
	$K_{p(\phi ru)}$	3.25	$K_{p,dyn}$	2.86	<i>Eq.6.14</i>
Pile (free head)	P_c	24812 kN	$P_{c,ru}$	4873 kN	<i>Eq. 6.21</i>
	P	3.7 kN	P	3.7 kN	
	E_{ref}/E_{test}	2.1	E_{ref}/E_{test}	2.1	
	δ_{max} (Horizontal deflection on pile head)	0.01 cm	δ_{max} (Horizontal def. on pile head)	1.2 cm	<i>Eq.6.22</i>



$r_u=0.90$



$r_u=0.80$



$r_u=0.70$



Legend	
Model 1	Model 2
	
$+\sigma$	$+\sigma$
$-\sigma$	$-\sigma$

Figure 6.35. Comparison between the measured and predicted pile head displacement by He, (2005)

6.6.4. CASE 4: Validation of the Model with Jakrapiyanun (2002) Study

Three (Test 5-7) were conducted by using a medium size laminar box at the University of California, San Diego (UCSD) and it included a single pile each (Jakrapiyanun, 2002) . Figure 6.36 shows the test setup and instrumentation of Test 7. The other tests, Models 5 and 6 had a similar setup and instrumentation pattern, which has different bending stiffness or base fixity.

Model 7 had a prototype steel pipe pile 1.71 m long, 0.25 m outside diameter. Model pile is an end-bearing pile and its tip is fixed to the bottom of the box. Saturated sand was prepared by the sedimentation method at a relative density of 40%- 50%, and saturated density was about 1940 kg/m³. The model was instrumented with accelerometers and pore pressure sensors within the soil. The piles were instrumented with strain gages to measure deformation during shaking.

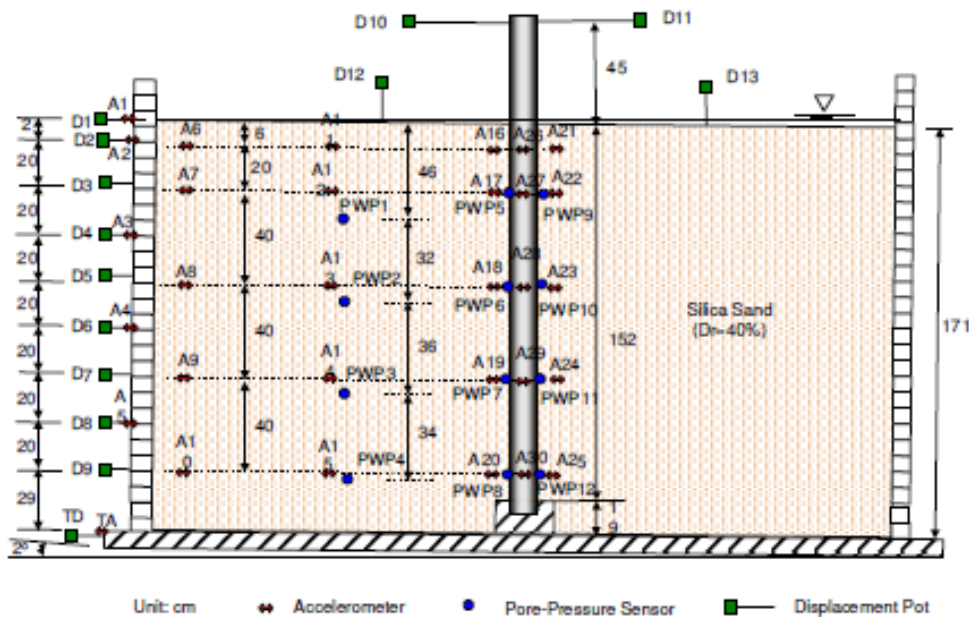


Figure 6.36. Setup of centrifuge model 7 (Jakrapiyanun, 2002)

The particular results from Model 7 test are reported as follows;

- i) Shaking of the model was carried out along the 2° sloping direction.
- ii) Input motions of the experiment were sinusoidal accelerations with a frequency of 1 Hz, 0.15 g amplitude.70 s duration.
- iii) It is stated that input motion was strong enough to liquefy the soil stratum almost completely.
- iv) Maximum bending moment on pile measured as 2.83 kN.m^2
- v) Recorded free-field displacement is reaches to 2.5 cm at the ground surface.
- vi) The pile head displacement reaches to maximum value of 1.2 cm

The experimental Test 7 is idealized as shown in Figure 6.37. Friction angle of the sand is taken as 32° . Pile is modeled as **free head condition**. Lateral load of 0.5 kN is applied at the pile head.

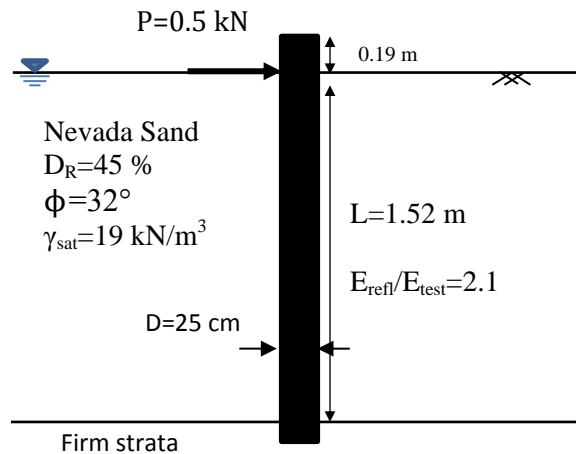


Figure 6.37. Idealized model of Jakrapiyanun (2005) large size laminar box model for semi-empirical approach

A summary of the assessments of semi-empirical Model 1 and Model 2 is given in Table 6.6. Elastic modulus ratio of the pile between semi-empirical models and experimental model is calculated as 2.1. So that deflections obtained from semi-

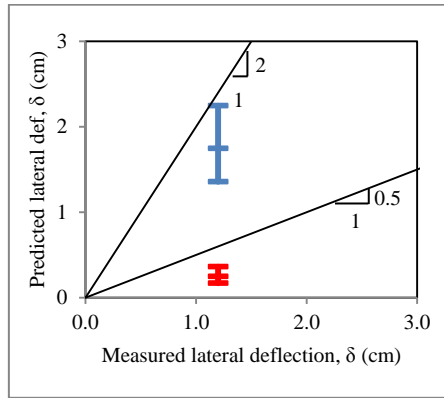
empirical models was multiplied with this ratio to compare with the experimental results. Ultimate lateral pile load capacity P_{ult} is obtained from Broms (1964b) method for free head piles given in Table 5.2.

Predicted and observed lateral deflection for both Model 1 and Model II at pile head are paired and shown on Figure 40 for excess pore pressure ratio $r_u = 0.7, 0.8$ and 0.9 along with the 1:2 and 1:0.5 boundary lines. Predicted values are given between $\pm 1\sigma_\epsilon$ bands.

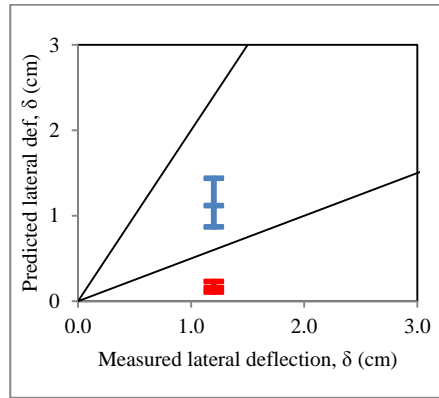
This case of centrifuge testing, no lateral load was applied to the pile head and predicted value obtained from model 2 gives smaller deflection results compared with observed value. Model 1 gives reasonable result and comparable with observed values.

Table 6.6. Summary of the Assessment of the Proposed models parameters for Case 4 (Jakrapiyanun, 2005)

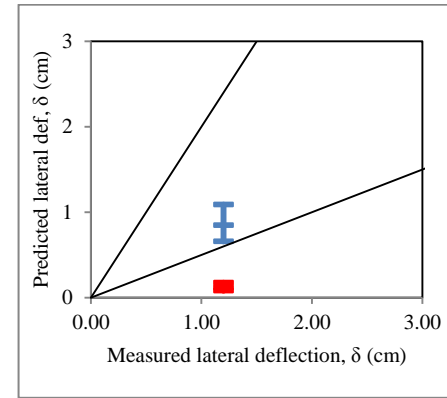
MODEL 1	Static Condition (NAVFAC Approach)		Dynamic Condition (Proposed Model-1)	
Sand ($D_R=45\%$)	r_u	0	r_u	0.80
	ϕ	32 °	ϕ_{ru}	28.8° <i>Eq.6.2</i>
	K_p	3.25	$K_{p,dyn}$	2.86 <i>Eq.6.3</i>
	f_s	5478 kN/m ³	f_{dy}	962 kN/m ³ <i>Eq.6.1</i>
Pile (free head)	P_{ult}	7.05 kN	P_{ult}	6.2 kN <i>Table 5.2</i>
	P	0.5 kN	P	0.5 kN
	T	1.0	T_{dyn}	1.42 <i>Eq. 6.4</i>
	L/T	1.52 > 2.0 short pile	L/T_{dyn}	1.1 < 4.0 short pile
	F_δ	2.0	$F_{\delta,dyn}$	20.9 <i>Eq.6.8</i>
	E_{ref}/E_{test}	2.1	E_{ref}/E_{test}	2.1
	δ_{max} (Horizontal deflection on pile head)	0.3 cm	δ_{max} (Horizontal deflection on pile head)	1.2 cm <i>Eq.6.9</i>
MODEL II	Static Condition (Characteristic Load Method)		Dynamic Condition (Proposed Model-II)	
Sand ($D_R=45\%$)	r_u	0	r_u	0.80
	ϕ	32 °	ϕ_{ru}	28.8° <i>Eq.6.13</i>
	$K_{p(\phi ru)}$	3.25	$K_{p,dyn}$	2.86 <i>Eq.6.14</i>
Pile (free head)	P_c	31787 kN	$P_{c,ru}$	6243 kN <i>Eq. 6.21</i>
	P	0.5 kN	P	0.5 kN
	E_{ref}/E_{test}	2.1	E_{ref}/E_{test}	2.1
	δ_{max} (Horizontal deflection on pile head)	<0.01 cm	δ_{max} (Horizontal def. on pile head)	0.16 cm <i>Eq.6.22</i>



$r_u=0.90$



$r_u=0.80$



$r_u=0.70$

Legend			
Model 1		Model 2	
	+ σ		+ σ
	- σ		- σ

Figure 6.38. Comparison between the measured and predicted pile head displacement by He, (2005)

6.6.5. A summary of the Validation Efforts

Predicted and observed lateral deflection of Cases1-4 at pile heads are paired and shown on Figure 6.39 for excess pore pressure ratio $r_u = 0.7, 0.8$ and 0.9 along with the 1:2 and 1:0.5 boundary lines. Predicted values are given between $\pm 1\sigma_e$ bands.

As expected, at these fully liquefied soil sites, $r_u=0.8-0.9$ values produce the best fit to the observed pile head deflections. Similarly, the predicted values match perfectly well with the observed pile head displacement values within a factor of 2. Comparisons with the centrifuge test results confirmed the general validity of the proposed models and its ability to capture pile-soil interaction including pile lateral deformation due to cyclic loading in liquefied soils.

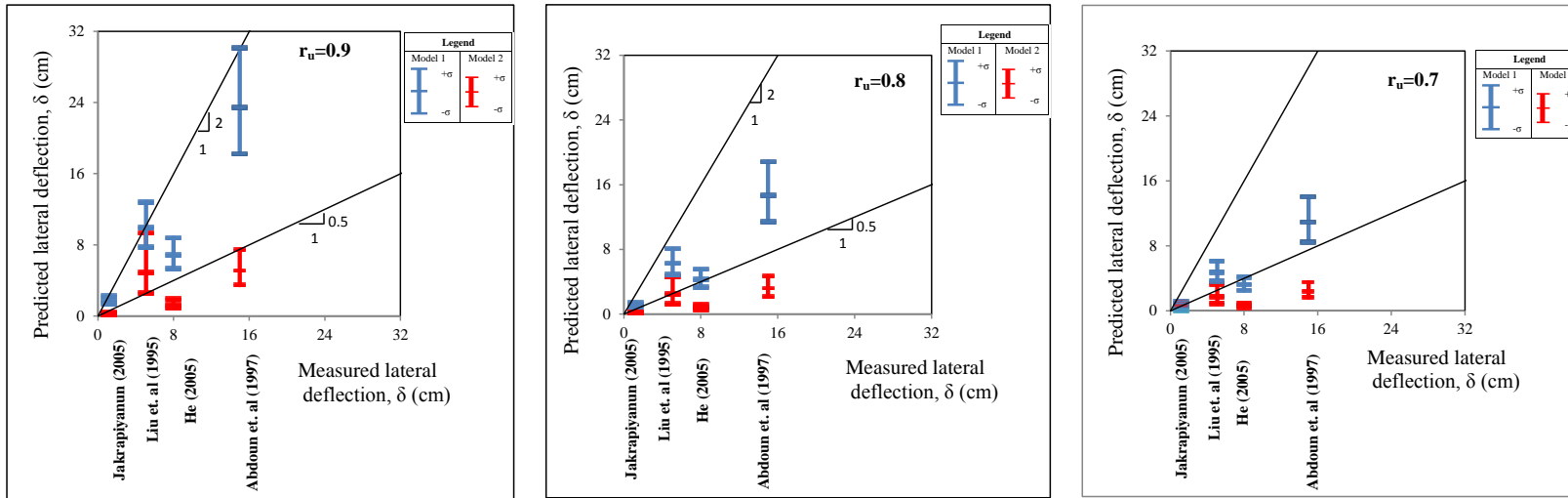


Figure 6.39. Comparison between the measured and predicted pile head displacements

6.7. Conclusion

In this section, in order to gain insight into inelastic behavior of piles, the response of a vertical pile embedded in potentially liquefiable sand, which was subjected to cyclic loading, was studied.

First, series of effective stress based numerical analysis were performed by using METUSAND model to understand the effect of lateral cyclic loading on ultimate lateral capacity of piles embedded in potentially cohesionless soil. Piles were modeled as elastic materials with material properties of reinforced concrete. This was due to the fact that currently available pile element in FLAC has some limitations such as;

- i) coupling spring parameters of FLAC depend on the relative shear displacement and normal displacement of the piles. Whereas, numerical analyses were performed to assess the response of pile/soil interaction for piles and
- ii) coupling spring properties of pile element is defined as *constant values* throughout the pile length, This limitation produced inconsistent and unrealistic results since Soil-pile interaction at different depths would be different, due to the fact that soil stiffness is different at these depths during cyclic loading.

Totally 160 analyses were performed in FLAC software by adopting different but realistic combinations of input variables as various lateral loads applied to pile head, various stiffness of surrounding soil, various embedded pile length and pile diameter for free and fixed head piles.

On the basis of these simulation results, semi-empirical models to assess cyclic response of piled foundation were developed and presented.

Semi-empirical **Model I** is a modified version of the original Naval Facilities Engineering Command (NAVFAC) “*Foundation and Earth Structures Design*

Manual 7.02, 1986 approach. As defined by NAVFAC, deflection coefficient F_δ is expressed by the ratio of pile lateral deflection and pile stiffness corresponding to relative stiffness factor and lateral load applied to the pile head. It is observed that, F_δ values increased with increasing r_u . With increasing r_u , soil stiffness degrades and initially "long" pile starts to behave as a "short" pile and rotate. Non-dimensional terms basically depend on relative stiffness factor, T , which was modified in terms of soil stiffness to make a reasonable normalization for dynamic approach. Hence, a probabilistically based semi-empirical model was proposed for the prediction of F_{δ_dyn} over a very wide range of relative stiffness factor and lateral load, by also considering the effect of excess pore water pressure generation. Predicted and measured F_δ values fall within the bounds of 1:3 and mostly accumulated along 1:1 line, suggesting an unbiased model.

Semi-empirical **Model II** is a modification of Duncan et.al. (1994). Characteristic Load Method (CLM) which is based on approximated relationships among dimensionless variables, was developed by performing nonlinear p-y analyses for a wide range of free-head and fixed-head. Characteristic load P_c is modified for saturated cohesionless soils to consider their excess pore pressure generation potential and the proposed P_{c,r_u} is defined which captured the observed response better. Hence, probabilistically-based semi-empirical model was proposed for prediction of $P/P_{c,r_u}$ and corresponding lateral deflection ratio y/D by considering the effect of excess pore water pressure generation. Predicted and measured P/P_c values fall within the bounds of 1:3 and mostly accumulated along 1:1 line, suggesting an unbiased model

Lastly, the proposed model was validated with actual well documented centrifuge experiments, aiming to assess the response of piles subjected to lateral loads in liquefiable soils. For this purpose, centrifuge model tests of Abdoun et. al. (2003) and Liu et. al. (1995), He (2005) and Jakrapiyanun (2002) were compared with the proposed semi-empirical model (Model 1 and Model II) predictions. Excess pore pressure response and liquefaction induced ground deformations were

presented and discussed in detail. Comparisons revealed that for $r_u=0.8-0.9$, semi empirical models produce reasonable results for pile head deflections at these fully liquefied centrifuge soil models. Predicted pile head lateral displacements are observed to scatter within a factor of 2 around the measured values. This confirmed the validity of the proposed semi empirical models.

CHAPTER 7

SUMMARY AND CONCLUSIONS

7.1. Summary

The scope of these studies involves i) the development of a constitutive model, METUSAND, to assess cyclic response of fully saturated cohesionless soils, including but not limited to cyclic shear straining and pore pressure increase and corollary strength and stiffness reduction, ii) implementation of METUSAND to FLAC 2-D software, and calibrating the model through a) laboratory cyclic test results, b) well-documented site response case histories of level sites (i.e.: Wildlife and Port Island sites) iii) numerical simulations of cyclic response of single pile constructed in liquefiable soils, iv) calibrating the simulation results with available pile-soil-earthquake interaction centrifuge laboratory test results as well as with well-documented case histories and v) development of semi empirical models to predict displacement response of piles subjected to static and cyclic loading, leading to cyclic mobility or full liquefaction of surrounding soils.

In the literature, there exist a number of constitutive models to assess liquefaction behavior, including but not limited to numerical methods, ranging from total-stress-based empirical assessments such as the UBCTOT model (Beatty and Byrne, 2000), to simplified effective-stress based shear-volume coupling schemes (e.g.: “Finn” model (Martin et al., 1975) and the “Roth” model (Dawson et al., 2001), to more comprehensive constitutive models (e.g.: UBCSAND model (Byrne et al., 1995); PM4Sand model (Boulanger et al., 2012), and Wang (1990) bounding surface model.

For the purpose of assessing cyclic response of fully saturated cohesionless soils, a simplified, effective stress-based, nonlinear (incrementally linear) constitutive

model, METUSAND, is developed within the framework of a hybrid analysis procedure. The model is capable of simulating the non-linear hysteretic stress - strain response, excess pore water pressure generation, and the associated post-cyclic straining potential of saturated clean sands. The proposed constitutive model is composed of two major components corresponding to the assessment of pre-liquefaction and post-liquefaction responses. Pre-liquefaction response is founded on the recent semi-empirical cyclic straining and pore pressure generation models of Cetin et al. 2009, Cetin and Bilge (2012, 2014) and post liquefaction behavior mostly follows the constitutive framework outlined by Shamoto et al. (1998). For the purpose, a FLAC 2-D built-in, elastic-plastic model with Mohr-Coulomb failure criterion (referred to as Mohr-Coulomb model in FLAC) is used as the backbone of the subroutine. Necessary modifications and additions are performed in C++ programming language, and the resulting subroutine is added to commercially available dynamic link library (DLL) of FLAC software. The analyses are carried out in the time domain with the possibility to assess fully coupled groundwater flow and cyclic loading.

As part of METUSAND, plastic straining, and induced pore pressure is defined to be a function of maximum shear strain level. Unloading is assumed to be linear, and dependent on strain compatible (degraded) shear modulus, which is also a function of initial mean effective stress ($\sigma'_{m,0}$). The parameters associated with the proposed constitutive model are grouped into three categories: parameters defining the i) elastic stress-strain ii) plastic stress-strain and cyclic pore pressure and iii) post liquefaction stress-strain responses.

In order to validate METUSAND model and illustrate the capabilities and limitations of it, seismic response assessment of Wildlife, California and Port Island, Kobe sites were numerically studied by METUSAND model. The comparisons with the actual responses of these sites expressed by recorded acceleration and pore pressure time histories revealed that despite its simplicity and relatively small number of input parameters, METUSAND model can predict

relatively reliably cyclic straining and pore pressure responses of these sites. These validation studies have shown that modulus degradation and damping (energy dissipation) responses of soils are the essential components of seismic ground response, and hence soil structure interaction problems.

Encouraged by closely matching results obtained during these calibration studies (i.e.: Wildlife and Port Island sites), series of numerical simulations were performed on generic soil, pile and cyclic loading combinations with intend of developing a simplified framework to assess the deformation response of laterally loaded piles in liquefiable soils. A number of procedures have been proposed to assess static response of laterally loaded piles. The ultimate lateral resistance of rigid piles based on earth pressure theory was developed by Hansen (1961) and Broms (1964a, b) method. Matlock and Reese (1960) developed a generalized iterative solution method for rigid and flexible laterally loaded piles embedded in soils with two forms of varying soil stiffness with depth. Duncan et al. (1994)'s methodology was developed on the basis of nonlinear p-y analyses for a wide range of free- and fixed-head piles and drilled shafts. More recently, Yang and Jeremic (2002) carried out finite element analyses to assess the behavior of single piles in elasto-plastic media, and developed generic p-y curves. Zamri et al. (2009) analyzed the response of piles under combined vertical and lateral load, considering the variation of the water table depths. In the design of laterally loaded pile foundations in liquefiable soils, both safe capacity and allowable deflections need to be estimated to ensure that the serviceability limits are satisfied. However, unfortunately, the response of a pile subjected to a sustained lateral load in cyclic loaded potentially liquefiable soil is still not fully understood.

In order to contribute to the improvement of current state of practice to assess lateral response of piles in liquefiable soils, effective stress based generic numerical simulations were performed for a number of soil, pile and cyclic loading combinations. METUSAND constitutive model was used for the

simulations. Static analyses were performed to compare the findings with the ones of currently available and widely used methods of NAVFAC (1986) and Duncan et al. (1994) approaches. Then, a total number of 160 dynamic analyses were performed by adopting different but realistic combinations of input soil and pile variables. On the basis of numerical simulation results and inspired from NAVFAC (1986) and Duncan et al. (1994) methodologies, probabilistically-based simplified frameworks were developed to assess cyclic response of laterally loaded piles in saturated cohesionless soils. Later, the validity of these simplified frameworks is then confirmed with actual well documented centrifuge model tests of Abdoun et al. (2003) and Liu et al. (1995), He (2005) and Jakrapiyanun, (2002), which were performed to assess the response of piles subjected to lateral loads in liquefiable soils. Comparisons with these centrifuge test results confirmed that i) semi-empirical models proposed for the assessment of lateral pile response in liquefiable soils can predict maximum dynamic lateral pile displacements in an unbiased manner within an accuracy factor of 2. ii) METUSAND model can reliably capture cyclic shear straining, corollary modulus degradation and pore pressure responses of piled foundation systems. After this brief summary, major conclusions of the research studies will be discussed next.

7.2. Conclusion

As the conclusions of these research studies, two major outputs were produced:

- i) A simplified semi-empirically and effective stress-based, fully coupled, nonlinear elasto-plastic constitutive model, METUSAND, developed to assess cyclic small to large strain responses of fully saturated cohesionless soils,
- ii) A probabilistically-based simplified framework to assess lateral pile deformations subjected to sustained static loads, constructed in cyclically loaded liquefiable soils.

Hence, conclusions will be presented separately following this natural order.

A schematic illustration of METUSAND response in effective stress-shear stress domain is presented in Figure 7.1. Some of the characteristics of METUSAND model are listed as: i) an effective stress based definition of G/G_{\max} , ii) excess pore pressure generation, as a function of plastic shear straining, iii) strain (and effective stress) compatible shear modulus degradation as suggested by Cetin and Bilge (2014), iv) realistic stiffer unloading responses. v) strain compatible hysteretic damping.

Until the maximum shear strain threshold level of 10^{-4} %, soil response is assumed to be fully elastic. Beyond this level, the nonlinear (or incrementally linear) plastic response, until the onset of failure, is referred to as *pre-liquefaction phase*. Soil system stiffness is reduced with increase in cyclic shear strain and pore pressure levels. The failure envelope is defined by Mohr-Coulomb criterion (shear yield function) with tension cutoff (tensile yield function). Plastic shear strains, and corollary pore pressure generation is assessed by an iterative procedure, since shear modulus is also defined to be a function of maximum shear strain levels. When the current stress state hits the failure envelope, with sustained cyclic shear stresses, a zero effective stress state is reached, which is referred to as “*initial liquefaction*”. Beyond the onset of initial liquefaction, the response will be governed by large deformations as defined in the *post-liquefaction phase*.

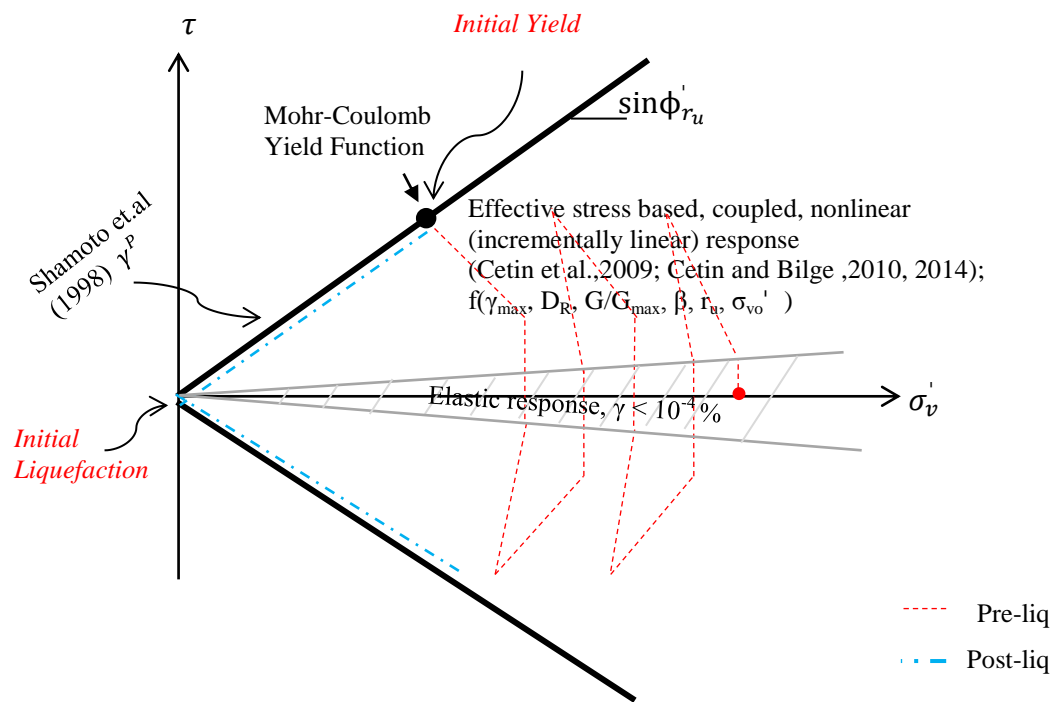


Figure 7.1. Schematic illustration of METUSAND

METUSAND model predictions in the elemental sense are compared with “Seed-like” empirical liquefaction triggering charts. After correcting for multidirectional shaking effects, the liquefaction initiation curves generated by METUSAND are shown to be in good agreement with the curve developed by Seed et al. (1984), NCEER (1997), Cetin et al. (2004) and Idriss and Boulanger (2008) (Figure 7.2).

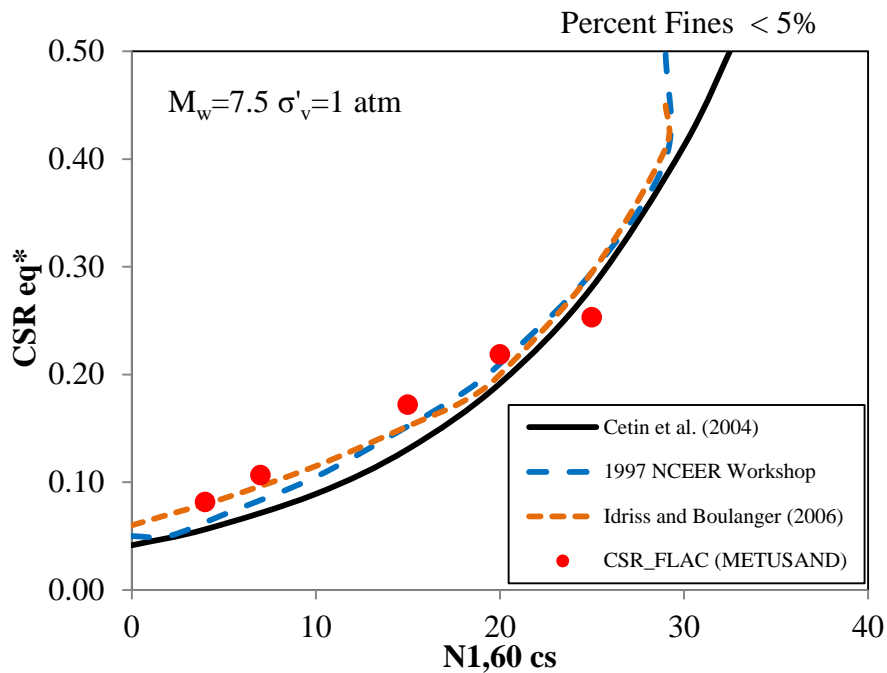


Figure 7.2. Values of CRR predicted by METUSAND and compared to probabilistic semi-empirical relationships.

On the basis of comparisons with well documented site response of liquefied case history sites of Wildlife and Port Island, it was shown that METUSAND model can reliably simulate effective stress-based coupled response of pore pressure generation and cyclic shear straining. Additionally, closely matching outcropping acceleration time histories at liquefied site also confirmed that the modulus degradation and damping responses could be reliably simulated by METUSAND in the wide range of very small to large strains. Currently, METUSAND model is available in FLAC 2-D as a C++ subroutine, ready to be used as a simple yet effective alternative to currently available methods of Byrne et al. (2004) and Boulanger et al. (2012).

Major advantage of the METUSAND model is that:

- i) it is a rather simple model with limited number of input parameters (f ($G_{max}, \phi', \gamma', D_R, \nu$)),

- ii) it is an intrinsically calibrated model due to the fact that it is based on already calibrated semi empirical models, and it does not require additional explicit adjustment factors to achieve a match with true response of soils,
- iii) Shear modulus is defined nonlinearly as a function of mean effective stress after the input of G_{max} at the reference stress condition,
- iv) since pore pressure generation is defined to be a function of initial static stresses, no additional stress correction (K_α and K_σ) is required. nonlinear (incrementally linear) soil response is simply achieved with a pre-defined modulus degradation curve,
- v) strain dependent pore pressure generation results in changes in effective stress, soil strength and soil modulus, which in turn triggers an iterative solution scheme,
- vi) damping is mainly hysteretic, and the resulting damping response is shown to be comparable with strain compatible damping curves available in the literature,
- vii) post-failure accumulation of large cyclic plastic strains can be estimated owing to post liquefaction formulation of dilation and contraction cycles.

However, followings are the weaknesses of the METUSAND model:

- vii) it does not follow a flow rule,
- viii) strain hardening response as a function of stress ratio and plastic shear strain cannot be modeled,
- ix) shear induced plastic expansion or dilation and plastic volumetric strains related to plastic deviatoric strains through the dilatancy is not considered,
- x) Stress-ratio controlled, critical state compatible, bounding surface plasticity based model responses are lacking,
- xi) Some material constants of Shamoto et al. (1998) post liquefaction constitutive relation was only applicable to Tayouro sand.

METUSAND, like other constitutive model predictions, are very sensitive to the selection of small strain shear modulus G_{\max} . A perfect or a poor match is quite possible depending on the G_{\max} value adopted. In the literature, there exist a number of formulations to estimate G_{\max} values. These recommended values may vary by a factor of 2. However, choosing values even within this recommended G_{\max} range may produce significantly different liquefaction triggering responses.

A second set of conclusions involves the development of a simplified framework to assess the lateral seismic deformation behavior of a single pile buried in liquefiable soils. On the basis of dynamic numerical simulation results, and inspired from NAVFAC-based normalization, and Duncan Characteristic Load Method (CLM) concepts, semi-empirical models to assess seismic deformation performance of piles buried in liquefiable soils were developed. These new semi-empirical approaches are referred to as “*Model I and Model II*” respectively in this dissertation. Flow chart solution of these models is given in Figure 7.3 and Figure 7.4. A summary of the calculation steps and remarks are listed below:

Model I

- Non-dimensional terms to calculate laterally loaded pile deformation and stresses are defined in Naval Facilities Engineering Command (NAVFAC) “Foundation and Earth Structures Design Manual 7.02, (1986)” which are based on Reese and Matlock (1974) p-y analyses.
- NAVFAC solution adopted a constant shear modulus with depth, whereas the proposed solution uses effective stress dependent modulus values.
- Coefficient of variation of subgrade reaction, f_{dyn} , depends on the stiffness of the soil, which decreases with increasing excess pore pressure.

- Non-dimensional graphs defined in NAVFAC (1986) are re-normalized with the proposed relative stiffness factor, T_{dyn} . The proposed T_{dyn} is valid for $0.10 < r_u < 0.8$.
- With increasing r_u , soil stiffness degrades and initially "long" pile starts to behave as a "short" pile.
- Laterally loaded piles with $L/T_{dyn} \leq 4$ is defined as a short pile due to rigid body rotational nature of their dynamic response.

Model II

- Duncan et.al. (1994) Characteristic Load Method (CLM), which is based on approximate relationships among dimensionless variables, was developed by performing nonlinear p-y analyses for a wide range of free-head and fixed-head.
- Characteristic load P_c is modified for saturated cohesionless soils to consider their excess pore pressure generation potential and the proposed P_{c,r_u} is defined in Figure 7.4. P_{c,r_u} depends, submerged unit weight, γ'_{ru} , friction angle, ϕ_{ru} and passive earth pressure constant, $K_{p,dyn}$.

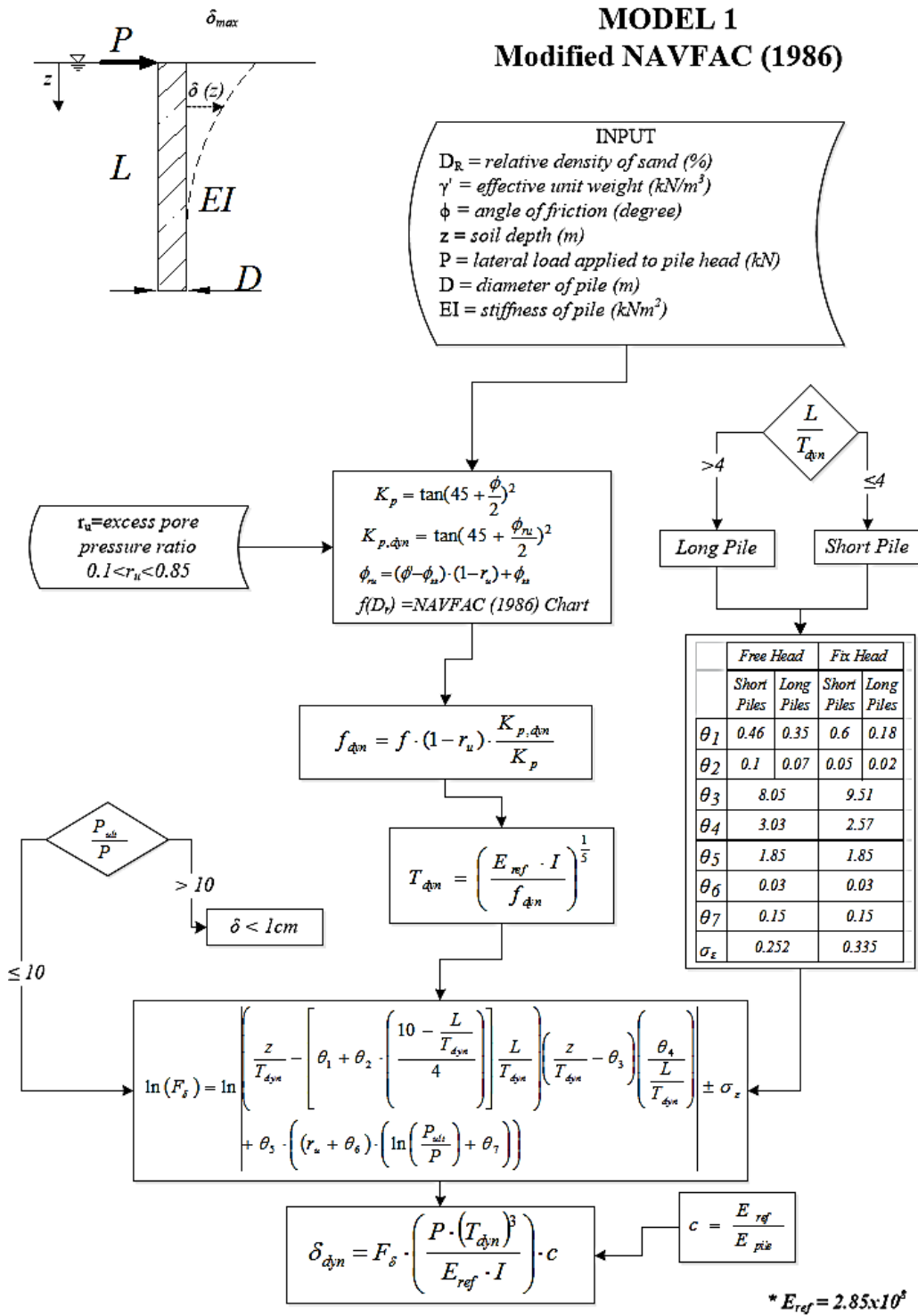


Figure 7.3. Flow Chart for Model I

MODEL 2 Modified Duncan et. al. (1994)

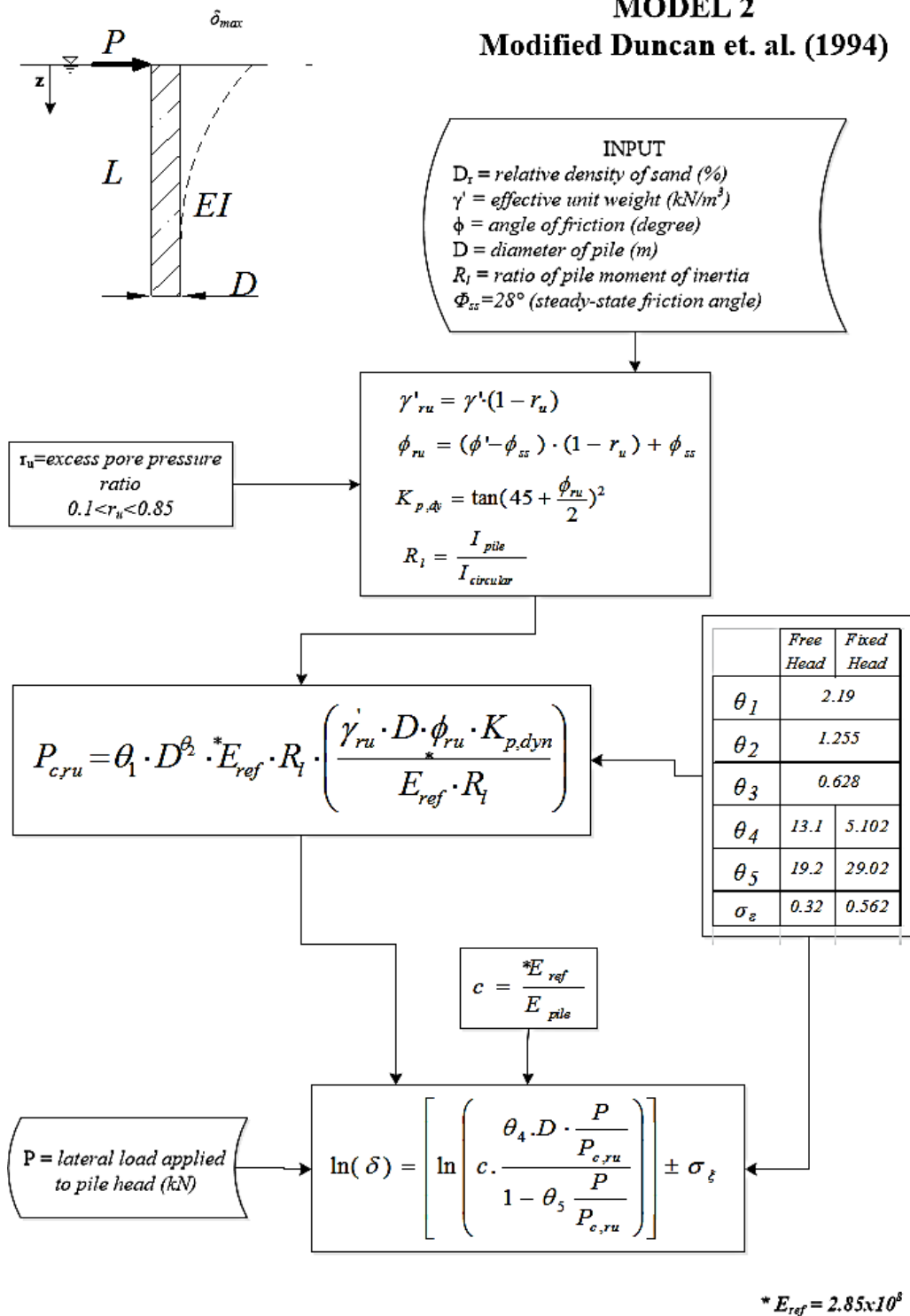


Figure 7.4. Flow Chart for Model II

The proposed models were validated with actual well documented centrifuge tests performed on piles subjected to lateral loads and constructed in liquefiable soils. Predicted and observed lateral pile head displacements by both Model 1 and Model II at pile head are shown in Figure 7.5 for excess pore pressure ratio $r_u=0.8$ along with the 1:2 and 1:0.5 boundary lines. The predicted displacement values match well with true observed pile head displacements. Hence, it can be concluded that the comparisons with the centrifuge test results confirmed the general validity of the proposed models and its ability to capture pile-soil interaction including pile lateral deformation due to cyclic loading in liquefied soils.

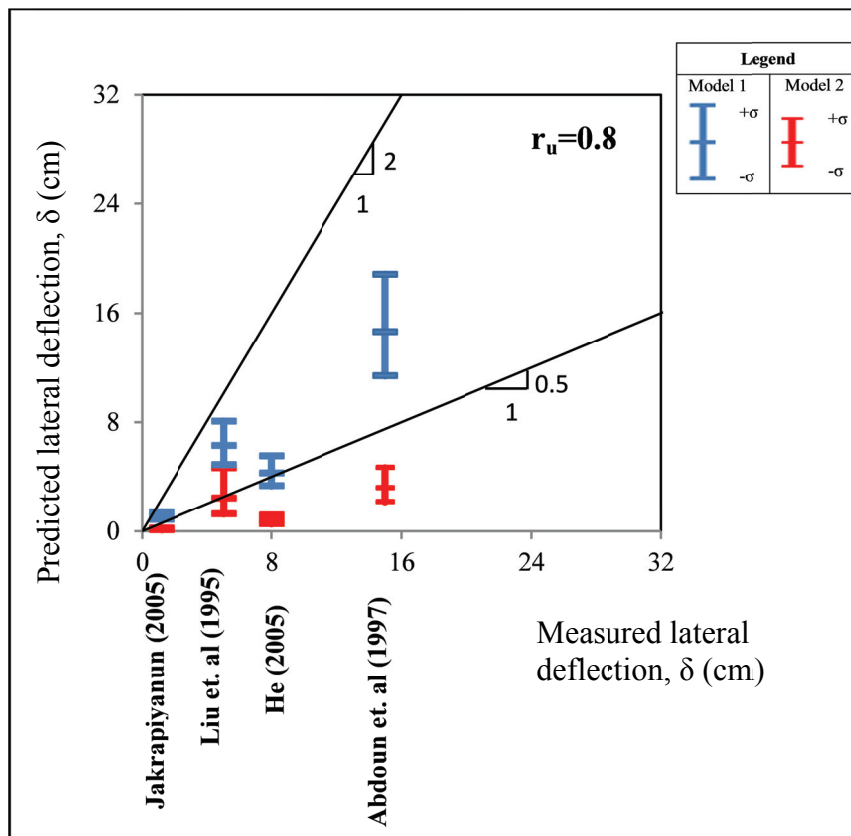


Figure 7.5. Comparison between the measured and predicted pile head displacements

7.3. Recommendations for Future Research

During the scope of this thesis, due to lack of data or analyses or testing tools, this research have been suffered, which established the basis of my recommendations for future research studies:

- i) large strain responses of soils and piles are not well-studied and understood. Both well-documented field case histories and well-instrumented laboratory large scale shaking table and centrifuge tests will improve our current state of knowledge and hence strongly recommended,
- ii) simple yet powerful constitutive models, which require the minimum number of input parameters may help to improve the state of practice and analysis habits,
- iii) dynamic numerical simulation can be performed with additional realistic combinations of input variables (i.e.: relative density of soil, length and diameter of pile etc.) to refine the proposed semi-empirical frameworks. Moreover transient excitations can be used to shake the pile – soil system,
- iv) The simplified framework of a single pile can be extended to pile groups by performing additional numerical analysis,
- v) In addition to lateral deformation response of piles, bending moment and shear performance can be assessed on the basis of new empirical methods.

REFERENCES

- Abdoun T., Dobry R., O'Rourke T. D., Goh S.H., 2003. "Pile response to lateral spreads: Centrifuge modeling." *Journal of Geotechnical and Geoenvironmental Engineering*, 129(10), pp. 869-878.
- Abdoun T., 1997. "Centrifuge modeling of seismically induced lateral spreading of multilayer sand deposit and its effects on pile foundations." PhD thesis, Dept. of Civil Engineering, Rensselaer Polytechnic Institute, Troy, N.Y.
- Aguirre J., Irikura K., 1997. "Nonlinearity, liquefaction, and velocity variation of soft soil layers in port island, kobe, during the hyogo-ken Nanbu earthquake." *The Seismological Society of America (Bulletin)*, 87(5), pp. 1244-1258.
- American Petroleum Institute (API), 2006. "Recommended practice for planning, designing and constructing fixed offshore platforms". RP-2A-WSD.
- Andrus R.D., Stokoe K.H., 2000. "Liquefaction resistance of soils from shear-wave velocity." *Journal of Geotechnical and Geoenvironmental Engineering*, ASCE, 126(11), pp. 1015-1025.
- Azizinamini A. and Ghosh S. K., 1997. "Steel reinforced concrete structures in 1995 Hyogoken Nanbu earthquake." *Journal of Structural Engineering*, ASCE, 123, pp. 986-992.
- Bardet J.P., Oka F., Sugito M., Yashima A., 1995. "The Great Hanshin Earthquake disaster." Preliminary Investigation Report. Dept. of Civil Engineering. University of Southern California, Los Angeles, CA.
- Basack S., Purkayastha R. D., 2007. "Behaviour of single pile under lateral cyclic load in marine clay." *Asian Journal of Civil Engineering (Building and Housing)* 8(4), pp. 443-458.
- Bazarra, A., 1967. "Use of the standard penetration test for estimating settlements of shallow foundations in sand." Ph.D. dissertation, University of Illinois, Civil Engineering, 379 pp.

- Beaty M. H., Perlea V. G., 2011. "Several observations on advanced analyses with liquefiable materials." 21st Century Dam Design – Advances and Adaptations, 31st Annual USSD Conference San Diego, California.
- Beaty, M. H., and P. Byrne., 2011. "UBCSAND constitutive model version 904ar." Documentation Report, UBCSAND Constitutive Model on Itasca UDM Web Site.
- Beaty M. H., and Byrne P., 2000. "A synthesized approach for predicting liquefaction and resulting displacements." Proceedings of the Twelve World Conference on Earthquake Engineering, Auckland, New Zealand, Paper No. 1589.
- Begum N. Al., Muthukkumaran K., 2008. "Numerical modeling for laterally loaded piles on a sloping ground." Proceedings of the 12th International Conference of International Association for Computer Methods and Advances in Geomechanics (IACMAG), Goa, India.
- Bennett M. J., McLaughlin P. V., Sarmiento J. S., and Youd T. L., 1984. "Geotechnical investigation of liquefaction sites." Imperial Valley, California, U.S. Geol. Surv. Open-File Rept., pp. 84-252.
- Bhattacharya S., 2003. "Pile instability during earthquake liquefaction." PhD Thesis, University of Cambridge.
- Biswas A., Naik A. N., 2010. "Study on liquefaction of soil." National Institute of Technology Rourkela.
- Bolton, M. D., 1986. "The strength and dilatancy of sands." *Géotechnique* 36(1), pp. 65–78.
- Bonilla, L. F., Archuleta R. J., and Lavalle D., 2005. "Hysteretic and dilatant behavior of cohesionless soils and their effects on nonlinear site response: field data observations and modeling." *Bull. Seism. Soc. Am.* 95, pp. 2373–2395.
- Boulanger R. W., Ziotopoulou K., 2012. "PM4SAND (Version 2): A Sand Plasticity Model for Earthquake Engineering Applications." Department of Civil and Environmental Engineering, University of California at Davis, Report no. UCD/CGM-12/01.

- Boulanger R. W., 2010. "A sand plasticity model for earthquake engineering applications." Report No. UCD/CGM-10-01, Center for Geotechnical Modeling, Department of Civil and Environmental Engineering, University of California, Davis, CA, 77 pp.
- Broms B., 1964a. "The lateral resistance of piles in cohesionless soils." *Journal of the Soil Mechanics & Foundation Division, ASCE*, 90 (SM2), pp. 27-63.
- Broms B., 1964b. "The lateral resistance of piles in cohesive soils." *Journal of the Soil Mechanics & Foundation Division, ASCE*, 90 (SM3), pp. 123-56.
- Byrne P.M., Park S.S., Beaty M., Sharp M.K., Gonzalez L., & Abdoun T., 2004. "Numerical modeling of liquefaction and comparison with centrifuge tests." *Canadian Geotechnical Journal*, Vol. 41(2), pp. 193-211.
- Byrne P.M., 1991. "A model for predicting liquefaction induced displacements." *Proceedings of Second International Conf. on Recent Advances in Geotechnical Earthquake Engineering and Soil Dynamics, St. Louis, Vol. 2*, pp. 1027-1035.
- Byrne P. M., and Anderson D. L., 1991. "Earthquake design in the Fraser Delta, task force report." City of Richmond, B.C. publication and Soil Mech. Series No. 150, Dept. of Civil Engineering, University of British Columbia, Vancouver, B.C.
- Castro G., Poulos S. J., 1977. "Factors affecting liquefaction and cyclic mobility." *J. Geotech. Engng Div. Am. Soc. Civ. Engrs.* 103, pp. 501-516.
- Cetin K.O., Bilge H. T., 2014 "Effective stress-based large strain modulus degradation response of fully saturated clean sands." (in progress).
- Cetin K.O., Bilge H. T., 2012. "Cyclic large strain and induced pore pressure models for saturated clean sands." *ASCE J. of Geotechnical and Geoenviron. Eng.* 138(3), pp. 309-323.
- Cetin K. O., Bilge H. T., Wu J., Kammerer A. M., Seed R. B., 2009. "Probabilistic model for the assessment of cyclically induced reconsolidation (volumetric) settlements." *ASCE J. of Geotechnical and Geoenviron. Eng.* 135(3), pp. 387-398.

- Cetin K. O., Bilge H. T., Wu J., Kammerer A. M., Seed R. B., 2009. "Probabilistic model for cyclic straining of saturated clean sands." *ASCE J. of Geotechnical and Geoenviron. Eng.* 135(3), pp. 371-386.
- Cetin K. O., Seed R. B., Der Kiureghian A., Tokimatsu K., Harder L. F., Kayen R. E., and Moss R. E. S., 2004. "Standard penetration test-based probabilistic and deterministic assessment of seismic soil liquefaction potential." *J. Geotechnical and Geoenvironmental Eng., ASCE* 130(12), pp. 1314–340.
- Comartin, C., Gree, M., and Tubbesing S., 1995. "The Hyogoken-Nanbu earthquake." Preliminary Reconnaissance Report, Earthquake Engineering Research Institute, Oakland CA.
- Cubrinovski M., Ishihara K., Tanizawa F., 1996. "Numerical simulation of the Kobe port island liquefaction." *Proceedings of 11th World Conference on Earthquake Engineering*, Paper No: 330.
- Cuellar P., 2011. "Pile foundations for offshore wind turbines: numerical and experimental investigations on the behavior under short-term and long-term cyclic loading." PhD Thesis, Technische Universität Berlin.
- Dafalias Y. F. and Manzari M. T., 2004. "Simple plasticity sand model accounting for fabric change effects." *Journal of Engineering Mechanics, ASCE*, 130(6), pp. 622-634.
- Davis R. O. and Berrill J. B., 2001. "Pore pressure and dissipated energy in earthquakes – field verification." *J. Geotech. Geoenviron. Eng.*, 127(3), pp. 269-274.
- Dawson E. M., et al., 2001. "A practice-oriented pore pressure generation model." *Proceedings of the 2th International FLAC Symposium, Lyon, France, May 2006*, pp. 47-52.
- Davisson M.T. and Gill H.L., 1963. "Laterally loaded piles in a layered soil system." *Journal of the Soil Mechanics and Foundations Engineering, ASCE*, 89(3), pp. 63-94.
- De Alba P., Chan C. K. and Seed H. B., 1975. "Determination of soil liquefaction characteristics by large-scale laboratory test." Report NO. EERC 75-14,

- Earthquake Engineering Research Center, University of California, Berkeley, California.
- Dobry R., Abdoun T., O'Rourke T. D., Goh S.H., 2003. "Single piles in lateral spreads: field bending moment evaluation." *Journal of Geotechnical and Geoenvironmental Engineering*, 129(10), pp. 879-889.
- Dobry R., Ladd R. S., Yokel F. Y., Chung R. M., Powell D., 1982. "Prediction of pore water pressure buildup and liquefaction of sands during earthquakes by the cyclic strain method." *National Bureau of Standards Building Science Series 138*, National Bureau of Standards, U.S. Dept. of Commerce.
- Duncan J. M., Evans L. T., Ooi P. S. K., 1994. "Lateral load analysis of single piles and drilled shafts." *J. Geotech. Engrg.*, 120(6), pp. 1018-1033.
- Edil T. B. and Luh G. F., 1978. "Dynamic Modulus and Damping Relationships for Sands." *Proceedings on the Specialty Conference on Earthquake Engineering and Soil Dynamics*, ASCE, Pasadena, CA, pp. 394-409.
- Elgamal A., 2007. "Nonlinear modeling of large-scale ground-foundation-structure seismic response." *ISET Journal of Earthquake Technology*, Paper no. 488, 44(2), pp. 325-339.
- Elgamal A., He L., Lu J., Abe A., Abdoun T., Dobry R., Sato M., Tokimatsu K., Shantz T., 2006. "Liquefaction-induced lateral load on piles." *4th International Conference on Earthquake Engineering*, Taipei, Taiwan.
- Elgamal A., Yang Z., Parra E., Ragheb A., 2003. "Modeling of cyclic mobility in saturated cohesionless soils." *International Journal of Plasticity*, 19, pp. 883-905.
- Elgamal A., Yang Z.H., Parra E., 2002. "Computational modeling of cyclic mobility and post-liquefaction site response." *Soil Dynamics and Earthquake Engineering*, 22, pp. 259-271.
- Elgamal A., Zeghal M., Parra E., 1996. "Liquefaction of reclaimed island in Kobe, Japan." *Journal of Geotechnical Engineering*, 122(1), pp. 39-49.
- Evans, L. T. and Duncan, J. M., 1982. "Simplified analysis of laterally loaded piles." *Rep. No. UCB/GT/82-04*, University of California, Berkeley, California.

- Finn W. D. L. and Thavaraj T., 2001. "Deep foundations in liquefiable soil" Proceedins of 4th Int.Conf. on Recent Adv. in Geotech. Earth. Engrg. And Soil Dynamics, San Diego.
- Finn W. D. L., Yogendrakumar M. and Yoshida N., 1986. "Response of 2D embankment systems to seismic loading – program TARA-3." Soil Mechanics Series, Univ. of British Columbia, Canada.
- Finn W. D. L., Lee K. W., and Martin G. R., 1977. "An effective stress model for liquefaction." J. Geotech. Engrg. Div., 103(6), pp. 517–533.
- Finn W. D. L., Martin G. R., and Byrne P. M. (1976). "Seismic response and liquefaction of sands." J. Geotech. Eng. Div., 102(8), pp. 841-856.
- "FLAC Manual, 2011. Itasca.Consulting Group Inc.
- Gerolymos N., Escoffier S., Gazetas G., Garnier J., 2009. "Numerical modeling of centrifuge cyclic lateral pile load experiments." Earthquake Engineering & Engineering Vibration 8, pp. 61-76.
- Giannakos S., Gerolymos N., Gazetas G., 2011. "On the lateral response of piles: numerical analysis against centrifuge experiments." 5th International Conference on Earthquake Geotechnical Engineering, Santiago, Chile.
- Gill, H. L., and Demars K. R., 1970. "Displacement of laterally loaded structures in nonlinearly responsive soil." Naval Civil Engineering Laboratory, Report R-670, Port Hueneme, California.
- Glaser S.,1996. "Insight into liquefaction by system identification." Geotechnique 46, pp. 641–655.
- Gu, W. H., Morgenstern N. R., and Robertson P. K., 1994. "Postearthquake deformation analysis of the Wildlife site." J. Geotech. Eng. ASCE 120, pp. 274–289.
- Hamada M., and O'Rourke T. D., 1992. "1983 Nihonkai Chubu Earthquake." Proceedins of 4th Japan-U.S. workshop on earthquake resistant design of lifeline facilities and countermeasures for soil liquefaction, Technical Rep. No. NCEER-92-0019, MCEER Publications, Buffalo, N.Y.
- Hansen, J.B., 1961. "The ultimate resistance of rigid piles against transversal forces." DanishGeotechnical Institute, Bulletin no.12, Copenhagen, pp. 5-9.

- Hardin B.O. and Drnevich V. P., 1972a. "Shear modulus and damping in soils: measurement and parameters effects." *J. of the Soil Mech. Found. Div.*, 98(7), pp. 603-624.
- Hardin B.O. and Drnevich V. P., 1972b. "Shear modulus and damping in soils: design equations and curves." *J. of the Soil Mech. Found. Div.*, 98(7), pp. 667-692.
- Hashash Y. M. A., 2009. "DEEPSOIL V3.5 1-D nonlinear and equivalent linear wave propagation analysis program for geotechnical seismic site response analysis of soil deposits." User Manual and Tutorial, Dept. of Civil and Environmental Engineering, University of Illinois at Urbana-Champaign.
- Hashash Y. M. A., and Park D., 2001. "Non-linear one dimensional seismic ground motion propagation in the Mississippi embayment." *Engineering Geology*, 62(1-3), pp. 185-206.
- He L., 2005. "Liquefaction-induced lateral spreading and its effects on pile foundations." Ph.D. Thesis, Dept. of Structural Engineering, University of California, San Diego, La Jolla, California.
- Hetenyi M., 1946. "Beams on Elastic Foundation; Theory with Applications in the Fields of Civil and Mechanical Engineering." The University of Michigan press, Ann Arbor.
- Horne J. C., 1996. "Effects of liquefaction-induced lateral spreading on pile foundations." PhD Thesis, University of Washington.
- Holzer T. L., Youd T. L., 2007. "Liquefaction, ground oscillation, and soil deformation at the wildlife array, California." *The Seismological Society of America (Bulletin)*, 97(3), pp. 961-976.
- Holzer T. L., Youd T. L. and Bennett M. J., 1989a. "Insitu measurement of pore pressure buildup during liquefaction." 20th Joint Meeting of the U.S.-Japan Cooperative Program in Natural Resources, Panel on Wind and Seismic Effects, National Institute of Standards and Technology Special Paper 760, pp. 118-130.

- Holzer T. L., Youd T. L., and Hanks T. C., 1989b. "Dynamics of liquefaction during the 1987 Superstition Hills, California, earthquake." *Science* 244, pp. 56–59.
- Hushmand B., Scott R. F. and Crouse C. B., 1992. "In-place calibration of USGS pore pressure transducers at Wildlife Liquefaction Site, California, USA." *Proceedings of 10th Earthquake Engineering World Conference*, Balkema, Rotterdam, The Netherlands, pp. 1263–1268.
- Idriss I. M., Boulanger R. W., 2008. "Soil liquefaction during earthquakes." *Earthquake Engineering Research Institute MNO-12*.
- Idriss I. M., and Boulanger R. W., 2006. "Semi-empirical procedures for evaluating liquefaction potential during earthquakes." *J. Soil Dynamics and Earthquake Eng.* 26, pp. 115–30.
- Idriss I. M., and Boulanger R. W., 2004. "Semi-empirical procedures for evaluating liquefaction potential during earthquakes." *Proceedings, 11th International Conference on Soil Dynamics and Earthquake Engineering, and 3rd International Conference on Earthquake Geotechnical Engineering*, D. Doolin et al., eds., Stallion Press, Vol. 1, pp. 32–56.
- Ishihara K., and Cubrinovski M., 1998. "Performance of large-diameter piles subjected to lateral spreading of liquefied deposits." *Proceedings of 13th Southeast Asian Geotechnical Conference*.
- Ishihara K., 1993. "Rankine Lecture: "Liquefaction and flow failure during earthquakes." *Geotechnique* 43, No-3, pp 351-415.
- Ishihara K., and Yoshimine M., 1992. "Evaluation of settlements in sand deposits following liquefaction during earthquakes." *Soils Found*, 32 (1), pp. 861–878.
- Ishihara K., 1985. "Stability of natural deposits during earthquakes." *Proceedings of 11th International Conference on Soil Mechanics and Foundation Engineering*, San Francisco, (1) pp. 321-376.
- Iwasaki, T. and Tatsuoka, F., 1977. "Effects of grain size and grading on dynamic shear moduli of sand." *Soils and Foundations, JSSMFE*, Vol. 17, No. 3, pp. 19-35.

- Jakrapiyanun, W., 2002. "Physical modeling of dynamic soil-foundation-structure-interaction using a laminar container." Ph.D. Dissertation, Department of Structural Engineering, University of California San Diego, La Jolla, U.S.A.
- Jang Y., Kim Y., 2013. "Centrifugal model behavior of laterally loaded suction pile in sand." *KSCE Journal of Civil Engineering* 17(5), pp. 980-988.
- Japanese Geotechnical Society, 1996. "Special issue on geotechnical aspects of the January 17 1995 Hyogoken-Nambu Earthquake." *Soils and Foundations Journal*.
- Japan Road Association, 2002. "Design specifications of highway bridges: Part V seismic design." Tokyo, Japan.
- Juan, C.H., Jiang T. and Andrus R.D., 2002. "Assessing probability-based methods for liquefaction potential evaluation." *Journal of Geotechnical and Geoenvironmental Engineering, ASCE*, 2002; 128(7), pp. 580-589.
- Juirnarongrit T., Ashford S. A., 2004. "Analyses of pile responses based on results from full-scale lateral spreading test: tokachi blast experiment." 13th World Conference on Earthquake Engineering, Vancouver, Canada.
- Kerciku A. A., Bhattacharya S., Lubkowski Z. A., Burd H. J., 2008. "Failure of showa bridge during the 1964 Niigata earthquake: lateral spreading or buckling instability?" The 14th World Conference on Earthquake Engineering, Beijing, China.
- Khoury, N. Q., 1984. "Dynamic properties of soils." Master Thesis, Department of Civil Engineering, Syracuse University.
- Kong L. G., Zhang L. M., 2007. "Rate controlled lateral-load pile tests using a robotic manipulator in Centrifuge." *Geotechnical Testing Journal* 30(3).
- Kramer S. L., 1996. "Geotechnical earthquake engineering", Publ. Prentice Hall.
- Kramer S. L., 1988. "Development of P-Y curves for analysis of laterally loaded piles in western Washington." Washington State Department of Transportation Center.
- Kokusho T., 1980. "Cyclic triaxial test of dynamic soil properties for wide strain range." *Soils and Foundations, JSSMFE*, Vol. 20, No. 2, pp. 45-60.

- Kubo M., 1968. "Lateral resistance of single free-head batter piles and single fixed-head vertical piles." Monthly Reports of Transportation, Technical Research Institute, Vol 12, No.2 (in Japanese).
- Laird J. and Stokoe K.H., 1993. "Dynamic properties of remolded and undisturbed soil samples tested at high confining pressures." Technical Report Geotechnical Engineering Report GR93-6, Electric Power Research Institute, Palo Alto, California.
- Law K. T., Cao Y. L. and He G. N., 1990. "An energy approach for assessing seismic liquefaction potential." Canadian Geotech. Eng., 27(3), 320-329.
- Liao S. S. C., Veneziano D., Whitman R. V., 1988. "Regression models for evaluating liquefaction probability." Journal of Geotechnical Engineering, ASCE, Vol. 114, No. 4, pp. 389-409.
- Liu L., Dobry R., 1995. "Effect of liquefaction on lateral response of piles by centrifuge model tests." National Center for Earthquake Engineering Research (NCEER) Bulletin, 9(1).
- Liyanapathirana D. S. and Poulos H. G., 2005a. "Seismic lateral response of piles in liquefying soil." Journal of Geotechnical and Geoenvironmental Engineering, ASCE, 131, pp. 1466–1479.
- Liyanapathirana D. S. and Poulos H. G., 2005b. "Pseudo-static approach for seismic analysis of piles in liquefying soil." Journal of Geotechnical and Geoenvironmental Engineering, ASCE, 131, pp.1480–1487.
- Liyanathirana D. S. and Poulos H. G. 2002. "A numerical model for dynamic soil liquefaction analysis." Soil Dyn. Earthquake Eng., 22 (9-12), pp. 1007–1015.
- Martin G. R., Finn W. D. L. and Seed H. B., 1975. "Fundamentals of liquefaction under cyclic loading." J. Geotech. Engrg. Div.,101 (GT5), 423 -438.
- Matlock, H., 1970. "Correlation for design of laterally loaded piles in soft clay." Proceedings of 2nd Offshore Technology Conference, Dallas, Tex., pp. 577-594.
- Matlock H. and Reese L. C., 1960. "Generalized solutions for laterally loaded piles." Journal of Soil Mech. & Foundation Division, ASCE, 86, pp. 63-91.

- Matasovic N., 2006. "D-MOD_2:A computer program for seismic response analysis of horizontally layered soil deposits, earthfill dams, and solid waste landfills." User's Manual, GeoMotions, LLC, Lacey, Washington, 20p.
- Matasovic J., Vucetic M., 1996. "Analysis of seismic records from the wildlife liquefaction site." Proceedings of 11th World Conference on Earthquake Engineering, Paper No: 209.
- Matasovic, N., and Vucetic, M., 1993. "Cyclic Characterization of Liquefiable Sands." ASCE Journal of Geotechnical and Geoenvironmental Engineering, 119(11), pp. 1805-1822.
- McClelland B., and Focht J. A., 1956. "Soil modulus for laterally loaded piles." Journal of the Soil Mechanics and Foundation Division, Proceedings Paper (101), pp.1049-1063.
- Meyer B. J., Reege L. C., 1979. "Development of the procedures for the design of drilled foundations for support of overhead signs." The University of Texas at Austin.
- Meyerhof G. G., Mathur S. K., and Valsangkar A. J., 1981. "Lateral resistance and deflection of rigid walls and piles in layered soils." Canadian Geotechnical Journal, 18(2), pp. 159-170
- Mizuno H. and Hirade T., 1995. "Damage of pile foundation during 1995 Hyougoken-Nanbu earthquake, part I damage patterns and damage cases." Architectural Institute of Japan, Summaries of Technical Papers of A.I.J. Annual Meeting (Hokkaidoh), B-1, pp. 1127- 1128.
- Miyamoto Y., Sako Y., Miura K., 1992. "Dynamic behavior of pile group in liquefied sand deposit." Earthquake Engineering, Tenth World Conference, Rotterdam.
- Mohamad R. and Dobry R., 1986. "Undrained monotonic and cyclic triaxial strength of sand." J. Geotech. Engrg., 112(10), pp. 941-958.
- Naesgaard E., 2011. "A hybrid effective stress- total stress procedure for analyzing soil embankments subjected to potential liquefaction and flow." PhD Thesis, The University of British Columbia.

- Naval Facilities Engineering Command (NAVFAC), 1986. "Foundation and Earth Structures". Design Manual 7.02.
- Nakakita Y., and Watanabe Y., 1981. "Soil stabilization by preloading in Kobe Port Island." Proceedings of 9th Int. Conf. on Soil Mech. and Found. Engrg., Japanese Soc. of Soil Mech. and Found. Engrg., pp.611-622.
- NCEER, 1997. "Proceedings of the NCEER workshop on evaluation of liquefaction resistance of soils." Edited by Youd, T. L., Idriss, I. M., Technical Report No. NCEER-97- 0022, December 31.
- New York State Department of Transportation Geotechnical Engineering Bureau, 2007. "Liquefaction potential of cohesionless soils." Geotechnical Design Procedure GPD-9 Revision #2.
- Papadimitriou A. G. and Bouckovalas G. D., 2002. "Plasticity model for sand under small and large cyclic strains: a multiaxial formulation." Soil Dynamics and Earthquake Engineering, 22, pp. 191-204.
- Papadimitriou A. G., Bouckovalas G. D. and Dafalias Y. F., 2001. "Plasticity model for sand under small and large cyclic strains." Journal of Geotechnical and Geoenvironmental Engineering, ASCE 127(11), pp. 973-983.
- Park S. S., and Byrne P. M., 2004. "Practical constitutive model for soil liquefaction." Proceedings of 9th Intl. Sym. on Numerical Models in Geomechanics (NUMOG IX), pp. 181-186.
- Parker F. J. and Cox W. R., 1969. "A method of analysis of pile supported foundations considering nonlinear soil behavior." Research Report No. 117-1, Center for Highway Research, The University of Texas at Austin.
- Parker F. J. and Reese L. C. 1970. "Experimental and analytical studies of behavior of single piles in sand under lateral and axial loading." Research Report No. 117-2, Center for Highway Research, The University of Texas at Austin, Austin, Texas.
- Parra-Colmenares E. J., 1996. "Numerical modeling of liquefaction and lateral ground deformation including cyclic mobility and dilation response in soil systems." PhD Thesis, Rensselaer Polytechnic Institute Troy, New York.

- Pastor M., Zienkiewicz O. C. and Chan, A. H. C., 1990. "Generalized plasticity and the modeling of soil behavior." *Proceedings of Int. J. Num. Anal. Meths. Geomech.*, 14, pp. 151-190.
- Patra N. R., and Pise P. J., 2001. "Ultimate lateral resistance of pile groups in sand." *Journal of Geotechnical and Geoenvironmental Engineering*, 127(6), pp. 481-487.
- Phanikanth V. S., Choudhury D., Reddy G. R., 2010. "Response of single pile under lateral loads in cohesionless soils." *Electronic Journal of Geotechnical Engineering*, 15.
- Prakash S., Sharma H. D., 1990. "Pile foundations in engineering practice." A Wiley-Interscience Publication, John Wiley & Sons, Inc.
- Prevost J.H., 2002. "DYNAFLOW - Version 02, Release 01 A." User's manual, Princeton University, Princeton, NJ.
- Polito C. P., Green, R. A., and Lee, J. H., 2008. "Pore pressure generation models for sands and silty soils subjected to cyclic loading." *Journal of Geotechnical and Geoenvironmental Engineering*, 134(10), pp. 1490-1500.
- Poulos H. G., & Davis E., 1980. "Pile Foundation Analysis and Design." New York: Wiley and Sons.
- Poulos H.G., 1971. "Behaviour of laterally loaded piles." *Journal of the Soil Mechanics and Foundations Division, ASCE*, Vol. 97, Nol. SM5, pp. 711-731.
- Puebla H., Byrne P.M., & Phillips R., 1997. "Analysis of CANLEX liquefaction embankments: prototype and centrifuge models." *Canadian Geotechnical Journal*, 34(5), pp. 641-657.
- Rahman M., Karim M., Baki A. L., Paul D. K., 2008. "Ultimate lateral load resistance of laterally loaded pile." 5th International Conference on Bored and Auger Piles (BAP V), Ghent, Belgium.
- Reese L.C., 1977. "Laterally loaded piles: Program documentation." *J. Geotech. Eng. Div., Am. Soc. Civ. Eng.*, 103(4), pp. 287-305.
- Reese L.C. and Welch R.C., 1975. "Lateral loading of deep foundations in stiff clay." *Journal of the Geotechnical Engineering Division, ASCE*, Vol. 101, No. GT7, pp. 633-649.

- Reese L. C., Cox W. R. and Koop F. D., 1974. "Analysis of laterally loaded piles in sand." Proceedings, Offshore Technology Conference, Houston, Texas, Vol. II, Paper No. 2080, pp. 473-484.
- Reese L. C. and Cox W. R., 1968. "Soil behavior from analysis of tests of uninstrumented piles under lateral loading." Proceedings, Seventy-first Annual Meeting, American Society for Testing and Materials, San Francisco, California, pp. 161-176.
- Reese L.C. and Matlock H., 1956. "Non-dimensional solutions for laterally-loaded piles with soil modulus assumed proportional to depth." Proceedings of the 8th Texas Conference on Soil Mechanics and Foundation Engineering, Austin, Texas, pp.1-41.
- Ricardo R., Abdoun T. H., Dobry R., 2000. "Effect of lateral stiffness of superstructure on bending moments of pile foundation due to liquefaction-induced lateral spreading." 12th World Conference on Earthquake Engineering.
- Robertson P. K. and Fear C. E., 1996. "Soil liquefaction and its evaluation based on SPT and CPT." Liquefaction Workshop, January 1996.
- Ruigrok J. A. T., 2010. "Laterally loaded piles." Faculty of Civil Engineering and Geosciences Section of Geo-engineering.
- Sastry V. R. N. and Meyerhof G. G., 1986. "Lateral soil pressures and displacements of rigid piles in homogeneous soils under eccentric and inclined loads." Canadian Geotechnical Journal, 23, pp. 281-286.
- Sasiharan N., 2006. "Mechanics of dilatancy and its application to liquefaction problems." PhD Thesis, Washington State University.
- Schofield A. N and Wroth C. P., 1968. "Critical state soil mechanics", London, McGraw Hil.
- Seed R. B., Dickenson S. E., Riemer M. F., Bray J. D., Sitar N., Mitchell J. K., Idriss I. M., Kayen R. E., Kropp A., Hander L. F., Power M. S., 1990. "Preliminary report on the principal geotechnical aspects of the October 17, 1989, Loma Prieta Earthquake." Report No. UCB/EERC-90/05". Earthquake Engineering Research Center. University of California, Berkeley, CA.

- Seed H. B., Romo M. P., Sun J. I., Jaime A., and Lysmer J., 1987. "Relationships between soil conditions and earthquake ground motions in Mexico City in the Earthquake of September 19, 1985." Rpt. No. UCB/EERC-87/15, Earthquake Engineering Research Center, University of California, Berkeley.
- Seed H. B., Wong R. T., Idriss I. M. and Tokimatsu K., 1984. "Moduli and damping factors for dynamic analyses of cohesionless soils." Rep. No. EERC 84-14, Earthquake Engineering Research Center, Univ. of California, Berkeley, Calif.
- Seed H. B., Tokimatsu, K., Harder, L. F., Chung, R. M., 1984. "The Influence of SPT procedures in soil liquefaction resistance evaluations." Earthquake Engineering Research Center Report No. UCB/EERC-84/15, University of California at Berkeley, October, 1984.
- Seed H. B., Martin G. R., and Lysmer J., 1976. "Pore-water pressure changes during soil liquefaction." *J. Geotech. Engrg. Div.*, 102(GT4), pp. 323–346.
- Seed H. B., Martin P.P., and Lysmer J., 1975. "The generation and dissipation of pore water pressures during soil liquefaction." Report No EERC 75-26, Earthquake Research Center, Univ. of California, Berkeley.
- Seed H. B., and Idriss, I. M., 1971. "Simplified procedure for evaluating soil liquefaction potential." *J. Soil Mech. Found. Div.*, 97(SM9), pp. 1249-1273.
- Seed H. B. and Idriss I. M., 1970. "Soil moduli and damping factors for dynamic response analysis." Report No EERC 70-10, Earthquake Engineering Research Center, University of California, Berkeley.
- Shamoto Y., Zhang J., Tokimatsu K., 1998. "New charts for predicting large residual post-liquefaction ground deformation." *Soil Dynamics and Earthquake Engineering*, 17, pp. 427-438.
- Shamoto Y., Zhang J. M. and Goto S., 1997. "Mechanisms of large post-liquefaction deformation in saturated sand." *Soils and Foundations*, 37(2), 71–80.
- Shamoto Y., Zhang J. M., Goto S. & Tokimatsu K., 1996. "A new approach to evaluate post-liquefaction permanent deformation in saturated sand." Proceedings, 11th WCEE, Acapulco, Mexico.

- Sherif M. A. and Ishibashi I., 1976. "Dynamic shear modulus for dry sands." *J. of Geotechnical Engineering Division, ASCE*, Vol. 102, No. GT 11, pp. 1171-1184
- Sitar N., 1995. "Geotechnical reconnaissance of the effects of the January 17, 1995, Hyogoken-Nanbu Earthquake Japan." Report No. UCB/EERC-95/01. Earthquake Engineering Research Center, Berkeley, CA.
- Sriskandakumar S., 2004. "Cyclic loading response of Fraser River sand and for validation of numerical models simulating centrifuge tests." MSc Thesis, University of Peradeniya, Sri Lanka.
- Taiebat M. and Dafalias Y. F., 2008. "SANISAND: simple anisotropic sand plasticity model." *International Journal for Numerical and Analytical Methods in Geomechanics*, 32(8), pp. 915–948.
- Tatsuoka F., Iwasaki T. and Takagi Y., 1978. "Histeretic damping of sand under cyclic loading and its relation to shear modulus." *Soils and Foundations, JSSMFE*, Vol. 18, No. 2, pp. 25-40.
- Terzaghi K. V., 1955. "Evaluation of Coefficient of Subgrade Reaction." *Geotechnique*, 5(4): pp. 297-326.
- Tsuchida H., 1970. "Prediction and countermeasure against the liquefaction in sand deposits." Seminar in the Port and Harbor Research Institute.
- Tsukamoto Y., Ishihara K., and Sawada S., 2004. "Settlement of silty sand deposits following liquefaction during earthquakes." *Soils Found.*, 44(5), pp. 135–148.
- Tokimatsu K., and Asaka Y., 1998. "Effects of liquefaction induced ground displacements on pile performance in the 1995 Hyogoken-Nambu Earthquake." *Soils and Foundations (Special Issue)*, pp. 163-177.
- Tokimatsu K., Mizuno H., and Kakurai M., 1996. "Building damage associated with geotechnical problems." *Soils Found.*,(1), pp. 219-234.
- Tokimatsu K., and Seed H. B., 1984. "Simplified procedures for the evaluation of settlements in clean sands." Rep. No. UCB/EERC-84/16, Earthquake

- Engineering Research Center, College of Engineering, Univ. of California, Berkeley, California.
- Touma F. T., 1972. "The behavior of axially loaded drilled shafts in sand." Doctoral dissertation, Department of Civil Engineering, The University of Texas at Austin, December.
- Vucetic M and Dobry R., 1991. "Effect of soil plasticity on cyclic response." *J. Geotech. Eng., ASCE*, 89-107.
- Wang Z. L., 1990. "Bounding surface hypoplasticity model for granular soils and its applications." Ph.D. dissertation, presented to the Faculty of the Graduate School of The University of California, Davis. Information Service, Order No. 9110679, Ann Arbor, MI 48106.
- Wang G. J., Takemura J. and Kuwano J., 1997. "Evaluation of excess pore water pressures of intermediate soils due to cyclic loading by energy method." *Computer Methods and Advances in Geomechanics*, ed. J. X. Yuan, A. A. Balkema Publishers, Rotterdam, Netherlands, 2215-2220.
- Wilson D. W., 1998. "Soil-pile-superstructure interaction in liquefying sand and soft clay." PhD Thesis, University of California at Davis.
- Winkler E., 1867. "Die lehre von elasticitat und festigkeit." H. Dominicus, Prague, 182-184.
- Wu J., Seed R. B., and Pestana J. M., 2003. "Liquefaction triggering and post liquefaction deformations of Monterey 0/30 sand under unidirectional cyclic simple shear loading." Geotechnical Engineering Research Report No. UCB/GE-2003/01, University of California, Berkeley, California.
- Wu J., and Seed R. B., 2004. "Estimating of liquefaction-induced ground settlement case studies." Proc., 5th Int. Conf. on Case Histories in Geotechnical Engineering, Paper 3.09, New York.
- Yang Z., 2000. "Numerical modeling of earthquake site response including dilation and liquefaction." PhD Thesis, Columbia University.
- Yang Z., and Jeremic B., 2002. "Numerical analysis of pile behaviour under lateral loads in layered elastic-plastic soils." *Intl. J. Num. Anal. Meth. Geomech.*, 26, pp. 1385-1406.

- Youd T. L. and Carter B. L., 2005. "Influence of soil softening and liquefaction on spectral acceleration." *J. Geotech. Geoenviron. Eng. ASCE* 131, pp. 811–825.
- Youd T. L., et al., 2001. "Liquefaction resistance of soils: Summary report from the 1996 NCEER and 1998 NCEER/NSF workshops on evaluation of liquefaction resistance of soils." *J. Geotech. Geoenviron.Eng.*, 127(10), pp. 817-833.
- Youd T. L., and Noble S. K., 1997. "Liquefaction criteria based on statistical and probabilistic analyses.", *Proc., NCEER Workshop on Evaluation of Liquefaction Resistance of Soils*, NCEER Technical Rep. No: NCEER-97-0022, pp. 201–205.
- Youd T. L., and Barlett S. F., 1988. "U.S. case histories of liquefaction induced ground displacement." *Proceedings of 1st Japan-U.S. Workshop on Liquefaction, Large Ground Deformations and their Effects on Lifeline Facilities*, Tokyo, Japan, pp. 22-31
- Zamri H. C., Jasim, M. A., Mohd, R. T., and Qassun S. M., 2009. "Lateral behavior of single pile in cohesionless soil subjected to both vertical and horizontal loads." *European Journal of Scientific Research*, 29(2), pp. 194-205.
- Zeevaert L., 1973. "Foundation Engineering for Difficult Subsoil Conditions." Van Nostrand Reinhold (International) Professional and Reference.
- Zeghal M., Elgamal A., Parra E., 1996. "Analyses of site liquefaction using downhole array seismic records." *Proceedings of 11th World Conference on Earthquake Engineering*, Paper No: 371.
- Zeghal M. and Elgamal A., 1994. "Analysis of site liquefaction using earthquake records." *J. Geotech. Eng. ASCE* 120, pp. 996-1017.
- Zhang G., Robertson P. K., and Brachman R. W. I., 2002. "Estimating liquefaction-induced ground settlements from CPT for level ground." *Can. Geotech. J.*, 39(5), pp.1168-1180.
- Zhang L., Silva F., and Grismala R., 2005. "Ultimate Lateral resistance to piles in cohesion less soils." *Journal of Geotechnical and Geoenvironmental Engineering*, 131(1), pp.78-83.


```

        Double e1_,e2_,g2_,nph_,csn_,sc1_,sc2_,sc3_,bisc_,e21_,rnps_,m_x1;
        Double TStrain11_, TStrain22_, TStrain33_, TStrain32_, TStrain31_,
        TStrain12_;
        Double shear_strainmax_,
        shear_strainmin_,eff_shear_stressmax_,eff_shear_stressmin_,
        ini_mean_eff_stress_, ini_mean_ver_stress_, ini_mean_hor_stress_;
        Double memini_;
        Double alpha_;
        Double ini_static_;
        Double Post_Liq, Gama_Max_pre,shear_post,Gamma_zero_limit;
        Double shear_unload2,shear_f, mean_f;
        Double q_s, p_s, ru_old_liq,caf_;

    };
} // namespace models

// EOF

/*****
// ModelMetusand.cpp
*****/

#include "ModelMetusand.h"
#include "../src/state.h"
#include "../src/convert.h"
#include "../version.txt"
#include <algorithm>
#include <limits>
#include <cmath>
#ifndef EXAMPLE_EXPORTS
int __stdcall DllMain(void *,unsigned, void *)
{
    return 1;
}
extern "C" EXPORT_TAG const char *getName()
{
#ifdef MODELDEBUG
    return "ModelMetusandd";
#else
    return "ModelMetusand";
#endif
}
extern "C" EXPORT_TAG unsigned getMajorVersion()
{
    return MAJOR_VERSION;
}
extern "C" EXPORT_TAG unsigned getMinorVersion()
{
    return MINOR_VERSION;
}
extern "C" EXPORT_TAG void *createInstance()
{
    models::ModelMetusand *m = new models::ModelMetusand();
    return (void *)m;
}

```

```

#endif // MOHR_EXPORTS
namespace models
{
    static const Double d4d3 = 4.0 / 3.0;
    static const Double d2d3 = 2.0 / 3.0;
    static const Double pi = 3.141592653589793238462643383279502884197169399;
    static const Double degrad = pi / 180.0;
    // Plasticity Indicators
    static const UInt shear_now = 0x01; /* state logic */
    static const UInt tension_now = 0x02;
    static const UInt shear_past = 0x04;
    static const UInt tension_past = 0x08;

    ModelMetusand::ModelMetusand() : bulk_(0.0), shear_(0.0), cohesion_(0.0), friction_(0.0),
    dilation_(0.0), tension_(0.0), relden_(0.0), posnu_(0.0), ru_old_(0.0), e1_(0.0), e2_(0.0), g2_(0.0),
    nph_(0.0), csn_(0.0), sc1_(0.0), sc2_(0.0), sc3_(0.0), bisc_(0.0), e21_(0.0), rnps_(0.0),
    TStrain11_(0.0), TStrain22_(0.0), TStrain33_(0.0), TStrain32_(0.0), TStrain31_(0.0),
    TStrain12_(0.0), shear_strainmax_(0.0), shear_strainmin_(0.0), eff_shear_stressmax_(0.0),
    eff_shear_stressmin_(0.0), ini_mean_eff_stress_(0.0), ini_mean_ver_stress_(0.0),
    ini_mean_hor_stress_(0.0), memini_(0.0), alpha_(0.0), ini_static_(0.0), Gama_Max_pre(0.0),
    Post_Liq(0.0), shear_post(0.0), Gamma_zero_limit(0.0), shear_unload2(0.0), shear_f(0.0),
    mean_f(0.0)
    {
    }
    String ModelExample::getName() const
    {
#ifdef MODELDEBUG
        return L"exampled";
#else
        return L"example";
#endif
    }
    String ModelMetusand::getFullName() const
    {
#ifdef MODELDEBUG
        return L"ExampleD";
#else
        return L"Example";
#endif
    }
    UInt ModelExample::getMinorVersion() const
    {
        return MINOR_VERSION;
    }
    String ModelMetusand::getProperties(void) const
    {
        return L"bulk,shear,cohesion,friction,dilation,tension,relden,posnu,ru_old,young,poisson,"
        L"TStrain11,TStrain22,TStrain33,TStrain32,TStrain31,TStrain12, shear_strainmax,"
        L"shear_strainmin,eff_shear_stressmax,eff_shear_stressmin,"
        L"ini_mean_eff_stress,ini_mean_ver_stress,ini_static,caf";
    }
    String ModelMetusand::getStates() const
    {
        return L"shear-n,tension-n,shear-p,tension-p";
    }
}

```

```

Variant ModelMetusand::getProperty(UInt index) const
{
    switch (index)
    {
        case 1: return bulk_;
        case 2: return shear_;
        case 3: return cohesion_;
        case 4: return friction_;
        case 5: return dilation_;
        case 6: return tension_;
        case 7: return relden_;
        case 8: return posnu_;
        case 9: return ru_old_ ;
        case 10:
            {
                Double young;
                getYPfromBS(bulk_,shear_,&young,0);
                return young;
            }
            break;
        case 11:
            {
                Double poisson;
                getYPfromBS(bulk_,shear_,0,&poisson);
                return poisson;
            }
        case 12: return TStrain11_ ;
        case 13: return TStrain22_ ;
        case 14: return TStrain33_ ;
        case 15: return TStrain32_ ;
        case 16: return TStrain31_ ;
        case 17: return TStrain12_ ;
        case 18: return shear_strainmax_ ;
        case 19: return shear_strainmin_ ;
        case 20: return eff_shear_stressmax_ ;
        case 21: return eff_shear_stressmin_ ;
        case 22: return ini_mean_eff_stress_ ;
        case 23: return ini_mean_ver_stress_ ;
        case 24: return ini_static_ ;
        case 25: return ini_mean_hor_stress_ ;
        break;
    }
    return 0.0;
}

void ModelMetusand::setProperty(UInt index,const Variant &prop,UInt restoreVersion)
{
    ConstitutiveModel::setProperty(index,prop,restoreVersion);

    switch (index)
    {
        {
        case 1: bulk_ = prop.toDouble(); break;//bulk modulus
        case 2: shear_ = prop.toDouble(); break;//shear modulus
        case 3: cohesion_ = prop.toDouble(); break;//cohesion- the shear
        strength along a plane across which there is no normal stress
        case 4: friction_ = prop.toDouble(); break;//friction angle
    }
    }
}

```

```

case 5: dilation_ = prop.toDouble(); break;// sin(friction angle)
case 6: tension_ = prop.toDouble(); break;//tensile stress
case 7: relden_ = prop.toDouble(); break;//relative density
case 8: posnu_ = prop.toDouble(); break;//poisson;
case 9: ru_old_ = prop.toDouble(); break;
case 10: // YOUNG
    {
        Double young,poisson;
        getYPfromBS(bulk_,shear_,&young,&poisson);
        young = prop.toDouble();
        getBSfromYP(young,poisson,&bulk_,&shear_);
    }
    break;
case 11: // POISSON
    {
        Double young,poisson;
        getYPfromBS(bulk_,shear_,&young,&poisson);
        poisson = prop.toDouble();
        getBSfromYP(young,poisson,&bulk_,&shear_);
    }
case 12: TStrain11_ = prop.toDouble(); break;
case 13: TStrain22_ = prop.toDouble(); break;
case 14: TStrain33_ = prop.toDouble(); break;
case 15: TStrain32_ = prop.toDouble(); break;
case 16: TStrain31_ = prop.toDouble(); break;
case 17: TStrain12_ = prop.toDouble(); break;
case 18: shear_strainmax_ = prop.toDouble(); break;
case 19: shear_strainmin_ = prop.toDouble(); break;
case 20: eff_shear_stressmax_ = prop.toDouble(); break;
case 21: eff_shear_stressmin_ = prop.toDouble(); break;
case 22: ini_mean_eff_stress_ = prop.toDouble(); break;
case 23: ini_mean_ver_stress_ = prop.toDouble(); break;
case 24: ini_static_ = prop.toDouble(); break;
case 25: ini_mean_hor_stress_ = prop.toDouble(); break;
break;
}
}
Double ModelMetusand::getStressStrengthRatio(const SymTensor &st) const
{
    DVect3 prin = st.getEigenInfo();
    Double rat = 10.0;
    Double tanf = std::tan(friction_*degrad);
    Double tcut = friction_ ? std::min(tension_,(cohesion_/tanf)) : tension_;
    if (tcut - prin.z() <= 0.0)
        rat = 0.0;
    else
    {
        Double sinf = std::sin(friction_*degrad);
        Double denom = 1.0 - sinf;
        Double npf = limits<Double>::max();
        if (denom) npf = (1.0 + sinf) / denom;
        Double sig1f = npf*prin.z() - 2.0*cohesion_*std::sqrt(npf);
        denom = prin.z() - prin.x();
        if (denom) rat = (prin.z() - sig1f) / denom;
    }
}

```

```

        rat = std::min(rat,10.0);
        return(rat);
    }
    void ModelMetusand::scaleProperties(const Double &scale,const std::vector<UInt>
&props)
    {
        for (UInt u=0;u<props.size();++u)
        {
            switch (props[u])
            {
            case 1: bulk_ *= scale; break;
            case 2: shear_ *= scale; break;
            case 3: cohesion_ *= scale; break;
            case 4: friction_ = std::max(0.0,std::min(85.0,std::atan(std::tan(friction_*degrad) * scale)/
degrad)); break;
            case 5: dilation_ = std::max(0.0,std::min(85.0,std::atan(std::tan(dilation_*degrad) *
scale)/ degrad)); break;
            case 6: tension_ *= scale; break;
            case 7: relden_ *= scale; break;
            case 8: posnu_ *= scale; break;
            case 9: // YOUNG
                {
                Double young,poisson;
                getYPfromBS(bulk_,shear_,&young,&poisson);
                young *= scale;
                getBSfromYP(young,poisson,&bulk_,&shear_);
                }
                break;
            case 10: // POISSON
                {
                Double young,poisson;
                getYPfromBS(bulk_,shear_,&young,&poisson);
                poisson *= scale;
                getBSfromYP(young,poisson,&bulk_,&shear_);
                }
            case 24: ini_static_ *= scale; break;
            case 25: ini_mean_hor_stress_ *= scale; break;
            }
        }
        setValid(0);
    }
    void ModelMetusand::copy(const ConstitutiveModel *m)
    {
        ConstitutiveModel::copy(m);
        const ModelMetusand *mm = dynamic_cast<const ModelMetusand *>(m);
        if (!mm) throw std::runtime_error("Internal error: constitutive model dynamic
cast failed.");
        bulk_ = mm->bulk_;
        shear_ = mm->shear_;
        cohesion_ = mm->cohesion_;
        friction_ = mm->friction_;
        dilation_ = mm->dilation_;
        tension_ = mm->tension_;
        relden_ = mm->relden_;
        posnu_ = mm->posnu_;
    }

```

```

ru_old_ = mm->ru_old_;
TStrain11_ = mm->TStrain11_;
TStrain22_ = mm->TStrain22_;
TStrain33_ = mm->TStrain33_;
TStrain32_ = mm->TStrain32_;
TStrain31_ = mm->TStrain31_;
TStrain12_ = mm->TStrain12_;
shear_strainmax_ = mm->shear_strainmax_;
shear_strainmin_ = mm->shear_strainmin_;
eff_shear_stressmax_ = mm->eff_shear_stressmax_;
eff_shear_stressmin_ = mm->eff_shear_stressmin_;
ini_mean_eff_stress_ = mm->ini_mean_eff_stress_;
ini_mean_ver_stress_ = mm->ini_mean_ver_stress_;
ini_static_ = mm->ini_static_;
ini_mean_hor_stress_ = mm->ini_mean_hor_stress_;
}
void ModelMetusand::initialize(UByte dim,State *s) {
    ConstitutiveModel::initialize(dim,s);
    e1_ = bulk_ + shear_*d4d3;//elastic constants
    e2_ = bulk_ - shear_*d2d3;//(2.73)
    g2_ = shear_*2.0;
    Double rsin = std::sin(friction_ * degrad);
    nph_ = (1.0 + rsin) / (1.0 - rsin);// (2.78)
    csn_ = 2.0 * cohesion_ * sqrt(nph_);
    if (friction_)
    {
        Double apex = cohesion_ * std::cos(friction_ * degrad) / rsin;
        tension_ = std::min(tension_,apex);
    }
    rsin = std::sin(dilation_ * degrad);
    rnps_ = (1.0 + rsin) / (1.0 - rsin);
    Double ra = e1_ - rnps_ * e2_;
    Double rb = e2_ - rnps_ * e1_;
    Double rd = ra - rb * nph_;
    sc1_ = ra / rd;
    sc3_ = rb / rd;
    sc2_ = e2_ * (1.0 - rnps_) / rd;
    bisc_ = std::sqrt(1.0 + nph_*nph_) + nph_;// (2.84)
    e21_ = e2_ / e1_;
}
double ModelMetusand::GetTheta(SymTensor& tensor_original) {
    return tensor_original.s12();
}
double ModelMetusand::GetTheta_Real(SymTensor& tensor) {
    Double tmp_eff_shear = tensor.getEffectiveShearStress();
    SymTensor Strain_Dev = tensor;
    double Eps_Trace = tensor.getTrace();
    Strain_Dev.rs11() = tensor.s11()-Eps_Trace/3.0;
    Strain_Dev.rs22() = tensor.s22()-Eps_Trace/3.0;
    Strain_Dev.rs33() = tensor.s33()-Eps_Trace/3.0;
    double Eps_J3 = Strain_Dev.getDeterminate();
    double Theta =0.0;
    if (tmp_eff_shear >0)
    {

```

```

        double sin3Theta = -
3.0*std::sqrt(3.0)*Eps_J3/(tmp_eff_shear*tmp_eff_shear*tmp_eff_shear)/2.0;
        if (sin3Theta >= 1.0 )
            Theta = (std::asin(1.0))/3.0;
        else if (sin3Theta <= -1.0)
            Theta = (std::asin(-1.0))/3.0;
        else
            Theta = (std::asin(sin3Theta))/3.0;
    }
    return Theta;
}

bool ModelMetusand::LoadingDirectionChanged(SymTensor& tensor,
SymTensor& d_tensor) {
    SymTensorInfo info;
    DVect3 prin = tensor.getEigenInfo(&info);
    DVect3 Direction1 = info.getAxes().e1();
    SymTensorInfo d_info;
    DVect3 d_prin = d_tensor.getEigenInfo(&d_info);
    DVect3 d_Direction1 = d_info.getAxes().e1();
    return true;
}

void ModelMetusand::run_Sevinc(State *s){
    if (!(memini_>=1.00))
    {
        if (s->sub_zone_ == s->total_sub_zones_-1) {
            memini_ = 1.0 ;
        }
        ini_mean_eff_stress_ =(s->stnS_.getTrace()/3.0);
        ini_mean_ver_stress_ =(s->stnS_.s22());
        ini_mean_hor_stress_ =(s->stnS_.s11());
    }

    Double ko_ =ini_mean_hor_stress_/ini_mean_ver_stress_;
    //Double ko_=1.0;
    if (!s->sub_zone_) {
        for (int i=1; i<s->max_working_; i++)
            s->working_[i]=0.0;
    }
    Double dEv = s->getSubZoneVolume();
    if (s->hysteretic_damping_>0.0) {
        // storing the State/Memory variables in the names that we like
        s->working_[11] += s->stnE_.s11()* dEv;
        s->working_[12] += s->stnE_.s22()* dEv;
        s->working_[13] += s->stnE_.s33()* dEv;
        s->working_[14] += s->stnE_.s32()* dEv;
        s->working_[15] += s->stnE_.s31()* dEv;
        s->working_[16] += s->stnE_.s12()* dEv;
    }
    SymTensor Strain_Total; SymTensor Stress_Trial; SymTensor Stress_Trial2;
    Strain_Total.rs11() = TStrain11_ ;
    Strain_Total.rs22() = TStrain22_ ;
    Strain_Total.rs33() = TStrain33_ ;
    Strain_Total.rs32() = TStrain32_ ;
    Strain_Total.rs31() = TStrain31_ ;

```



```

Strain_Total.rs12() = TStrain12_ ;
// End of storing State/Memory variables
Double shear_strainmin_limit = -0.01;
Double shear_strainmax_limit = +0.01;
// calculate the Gama_max_N
Double shear_strain = Strain_Total.s12();
if (shear_strain>=shear_strainmax_)
    s->working_[2]+=shear_strain* dEv;
if (shear_strain<=shear_strainmin_)
    s->working_[3]+=shear_strain* dEv;
Double Gama_Max_N_ =std::min(100*(std::abs(2*shear_strainmax_ -
2*shear_strainmin_)),50.0);
// End of calculating the Gama_max_N
//s->working_[6]=Gama_Max_N_;
s->working_[6]=std::abs(200*shear_strain);
if (Post_Liq <= 0.0) { // pre_liquefaction
    // calculate the Ru (pore pressure factor)
    bool if_Elastic = false;
    Double ru_=0.0;
    if (!(Gama_Max_N_>2.0e-4))
        if_Elastic = true;
    else
        ru_=std::min(1.0,1-std::exp((-(-0.407*Gama_Max_N_)/(-
0.486+0.025*(std::log(ini_mean_ver_stress_))-
(relden_/100))))*(0.620/(1+Gama_Max_N_)+1));

    // End of Calculating Ru
    // Calculating the pore water pressure and the
loading/unloading elastic modulus
    Double shear_unload = shear_;
    Double shear_load = shear_;
    Double Grat=1;
    Double PWP_=0.0;
    if ((if_Elastic))
    {
        shear_unload = shear_;
        shear_load = shear_;
    }
    else
    {
shear_load=std::max((shear_*(1+37.1*(std::pow(std::pow(10.0,-
4.0),1.060)))/(1+37.1*std::pow(Gama_Max_N_/2,1.060))*(std::pow(((1-
ru_+0.05)*0.0479*(ini_mean_eff_stress_),(0.5+0.01*Gama_Max_N_/2)))/(std::pow(((1+0.05)*0.
0479*(ini_mean_eff_stress_),(0.5+0.01*10e-4)))),1.0);
        s->working_[31]=shear_load;
        Grat= std::max((shear_load/shear_),0.0005);
        shear_unload=shear_load*(2.5-(Grat));
        s->working_[32]=shear_unload;
        s->working_[30]=std::abs(shear_unload);
    }
    PWP_ = ini_mean_ver_stress_* (ru_-ru_old_);
    //PWP_ = ini_mean_ver_stress_* (ru_);
    // End of calculating the pore water pressure and the
loading/unloading elastic modulus
    // trial for checking loading or unloading

```

```

// Use unloading modulus for the calculation
posnu_=(3*bulk_-2*shear_)/(2*(shear_+3*bulk_));
double Bulk = 2.0*shear_unload*(1.0+posnu_) / (3.0 * (1-
2.0*posnu_));

Double e1a_ = Bulk + shear_unload * d4d3;
Double e2a_ = Bulk- shear_unload * d2d3;
Double g2a_ = 2.0 * shear_unload;
Double e11 = s->stnE_.s11();//strain tensors normal

components
Double e22 = s->stnE_.s22();
Double e33 = s->stnE_.s33();
Stress_Trial.rs11()=-PWP_*ko_+std::min(+s->stnS_.s11() + e11 * e1a_ + (e22 + e33) *
e2a_,10.0);//-PWP+ ;
Stress_Trial.rs22()=-PWP_+std::min(+s->stnS_.s22() + (e11 + e33) * e2a_ + e22 *
e1a_,10.0);//-PWP;
Stress_Trial.rs33()=-PWP_*ko_+std::min(+s->stnS_.s33() + (e11 + e22) * e2a_ + e33 *
e1a_,10.0);//-PWP;
Stress_Trial.rs12() = s->stnS_.s12() + s->stnE_.s12() * g2a_;
Stress_Trial.rs13() = s->stnS_.s13() + s->stnE_.s13() * g2a_;
Stress_Trial.rs23() = s->stnS_.s23() + s->stnE_.s23() * g2a_;
// Trial Stress has been calculated
// check for loading/unloading
Double Trial_Shear_Stress = std::abs(Stress_Trial.s12());//
Stress_Trial.getEffectiveShearStress();
Double Trial_Theta_Stress = GetTheta(Stress_Trial);
// if unloading accept the stress trial
bool if_Loading = true;
if ((Trial_Shear_Stress < eff_shear_stressmax_) &&
(Trial_Theta_Stress >= 0.0))
{
s->stnS_ = Stress_Trial;
if_Loading = false;
s->working_[4] += eff_shear_stressmax_ *dEv;
s->working_[5] += 0.0 * dEv;
}
if ((Trial_Shear_Stress < eff_shear_stressmin_) &&
(Trial_Theta_Stress <= 0.0))
{
s->stnS_ = Stress_Trial;
if_Loading = false;
s->working_[4] += 0.0 *dEv;
s->working_[5] += eff_shear_stressmin_ * dEv;
}
// if loading re calculate the stress using loading modulus
if ((if_Loading)&&!(if_Elastic))
{
Bulk = 2.0*shear_load*(1.0+posnu_) / (3.0 * (1-2.0*posnu_));
e1a_ = Bulk + shear_load * d4d3;
e2a_ = Bulk- shear_load * d2d3;
g2a_ = 2.0 * shear_load;
Stress_Trial.rs11()=-PWP_*ko_+std::min(+s->stnS_.s11() + e11 * e1a_ + (e22
+ e33) * e2a_,10.0);//-PWP+ ;
Stress_Trial.rs22()=-PWP_+std::min(+s->stnS_.s22() + (e11 + e33) * e2a_ +
e22 * e1a_,10.0);//-PWP;

```

```

Stress_Trial.rs33()=-PWP_*ko_+std::min((s->stnS_.s33() + (e11 + e22) * e2a_
+ e33 * e1a_),10.0);//-PWP;

//Stress_Trial.rs33()=(Stress_Trial.rs11()+Stress_Trial.rs22())/2.0;

Stress_Trial.rs12() = s->stnS_.s12() + s->stnE_.s12() * g2a_;
Stress_Trial.rs13() = s->stnS_.s13() + s->stnE_.s13() * g2a_;
Stress_Trial.rs23() = s->stnS_.s23() + s->stnE_.s23() * g2a_;
// update the stress and the state variables and exit
Trial_Shear_Stress = std::abs(Stress_Trial.s12());
//Stress_Trial.getEffectiveShearStress();
Trial_Theta_Stress = GetTheta(Stress_Trial);

if ((Trial_Shear_Stress > eff_shear_stressmax_) && (Trial_Theta_Stress >= 0.0))
{
s->working_[4] += Trial_Shear_Stress* dEv;
s->working_[5]=0.0;

}

if ((Trial_Shear_Stress > eff_shear_stressmin_) && (Trial_Theta_Stress <= 0.0))
{
s->working_[4] = 0.0;
s->working_[5] += Trial_Shear_Stress* dEv;
}
}

// Update the stress state and state/memory variables and exit
s->working_[1] += ru_ * dEv;
/*PWP_ = ini_mean_ver_stress_* (ru_-ru_old_);
SymTensorInfo info;
DVect3 prin = s->stnS_.getEigenInfo(&info);
prin.rx()=prin.x()-PWP_;
prin.ry()=prin.y()-PWP_*ko_;
prin.rz()=prin.z()-PWP_*ko_;
Stress_Trial2 = info.resolve(prin);
Stress_Trial.rs11()=Stress_Trial2.s11();
Stress_Trial.rs22()=Stress_Trial2.s22();
Stress_Trial.rs33()=Stress_Trial2.s33());*/
s->stnS_ = Stress_Trial;
s->working_[33]=Stress_Trial.s12();
s-
>working_[34]=(Stress_Trial.s11()+Stress_Trial.s22()+Stress_Trial.s33())/3;
//;-- update stored strains and plastic strain ---
if (s->sub_zone_ == s->total_sub_zones_-1) {
Double Ev = s->getZoneVolume();
Double Aux = 1./Ev;
if (s->overlay_==2) Aux *= 0.5;
ru_old_ = s->working_[1] * Aux;
if ((s->working_[2] * Aux)> shear_strainmax_)
shear_strainmax_ = s->working_[2] * Aux;
if ((s->working_[3] * Aux)< shear_strainmin_)
shear_strainmin_ = s->working_[3] * Aux;
eff_shear_stressmax_ = s->working_[4] * Aux;
eff_shear_stressmin_ = s->working_[5] * Aux;
TStrain11_+= s->working_[11] * Aux;
TStrain22_+= s->working_[12] * Aux;

```

```

TStrain33_+= s->working_[13] * Aux;
TStrain32_+= s->working_[14] * Aux;
TStrain31_+= s->working_[15] * Aux;
TStrain12_+= s->working_[16] * Aux;
Gama_Max_pre = s->working_[6] * Aux*2.0;
shear_post=s->working_[30] * Aux*2.0;
shear_f=s->working_[33] * Aux*2.0;
mean_f=s->working_[34] * Aux*2.0;
if(!(if>Loading))
shear_unload2= s->working_[32] * Aux*2.0;
    }
    //return;
    // plasticity indicator:
    // store 'now' info. as 'past' and turn 'now' info off
    int plas = 0;
    Double frictionf = friction_;//-(friction_-28)*ru_;
    double dilationf = dilation_;//-(friction_-frictionf);
    double rsinf = std::sin(frictionf * degrad);
    double nphf = (1.0 + rsinf) / (1.0 - rsinf);// (2.78)
    double csnf = 2.0 * cohesion_ * sqrt(nphf);
    Double tensionf= tension_;
    if (frictionf)
    {
    Double apexf = cohesion_ * std::cos(frictionf * degrad) / rsinf;
    tensionf = std::min(tension_,apexf);
    }
    rsinf = std::sin(dilationf * degrad);
    Double rnpsf = (1.0 + rsinf) / (1.0 - rsinf);
    Double raf = e1a_ - rnpsf * e2a_;
    Double rbf = e2a_ - rnpsf * e1a_;
    Double rdf = raf - rbf * nphf;
    Double sc1f = raf / rdf;
    Double sc3f = rbf / rdf;
    Double sc2f = e2a_ * (1.0 - rnpsf) / rdf;
    Double biscf = std::sqrt(1.0 + nphf*nphf) + nphf;
    Double e21a_ = e2a_ / e1a_;
    // default settings, altered below if found to be failing
    s->viscous_ = true; // Allow stiffness-damping terms
    s->mean_plastic_stress_change_ = 0.0;
    if (canFail())
    {
    // Calculate principal stresses
    SymTensorInfo info;
    DVect3 prin = s->stnS_.getEigenInfo(&info);
    /* --- Mohr-Coulomb failure criterion --- */
    Double fsurf = prin.x() - nphf * prin.z() + csnf;//(2.76)
    /* --- Tensile failure criteria --- */
    Double tsurf = tensionf - prin.z();// (2.77)
    Double pdiv = -tsurf + (prin.x() - nphf * tensionf + csnf) * biscf;
    /* --- tests for failure */
    if (fsurf < 0.0 && pdiv < 0.0)
    { //this is domain 1 in fig 2.6
    plas = 1;
    /* --- shear failure: correction to principal stresses ---*/
    s->state_ |= shear_now;

```

```

    prin.rx() -= fsurf * sc1f; //(2.87) plastic corrections (2.88) and (2.91)
    prin.ry() -= fsurf * sc2f;
    prin.rz() -= fsurf * sc3f;
    }
    else if (tsurf < 0.0 && pdiv > 0.0)
    { // domain 2
    plas = 2;
    /* --- tension failure: correction to principal stresses ---*/
    s->state_ |= tension_now;
    Double tco = e21_ * tsurf;
    prin.rx() += tco; //(2.93)
    prin.ry() += tco;
    prin.rz() = tensionf;
    }
    if (plas)
    {
    s->working_[10] += 1.0;

    if (s->sub_zone_ == s->total_sub_zones_-1) {
    Double Ev = s->getZoneVolume();
    Double Aux = 1./Ev;
    if (s->overlay_==2) Aux *= 0.5;
    Post_Liq += s->working_[10] * Aux;
    }
    //Double smelas3 = s->stnS_.s11() + s->stnS_.s22() + s->stnS_.s33();
    //s->stnS_ = info.resolve(prin); // transform back to reference frame
    //s->viscous_ = false; // Inhibit stiffness-damping terms
    //s->mean_plastic_stress_change_ = (smelas3 - s->stnS_.s11() - s->stnS_.s22() - s->stnS_.s33()) /
    3.0;
    }
    }

    } // pre_liquefaction

    else
    { // post_liquefaction
;
    Stress_Trial.rs11() = s->stnS_.s11() ;//-PWP+ ; //(2.12) (2.72)
    Stress_Trial.rs22() = s->stnS_.s22() ;//-PWP;
    Stress_Trial.rs33() = s->stnS_.s33() ;//-PWP;
    Stress_Trial.rs12() = s->stnS_.s12() ;
    Stress_Trial.rs13() = s->stnS_.s13() ;
    Stress_Trial.rs23() = s->stnS_.s23() ;

    //Double fric_f= (-ini_mean_eff_stress_/ini_mean_ver_stress_2)*(std::max((friction_-5.0),26.0));
    Double ru_=std::min(std::abs(1-(std::abs(Stress_Trial.s12()/ini_mean_ver_stress_2)
    /std::tan(friction_*degrad))),1.0);
    Double PWP_ = ini_mean_ver_stress_* (ru_-ru_old_);
    bool Gama_Limit_Factor = true;
    posnu_=(3*bulk_-2*shear_)/(2*(shear_+3*bulk_));
    Double Bulk = 2.0*shear_*(1.0+posnu_) / (3.0 * (1-2.0*posnu_));
    Double e1a_ = Bulk + shear_* d4d3;
    Double e2a_ = Bulk- shear_* d2d3;
    Double g2a_ = 2.0 * shear_;
    Double e11 = s->stnE_.s11(); //strain tensors normal components
    Double e22 = s->stnE_.s22());

```

```

        Double e33 = s->stnE_.s33();
        Stress_Trial.rs11() = -PWP_*ko_+std::min(+ (s->stnS_.s11() + e11 *
        e1a_ + (e22 + e33) * e2a_),10.0);//-PWP+ ;
        Stress_Trial.rs22() = -PWP_+std::min(+ (s->stnS_.s22() + (e11 + e33) *
        e2a_ + e22 * e1a_),10.0);//-PWP;
        Stress_Trial.rs33() = -PWP_*ko_+std::min(+ (s->stnS_.s33() + (e11 +
        e22) * e2a_ + e33 * e1a_),10.0);//-PWP;
        Stress_Trial.rs12() = s->stnS_.s12() + s->stnE_.s12() * g2a_;

        Stress_Trial.rs13() = s->stnS_.s13() + s->stnE_.s13() * g2a_;
        Stress_Trial.rs23() = s->stnS_.s23() + s->stnE_.s23() * g2a_;

        // Trial Stress has been calculated
        // check for loading/unloading
//Double Trial_Shear_Stress =std::abs(Stress_Trial.getEffectiveShearStress());
Double Trial_Shear_Stress = std::abs(Stress_Trial.s12());
Double Trial_Theta_Stress = GetTheta(Stress_Trial);
// if unloading accept the stress trial
        bool if_Loading = true;
if ((Trial_Shear_Stress < eff_shear_stressmax_) && (Trial_Theta_Stress >= 0.0))
        {
                s->stnS_ = Stress_Trial;
                if_Loading = false;
                s->working_[4] += eff_shear_stressmax_ *dEv;
                s->working_[5] += 0.0 * dEv;
        }

if ((Trial_Shear_Stress < eff_shear_stressmin_) && (Trial_Theta_Stress <= 0.0))
        {
                s->stnS_ = Stress_Trial;
                if_Loading = false;
                s->working_[4] += 0.0 *dEv;
                s->working_[5] += eff_shear_stressmin_ * dEv;
        }

// if loading re calculate the stress using loading modulus
        if(if_Loading)
        {
                /* SHAMATO POST LIQ STRAINS*/
                Double Gama_Entry=Gama_Max_pre;
                Double Theta_Mc = GetTheta_Real(s->stnS_);
                Double n=(2*(std::pow(3,0.5))*(std::sin(friction_*degrad)))/(3-
                (std::sin(friction_*degrad)));
                Double gtheta=(3-
                (std::sin(friction_*degrad)))/((2*(std::pow(3,0.5))*std::cos(Theta_Mc))-
                (2*std::sin(Theta_Mc)*std::sin(friction_*degrad)));
                Double Mcs= n*gtheta*std::pow(3,0.5);
                Double Mco1= 0.142*Mcs;
                //CONSTANTS
                Double sh_R0=2.0; // R0', R0* and m are constants independent of type of sand
                Double sh_m=0.76;
                Double sh_A=1;//A, B and K are coefficients for Toyoura Sand when (p_i')/p_a =1
                Double sh_B=0.44;
                Double sh_K= 0.554;
                Double sh_alpha=2.598; //Constant related to dilatancy for toyoura sand
                Double sh_Mo=std::tan(25*degrad);

```

```

Double sh_Pa=-100; //atm pressure
    // void ratios
Double e_min=0.635;
Double e_min_star=e_max-1.3*(e_max-e_min);
Double e0=e_max-((relden_/100)*(e_max-e_min));
    // Calculation of Gama_zero (perfectly plastic material state)
//Double q_s =std::pow(std::abs(0.5*(std::pow(std::abs(prin.x()-
prin.z()),2)+std::pow(std::abs(prin.x()-prin.y()),2)+std::pow(std::abs(prin.y()-
prin.z()),2))),0.5);
Double q_n = std::abs(s->stnS_.s12());
Double Gamma_zero = 0.0;
Double Gamma_d=0.0;
Double Gama_Start_negative, Gama_Start_positive;
if (q_n < 1.00)
    {
Gama_Limit_Factor =false;
Double Gama_term = (Gama_Max_N_-Gama_Entry);
Gamma_zero= std::max((sh_R0/Mcsol)*((e0-
e_min_star)/(1+e0))*std::pow(Gama_term,sh_m),Gama_Max_N_);
Gama_Start_negative = std::min(200*shear_strainmax_ - Gamma_zero, 0.0);
Gama_Start_positive = std::max(200*shear_strainmin_ + Gamma_zero, 0.0);
        if (( shear_strain >= 0.0))
            {
Gamma_d = shear_strain *200.0 - Gama_Start_positive;
            }
        if (( shear_strain < 0.0))
            {
Gamma_d = -shear_strain *200.0 + Gama_Start_negative;
            }
        s->working_[35]=Gamma_zero;
Double shear_plastic= std::max(q_n/std::abs(Gamma_zero/200),5.0);
//shear modulus at perfectly plastic material state
Double Bulk_plastic = 2.0*shear_plastic*(1.0+posnu_) / (3.0 * (1-2.0*posnu_));
Double e1a_ = Bulk_plastic + shear_plastic * d4d3;
Double e2a_ = Bulk_plastic - shear_plastic * d2d3;
Double g2a_ = 2.0 * shear_plastic;
Double e11 = s->stnE_.s11();//strain tensors normal components
Double e22 = s->stnE_.s22();
Double e33 = s->stnE_.s33();
Stress_Trial.rs11() =-PWP_*ko_+std::min(+s->stnS_.s11() + e11 * e1a_ + (e22 + e33) *
e2a_),10.0);
Stress_Trial.rs22() =-PWP_+std::min(+s->stnS_.s22() + (e11 + e33) * e2a_ + e22 *
e1a_),10.0);//-PWP;
Stress_Trial.rs33() =-PWP_*ko_+std::min(+s->stnS_.s33() + (e11 + e22) * e2a_ + e33 *
e1a_),10.0);//-PWP;
Stress_Trial.rs12() = s->stnS_.s12() + s->stnE_.s12() * g2a_;
Stress_Trial.rs13() = s->stnS_.s13() + s->stnE_.s13() * g2a_;
Stress_Trial.rs23() = s->stnS_.s23() + s->stnE_.s23() * g2a_;
    }
    else
    {
SymTensorInfo info;
DVect3 prin = s->stnS_.getEigenInfo(&info);

```

```

Double pr_q=std::pow(std::abs(0.5*(std::pow(std::abs(prin.x()-
prin.z()),2)+std::pow(std::abs(prin.x()-prin.y()),2)+std::pow(std::abs(prin.y()-
prin.z()),2))),0.5);
Double a_factor = ((sh_alpha*sh_K)/(Mcs-
sh_Mo))*std::abs(std::pow((ini_mean_eff_stress_/sh_Pa),sh_A));
Double Gamma_d0 =
(a_factor*(std::pow((std::abs(pr_q/(Mcs*ini_mean_eff_stress_))),sh_B)));
if(Gamma_zero_limit!= 0.0)
Gamma_d0 =
std::min((a_factor*(std::pow((std::abs(pr_q/(Mcs*ini_mean_eff_stress_))),sh_B))),
Gamma_zero_limit);
if (( shear_strain >= 0.0))
Gamma_d=(Gamma_d0 + std::abs(s->stnE_.s12()*200));
      if (( shear_strain < 0.0))
Gamma_d = (-Gamma_d0 + std::abs(s->stnE_.s12()*200));
Double shear_granular= std::max(q_n/std::abs(Gamma_d0/200),5.0);
//shear modulus at granular material state
Double Bulk_granular = 2.0*shear_granular*(1.0+posnu_) / (3.0 * (1-2.0*posnu_));
Double e1a_ = Bulk_granular + shear_granular * d4d3;
Double e2a_ = Bulk_granular - shear_granular* d2d3;
Double g2a_ = 2.0 * shear_granular;
Double e11 = s->stnE_.s11();//strain tensors normal components
Double e22 = s->stnE_.s22();
Double e33 = s->stnE_.s33();
Stress_Trial.rs11()=-PWP_*ko_+std::min(+ (s->stnS_.s11() + e11 * e1a_ + (e22 + e33) *
e2a_),10.0);//-PWP+ ;
Stress_Trial.rs22()=-PWP_+std::min(+ (s->stnS_.s22() + (e11 + e33) * e2a_ + e22 *
e1a_),10.0);//-PWP;
Stress_Trial.rs33()=-PWP_*ko_+std::min(+ (s->stnS_.s33() + (e11 + e22) * e2a_ + e33 *
e1a_),10.0);//-PWP;
Stress_Trial.rs12() = s->stnS_.s12() + s->stnE_.s12() * g2a_;
Stress_Trial.rs13() = s->stnS_.s13() + s->stnE_.s13() * g2a_;
Stress_Trial.rs23() = s->stnS_.s23() + s->stnE_.s23() * g2a_;
}
// update the stress and the state variables and exit
Trial_Shear_Stress = std::abs(Stress_Trial.s12());
Trial_Theta_Stress = GetTheta(Stress_Trial);
if ((Trial_Shear_Stress > eff_shear_stressmax_) && (Trial_Theta_Stress >= 0.0))
{
s->working_[4] += Trial_Shear_Stress* dEv;
s->working_[5] =0.0;
}
if ((Trial_Shear_Stress > eff_shear_stressmin_) && (Trial_Theta_Stress <= 0.0))
{
s->working_[4] = 0.0;
s->working_[5] += Trial_Shear_Stress* dEv;
}
}
// Update the stress state and state/memory variables and exit
//Double PWP_ = ini_mean_ver_stress_* (ru_-ru_old_);
s->working_[1] += ru_* dEv;
/*SymTensorInfo info;
DVect3 prin = s->stnS_.getEigenInfo(&info);
prin.rx()=prin.x()-PWP_;
prin.ry()=prin.y()-PWP_*ko_;
```



```

        prin.rz()=prin.z()-PWP_*ko_;
        Stress_Trial2 = info.resolve(prin);
        Stress_Trial.rs11()=Stress_Trial2.s11();
        Stress_Trial.rs22()=Stress_Trial2.s22();
        Stress_Trial.rs33()=Stress_Trial2.s33();*/
        s->stnS_ = Stress_Trial;
        //s->working_[1] += ru_* dEv;
        //;-- update stored strains
        if (s->sub_zone_ == s->total_sub_zones_-1) {
            Double Ev = s->getZoneVolume();
            Double Aux = 1./Ev;
            if (s->overlay_==2) Aux *= 0.5;
            ru_old_ = s->working_[1] * Aux;
if (((s->working_[2] * Aux)> shear_strainmax_) && Gama_Limit_Factor)
            shear_strainmax_ = s->working_[2] * Aux;

if (((s->working_[3] * Aux)< shear_strainmin_)&& Gama_Limit_Factor)
            shear_strainmin_ = s->working_[3] * Aux;
            eff_shear_stressmax_ = s->working_[4] * Aux;
            eff_shear_stressmin_ = s->working_[5] * Aux;
            TStrain11_+= s->working_[11] * Aux;
            TStrain22_+= s->working_[12] * Aux;
            TStrain33_+= s->working_[13] * Aux;
            TStrain32_+= s->working_[14] * Aux;
            TStrain31_+= s->working_[15] * Aux;
            TStrain12_+= s->working_[16] * Aux;
            Gamma_zero_limit = s->working_[35] * Aux*2.0;
        }

        }// post_liquefaction
    }
}
void ModelMetusand::run_Elastic(State *s)
{
    if (s->hysteretic_damping_>0.0)
    {
        Double shear_new = shear_* s->hysteretic_damping_;
        e1_ = bulk_ + shear_new * d4d3;
        e2_ = bulk_ - shear_new * d2d3;
        g2_ = 2.0 * shear_new;
        Double ra = e1_ - rnps_* e2_;
        Double rb = e2_ - rnps_* e1_;
        Double rd = ra - rb * nph_;
        sc1_ = ra / rd;
        sc3_ = rb / rd;
        sc2_ = e2_* (1.0 - rnps_) / rd;
        e21_ = e2_ / e1_;
    }
    // plasticity indicator:
    // store 'now' info. as 'past' and turn 'now' info off
    if (s->state_ & shear_now) s->state_ |= shear_past;
    s->state_ &= ~shear_now;
    if (s->state_ & tension_now) s->state_ |= tension_past;
    s->state_ &= ~tension_now;
}

```

```

int plas = 0;

/* --- trial elastic stresses --- */
Double e11 = s->stnE_.s11();//strain tensors normal components
Double e22 = s->stnE_.s22();
Double e33 = s->stnE_.s33();
s->stnS_.rs11() += e11 * e1_ + (e22 + e33) * e2_;//(2.12) (2.72)
s->stnS_.rs22() += (e11 + e33) * e2_ + e22 * e1_;
s->stnS_.rs33() += (e11 + e22) * e2_ + e33 * e1_;
s->stnS_.rs12() += s->stnE_.s12() * g2_;
s->stnS_.rs13() += s->stnE_.s13() * g2_;
s->stnS_.rs23() += s->stnE_.s23() * g2_;
// default settings, altered below if found to be failing
s->viscous_ = true; // Allow stiffness-damping terms
s->mean_plastic_stress_change_ = 0.0;
}
void ModelMetusand::run(UByte dim,State *s) {
    ConstitutiveModel::run(dim,s);
    if (ini_static_)
        run_Sevinc(s);
    else
        run_Elastic(s);
}
} // namespace models
// EOF

```

B. Generic Simple Shear Test Input for METUSAND

```
*****
SIMPLE SHEAR TEST DATA
Input file
*****
;SPT 7, ko=0.5
config gwflow cppudm
grid 1,1
mo dll exempld
set flow=off
def inputvariables
$scopy=12
$scopyI=0
numsteps = 300000
$EsyyC= -100
end
inputvariables
prop shear=58696 bulk=273919 dens=2.0 relden=39 fric 29 dil 0 ten 0
; Cetin and Bilge, 2014
;prop shear=89866 bulk=234356 dens=2.0 relden=42 fric 29 dil 0 ten 0
;Seed et al. 1970
;prop shear=51200 bulk=133522 dens=2.0 relden=42 fric 29 dil 0 ten 0
; JRA (2002)
;prop shear=46818 bulk=136880 dens=2.0 relden=42 fric 29 dil 0 ten 0
;Andrus and Stoke (1997)
;prop shear=36450 bulk=95056 dens=2.0 relden=42 fric 29 dil 0 ten 0
; Juang (2002)
prop ini_static=1
prop porosity =0.5
fix x
fix y j = 1
attach aside from 1 1 to 1 2 bside from 2 1 to 2 2
;---SET INITIAL STRESSES
apply sxx=-50 i=2
apply sxx -50 i=1
apply syy=-100 j=2
apply sxy=$scopyI j=2
ini sxx=-50
ini syy=-100
ini szz=-50
ini sxy=$scopyI
water bulk = 50000000
solve
print pp
print syy
print esyy
print sxx
print esxx
ini xdisp = 0.0
ini ydisp = 0.0
ini xvel = 1.e-6 j=2
DEF _record_variables
```

```

;
_disp_0 = 0.5*(xdisp(1,1) + xdisp(1,2))
_disp_1 = 0.5*(xdisp(2,1) + xdisp(2,2))
_eps_xx = -100*( _disp_0 - 0)/1.0
;
_disp_0 = 0.5*(ydisp(1,1) + ydisp(2,1))
_disp_1 = 0.5*(ydisp(1,2) + ydisp(2,2))
_eps_yy = -( _disp_0 - _disp_1)/1.0
;
_sig_zz = szz(1,1)
_sig_xx = sxx(1,1)
_sig_yy = syy(1,1)
;
_record_variables = 1.0
;
END
;-----APPLY LOADING
def setup
  $BegSxy = $SxyI - $Sxy15
  $EndSxy = $SxyI + $Sxy15
  $Lside = 1.0
end
setup
def load
  while_stepping
  $sxy = sxy(1,1)
  if $sxy > $sxy15 + $SxyI then
  if $Lside = 1.0 then
    xvel(1,2) = -xvel(1,2)
    xvel(2,2) = -xvel(2,2)
    $BegSxy = $SxyI + $Sxy15
    $EndSxy = $SxyI - $Sxy15
    $Lside = -1.0
  endif
  endif
  if $sxy < -$sxy15 + $SxyI then
  if $Lside = -1.0 then
    xvel(1,2) = -xvel(1,2)
    xvel(2,2) = -xvel(2,2)
    $BegSxy = $SxyI - $Sxy15
    $EndSxy = $SxyI + $Sxy15
    $Lside = 1.0
  endif
  endif
end
def z_val
  while_stepping
  gamma = xdisp(2,2) * 100.0
  $Ru = 1. - (syy(1,1)+pp(1,1))/$EsyyC
  sm=(sxx(1,1)+syy(1,1)+szz(1,1)+3*pp(1,1))/3

  end
;*****
his gamma
his xdis i=1 j=2

```

```
his ydis i=1 j=2
his syy i=1 j=1
his sxx i=1 j=1
his esyy i=1 j=1
his esxx i=1 j=1
his sxy i=1 j=1
his pp i=1 j=1
his $Ru
his ru
his sm
step 1000
plot history 8 line vs 1
plot his 6
plot his 10
plot his 11
plot his 8 vs -6
plot his 8 vs -7
plot his 8 vs -12
```

C. Dynamic Analyses Combinations of Laterally Loaded Piles

Table C.1 Dynamic Analyses Combinations of Laterally Loaded Piles

No	SPT-N	D _R (%)	Pile Length (m)	Pile Diameter (m)	Type	Lateral Load at Pile Head (kN)	Dyn_Acc Factor	Analyses Codes		Analyses Variables
								Free	Free	
1	20	66	15	1.0	Free/Fixed Headed	150	0.05	30C1	30FX1	Basic
2	20	66	15	1.0	Free/Fixed Headed	150	0.1	30C2	30FX2	Basic
3	20	66	15	1.0	Free/Fixed Headed	150	0.2	30C3	30FX3	Basic
4	20	66	15	1.0	Free/Fixed Headed	150	0.3	30C4	30FX4	Basic
5	20	66	15	1.0	Free/Fixed Headed	75	0.05	30C5	30FX5	Load
6	20	66	15	1.0	Free/Fixed Headed	75	0.1	30C6	30FX6	Load
7	20	66	15	1.0	Free/Fixed Headed	75	0.2	30C7	30FX7	Load
8	20	66	15	1.0	Free/Fixed Headed	75	0.3	30C8	30FX8	Load
9	20	66	15	1.0	Free/Fixed Headed	40	0.05	30C9	30FX9	Load
10	20	66	15	1.0	Free/Fixed Headed	40	0.1	30C10	30FX10	Load
11	20	66	15	1.0	Free/Fixed Headed	40	0.2	30C11	30FX11	Load
12	20	66	15	1.0	Free/Fixed Headed	40	0.3	30C12	30FX12	Load
13	20	66	20	1.0	Free/Fixed Headed	150	0.05	30C13	30FX13	Length
14	20	66	20	1.0	Free/Fixed Headed	150	0.1	30C14	30FX14	Length
15	20	66	20	1.0	Free/Fixed Headed	150	0.2	30C15	30FX15	Length
16	20	66	20	1.0	Free/Fixed Headed	150	0.3	30C16	30FX16	Length
17	20	66	8	1.0	Free/Fixed Headed	75	0.05	30C17	30FX17	Length
18	20	66	8	1.0	Free/Fixed Headed	75	0.1	30C18	30FX18	Length
19	20	66	8	1.0	Free/Fixed Headed	75	0.2	30C19	30FX19	Length
20	20	66	8	1.0	Free/Fixed Headed	75	0.3	30C20	30FX20	Length
21	20	66	15	0.8	Free/Fixed Headed	150	0.05	30C21	30FX21	Diameter
22	20	66	15	0.8	Free/Fixed Headed	150	0.1	30C22	30FX22	Diameter
23	20	66	15	0.8	Free/Fixed Headed	150	0.2	30C23	30FX23	Diameter
24	20	66	15	0.8	Free/Fixed Headed	150	0.3	30C24	30FX24	Diameter
25	20	66	15	0.5	Free/Fixed Headed	150	0.05	30C25	30FX25	Diameter
26	20	66	15	0.5	Free/Fixed Headed	150	0.1	30C26	30FX26	Diameter

**Table C.1 Dynamic Analyses Combinations of Laterally Loaded Piles (to
be continued)**

No	SPT-N	D _R (%)	Pile Lenght (m)	Pile Diameter (m)	Type	Lateral Load at Pile Head (kN)	Dyn_Acc Factor	Analyses Codes		Analyses Variables
								Free	Free	
27	20	66	15	0.5	Free/Fixed Headed	150	0.2	30C27	30FX27	Diameter
28	20	66	15	0.5	Free/Fixed Headed	150	0.3	30C28	30FX28	Diameter
29	15	57	15	1.0	Free/Fixed Headed	150	0.05	30C29	30FX29	D _R
30	15	57	15	1.0	Free/Fixed Headed	150	0.1	30C30	30FX30	D _R
31	15	57	15	1.0	Free/Fixed Headed	150	0.2	30C31	30FX31	D _R
32	15	57	15	1.0	Free/Fixed Headed	150	0.3	30C32	30FX32	D _R
33	15	57	15	0.8	Free/Fixed Headed	150	0.05	30C33	30FX33	Diameter
34	15	57	15	0.8	Free/Fixed Headed	150	0.1	30C34	30FX34	Diameter
35	15	57	15	0.8	Free/Fixed Headed	150	0.2	30C35	30FX35	Diameter
36	15	57	15	0.8	Free/Fixed Headed	150	0.3	30C36	30FX36	Diameter
37	15	57	15	0.5	Free/Fixed Headed	150	0.05	30C37	30FX37	Diameter
38	15	57	15	0.5	Free/Fixed Headed	150	0.1	30C38	30FX38	Diameter
39	15	57	15	0.5	Free/Fixed Headed	150	0.2	30C39	30FX39	Diameter
40	15	57	15	0.5	Free/Fixed Headed	150	0.3	30C40	30FX40	Diameter
41	15	57	15	1.0	Free/Fixed Headed	75	0.05	30C41	30FX41	Load
42	15	57	15	1.0	Free/Fixed Headed	75	0.1	30C42	30FX42	Load
43	15	57	15	1.0	Free/Fixed Headed	75	0.2	30C43	30FX43	Load
44	15	57	15	1.0	Free/Fixed Headed	75	0.3	30C44	30FX44	Load
45	15	57	15	1.0	Free/Fixed Headed	40	0.05	30C45	30FX45	Load
46	15	57	15	1.0	Free/Fixed Headed	40	0.1	30C46	30FX46	Load
47	15	57	15	1.0	Free/Fixed Headed	40	0.2	30C47	30FX47	Load
48	15	57	15	1.0	Free/Fixed Headed	40	0.3	30C48	30FX48	Load
49	15	57	20	1.0	Free/Fixed Headed	150	0.05	30C49	30FX49	Length
50	15	57	20	1.0	Free/Fixed Headed	150	0.1	30C50	30FX50	Length
51	15	57	20	1.0	Free/Fixed Headed	150	0.2	30C51	30FX51	Length
52	15	57	20	1.0	Free/Fixed Headed	150	0.3	30C52	30FX52	Length
53	15	57	8	1.0	Free/Fixed Headed	40	0.05	30C53	30FX53	Length-Load
54	15	57	8	1.0	Free/Fixed Headed	40	0.1	30C54	30FX54	Length-Load

**Table C.1 Dynamic Analyses Combinations of Laterally Loaded Piles
(to be continued)**

No	SPT-N	D _R (%)	Pile Length (m)	Pile Diameter (m)	Type	Lateral Load at Pile Head (kN)	Dyn_Acc Factor	Analyses Codes		Analyses Variables
								Free	Free	
55	15	57	8	1.0	Free/Fixed Headed	40	0.2	30C55	30FX55	Length-Load
56	15	57	8	1.0	Free/Fixed Headed	40	0.3	30C56	30FX56	Length-Load
57	15	57	15	0.8	Free/Fixed Headed	75	0.05	30C57	30FX57	Diameter-Load
58	15	57	15	0.8	Free/Fixed Headed	75	0.1	30C58	30FX58	Diameter-Load
59	15	57	15	0.8	Free/Fixed Headed	75	0.2	30C59	30FX59	Diameter-Load
60	15	57	15	0.8	Free/Fixed Headed	75	0.3	30C60	30FX60	Diameter-Load
61	8	42	15	1.0	Free/Fixed Headed	150	0.05	30C61	30FX61	D _R
62	8	42	15	1.0	Free/Fixed Headed	150	0.1	30C62	30FX62	D _R
63	8	42	15	1.0	Free/Fixed Headed	150	0.2	30C63	30FX63	D _R
64	8	42	15	1.0	Free/Fixed Headed	150	0.3	30C64	30FX64	D _R
65	8	42	15	0.8	Free/Fixed Headed	150	0.05	30C65	30FX65	Diameter
66	8	42	15	0.8	Free/Fixed Headed	150	0.1	30C66	30FX66	Diameter
67	8	42	15	0.8	Free/Fixed Headed	150	0.2	30C67	30FX67	Diameter
68	8	42	15	0.8	Free/Fixed Headed	150	0.3	30C68	30FX68	Diameter
69	8	42	15	0.8	Free/Fixed Headed	75	0.05	30C69	30FX69	Diameter-Load
70	8	42	15	0.8	Free/Fixed Headed	75	0.1	30C70	30FX70	Diameter-Load
71	8	42	15	0.8	Free/Fixed Headed	75	0.2	30C71	30FX71	Diameter-Load
72	8	42	15	0.8	Free/Fixed Headed	75	0.3	30C72	30FX72	Diameter-Load
73	8	42	15	0.8	Free/Fixed Headed	40	0.05	30C73	30FX73	Diameter-Load
74	8	42	15	0.8	Free/Fixed Headed	40	0.1	30C74	30FX74	Diameter-Load
75	8	42	15	0.8	Free/Fixed Headed	40	0.2	30C75	30FX75	Diameter-Load
76	8	42	15	0.8	Free/Fixed Headed	40	0.3	30C76	30FX76	Diameter-Load
77	8	42	20	0.8	Free/Fixed Headed	40	0.05	30C77	30FX77	Diameter-Length
78	8	42	20	0.8	Free/Fixed Headed	40	0.1	30C78	30FX78	Diameter-Length
79	8	42	20	0.8	Free/Fixed Headed	40	0.2	30C79	30FX79	Diameter-Length
80	8	42	20	0.8	Free/Fixed Headed	40	0.3	30C80	30FX80	Diameter-Length

CURRICULUM VITAE

Sevinç ÜNSAL ORAL

Address : Öveçler 4. Cad. 97/5, Çankaya, Ankara
Mobile Phone : +90 505 4686109
E-mail : sevinc.unsal@gmail.com
Date of birth : 16 July, 1983, Karabük, Turkey
Nationality : Republic of Turkey

EDUCATION

2009 – 2014 (anticipated)	Ph. D. Degree Middle East Technical University Department of Civil Engineering, Division of Geotechnical Engineering, Ankara, Turkey
2006 - 2009	M.Sc. Degree Middle East Technical University Department of Civil Engineering, Division of Geotechnical Engineering, Ankara, Turkey
2001 - 2006	B.S. Degree Middle East Technical University Department of Civil Engineering, Ankara, Turkey
1994 - 2001	High School Safranbolu Anatolian High School, Karabük, Turkey

PROFESSIONAL EXPERIENCE

Nov. 2006 - Dec. 2013	Research Assistant at Middle East Technical University, Department of Civil Engineering, Division of Geotechnical Engineering Ankara, Turkey
Feb. 2012 – Feb. 2014	Researcher at GeoDestek Ltd. Sti. KOSGEB Branch Office, METU, Ankara, Turkey
July 2012 - Feb. 2013	Researcher at Rocscience Inc., Toronto, Canada
July 2006 – Nov. 2006	Project Engineer at Yapı Teknik Eng. Company, Ankara, Turkey
Summer 2004	Intern Site Engineer at Prokon Engineering Company, Ankara, Turkey
Summer 2005	Intern Project Engineer at Prokon Engineering Company, Ankara, Turkey

THESIS AND DISSERTATION

Unsal Oral, S. (2009) An Integrated Seismic Hazard Framework for Liquefaction Triggering Assessment of Earthfill Dams' Foundation Soils. M.Sc. thesis, Department of Civil Engineering, Middle East Technical University, Ankara, 150 pages.
(Supervisor: Prof. Dr. Kemal Önder ÇETİN)

TECHNICAL MANUSCRIPTS

- Oral S. U., Cetin K. O., Erol O, İnci G., Delice M, 2011. "Performance Assessment of Izmirspor Metro Station." 15th European Conference on Soil Mechanics and Geotechnical Engineering (ECSMG 2011), Athens, Greece, September 12-15 2011.
- Unsal, S., Cetin, K. O., 2010. "Effective Stress Based Numerical Assessment of Liquefaction Induced Landslide at Degirmendere Cape, Izmit Bay During Kocaeli (Izmit)-Turkey Earthquake." Fifth International Conference on Recent Advances in Geotechnical Earthquake Engineering and Soil Dynamics and Symposium in Honor of Profesor I.M. Idriss, San Diego, California, U.S.A, May 24-29 2010.
- Unsal, S., Yunatci, A., Cetin, K. O., 2009. "An Integrated Seismic Hazard Framework for Assessing the Liquefaction Triggering of Dam Foundation Soils." International Conference on Performance Based Design in Earthquake Geotechnical Engineering, IS-Tokyo 2009, Tsukuba, Japan, 15-17 June 2009.
- Cetin, K. O., Unsal, S., Yunatci, A., 2009. "Baraj Temellerinde Sıvılaşma Tetiklenmesi Belirlemesi için Tümüleşik Sismik Tehlike Analizi Yaklaşımı." Uluslararası Katılımlı II. Ulusal Baraj Güvenliği Sempozyumu, Osmangazi Üniversitesi, Eskisehir, 13-15 Mayıs 2009.

AWARDS AND HONORS

July 2012 – Feb. 2013 International Research Fellowship provided by the Scientific Research and Technical Council of Turkey (TUBITAK).

LANGUAGES

English : Advanced level
German : Beginner level

COMPUTER SKILLS

Various softwares related to geotechnical engineering and geotechnical earthquake engineering (finite element / finite difference software) as well as computer programming in C++ in Visual Basic.

HOBBIES

Plates, swimming, piano.